UC Riverside
UC Riverside Electronic Theses and Dissertations

Title
Dynamic High Pressure Study of Chemistry and Physics of Molecular Materials

Permalink
https://escholarship.org/uc/item/61t6j36v

Author
Jezowski, Sebastian Ryszard

Publication Date
2013

Peer reviewed|Thesis/dissertation

UNIVERSITY OF CALIFORNIA
RIVERSIDE

Dynamic High Pressure Study of Chemistry and Physics
of Molecular Materials

A Dissertation submitted in partial satisfaction
of the requirements for the degree of

Doctor of Philosophy

in

Chemistry

by

Sebastian Ryszard Jezowski

March 2013

Dissertation Committee:
      Dr. Eric L. Chronister, Chairperson
      Dr. Christopher J. Bardeen
      Dr. Yadong Yin

The Dissertation of Sebastian Ryszard Jezowski is approved:

_____

_____

_____
Committee Chairperson

University of California, Riverside

ACKNOWLEDGEMENTS

in general in the USA. This is thanks to Dr. Leonard Mueller and Dr. Kevin Simpson that I was able to continuously teach the "Discussion in Chemistry" sections while researching at UCR.

My desire to pursue research in Physical Chemistry is thanks to Dr. hab. Anna Szemik-Hojniak and Dr. hab. Zdzislaw Latajka, both fantastic mentors from University of Wroclaw, Poland.

I would like to thank Dr. Ming Lee Tang who was kind enough to allow me to get more insight into Single Molecule Spectroscopy towards the end of my graduate program at UCR.

FORMAL ACKNOWLEDGEMENTS

This dissertation is dedicated to Chelsea Hertzog who is too sick to complete her graduate work at Harvard University

ABSTRACT OF THE DISSERTATION

Dynamic High Pressure Study of Chemistry and Physics
of Molecular Materials

by

Sebastian Ryszard Jezowski

Doctor of Philosophy, Graduate Program in Chemistry
University of California, Riverside, March 2013
Dr. Eric Chronister, Chairperson

Both temperature and pressure control and influence the packing of molecules in crystalline phases. Our molecular simulations indicate that at ambient pressure, the cubic polymorph of tetracyanoethylene, TCNE, is the energetically stable form up to ~ 160 K. The observed transition from the cubic to the monoclinic polymorph occurs however only at temperatures above ~ 318 K due to the large transition barrier. The temperature-induced phase transition in TCNE studied with high-resolution IR spectroscopy is explained in terms of the increased vibrational entropy in the crystals of the monoclinic polymorph.

Based upon the inverted design of the Merril-Bassett Diamond Anvil Cell, an improved, second generation dynamic Diamond Anvil Cell was developed. Based on the fluorescence of ruby crystals, we were able to demonstrate that the pressure variation range can be further increased at least up to 7 kbar and that the dynamic pressure compression of up to 1400 GPa/s can be achieved.

A new class of mechanophoric system, bis-anthracene, BA, and its photoisomer, PI, is shown to respond reversibly to a mild, static pressure induced by a Diamond Anvil Cell as well as to shear deformation based on absorption spectroscopic measurements. The forward reaction occurs upon illumination with light while the back-reaction may be accelerated upon heating or mechanical stress, coupled to a rehybridization on four equivalent carbon atoms. It is an intriguing result as high pressure stabilizes the photodimerized species in related systems. Our molecular volume simulations ruled out significant differences in the volumes between bis-anthracene and its photoisomer. Kinetic absorption measurements at several different pressures reveal a negative volume of activation in the exothermic back-reaction at room temperature. Through a series of temperature-dependent kinetic measurements it is shown that the barrier of activation for the back-reaction is reduced by more than an order of magnitude at several kbar pressure. Results are compared to the photoisomer of 9-anthroic anhydride and to the Dewar photoisomer. A two-step model involving the transition state is proposed for the pressure-induced PI-to-BA conversion, explaining the mechanism of the reaction occurring upon the application of homogeneous stress.

TABLE OF CONTENTS

Chapter 3: Improvements in the Performance of the Dynamic Diamond Anvil Cell (dDAC)

Chapter 4: Spectroscopy, Thermodynamics and Molecular Modeling of Bis-Anthracene and its Photoisomer

Chapter 5: Mechanochemistry and Energetics of Selected Strained Photoisomers

TABLE OF FIGURES

Chapter 5:

Appendix:

TABLE OF TABLES

Appendix:

Chapter I

An Introduction to Polymorphism, High-Pressure Experimental

Studies and Mechanochemistry

1.1 The Importance of Phase Change

Unlike gasses, liquids and amorphous solids, many molecular solids are known to exist in various types of crystal structures that differ in structural motifs[1]. These unique crystalline phases, referred to as polymorphs, form at different thermodynamic conditions: pressure and/or temperature with only one polymorphic form thermodynamically stable. The process is dynamic. Once the conditions change, the higher energy (metastable) polymorphs have the tendency to evolve with time into the more thermodynamically stable polymorphs in a process referred to as polymorphic phase transition. Often however, due to kinetic constrains, metastable forms may co-exist in the presence of the thermodynamically stable polymorphs. While all polymorphs have identical chemical composition for a given solid, they often manifest very different physico-chemical properties, even the melting temperature.

Polymorphism is a very common phenomenon and is found in a variety of crystalline materials exhibiting rich solid-state behavior: minerals (such as calcium carbonate), metals (tin), many molecular crystals (tetracyanoethylene, TCNE presented in Chapter 2) and in certain types of crystalline polymers.

Crystal polymorphism was recognized as a phenomenon by the work of Mitscherlich[2] in 1823. In an earlier work however, published much sooner, in 1788, Klaproth[3] described three distinct crystal forms of a mineral calcium carbonate, now known as calcite, aragonite and vaterite with the latter and the former being the metastable forms of the calcite mineral, spontaneously converting at ambient conditions.

The conversion of thermodynamically unstable polymorphs is often accompanied by the change in some physical and chemical properties such as color, shape and size of crystals (surface area), mechanical properties (thermal expansion, hardness) and even altered chemical reactivity.

In fact it may come as a surprise to the reader of this Chapter that chocolate and especially one of its main ingredients, the cocoa butter, is a crystalline, polymorphic substance. Depending on the conditions, cocoa butter can crystallize into six polymorphic forms[4] at ambient pressure. This is due to the different arrangement of the lipid molecules and not the chemical composition of this delicious product. With each polymorph represented by different texture and

melting points, only the crystal form named "V" is the well-known and most appreciated glossy, relatively hard form of cocoa butter.

The process of screening for different polymorphic forms is a tedious task and is usually accomplished with the use of a wide variety of analytical tools, such as the spectroscopic techniques (absorption, emission), differential scanning calorimetry, thermogravimetric analysis and X-ray as well as neutron powder diffraction. For forms thermodynamically stable only at low temperatures, either IR absorption (or transmission), Raman spectroscopy or X-ray diffraction are the preferred analytical methods to be applied. These most suitable techniques deliver quantitative information and unveil polymorphs as they undergo a phase transition to another form.

Since both temperature and pressure have the power to influence the outcome of a crystallization process in molecular solids, tuning either of the two thermodynamic parameters will thus allow the exploration of different crystalline forms and observe their mutual interconversion.

Specifically, in Chapter 2 we use ultra-high resolution IR spectroscopy technique (down to 0.01 cm^{-1} resolution) to understand and to explain the temperature-induced phase transition in crystals of tetracyanoethylene (TCNE). By varying the temperature by several Kelvin at ambient pressure, two forms of crystalline TCNE have been grown out of a solution. X-ray[5,6] and neutron[7] powder diffraction have also been applied to TCNE to describe the changes

observed in the crystals of this relatively simple molecular compound. Unintentionally we have been able to grow mixed crystals of two different polymorphs of TCNE and record their IR spectrum, presented in Chapter 2.

What is more, TCNE is an example of a molecular solid that shows an energy barrier (activation energy) for a phase transition[7]. The existence of such barrier renders certain polymorphs metastable at given temperature and pressure conditions.

To explain the relative stabilities of the different polymorphic forms of TCNE at ambient pressure, we performed DFT+vdW quantum computation analysis on the cubic and monoclinic phases of the molecular solid. In combination with the experimental analysis we were able to explain their relative stability on the basis of increased vibrational entropy of the monoclinic polymorph as a result of higher number of close contacts as compared to the cubic phase[8].

In spite of the scientific progress on understanding the phenomenon of polymorphism, to date it still remains a great challenge to predict exactly how many polymorphic forms will a newly synthesized or extracted substance form and at what temperatures are they thermodynamically stable. More work is also necessary on understanding whether stable co-crystals can be grown with other substances.

1.2 Static and Dynamic Pressure Methods: History and State-of-the Art

The static high-pressure method

At the times when high-pressure research was still in its infancy, scientists realized that it would be beneficial to watch the sample while being exposed to high pressure at the same time. In 1949 Andrew W. Lawson and Ting Y. Tang applied the hardest substance known, the transparent diamond in their high-pressure research. This is not yet the final version of a diamond anvil cell in use today but was a revolutionary device at those times. Two halves of a diamond were pressed against each other on the principle of a mechanical press, supported by two metal pins through holes drilled in the gemstone. It was called by its inventors the "split-diamond bomb" and was capable of generating pressures up to 20 kbar[9].

The most important physical properties of a diamond that made it the essential part of a high-pressure tool are its hardness, lowest compressibility of all known materials, transparency to IR, visible and UV light as well as to X-rays. All of that translates into the wide variety of noninvasive analytical techniques that can be applied to samples at high-pressure. Due to the low molar mass of carbon, diamond is highly transparent to X-ray radiation and thus it is an ideal material to contain crystalline samples to a very small volume.

With the very basic formula that relates the area (A) of the culets with a force (F) applied to the diamond, the amount of pressure (P) could be estimated:

$$P = \frac{F}{A}$$

As strange as it may seem today, in the early stages of high-pressure research no gasket was applied between the two diamond culets - the flat tips of diamond anvils, Figure 1.1. As a result of misaligned culets, in certain materials, such as the CuBr[9], a pressure gradient could clearly be resolved under an optical microscope as a change in color. With no gasket in place, the gradient in pressure was seen as a unique opportunity and was explored by guiding the various analytical beams of photons through different regions of the cullet. During careless experiments however, diamond would easily scratch another diamond and render it useless for further experiments. Therefore a great care had to be taken to prevent that from happening. This problem was nearly completely eliminated with the application of a metal gasket introduced in later designs.

It was only a matter of time before the application of a diamond in high-pressure research, allowing for visual inspection of samples. Years after the first application of a diamond into high-pressure research, another revolutionary addition to the diamond anvil cell (DAC) changed the field forever. A thin, supporting gasket was introduced in between the culets, an event triggered by the pioneer in this field, Alvin Van Valkenburg. This integral part of nearly each

DAC soon allowed for the rates of many phase transitions to be accurately measured. With the use of a microscope, phase boundaries, recrystallization and even chemical reactions could be observed in solid samples suspended in a pressure-mediating liquid. The mixture of three liquids methanol, ethanol and small amount of water in strict proportions was soon discovered to support the hydrostatic pressure to slightly above 10 GPa[9]. As it turned out, the introduction of an elastic gasket further increased the limit of pressure and allowed for uniform (homogeneous) pressure redistribution throughout the sample.

With time, the DAC evolved into the modern, relatively compact design brought by Leo Merril and William Bassett[9], with a metal gasket that contains the sample, Figure 1.1. Slowly, the Merril-Basset diamond anvil cell has been widely accepted in high-pressure laboratories around the world and used in studies on liquid and solid samples, with the pressure range up to 100 kbar. The body of a typical DAC consists of two triangular platens, pulled against each other along guiding rods by three screws. The relatively compact design of DAC allows for an easy attachment within most optical absorption spectrometers, as we discuss in Chapter 4. It also fits into most FTIR spectrometers or on top of a stage of an IR microscope and can be easily mounted on a goniometer head.
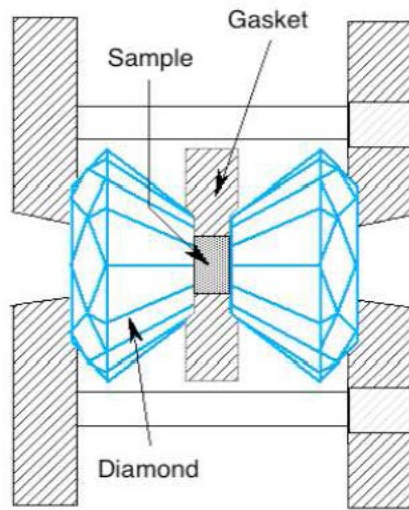
Figure 1.1: An illustration of a Merril-Basset DAC in use in the laboratories

The determination of the homogeneous pressure within a DAC initially posed great challenge. Dan Decker[10] provided reliable compressibility scale based on the lattice parameters of crystalline NaCl from its equation of state. Crystal lattice parameters could however only be determined by X-ray analysis with samples in DAC. Only a few years later, in 1971 the ruby calibration methods had been widely accepted. This secondary, spectroscopic method allowed for a relatively easy method to determine the pressure, with two closely-spaced ruby emission peaks named R_1 and R_2. The spacing between the two peaks is sensitive to any pressure inhomogeneity in that peaks broaden to the point that they begin overlapping each-other. The emission of ruby dust was calibrated against the NaCl standard. With the advances in laser technology

8

allowing for higher-power green lasers to induce emission in the smallest amount of the material, the ruby method became widely accepted throughout the world.

An empirically-derived formula allowing for the pressure determination from the spectral shift of ruby emission has been proposed[11] by Mao *et al.*:

$$P(Mbar) = \frac{a}{b}\left[\left(1 + \frac{\Delta\lambda}{\lambda_0}\right)^b - 1\right]$$

with the following experimental parameters:

a=19.04 Mbar, b=5, λ_0=6942 Å. The $\Delta\lambda$ corresponds to the observed pressure-dependent shift of the R_1 ruby peak in Å.

Many research interests involve the application of high-temperature to overcome kinetic barriers in samples already exposed to homogeneous pressures. This was initially achieved with wrapping resistance wires around the diamonds, a method that we applied in the experimental work on the BA/PI pair of mechanophores[12], and later with high-intensity lasers directed at the sample compartment. The temperature within the DAC can be determined either with a thermocouple or at extreme temperatures with the help of a spectrometer by referencing the visible spectrum emanating from the sample to a blackbody spectra published in the literature.

The advent of dynamic high-pressure methods

Kinetics of pressure-induced phase changes of crystalline materials have sparsely been examined due to the unavailability of a dynamic high-pressure method operating on a time scale comparable to the rate of such transition. The recent emergence of such method was initiated by the development of a new tool on the basis of the static high-pressure device[13]: the dynamic Diamond Anvil Cell, dDAC, Figure 1.2.
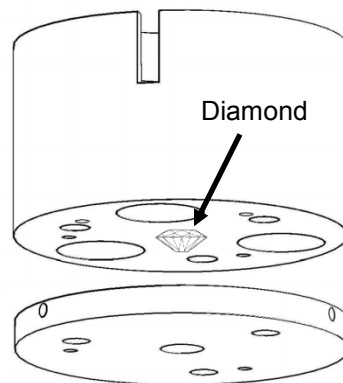
Figure 1.2: An illustration of a second generation dDAC: the top (body) and the bottom (backing) plates with two diamonds in between. Plates are held together by three long bolts

Because dynamic and static experiments operate at very different time-scales, they are complimentary, high-pressure techniques. Phase and structure of many important materials (i.e. water) are not only affected by temperature and pressure but also by the rate at which such pressure change is applied. The

compression rate of a material is defined as how quickly the anvils can come close together, apply and release the pressure, all in one cycle. These are the large[14] (>5 kbar) and fast (µs) pressure jumps that trigger the physical and/or chemical changes. Such reversible, fast pressure changes at high repetition rates will allow for new technologies to emerge and be evaluated with this promising tool[14].

Certain structural properties of polymers change on relatively long time-scales. The evolution of these disordered systems towards the equilibrium global minimum proceeds through small but constant changes in physical properties. These structural changes can be greatly accelerated with repetitive pressure-jump method, available through dDAC, causing so called aging in polymers[14].

Both static and dynamic pressure alter the rates and types of phase transitions in crystalline materials. The influence of the dynamic pressure on the phase transitions in water was observed with the use of a dDAC[15,16]. The shape and the duration of the compression rate play an important role in the growth of the different phases of ice. Several different types of dDAC devices were developed at University of California, Riverside. The reversible phase transition of water to Ice VI and Ice VI to Ice VII, initiated with an original design (the first generation) of a dDAC has been documented in the laboratories of Dr. E. Chronister[17]. In Chapter 3 we describe the modifications of our existing first generation design with the main goal of increasing the variation range at a given

pressure. We also increase and evaluate the dynamic range of this device. As a result of this work we manufactured, improved and characterized the second generation dDAC.

1.3 Mechanochemistry in Molecular Materials

The effects of mechanical energy in certain physico-chemical processes were observed and applied in practice as early as in the era of Aristotle. One example is mercury extracted by mechanical treatment of cinnabar (HgS) in a brass mortar equipped with a pestle in the presence of vinegar[18]. This method of recovering mercury from its naturally occurring mineral was described by Theophrastus of Eresus (371 – 286 B.C.). The other known way to extract mercury from its mineral is by applying harsh conditions with the release of toxic fumes, by roasting at elevated temperatures in furnaces in the presence of oxygen.

The two important benefits of conducting mechano-activated reactions are the possibility of performing identical reactions at low instead elevated temperatures and the much increased reaction rates at comparable temperatures. This comes as a result of lowered activation energy for a chemical

reaction. The term mechanochemistry was introduced into physical chemistry as early as in 1891 by Ostwald[19].

In order to break a typical C-C covalent bond present in majority organic compounds, one needs to apply pressure on the order of 100 kbar (or 10 GPa). These very high pressures cannot be easily generated. Anisotropic or directed forces can be induced in several ways, for instance by generating shock-waves, with scanning probe microscopy tips (AFM) or by bubble cavitation under ultrasonic treatment. There are also other, less popular methods to generate pressure gradient that are more specifically intended to study polymers with mechanophoric centers[20]. Milling and grinding have always been the alternative methods to apply shear stress and pressure and are still popular in the industry. There are of course limitations to each of the methods above.

The Diamond Anvil Cell (DAC) is yet another tool that allows for the generation of isotropically-distributed compressive force. High pressure study of mechanophoric systems is possible theoretically up to ~ 100 kbar with the use of a DAC device. It has an advantage over the popular sonication methods in that any heat that is generated in the process is quickly dissipated through the diamonds to the bulk metal casing. Molecules that are known to undergo bond cleavage by mild pressure may also respond in a similar way to high temperature[12,21] which is intrinsic to the bubble-cavitation method. Once the liquid-free (bubble) zone is formed during sonication process, the bubble

collapses rapidly, generating locally thousands of Kelvins of parasitic heat. As is shown in Chapter 5, both temperature and pressure have the same effect on the BA/PI pair, accelerating the recovery of BA from its photoisomer: heat provides enough energy to cross-over the free energy barrier for the PI-to-BA conversion while mild pressure lowers the same activation barrier by more than one order of magnitude, allowing the photoproduct to dissociate at room temperature[12]. Thus, it is essential to decouple the two thermodynamic parameters, pressure and temperature in studies on mechanophoric systems. This can be achieved with the use of a DAC device.

For specific industrial applications it is often more feasible to make the pressure- or stress-sensitive chemical bond a part of a backbone of a polymer chain which would be aware of its local mechanical environment. Once successfully incorporated by synthetic methods, mechanophores and thus the initially (nearly) colorless polymer signal a breaking point by changing its color[22] to bright red. This stress-induced changes take place thanks to spiropyran-based units which undergo 6-π electrocyclic ring-opening reaction and turning red only when sufficient amount of mechanical energy or heat is transduced to the enhanced polymer.

It seems therefore that the first and most obvious application for molecules showing mechanophoric properties is damage sensing. An early warning sign in the form of a change in color could inform an engineer that a material had

already accumulated enough mechanical stress. Special, intelligent coatings may signal that the crucial parts of a bridge or an airplane wing need to be replaced after having been exposed to overwhelming forces. Tiny fibers containing mechanophoric polymers could be incorporated into suspension lines of parachutes, possibly saving lives by signaling methods.

Mechanical stress was shown to control reactions that are otherwise inaccessible[23]. In chemistry we are used to applying energy in the form of heat, electricity or light to induce changes and thus control reaction pathways. With mechanical force it is possible to deform reactants along a specific direction and alter the shape of potential energy surfaces which results in the formation of reaction products that cannot be generated with the application of heat or light.

It has been shown that certain small molecules on their own, such as BA/PI are capable of storing some fraction of the electromagnetic energy released from the Sun in the form of visible light, and expelling it in the form of heat only when exposed to higher temperatures[24] or mild pressures[12]. Such systems could operate in a closed-cycle, in areas where solar energy is abundant. A solar-thermal energy conversion unit has even been proposed in the literature[24] in the late 70's. The amount of heat generated in the back-reaction can be engineered by varying the length and the type of linkers in linked anthracenes[25], such as the BA/PI pair. Changing the type of molecular linker from dimethyl to $[-CH_2-N(-R)-CH_2-]$ and substituting numerous groups into the R

position has been shown to dramatically affect the thermodynamics of the dimerization process[25]. The absorption spectrum of the energy-conversion materials can be tuned by replacing anthracenes with other polyacenes such as tetracene and pentacene. Longer polyacenes absorb longer (lower energy) wavelengths which are more readily available at the surface of the Earth.

Isotropic high-pressure (13 kbar) generated in a DAC in our research laboratories, led by Dr. Eric Chronister was shown to stabilize dipentacene dimers[26]. Surprisingly, in the case of linked anthracenes, the BA/PI pair, the effect of high-pressure on the molecular system is opposite: higher pressure disfavors the presence of dimerized species[12]. On one hand the two dimethyl linkers present in BA facilitate the intramolecular [4+4] cycloaddition reaction by light at ambient pressure (0 kbar) with the formation of a geometrically-strained photoisomer. On the other hand, the same linkers dramatically influence the behavior of the "dimer" (PI) exposed to higher pressures as compared to a structurally similar dianthracene (An_2).

In the last words of this introduction we wanted to stress that mechanochemistry is a relatively new field which requires major advancements through careful studies. New classes of mechanophoric materials are much needed for this new field to evolve and find applications in the lives of modern societies.

1.4 References

(1)   Braga, D.; Grepioni, F.; Maini, L.; Polito, M. *Struct Bond* **2009**, *132*, 25.

(2)   Mitscherlich, E. *Abhl Akad Berlin* **1823**, 43.

(3)   Klaproth, M. H. *Bergmannische J. I* **1798**, 294.

(4)   Roth, K. *Chemie in unserer Zeit* **2005**, *39*, 416.

(5)   Little, R. G.; Pautler, D.; Coppens, P. *Acta Crystall B-Stru* **1971**, *B 27*, 1493.

(6)   Bekoe, D. A.; Trueblood, K. N. *Zeitschrift für Kristallographie* **1960**, *113*, 1.

(7)   Mukhopadhyay, R.; Chaplot, S. L.; Rao, K. R. *Phys Status Solidi A* **1985**, *92*, 467.

(8)   Schatschneider, B.; Liang, J. J.; Jezowski, S.; Tkatchenko, A. *Crystengcomm* **2012**, *14*, 4656.

(9)   Bassett, W. A. *High Pressure Res* **2009**, *29*, Cp5.

(10)   Decker, D. L. *J Appl Phys* **1965**, *36*, 157.

(11)   Mao, H. K.; Bell, P. M.; Shaner, J. W.; Steinberg, D. J. *J Appl Phys* **1978**, *49*, 3276.

(12)   Jezowski, S. R.; Zhu, L. Y.; Wang, Y. B.; Rice, A. P.; Scott, G. W.; Bardeen, C. J.; Chronister, E. L. *J Am Chem Soc* **2012**, *134*, 7459.

(13)   Evans, W. J.; Yoo, C. S.; Lee, G. W.; Cynn, H.; Lipp, M. J.; Visbeck, K. *Rev Sci Instrum* **2007**, *78*.

(14)   Chronister, E. L. *SGER: Development of Dynamic Diamond Anvil Cell Spectroscopy*; University of California, 2007.

(15)   Lee, G. W.; Evans, W. J.; Yoo, C. S. *P Natl Acad Sci USA* **2007**, *104*, 9178.

(16)   Lee, G. W.; Evans, W. J.; Yoo, C. S. *Phys Rev B* **2006**, *74*.

(17)   Rice, A.; Proquest, 2011Dynamic High Pressure Measurements and Molecular Dynamic Simulations of Phase Changes and Vibrational Dynamics in Molecular Solids.

(18)   Baláž, P.; Choi, W. S.; Fabián, M.; Godočíková, E. *Acta Montanistica Slovaca* **2006**, *2*, 122.

(19)   Todres, Z. V. *Organic Mechanochemistry and Its Practical Applications*; CRC Press Taylor & Francis, 2006.

(20)   Potisek, S. *PhD Thesis, Urbana, Illinois* **2003**.

(21)   Karthikeyan, S.; Sijbesma, R. P. *Nat Chem* **2010**, *2*, 436.

(22)   Davis, D. A.; Hamilton, A.; Yang, J. L.; Cremar, L. D.; Van Gough, D.; Potisek, S. L.; Ong, M. T.; Braun, P. V.; Martinez, T. J.; White, S. R.; Moore, J. S.; Sottos, N. R. *Nature* **2009**, *459*, 68.

(23)   Hickenboth, C. R.; Moore, J. S.; White, S. R.; Sottos, N. R.; Baudry, J.; Wilson, S. R. *Nature* **2007**, *446*, 423.

(24)   Jones, G.; Reinhardt, T. E.; Bergmark, W. R. *Sol Energy* **1978**, *20*, 241.

(25)   Usui, M.; Shindo, Y.; Nishiwaki, T.; Anda, K.; Hida, M. *Chem Lett* **1990**, 419.

(26)   Berg, O.; Chronister, E. L.; Yamashita, T.; Scott, G. W.; Sweet, R. M.; Calabrese, J. *J Phys Chem A* **1999**, *103*, 2451.

Chapter II

The Relative Stabilities of TCNE Polymorphs

2.1 Introduction

Crystalline tetracyanoethylene, TCNE (C_6N_4), Figure 2.1, displays rich solid state phase behavior under different temperature and pressure conditions. Two carbon atoms are in sp^2 and four in sp configuration which makes TCNE a planar molecule. It is the strongest π acid[1] and an electron acceptor in numerous charge-transfer complexes. Tetracyanoethylene has been found to be particularly useful in studies on organic superconductors[2] and molecule-based magnets[3]. It is readily soluble in organic solvents, including ethyl acetate and over time, TCNE decomposes in moist air with the release of toxic hydrogen cyanide gas.
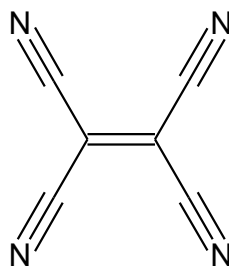
Figure 2.1: The molecular structure of tetracyanoethylene, TCNE (C_6N_4)

2.1.1 The Cubic and Monoclinic Phases of TCNE

The thermodynamic and kinetic properties of TCNE are relatively complex and a variety of phases can be obtained by slight variations in temperature and pressure conditions. To date, four polymorphic forms of TCNE have been reported: monoclinc, cubic, hexagonal/trigonal and a metastable phase lacking a long-range order. In addition to the various crystal forms of TCNE, this fairly simple molecule was also reported to polymerize at elevated pressure conditions[4-6].

At ambient pressure however, TCNE adopts two crystalline polymorphs depending on the temperature at which crystals were grown and later stored. The most common phase is the monoclinic polymorph ($P2_1/n$, z=2), Figure 2.2, where each molecule is aligned "one by one"[7] in the same plane, forming molecular chains. They are stacked in a zig-zag pattern along the *a* crystalline axis. The monoclinic form of TCNE can be grown in a number of different ways: from the saturated solution of a solvent, such as ethyl acetate at room temperature[8,9], rapid evaporation of ethyl acetate at low temperature[9] and finally through sublimation[10,11].

The second abundant polymorph of TCNE, the cubic phase (Im3, z=3), Figure 2.2, is known to form only when ethyl acetate is slowly evaporated from the saturated solution below room temperature. In cubic phase, six molecules of

TCNE occupy the face-centered positions, with each carbon-to-carbon double bonds facing the center of a cube[12]. Also the density of the cubic polymorph is 5% higher than that of the monoclinic phase[13] due to more efficient packing.

Yet another, less abundant phase of TCNE with hexagonal/trigonal symmetry has been grown from a mixture of methyl chloride with ethyl acetate at room temperature[12]. As can be seen, TCNE as well as many other molecular systems can form different forms of molecular crystals with significant differences in packing and thus enthalpies of crystallization.

2.1.2 Polymerization of TCNE at High Pressure

Both the monoclinic and the cubic phase of TCNE polymerize when exposed to high pressures at room temperature[13]. The cubic polymorph is stable up to 14 GPa[14] and the monoclinic polymerizes already above 6.4 GPa. Attempts have been made to estimate the molecular structure of the polymer formed at elevated pressures. From inelastic neutron scattering along with X-ray diffraction experiments the ratio of carbon to nitrogen has been found to be 7 to 1 in a polymer, as opposed to 3 to 2 for TCNE crystals at ambient pressure conditions. As a result of the polymerization process, colorless crystals of TCNE gradually turn brown along with the appearance of broad peaks near 1600 cm^{-1} (C=N and

C=C stretching vibrations). While the TCNE C=C stretch is inactive in IR due to the symmetry, it is clearly visible as a result of lowered symmetry once the small TCNE molecule reacts and forms polymer chains[13].

2.1.3 Temperature- and Pressure-Induced Phase Transformations in TCNE

At temperatures above 318 K, 1 atm pressure, an irreversible phase transition occurs from the cubic to the monoclinic polymorph[13]. The back-transition does not occur on cooling, and for that reason the cubic polymorph is considered a metastable phase of TCNE at room temperature. An intermediate, disordered phase has been reported to form at pressures between 2.0 to 6.3 GPa[13]. Given the amount of time the disordered phase was allowed to stay at high pressure, either the monoclinic phase is reformed when the pressure is released back to ambient or, when the higher pressure is maintained for a longer period of time, the cubic polymorph can be obtained.

To establish the temperature of the phase transition from the cubic to the monoclinic polymorph at ambient pressure, difference scanning calorimetry (DSC) method was performed on the cubic crystals of TCNE[9] with varying

scanning rates. A sharp exothermic peak was observed indicating a first-order phase transition to the monoclinic polymorph. Once the transition completed, the crystal in study was cooled to liquid nitrogen temperature (77 K) with an intention to reverse the newly obtained monoclinic form back to the cubic polymorph. Once this step was completed, the sample was reheated in the calorimeter and new DSC traces were recorded. No phase-transition related peak was observed upon heating. The cooling followed by reheating set of experiments only reassured the authors[9] that an irreversible process occurred, namely the monoclinic polymorph did not revert back to its cubic cousin down to 77 K, far below the temperature at which the cubic crystals were grown out of a solution. During the series of DSC experiments on crystals of TCNE, it was reported[9] that the phase-transition temperatures for the cubic-to-monoclinic polymorph varied with the scanning rate programmed into the DSC instrument. In the end, numerous experiments gave fairly similar but not identical values of the transition temperature. These phase-transition temperatures were extrapolated to zero-scanning rate yielding 326 ± 2 K as the reported phase-transition temperature measured with DSC[9]. The fact that the phase transition temperature varied with the rate of the temperature ramp points to the existence of an activation barrier to the phase transition. With the Kissinger method[9,15] the height of the barrier was estimated at 230 ± 20 kJ/mol. Based on the area of the DSC peak[9], the enthalpy of the phase-transition from the cubic to the monoclinic polymorph was found to be 3.5 ± 0.2 kJ/mol.

Temperature-dependent neutron powder diffraction experiments[9] were also performed by R. Mukhopadhyay *et al.* with the goal to compare the temperature of the cubic-to-monoclinic phase transition to the data collected with the DSC experimental method. The neutron powder diffraction method yielded 318 K as the polymorphic phase transition temperature, with the transformation completed within 8 hours, while at 330 K, it only took 1 hour to complete the polymorphic transition in TCNE due to the activation barrier to the phase transition.

Finally, the phase transformation was also investigated with the use of a polarizing microscope equipped with a heating stage[9]. Numerous cracks were observed to form at around 320 K in cubic crystals of TCNE as a result of the polymorphic transformation to the monoclinic form.

2.1.4 Relative Stabilities of the Cubic and Monoclinic Polymorphs as a Function of Temperature

To shed some light on the energetics of the temperature-dependent phase transition observed in TCNE, molecular calculations have been performed with the application of empirically-corrected force field[16]. Attempts have been made to explain the relative stabilities of the various forms of TCNE on the basis of free

energy values. This important thermodynamic parameter can be extracted from molecular simulations performed on the simple molecular compound. A phase diagram reconstructed from these simulations proved that at temperatures down to 0 K, the cubic phase has higher energy than the monoclinic phase at all temperatures. This argument however remains in disagreement with experimental observations as this would mean that the cubic phase cannot be spontaneously grown from the saturated solution of TCNE at low temperatures through slow evaporation of the solvent. Given sufficiently low temperature and enough time for the crystallization to occur, the cubic form is the energetically-preferred polymorph, contradicting the predictions outlined in ref. 16.

	Calculations monoclinic	X-ray monoclinic	Calculations cubic	X-ray cubic
a [Å]	7.69	7.51	9.83	9.74
b [Å]	6.17	6.21	9.83	9.74
c [Å]	6.96	7.00	9.83	9.74
Molecular volume [Å^3]	164.9	163.2	158.52	154.00
Density [g/cm^3]	1.300	1.313	1.342	1.383
Zero point energy [eV]	1.23		1.26	
$\Delta H_{lattice}$ [eV]	-0.93		-0.97	

Table 2.1: Comparison of lattice and physical parameters found through computations[17] and X-ray analysis

In order to clarify the discrepancy between the experimental and theoretical predictions, more advanced (purely quantum-based) calculations employing Density Functional Theory (DFT[18]) augmented with Van der Waals forces have recently been performed on TCNE[17]. The addition of the Van der Waals component to the DFT method assures that the relatively weak electrostatic forces that result in attraction of neutral molecules to each other are taken into consideration within the framework of this simulation. Van der Waals interactions are known to prevail in crystals composed of neutral organic molecules such as TCNE and are responsible for controlling the packing of crystals. The detailed description of the computational techniques used in the quantum simulation can be found in ref. 17. Structures submitted for the molecular simulations were based on literature X-ray data for each of the two polymorphs[7,12]. Their corresponding crystal lattices are shown in Figure 2.2 and the unit cell parameters are summarized in Table 2.1. The structure of the cubic polymorph of TCNE can be found in the Cambridge Structural Database (CSD) under the TCYETY01 designator while the monoclinic form is designated as TCYETY.
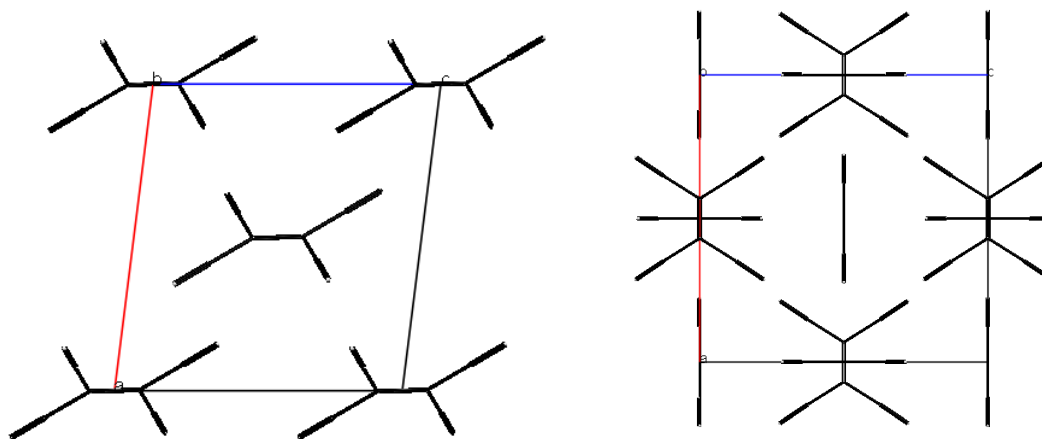
Figure 2.2: The monoclinic (left) and cubic (right) crystal lattices viewed along the **b** unit cell axis. Structures based on X-ray information[7,12] and visualized with the CSD software package

2.2 Experimental Section

2.2.1 Sample Preparation and IR Data Evaluation

The monoclinic phase of TCNE (Sigma-Aldrich, 98%) was obtained by quick sublimation at elevated temperature, in vacuum. The cubic polymorph was slowly grown from a saturated solution of ethyl acetate at temperatures below 273 K and maintained in an ice bath with added NaCl until well-resolved cube-shaped crystals formed (after ~ 3 days). The melting ice was replaced on regular basis while the temperature of the solution was monitored. Once the two polymorphs of TCNE were grown, thin (<1 mm) KBr pellets (Sigma-Aldrich,

spectral grade) of each form were produced and mounted on the tip of a closed

cycle helium cryostat, inside the sample compartment of a high-resolution Bruker

HR-120 FTIR instrument. Only few stretching vibrations are IR active in this

highly-symmetrical molecule. The vibrations of the terminal cyano-groups (C≡N)

are especially sensitive to molecular approach (occurring for instance during

phase transitions) and rearrangements occurring on compression (high

pressure). Lorentzian bands were summed-up to form a fit to the C≡N stretching

vibrations (listed in Table 2.2) in the range between 2200 and 2270 cm^{-1}, Figure

2.3, of the two different polymorphs at different temperatures.

Cubic	Monoclinic
~ 2259 cm^{-1}	~ 2261 cm^{-1}
~ 2255 cm^{-1}	~ 2227 cm^{-1}
~ 2221 cm^{-1}	~ 2213 cm^{-1}

Table 2.2: Energies of the IR-active C≡N vibrons observed in TCNE at 298K, ambient pressure based on IR spectra in Figure 2.3
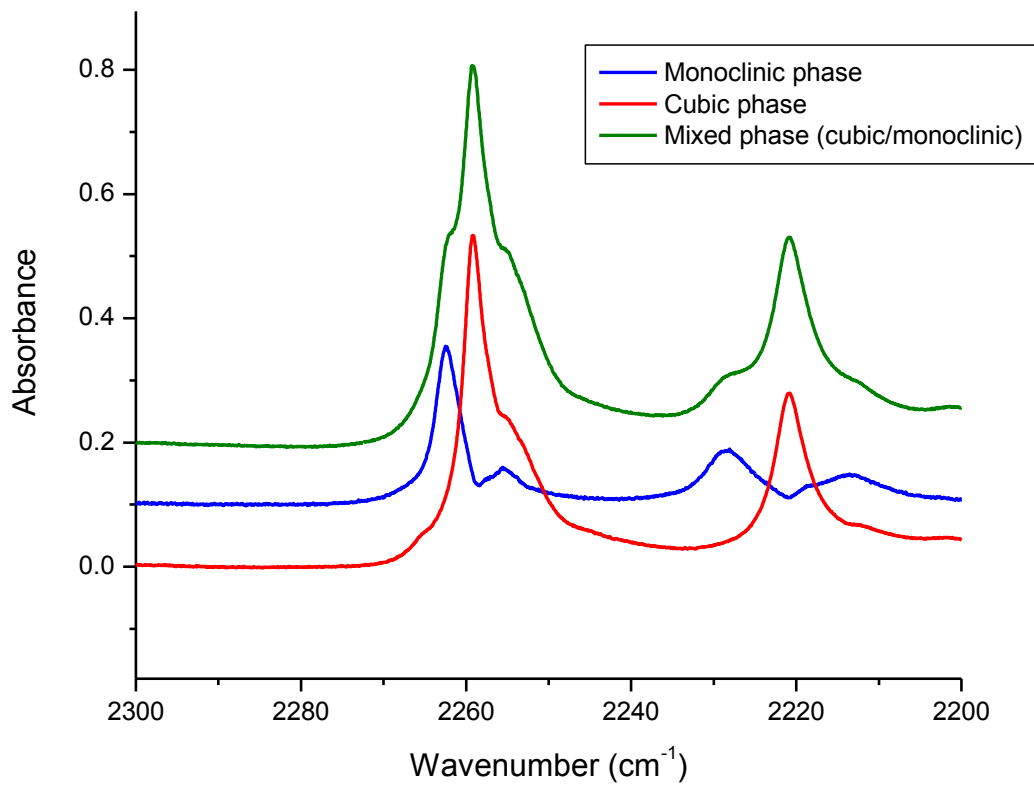
Figure 2.3: The cyano-groups C≡N stretching modes in IR spectra of two major polymorphs of TCNE at room temperature: monoclinic (blue), cubic (red) and crystals of mixed cubic/monoclinic forms (green). The cubic polymorph is the metastable form of TCNE at 298 K. The mixed crystals feature all vibrational peaks that are found in the monoclinic and cubic polymorphs

2.3 Results and Discussion

2.3.1 Relative Changes in Free Energies

The calculated unit cell parameters, density and molecular volume for the

monoclinic and the cubic phases are summed up in Table 2.1 and are compared

to the experimental X-ray values found in the literature[7,12]. The calculated bond

lengths (not shown here) are overall in an excellent agreement with the neutron

diffraction and double atom refinement molecular geometries[17].

Important thermodynamic properties such as the temperature-dependent

free energy (Figure 2.4), entropy and the enthalpy[17] change have been found for

monoclinic and cubic phases of TCNE. These results[17] differ from earlier

empirically-corrected simulations[16] in that at 0 K the cubic polymorph is

energetically more favorable, up to ~160 K, Figure 2.4. Above this temperature

point its cousin, the monoclinic polymorph is the preferred, thermodynamically

stable form. In experiments however, the transition from the cubic to the

monoclinic polymorphs was confirmed to occur only at temperature around ~ 318

K or higher[9]. This discrepancy between experimental data and theoretical

predictions can be attributed to the relatively large phase transition energy barrier

surrounding this polymorphic transition and amounting to 230 ± 20 kJ/mol[9]. This

energy barrier is necessary for the molecular reorientation to take place[9] within a

crystal which eventually leads to a new polymorph. The barrier causes the

apparent metastability of the cubic phase between the theoretical (160 K[17]) and the experimentally-confirmed phase-transition temperature value (318 K[9]). That same transition barrier is responsible for the lack of the opposite transition from the monoclinic to the cubic polymorph, as was demonstrated in an experiment[9] involving cooling the monoclinic crystals of TCNE down to 77 K.

Slow crystallization of TCNE at low temperature resulting in the cubic phase and the fast crystallization at that same low temperature but resulting in the monoclinic polymorph are accounted for the very small difference in crystal packing energy (0.04 eV, Table 2.1, Figure 2.4) between the cubic and the monoclinic polymorph, value found with the recent computations[17].

Accidentally we were able to grow crystals of mixed cubic and monoclinic polymorphs (Figure 2.3, green spectrum) in one of our experiments. This probably happened when the evaporating solution of TCNE in ethyl acetate was not sufficiently cooled throughout the entire time it takes to evaporate the solvent and form crystals of the desired (cubic) polymorph or perhaps because the solvent was let to evaporate too quickly at sufficiently low temperatures. As can be seen in Figure 2.3, the mixed crystals of TCNE feature the C≡N vibrational peaks characteristic of both the cubic and monoclinic polymorph.

The electron density surrounding the molecules packed in a crystal have been visualized in the form of D_{norm} Hirshfeld surfaces[17] based on available X-ray structures in both polymorphs. The cut-off value for each contact between neighboring molecules is the Van der Waals radius of a given atom. In TCNE

there are only two types of molecular contacts possible: carbon-to-nitrogen and carbon-to-carbon. While most contacts occur at or near the VdW separation distance, some may appear at shorter or longer distances. If a particular distance between close contacts is longer than the sum of their VdW distances, the resulting gap in electron density is considered to be a void in a crystal lattice. If it is shorter, the vibrations of the two atoms in close contact are coupled to each other, resulting in faster dephasing times and increased entropy of the affected vibrational modes[17].

The electron density analysis reveals that the monoclinic phase of TCNE displays 20 carbon-to-nitrogen contacts occurring at distances shorter than the Van der Waals length while the cubic phase shows only 16 identical contacts[17]. The D_{norm} Hirshfeld surfaces also uncover empty pockets - voids, in crystals of the cubic phase. No voids are observed in the monoclinic phase of TCNE. Due to the larger number of close contacts in the monoclinic phase, the intermolecular coupling between the C≡N vibrons of neighboring molecules is stronger than in the cubic phase. This effect in turn affects the dephasing of the molecular modes, manifesting itself in a broader linewidth (larger FWHM value) of the affected C≡N vibrations.

The FWHM values have been extracted[19] from temperature-dependent C≡N vibrational modes and plotted in Figure 2.5. The monoclinic phase of TCNE displays larger FWHM (faster dephasing time) than the cubic phase at temperatures higher than ~ 220 K and within the error bar at 180 K. This

observation corresponds fairly well with the phase transition temperature in TCNE predicted with molecular simulations[17] (160 K). It is possible that the increased vibrational entropy of the monoclinic phase at higher temperatures remains the main source of the phase transition at ambient pressure in TCNE.
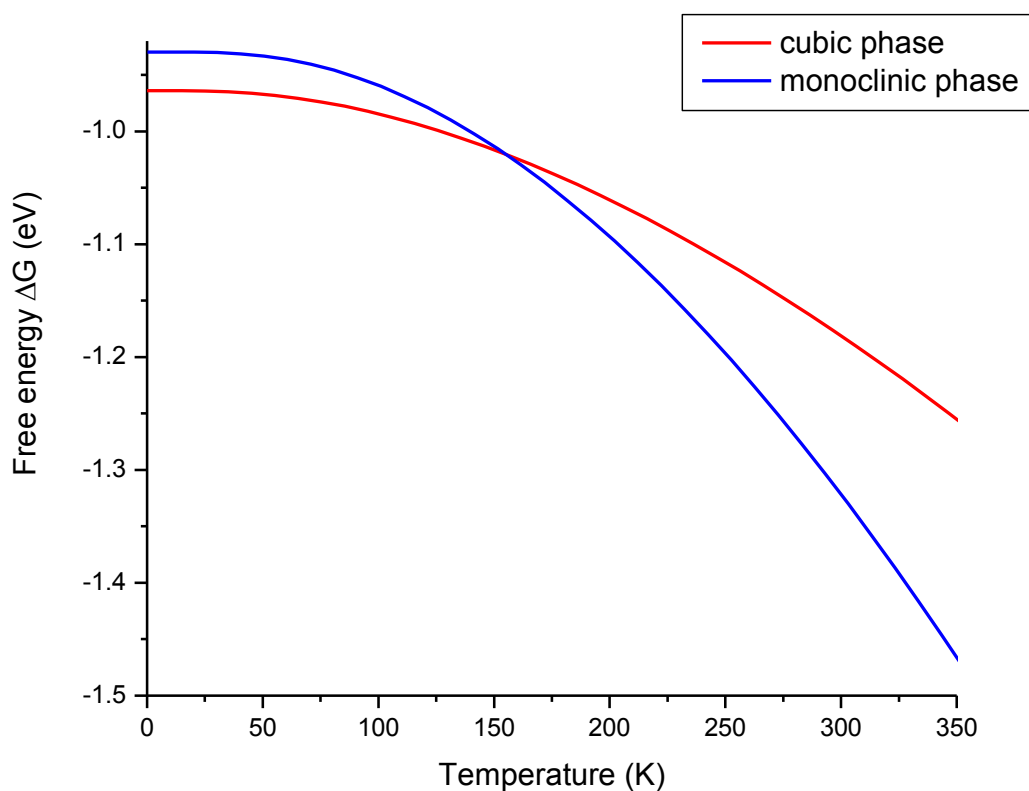
Figure 2.4: Calculated[17] free energy change as a function of temperature in the monoclinic phase (blue) and cubic phase (red) of TCNE. At temperatures below 160 K, the cubic polymorph is the energetically more stable form. At temperatures above 160 K, the monoclinic form has the lowest enthalpy of formation
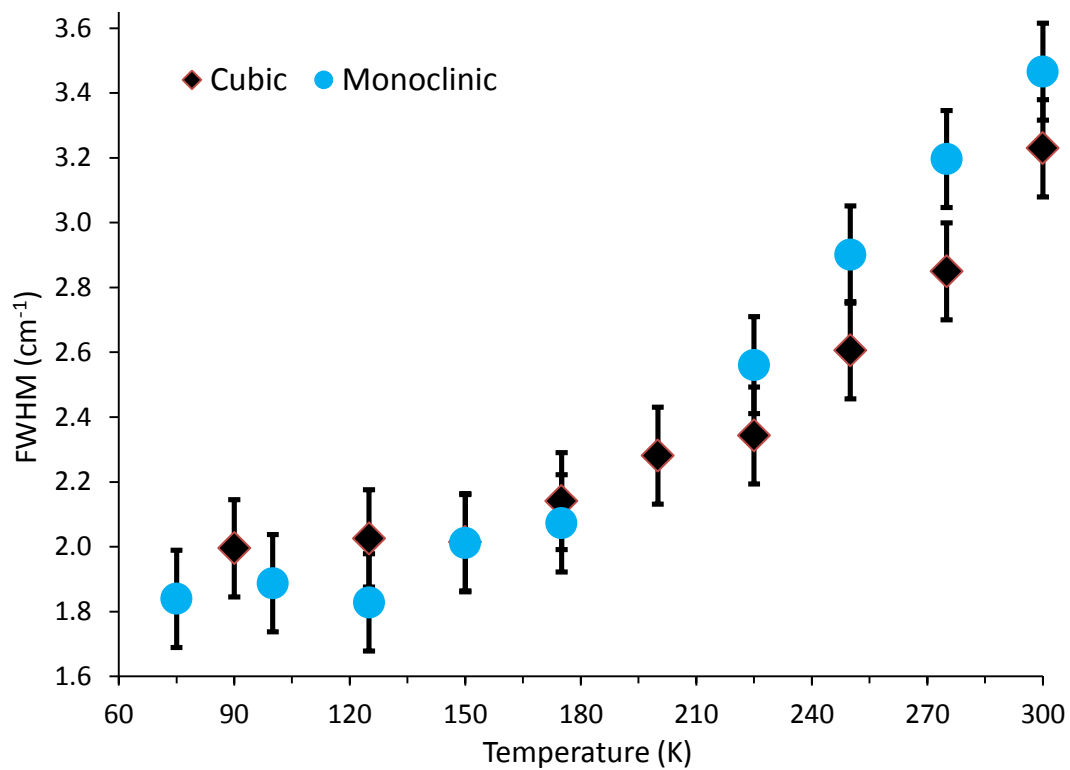
Figure 2.5: FWHM linewidths of the C≡N vibrons of cubic (2259 cm^{-1}, black) and monoclinic (2261 cm^{-1}, blue) polymorphs as a function of temperature. Values extracted from temperature-dependent high-resolution IR measurements

2.3.2 Conclusions

With the use of the DFT method augmented with Van der Waals interactions we found that the difference in free energy between the cubic and the monoclinic polymorphs is only 0.04 eV at 0 K. What is more, the molecular simulations reveal that the cubic form is energetically stable up to 160 K, 1 atm pressure, and becomes the less favorable polymorph at higher temperatures. No temperature-induced transition from cubic to monoclinic polymorph is observed in crystals of TCNE until ~ 318 K (neutron diffraction[9]). This large temperature hysteresis is due to the relatively large transition barrier. The observed temperature-induced phase transition in crystals of TCNE has been explained in terms of increased vibrational entropy in the monoclinic polymorph occurring around 180 K (or higher, FWHM) caused by a higher number of close contacts as compared to the cubic form.

2.4 References

(1)   Chetkina, L. A.; Bel'ski, V. K. *Crystallogr. Rep.* **2002**, *47*, 581.

(2)   Jerome, D.; Mazaud, A.; Ribault, M.; Bechgaard, K. *J Phys Lett-Paris* **1980**, *41*, L95.

(3)   Pejakovic, D. A.; Kitamura, C.; Miller, J. S.; Epstein, A. J. *J Appl Phys* **2002**, *91*, 7176.

(4)   Rao, R.; Sakuntala, T.; Deb, S. K.; Mukhopadhyay, R. *J Phys-Condens Mat* **2005**, *17*, 2633.

(5)   Mukhopadhyay, R.; Chaplot, S. L. *J Phys-Condens Mat* **2002**, *14*, 759.

(6)   Yamawaki, H.; Sakashita, M.; Aoki, K.; Takemura, K. *Phys Rev B* **1996**, *53*, 11403.

(7)   Little, R. G.; Pautler, D.; Coppens, P. *Acta Crystall B-Stru* **1971**, *B 27*, 1493.

(8)   Onda, S.; Ikeda, R.; Nakamura, D.; Kubo, M. *B Chem Soc Jpn* **1969**, *42*, 2740.

(9)   Mukhopadhyay, R.; Chaplot, S. L.; Rao, K. R. *Phys. Status Solidi A* **1985**, *92*, 467.

(10)   Chaplot, S. L.; Mierzejewski, A.; Pawley, G. S. *Acta Crystallogr C* **1984**, *40*, 663.

(11)   Chaplot, S. L.; Mierzejewski, A.; Pawley, G. S.; Lefebvre, J.; Luty, T. *J Phys C Solid State* **1983**, *16*, 625.

(12)   Bekoe, D. A.; Trueblood, K. N. *Zeitschrift für Kristallographie* **1960**, *113*, 1.

(13)   Yamawaki, H.; Aoki, K.; Kakudate, Y.; Yoshida, M.; Usuba, S.; Fujiwara, S. *Chem Phys Lett* **1992**, *198*, 183.

(14)   Mukhopadhyay, R.; Deb, S. K.; Das, A.; Chaplot, S. L. *Solid State Commun* **2009**, *149*, 1914.

(15)   Kissinger, H. E. *Anal Chem* **1957**, *29*, 1702.

(16)   Chaplot, S. L. *Phys Rev B* **1987**, *36*, 8471.

(17)   Schatschneider, B.; Liang, J. J.; Jezowski, S.; Tkatchenko, A. *Crystengcomm* **2012**, *14*, 4656.

(18)   Tkatchenko, A.; Scheffler, M. *Physical review letters* **2009**, *102*.

(19)   Schatschneider, B. H. *PhD Thesis, University of California, Riverside* **2008**.

Chapter III

Improvements in the Performance of the Dynamic

Diamond Anvil Cell (dDAC)

3.1 Introduction

3.1.1 The Advent of Dynamic High-Pressure Research

Until recently, researchers were forced to perform time-resolved high-pressure experiments with the use of a "static" Diamond Anvil Cell (DAC) device, Figure 3.1. The pressure changes occur on a few second time scale (Δt) as a result of the manually tightened bolts, difference in pressure of at least 40 kbar (ΔP) can easily be achieved in nearly each DAC and thus rates of reactions occurring within minutes ($k \geq min^{-1}$) can be resolved. The second generation dDAC that was built in Dr. E. Chronister group, UC Riverside, allows for truly dynamic changes in pressure, occurring on the order of less than 1 ms with changes in pressure up to 7 kbar. Rates of phase transitions or chemical reactions induced by high-pressure on the ms (10^{-3} s) time-scale can now be studied. With the newly designed high-voltage controller box, the 7 kbar pressure

difference was shown to occur within ~ 0.5 ms, bringing the compression rate up to 1400 GPa/s. This value is almost 3 times larger than the literature-reported strain rate for a dDAC[1].

3.1.2 Pressure Calibration

The presented pressure calibration method is independent of the pressure-generating tool. Both devices, DAC and the dDAC, Figure 3.1, can be calibrated against ruby. Naturally occurring crystals of aluminum oxide doped with chromium ions, a variety of the mineral corundum, absorb at ~ 400 and 550 nm. Upon illumination with a green laser light, strong emission peaks, named R_1 and R_2 with uneven intensities can be easily distinguished in the red part of the ruby spectrum. Their shift is strongly dependent on the magnitude of the *in-situ* pressure[2]. The calibration of ruby fluorescence as a function of pressure for the R_1 line has been accomplished with the help of the Decker equation of state for $NaCl$[3], based originally upon X-ray scattering data. The fluorescence observed from the R_1 line is of longer wavelength and larger intensity than from R_2 and therefore has been chosen as the primary reference line for pressure determination.

Under hydrostatic pressure conditions, the ruby emission lines shift by the same amount in wavenumbers, with an equal spacing of $\Delta R = 29.7 \pm 0.2$ cm^{-1} at room temperature[4], Figure 3.2. Any deviations from hydrostatic pressure conditions result in changes in ΔR as well as in the half-width-at-half-maximum (HWHM) of the R_1 line, defined as $v_{1/2}$[5].

All ruby fluorescence measurements described in Chapter 3 and 4 aimed at determining the pressure inside the DAC were performed with the use of a Dilor XY Laser Raman Spectrometer equipped with a 532 nm (green excitation wavelength) DPSS laser. The maximum power generated from the laser head is ~ 200 mW. The light intensity was further attenuated and maintained with with a neutral density filter, OD, between 1 to 2.

3.1.3 The Procedure of Loading a Sample

In spite of the differences in operation, the procedure of loading a sample into the DAC or the dDAC is very similar. Loading a sample and maintaining the pressure is a tedious and responsible job, requiring all the attention from the researcher. As a gasket, a pre-indented Inconel material (0.01'') has been used. A small hole, depending on the size of the culet, but usually 0.2 – 0.3 mm in diameter is drilled in the gasket with a micro-drill press and provides the sample

compartment in which only a very limited volume of material can be researched. Any rough edges around the gasket hole were removed with a razor blade prior to assembly. The alignment was maintained by positioning the hole as close to the center of the culet as possible. At this point, ruby chips were added with the use of a sharp needle. The DAC is sealed with three Super Invar Allen cap screws in small increments after which the parallelism of the diamond anvils are maintained with the use of a micrometer. Occasionally, a failure of the chamber seal occurred which usually manifests itself in a significantly-deformed gasket hole seen under a microscope. If that is the case, the gasket and the sample were replaced and the DAC resealed.

In dDAC, prior to inserting the Allen cap screws, appropriate combination of spring washers is inserted first, Figure 3.3. Only then the screws are uniformly tightened and torqued until the maximum, desirable static pressure is achieved. Once this step is completed, the three identical piezoelectric actuators are inserted into the body of the dDAC and secured with three thick keeper plugs, Figure 3.3. For optimal results, the researcher needs to reassure there are no gaps between the backing plate of the dDAC and the extension elements (tips) of the three piezoelectric actuators, PE. The leads from the PE elements are connected in parallel to a high-voltage unit (driver) which is controlled by a function generator. Voltage in the range from 0 to 130 V causes the PE elements to apply expansive load in between the two anvils (the body and the backing plate) working against the load imposed by the three sets of spring washers.
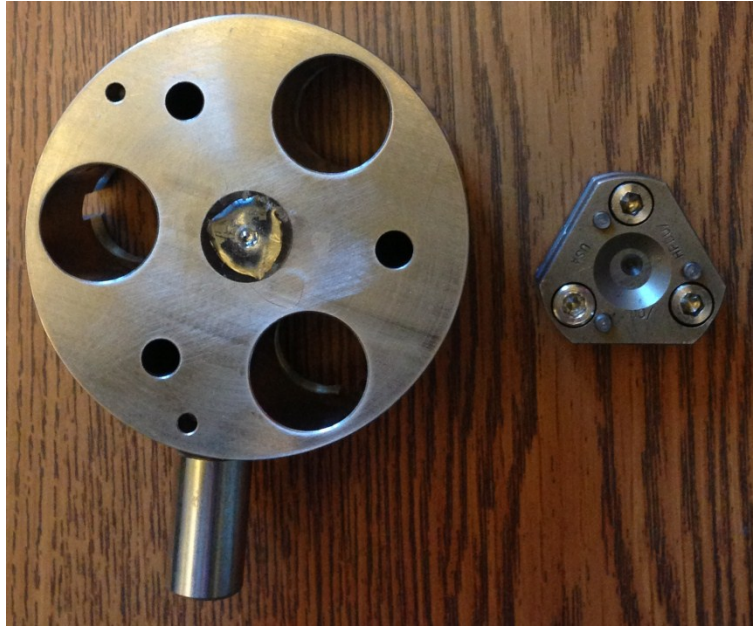
Figure 3.1: A photograph of the classic Merril-Basset DAC, right, and the body of the second generation dDAC, left
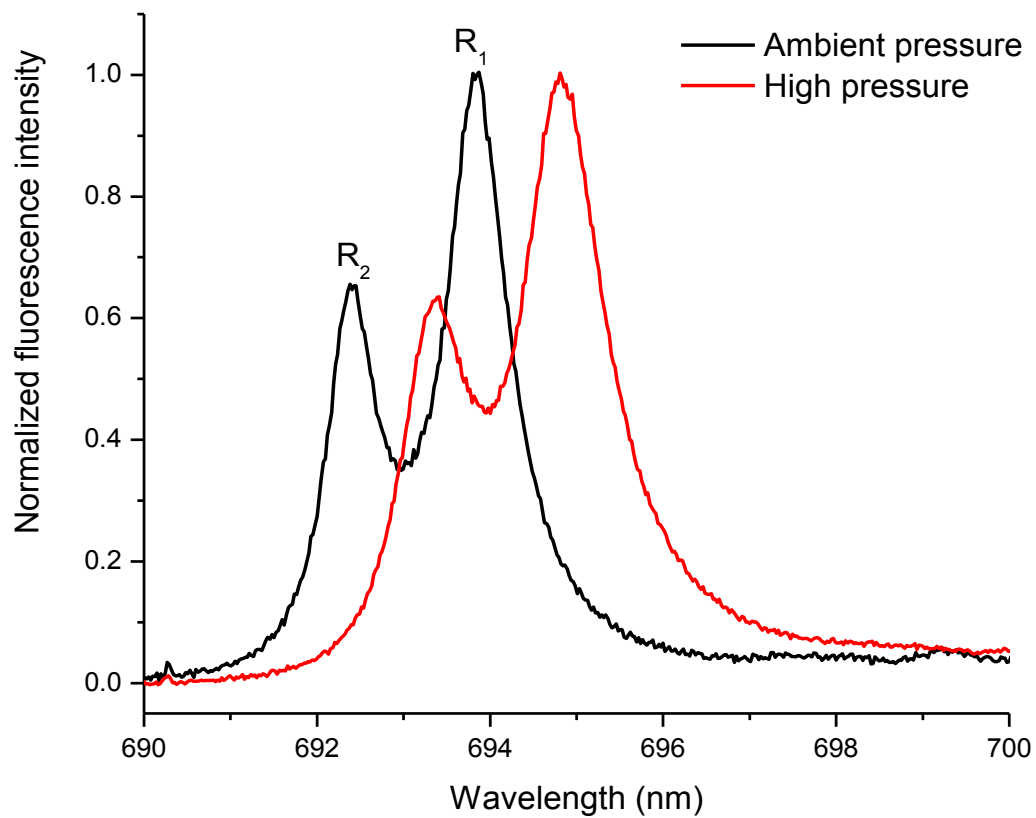
Figure 3.2: Ruby fluorescence spectra at ambient, black, and high pressure, 27.0 kbar, red

3.2 Variations in Dynamic High-Pressure Tools

3.2.1 The First Generation dDAC

The original design of the dDAC device, also called the first generation, is a modification of the Merril-Basset DAC in which all three Allen bolts were replaced by piezoelectric actuators[6,7]. The extension of the piezo stack, triggered by a high-voltage, causes one of the diamond anvils to press against another, resulting in a pressure generated within the sample compartment (gasket hole). The starting pressure is not always the ambient value. With additional knobs adjusted manually it is possible to set the desired static pressure before inducing additional stress on the sample.

After several improvements to the initial version, the first generation dDAC was capable of generating up to 6 kbar difference in pressure with a time response of 4 ms to induce such difference, ΔP. The maximum possible compression rate that can be achieved in the first generation dDAC is 150 GPa/s. The detailed characterization of the device is presented by Dr. A. Rice[6].

3.2.2 The Second Generation dDAC

3.2.2.1 Improvements in the Design

The second generation dDAC is based on already built and tested design[1], Figure 3.3. The three static load Allen cap screws, combined with a set of spring washers, apply a steady compressive load (static pressure) to the sample. The role of the electromechanical actuators is to expand the static load, counteracting the load exerted by the three load screws and thus reducing the pressure on the sample, to the contrary to the first generation.
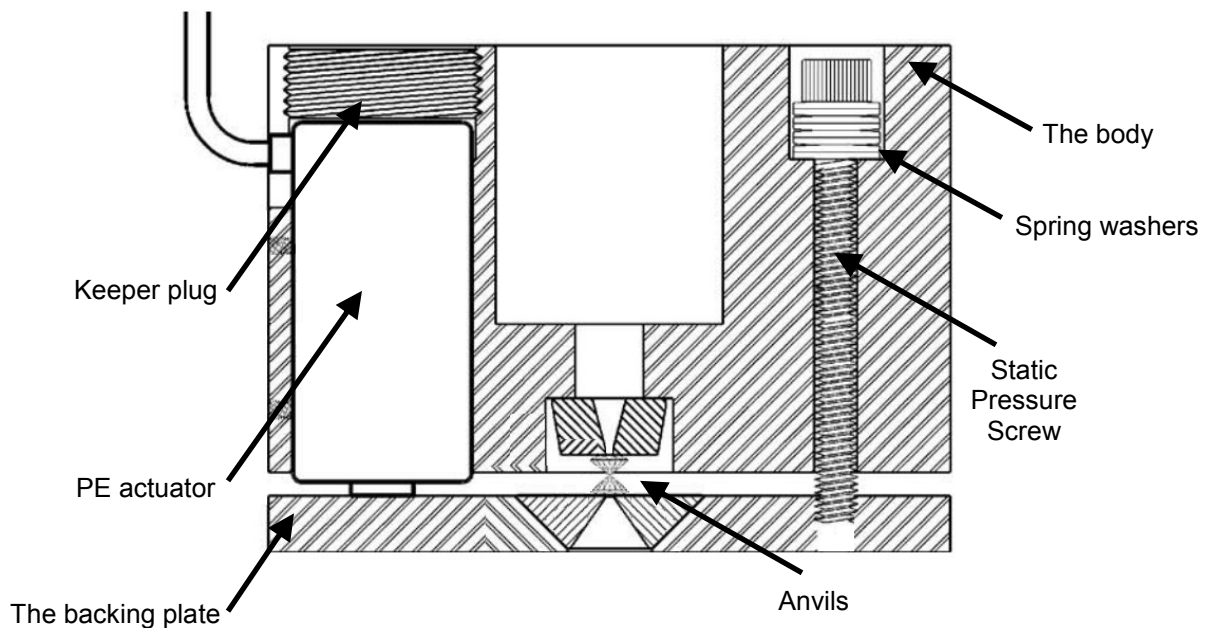
Figure 3.3: The original design of dDAC as presented[1] by Evans *et al;* reprinted from the American Institute of Physics with permission

The three piezoelectric actuators are placed into holes in the cylindrical, large metal body of the dDAC, Figure 3.3. The tightly inserted keeper plugs will insure no spacing between the actuators and the dDAC. The spring washers will allow for a few microns of the backing-plate movement as a result of the expansion of the three PE so that the change in load is accompanied by a small change in the culets' distance with respect to each other. The PE actuators are also capable of withstanding larger loads at a cost of slower response time. Each piezo-stack can deliver up to 3500 N (and 10500 N when combined) at a maximum frequency of 20 kHz (Piezosystem Jena GmbH)

3.2.2.2 The Body of the dDAC

The body of the dDAC (stainless steel T304) is the largest single-piece element of the dDAC and serves two main purposes: with the help of the three Allen cap screws, the body holds the backing-plate against another diamond cullet. It is also housing the piezoelectric actuators with the help of three plugs, Figure 3.3. To probe the molecular dynamics at varying pressures, the analytical beams of photons can travel through the entire body thanks to a cone-shaped channel shown in Figure 3.4B and 3.5.
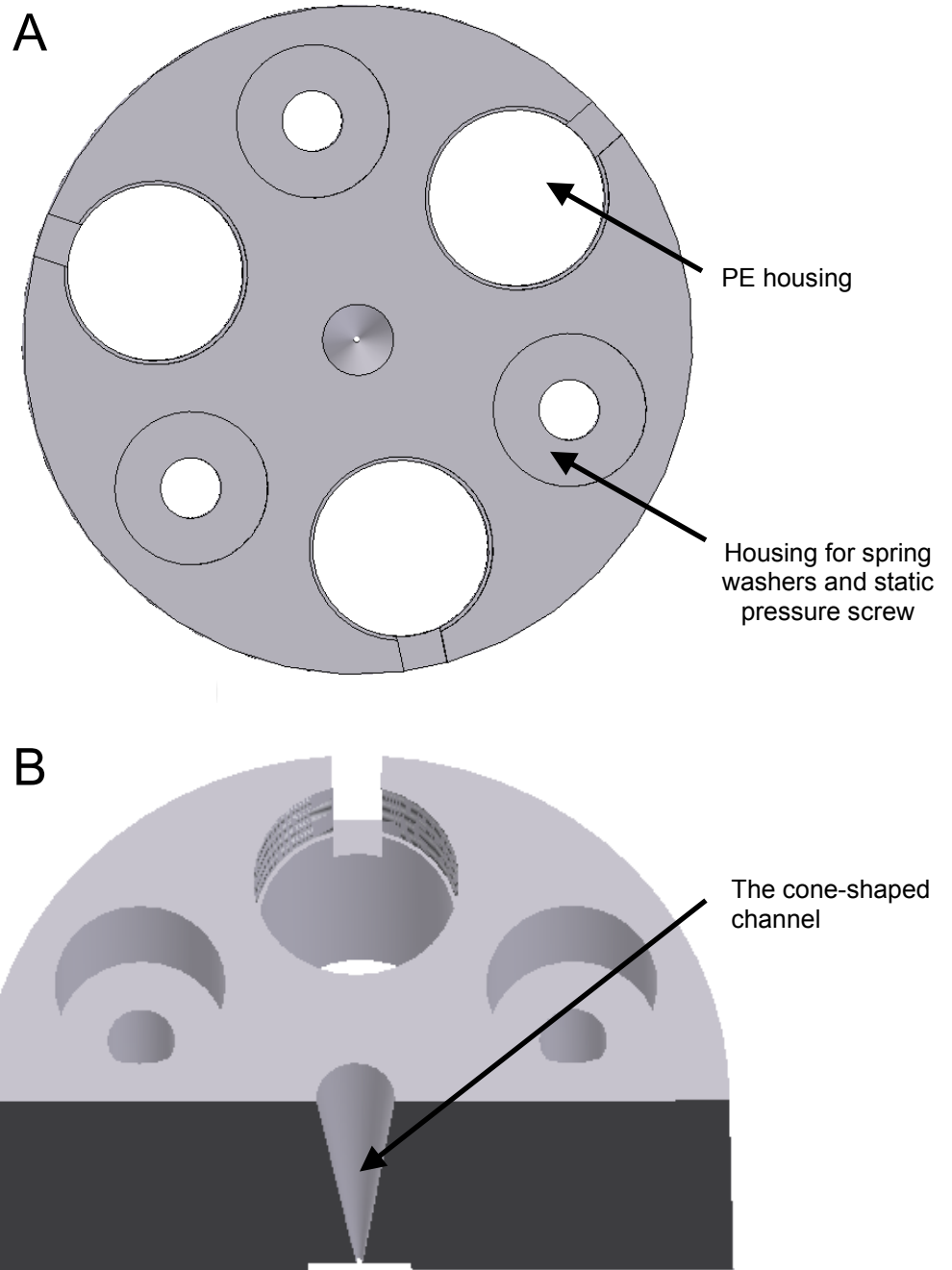
Figure 3.4: Top view, A, and cross-section, B, of the second generation dDAC; only the body part is shown

The cone-shaped channel

Housing for the diamond anvil
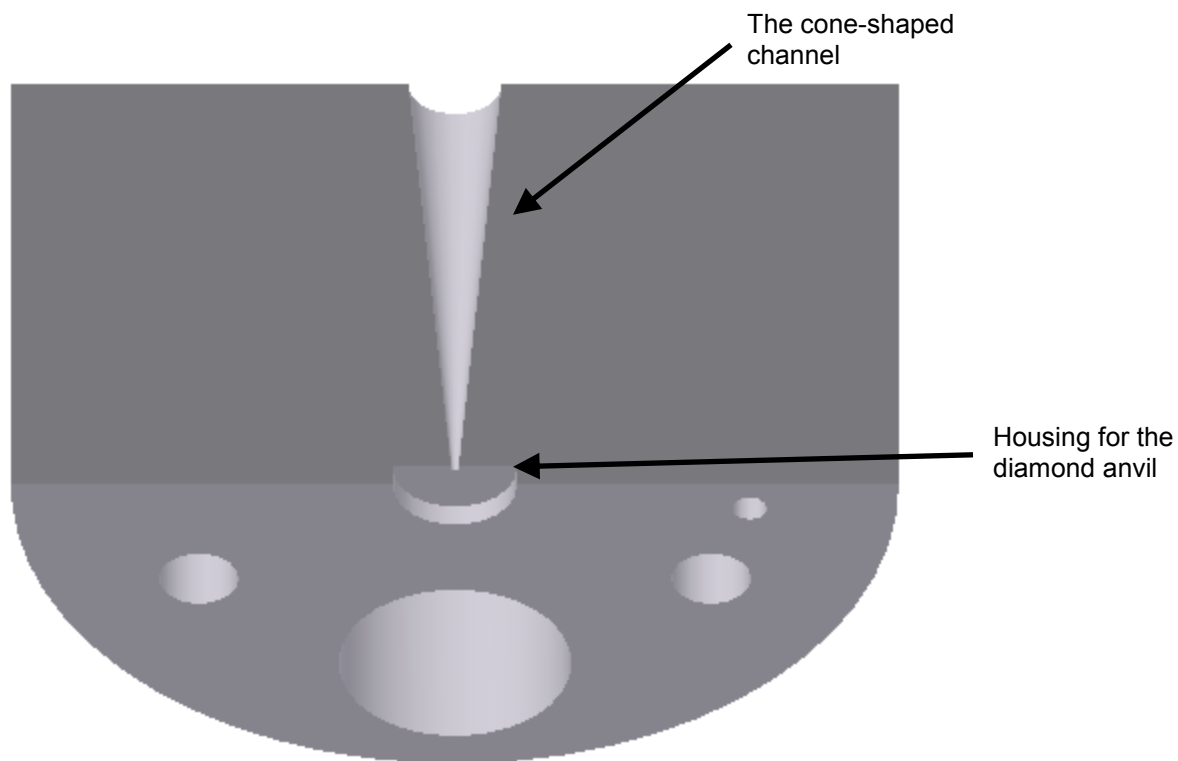
Figure 3.5: Bottom view of the cross-section of a metal body of the dDAC. One diamond anvil is centered at the tip of the cone

3.2.2.3 The Backing Plate

The stiffness and the weight of the backing plate are of tremendous importance for the success of this dynamic high-pressure device. The backing plate must present negligible bending achieved either by increasing the thickness of the material or by implementing hard materials preferably of low weight. An ideal solution is a backing plate entirely made from a diamond (CVD). In the

center of the backing plate an anvil holder is inserted and can be aligned with

respect to the immobilized culet, permanently mounted to the body of the dDAC.

Housing for the
anvil holder
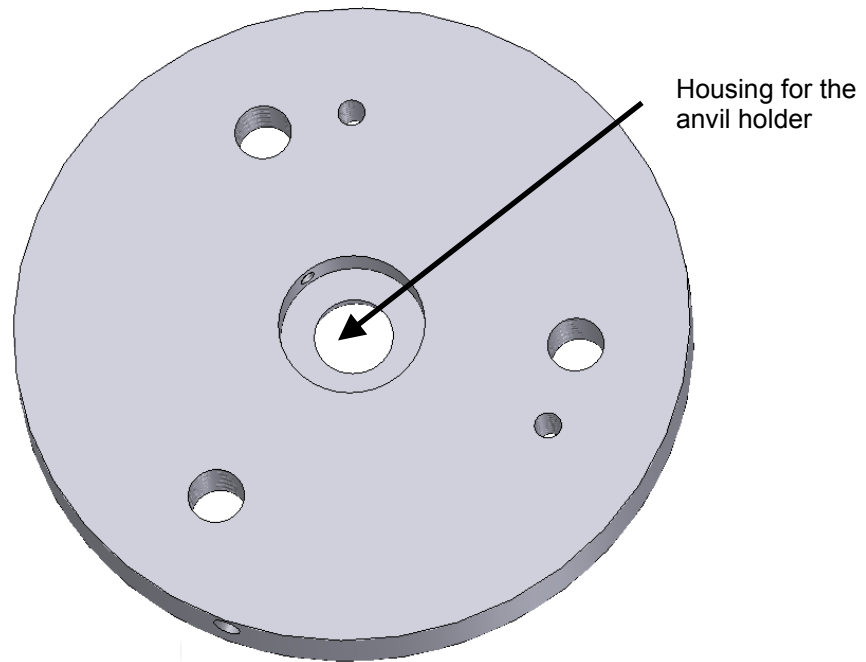
Figure 3.6: The backing plate presented at an angle
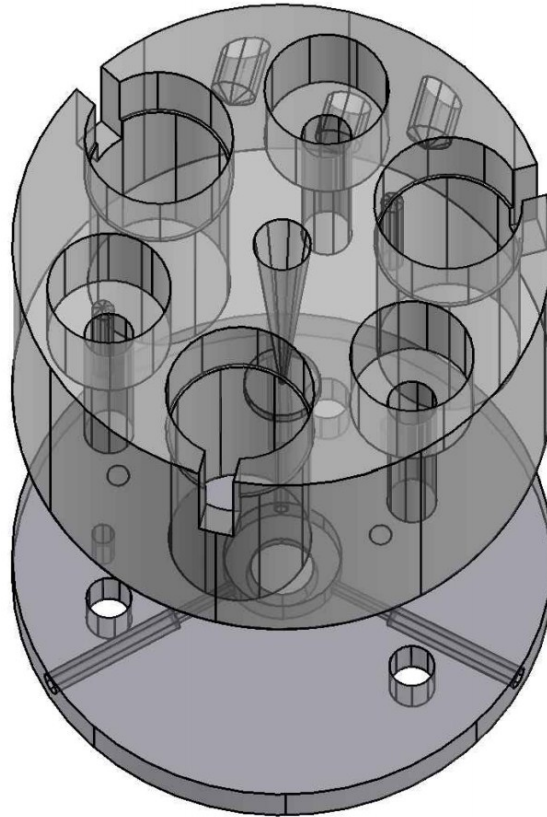
Figure 3.7: The backing plate and the body of the dDAC; an "X-ray" view

3.2.2.4 Loading the Static Pressure

The thickness and the tilt angle of a spring washer, Figure 3.8, will dictate

the maximum pressure difference that can be achieved within dDAC. Thick

spring washers will help apply large static pressure. They may also prevent the

piezoactuators from expanding to their full length if the static load is too large.

Thin spring washers on the other hand will not allow for the static pressure to be high enough to make use of the available range of pressures. If the Allen cap bolts are tightened too much, the thin spring washers tend to flatten.

Spring washers, also known as Belleville disc springs, will deflect upon the application of force. The spring force, F and the spring deflection, f, Figure 3.8, can be found from these two equations:

$$F = \frac{\delta^2}{1 - 2/3 \, r_0/r} \sigma$$

$$f = \frac{0.65 \, r^2}{E\delta(1 - 2/3 \, r_0/r)} \sigma$$

where σ is the tensile strength and E is the modulus of elasticity.

The variance in pressure is a complex function of the thickness, number and arrangement of the spring washers, the initial static pressure, the area of the culets, the gasket material and its thickness as well as the applied voltage. Being a multi-dimensional function, variance in pressure has one global minimum which either has to be predicted or found experimentally through a set of numerous and often tedious experiments in which the shift in ruby emission is explored.

In a series of experiments involving the second generation dDAC, only a few parameters were explored: a set of spring washers along with varying initial static pressure with the use of an Inconel gasket, 0.01". The voltage was

changed from 0 to 130 V, a maximum value for Jena PE. Figure 3.9 shows the

pressure variation range at a given nominal pressure for two different culets. The

maximum pressure difference that can be achieved is between 7 to 8 kbar and

occurs around 10 kbar of static pressure for either of the two culets. The

pressure difference experiences a dip at around 20 kbar and rises again at ~ 25

kbar for the smaller diameter pair of culets.
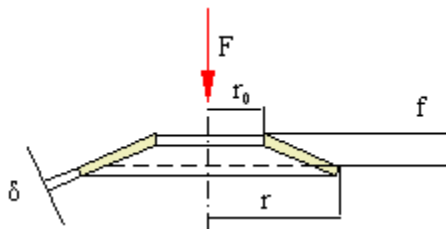
Figure 3.8: Spring washer critical dimensions. The red arrow shows the direction
in which the force, F, is applied
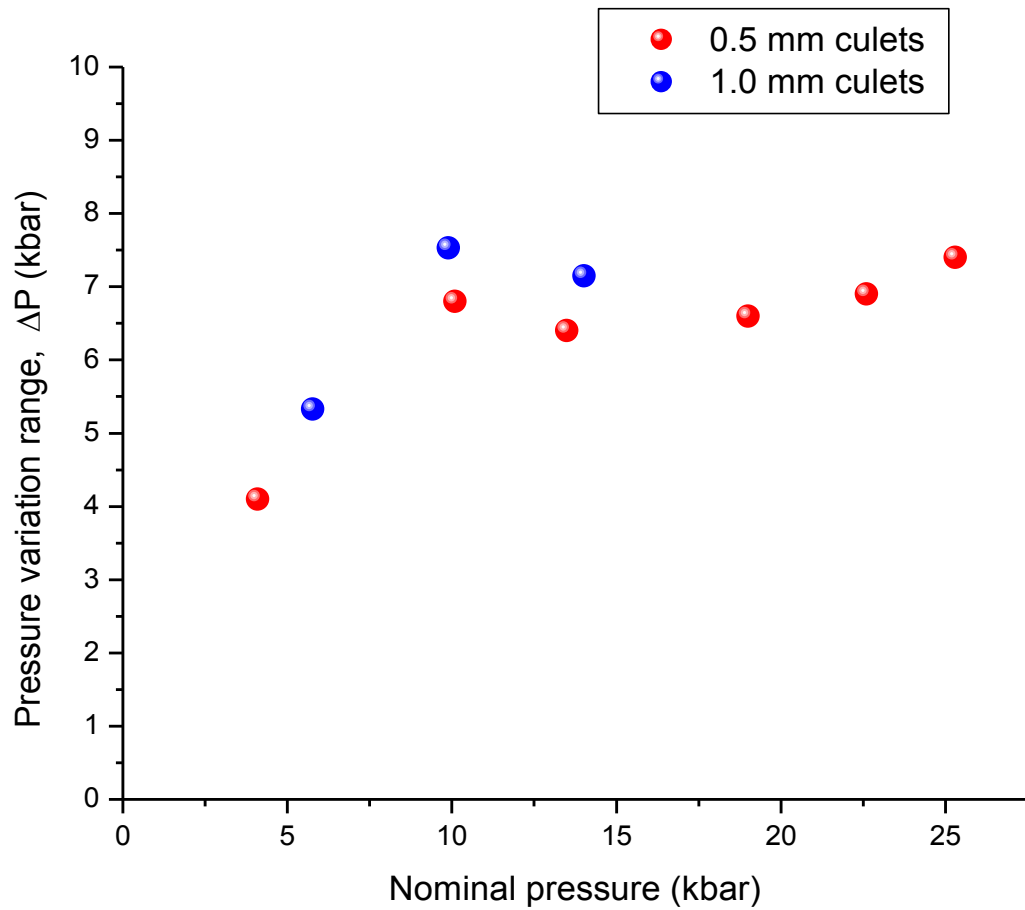
Figure 3.9: Second generation dDAC pressure variation range at a given nominal pressure for two different culet sizes (diameter) with the use of a PMMA polymer and ruby in the sample compartment. An Inconel gasket material has been applied between the culets

3.3 Characterization of the Dynamic Properties of the Second Generation dDAC

3.3.1 Rate-Limiting Steps in Dynamic Pressure Variation

The piezoelectric actuators are at the heart of the dynamic Diamond Anvil Cell, dDAC. They serve two purposes: deliver the load (force) necessary for pressure changes as well as dictate the maximum rate at which such pressure changes can occur. The latter parameter is often limited by the time it takes to inject charge into the PE stack and the discharge time combined. The three identical piezoelectric (PE) actuators in the second generation dDAC (Jena, PAHL 18/20) can sustain a load of up to 3500 N with the difference in motion of up to 18 μm. They are 36 mm long and have a diameter of 20 mm. In an electrical circuit the PE acts as an effective capacitor, 7 μF each (PAHL 18/20). When connected in parallel, the capacitance triples to 21 μF. This relatively large capacitance needs to be fully charged and discharged in each cycle by the high voltage driver unit. The discharge event puts constraints on the time in which the mechanical bolt attached to the stack can contract to return to its starting position. The circuitry that limits the contraction time by accelerating the discharge has been integrated into the home-made (MOSFET) piezo controller, outlined in the Appendix section, in the (passive) form of a resistor. A fast, active

injection method of delivering the charge to the PE was utilized in the home-made driver, greatly accelerating the extension of the mechanical bolt.

The time response of the extending and contracting movements of the second generation dDAC piezoelectric actuators, PAHL 18/20 and of the first generation dDAC, PE4 Thorlabs piezo stacks are represented as the change in the intensity of the attenuated light, emitted by a DPSS green laser source, and imaged on an active element of a silicon photodiode fed to a digital oscilloscope. The evaluation was performed without exceeding the voltage specifications for the PE, with an abrupt jump in voltage from 0V to 130V (limiting voltage) for PAHL 18/20 and from 0V to 150V for Thorlabs PE4.

3.3.2 Characterizing the Pressure Variation

In the first set of time-dependent experiments, the PAHL 18/20 stack, second generation dDAC, is driven by the commercial Thorlabs MDT693A (Figure 3.10B, black traces) and by the home-made control box equipped with a MOSFET transistor in its end-stage (Figure 3.10A, red traces). Only kinetic traces triggered by low-to-high input signals (extension) as well as by high-to-low input signals (contraction, traces C and D) are shown. The rising slope induced

by the MDT693A controller combined with PAHL 18/20 has a rise-time of about

20 ms while the same slope induced by the MOSFET controller has a rise-time of

about 0.5 ms. This is a factor of 40 quicker. For comparison, the corresponding

changes in high voltage generated by the controllers (data not shown) are: ~ 19

ms (MDT693A combined with PAHL 18/20) and 0.08 ms (or 80 µs with the

MOSFET and PAHL 18/20), a difference of 237 times.

From these data it becomes apparent that the PAHL 18/20 extension

follows the voltage supplied by the Thorlabs control box (20ms vs. 19 ms). In

case of the MOSFET controller box, the charge is injected within ~ 0.08 ms while

the extension takes relatively more time, and is completed within ~ 0.5 ms (or

500 µs) measured from the trigger event. With the MOSFET controller coupled to

the PAHL 18/20 PE, the mechanical extension of the stack (and not the charge

delivery time) is the rate limiting step. The MOSFET driver is designed to provide

very rapid potential injection in a unit time (dV/dt) capable of charging

capacitance in a relatively short time interval.

The contraction times (discharge events) of the PE stack employed in the

second generation dDAC, triggered by the falling positive edge, Figure 3.10C

and 3.10D, seem to be independent on the controller used and take

approximately 15 ms in either case to full contraction. It is clear however that the

rate of contraction facilitated by the circuitry embedded into the MOSFET box is

much quicker in the initial stages. The discharge times induced by the MOSFET

controller resemble the classic discharge curves of a capacitor through a resistor,

Figure 3.10C. This is what the MOSFET box was also designed to support: rapid discharge of the PE capacitance through a small-value resistor during the "off" states.

The contraction times are slightly shorter than the time it takes to extend the PAHL 18/20 with the use of MDT693A controller (20 ms) but significantly longer than the time it takes to extend the PAHL 18/20 with the use of the MOSFET (0.5 ms) and are the rate-limiting steps in each extension-contraction cycle.

The full extension-contraction cycle (0-130 V) with the Thorlabs controller paired with the PAHL 18/20 from the second generation dDAC takes on average 35 ms (20 ms plus 15 ms), yielding the maximum possible frequency of a little over 28 Hz (for a maximum pressure difference). With the MOSFET controller and the same piezo stack (PAHL 18/20) the maximum frequency for the full extension-contraction cycle (0.5 ms plus 15 ms) is estimated at a little over 64 Hz. Identical measurements were performed with the Thorlabs PE4 piezoelectric actuator from the first generation dDAC. The extension and contraction time-dependent traces are shown in Figure 3.11.

In combination with the Thorlabs MDT693A control box, the physical full extension takes about 5 ms to complete while the contraction lasts ~ 10 ms, giving a period of ~ 15 ms, and maximum frequency of 66 Hz. When combined with the (home-made) MOSFET end-stage control box, the period (extension 0.4

ms, contraction 10 ms) is shortened to ~ 10.4 ms, and maximum frequency raised to 96 Hz for a maximum pressure difference.

In order to exploit all capabilities of the dDAC device at maximum frequency and maximum pressure difference, each square (TTL-like) pulse needs to have its ON duration time short enough not to interfere with the contraction (coupled to the discharge of the capacitance) of the PE stack. For the PAHL 18/20 stack, the duration of the ON pulse cannot be longer than the time it takes to fully extend the bolt attached to the PE, which was found to be 0.5 ms. With the full cycle estimated at 15.5 ms (at 64 Hz) long, the duty cycle should be less than 3.2 %. For the first generation PE, the duty cycle for the high-voltage pulse must remain less than 3.8 %.
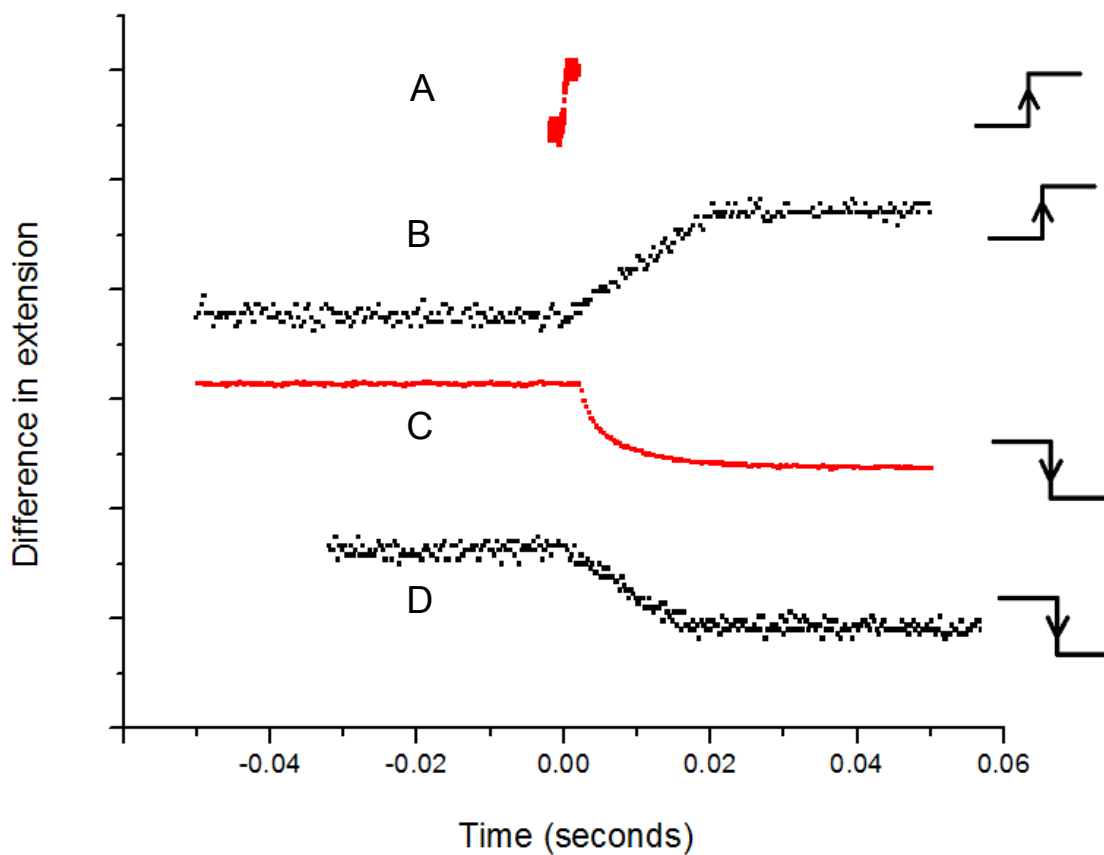
Figure 3.10: The extension (A, B) and contraction (C, D) events for the second generation PE actuator (Jena). The red traces (A, C) are generated with the MOSFET piezo controller while the black traces (B, D) are generated with Thorlabs high-voltage controller. When enlarged (not shown), the first trace (A) represents the full extension occurring within ~ 500 μs
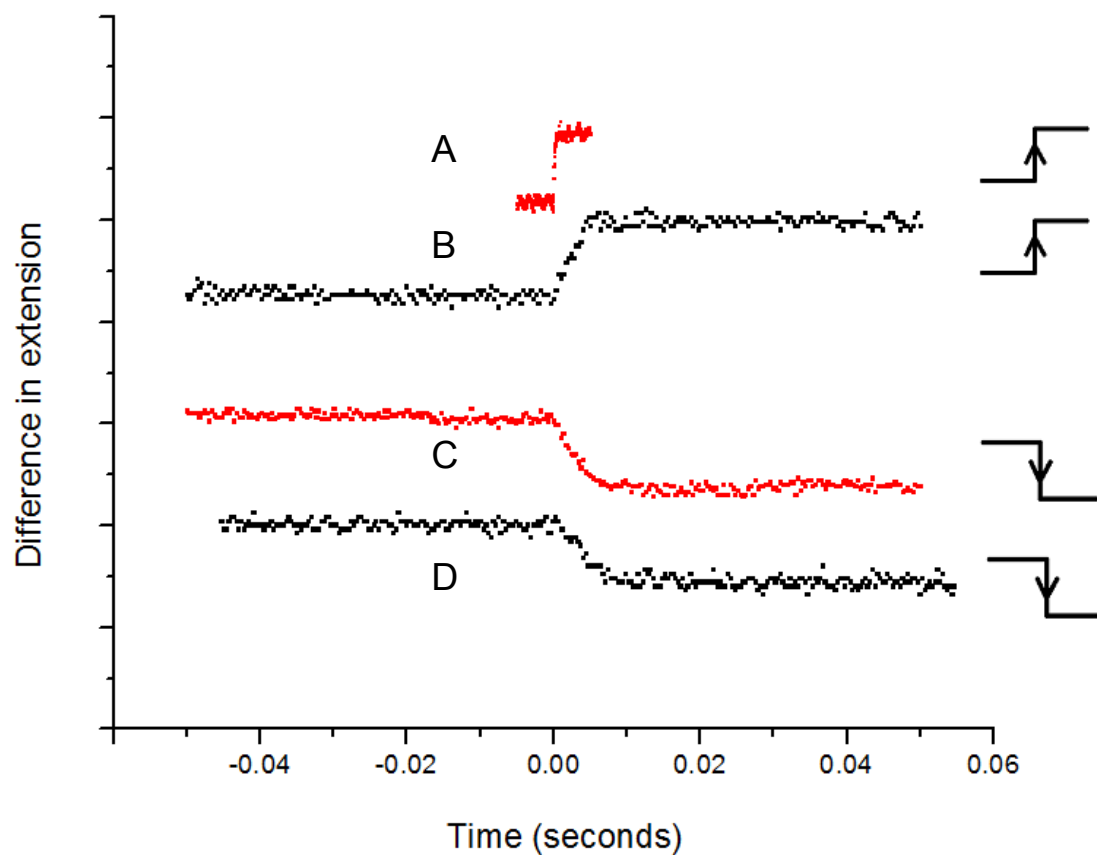
Figure 3.11: The extension (A, B) and contraction (C, D) events for the first generation PE actuator (Thorlabs). The red traces (A, C) are generated with the MOSFET piezo controller while the black traces (B, D) are generated with Thorlabs high-voltage controller. When enlarged, the first trace (A) represents the full extension occurring within ~ 400 µs

3.4 Summary

While the modern DAC allows for static and dynamic pressure measurements with low compression rates, the dDAC will soon become the true universal tool for high-pressure measurements. Advances in technology will allow for further reduction in size and increase in pressure variation and will help to explore the multiple analytical techniques that can be applied to small volumes of samples exposed to pressure variations within dDAC.

Especially the Raman spectroscopic technique is well-suited for resolving different polymorphs. Various forms of molecular crystals have distinct and unique Raman vibrations, the most notable example of which are the different phases of ice. The kinetics of the dynamic pressure-induced changes in materials can also be investigated by the amplitude change and the phase-shift of the optical signal while the cycling is in progress. Comprehensive models of pressure-induced phase transitions at different temperatures can be built upon the kinetic measurements with the use of a dDAC. The second generation dDAC is a well suited tool to achieve such goals.

3.5 References

(1)   Evans, W. J.; Yoo, C. S.; Lee, G. W.; Cynn, H.; Lipp, M. J.; Visbeck, K. *Rev Sci Instrum* **2007**, *78*.

(2)   Bassett, W. A. *High Pressure Res* **2009**, *29*, Cp5.

(3)   Piermarini, G. J.; Block, S.; Barnett, J. D.; Forman, R. A. *J Appl Phys* **1975**, *46*, 2774.

(4)   Barnett, J. D.; Block, S.; Piermari.Gj *Rev Sci Instrum* **1973**, *44*, 1.

(5)   Adams, D. M.; Appleby, R.; Sharma, S. K. *J Phys E Sci Instrum* **1976**, *9*, 1140.

(6)   Rice, A.; Proquest, 2011 Dynamic High Pressure Measurements and Molecular Dynamic Simulations of Phase Changes and Vibrational Dynamics in Molecular Solids.

(7)   Chronister, E. L. *SGER: Development of Dynamic Diamond Anvil Cell Spectroscopy*; University of California, **2007**.

Chapter IV

Spectroscopy, Thermodynamics, and Molecular Modeling

of Bis-Anthracene and its Photoisomer

4.1 Introduction

4.1.1 The Classic [4+4] Cycloaddition Reaction

Given the proper circumstances, 4π electrons from one molecule may "react" upon illumination with 4π electrons from another molecule in a cycloaddition reaction. The entire process involves 8π electrons and the intermediate proceeds through an excited state to form the reaction's product. Probably the oldest [4+4] cycloaddition reaction known to humanity is the light-induced dimerization of anthracene, An, in a solution[1] with the formation of low-solubility dianthracene dimer, An_2, observed in 1866. The reactant, anthracene and the product, dianthracene are both thermally stable up to 200 °C and yet photoreversible - illumination of An_2 with sufficiently high-energy photons gives back crystalline anthracene, Figure 4.1.

According to the topochemical postulate[2], reactions in the solid state normally proceed with a minimum of atomic or molecular motion. This is because of the dense molecular packing in a crystal lattice. For this reason, topochemical reactions in solid-state are more stereoselective, often giving rise to products otherwise inaccessible in an identical reaction in a solution. Unfortunately, the dimerization of anthracene in a solid state is topochemically forbidden due to the reaction centers, C(9) and C(10), being too far from neighboring An molecule. According to Schmidt[2], the reaction will involve the nearest neighbor. In [2+2] photoreactions studied by Schmidt[2], double bonds of the reacting molecules need to be separated by distances shorter than 4.2 Å and aligned in parallel for the p(z) orbitals to overlap sufficiently with the formation of photoproducts. Only very few linker-less systems with the anthracene moieties are capable of the [4+4] dimerization in a crystal phase when exposed to appropriate wavelengths. This limitation arises from the fact that not many anthracene derivatives crystallize in a sandwich-like configuration, arrangement required for the [4+4] photodimerization reaction. Such geometrical requirement is however met in few 9-substituted anthracenes, such as the anthracene-9-carboxylic acid (9-AC). This aromatic carboxylic acid reversibly photodimerizes and dissociates back at room temperature within minutes in a crystal phase, Figure 4.2, and, unlike other 9-substituted anthracenes, crystallizes in the head-to-head arrangement. This interesting cycloaddition reaction was explored in detail by Dr. Chris Bardeen.

Reversible, large shape changes in crystalline organic nanorods of 9-AC have been induced by localized photoexcitation[3].

In recent years, a variety of approaches have been explored in the field of crystal engineering to facilitate the photodimerization reaction in a crystal phase. Topochemical, supramolecular and catalytic methods have attracted special attention with the main goal of inducing favorable arrangement of the substrate molecules for a [4+4] photodimerization.

In certain systems, the preorientation of the reactant molecules is not necessary prior to irradiation. The family of bichromophoric systems linked by one or two linkers of different types has been explored. An intramolecular cycloadduct has been often obtained upon illumination[4], such as in the linked anthracene sub-family.

In published studies on linked-anthracenes, special attention was given to 9,9'- as well as to the 10,10'-linked bis-anthracenes due to their unique stereochemical arrangement and the fact that the light-induced reaction in these systems occurs as an intramolecular process[4]. In the next two Chapters we have devoted much of our effort and time to explore selected aspects of the light-induced photodimerization and the dissociation reaction of the bi(anthracene-9,10-dimethylene), BA. This molecule constitutes two anthracene units held together by two dimethyl linkers, Figure 4.3, in a face-to-face position. Such molecular design ensures photochemically reactive topology provided the linkers

are of appropriate length. The distance between the reactive centers in BA[5], 2.76

Å, is far less than the anticipated limit of 4.2 Å measured by Schmidt[2] and

required for the proper overlap of the p(z) orbitals on reaction centers (carbon

atoms).

254 nm or 200 °C

366 nm

2

An

An_2
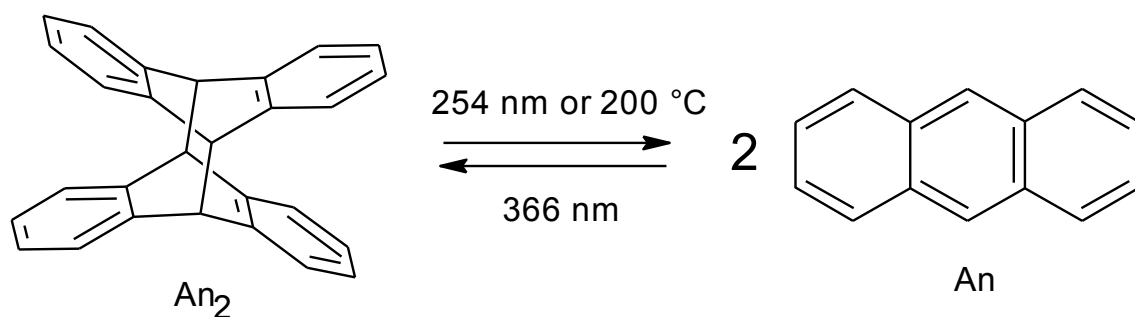
Figure 4.1: Anthracene (An) dimerizes under deep-UV illumination in a solution with the formation of dianthracene (An_2); the reverse reaction takes place with shorter wavelength illumination or with intense heating
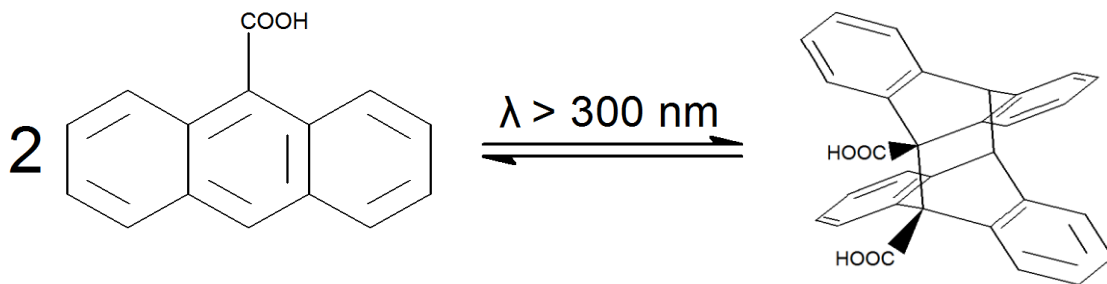
Figure 4.2: The intermolecular [4+4] photocycloaddition reaction in 9-AC occurs in the crystal phase
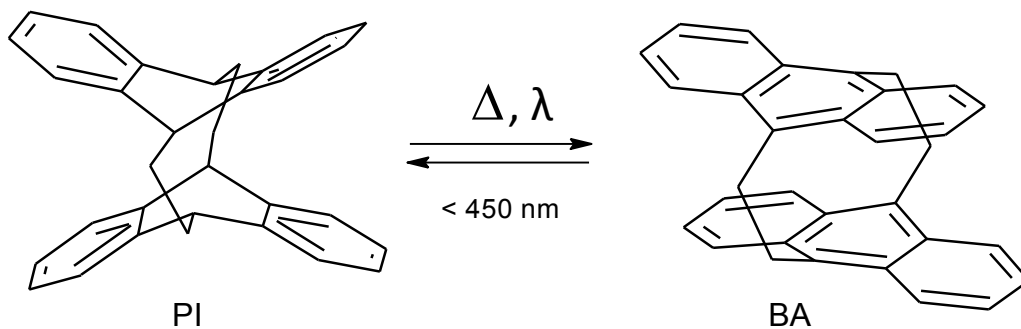
Figure 4.3: The classic [4+4] cycloaddition reaction in BA induced by light; the back-reaction, PI-to-BA was shown to be facilitated by heat or deep-UV light illumination[6]

4.1.2 The Influence of Conjugation on the Spectral Properties of Polyacenes and Their Photoisomers

A family of four linear aromatic hydrocarbons, polyacenes, shown in Figure 4.4: benzene, naphthalene, anthracene and tetracene are characterized by their complex absorption spectra shown in Figure 4.5.

The simplest polyacene in this family, benzene, features rich-in-structure absorption spectrum shifted most to the high energy end of the absorption spectrum. One of the three main $\pi \rightarrow \pi^*$ transitions, the so called "b-band" in benzene is located at around 255 nm and also manifests its presence in most substituted benzene derivatives.

Anthracene (An) consisting of three aromatic rings, and absorbs slightly further towards lower energies when compared to benzene or naphthalene. When illuminated with UV light (~ 366 nm) in a solution, the intermolecular photocycloaddition occurs between two anthracene molecules with the formation of dianthracene (An$_2$, Figure 4.1). This intermolecular dimerization reaction (also referred to as [4+4] cycloaddition reaction) between anthracenes is inhibited in a crystal phase for topochemical reasons. In an inert atmosphere, under continuous illumination with a UV source capable of emitting a broad spectral range of high-energy photons, a photostationary equilibrium mixture can often be formed. Dianthracene, when illuminated with deep-UV photons (<300 nm)

dissociates back to anthracene[4], thus rendering the reaction reversible. Extensive heating is also known to cause the back-reaction, called the dissociation reaction. Temperatures as high as 200 °C are required for this process to occur[4].

If oxygen is present during the anthracene photodimerization reaction under UV light, the photoproduct is often partially photooxidized under these oxidizing conditions, forming not only the photodimer- dianthracene, but also a byproduct, endoperoxide[4]. Structurally, a molecule of dianthracene consists of four identical ortho-substituted benzene rings mutually connected to each other, as shown in Figure 4.1.

The reacted bis-anthracene molecule, referred to as a bis-anthracene photoisomer, and abbreviated to PI, Figure 4.3 is a product of a light-induced intramolecular reaction in bis-anthracene (BA) and is structurally similar to dianthracene - four ortho-substituted benzene rings interconnected with each other. The only structural difference between PI and An_2 are the 4 additional methyl groups added to both sides in the C(9) and C(10) positions in either of the two anthracene planes. The molecule of PI additionally holds two cyclobutane rings at either side of the dianthracene skeletal structure. Similar to benzene, PI features a *b-band* at around 255 nm. This low-intensity band can be resolved in absorption spectroscopy after all BA is transformed to PI with light.

Benzene   Naphthalene   Anthracene   Tetracene
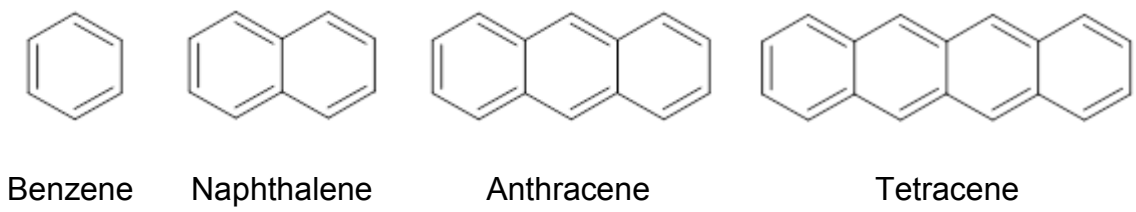
Figure 4.4: Structures of the first four linear aromatic hydrocarbons, polyacenes
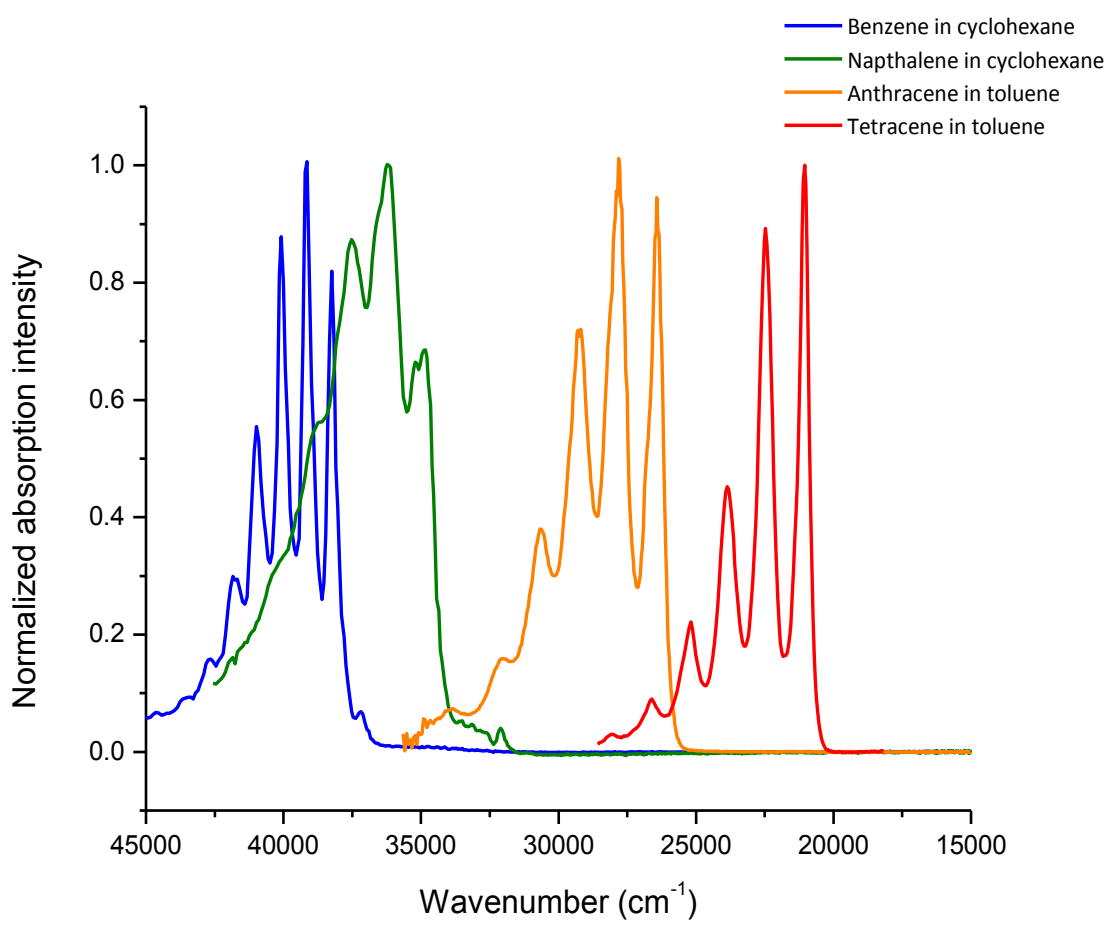
Figure 4.5: Absorption spectra of the first four polyacenes in solution: benzene, naphthalene, anthracene and tetracene

4.2 Spectroscopic, Thermodynamic and Physical Properties of Bis-Antracene

4.2.1 Absorption Spectroscopy Measurements

Absorption in cyclohexane solution

In spite of the fact that only miniscule amounts of BA and PI dissolve in cyclohexane, BA is characterized by very large extinction coefficient at the maximum of its absorption and therefore the absorption spectra of BA are easy to recognize due to their characteristic shape, Figure 4.6, red spectrum. The absorption spectrum of BA drops nearly to zero at ~ 325 nm and continues to rise with a broad feature between ~ 350 to 450 nm, Figure 4.7, red spectrum. Beyond this wavelength, BA has no absorption in the visible part of the electromagnetic spectrum.

Absorption in governed by the Beer-Lambert law and is defined as a product of three variables:

$$A = \varepsilon l c$$

where ε is the extinction coefficient ($L*mol^{-1}*cm^{-1}$) of the sample in study at a given wavelength, l is the thickness of the solution containing the sample (cm) and c is the molar concentration ($mol*L^{-1}$).

The bis-anthracene photoisomer, PI, Figure 4.6, blue spectrum, besides its low extinction coefficient b-band around 255 nm shows most of its absorption at wavelengths shorter than 230 nm which are typically difficult to resolve optically. The absorption spectrum of a cyclohexane solution of selectively-deuterated BA(d) has been recorded and compared to BA. As expected, their absorption spectra are identical, Figure 4.8, which only confirms that the synthesis yielded BA(d) as the main product.
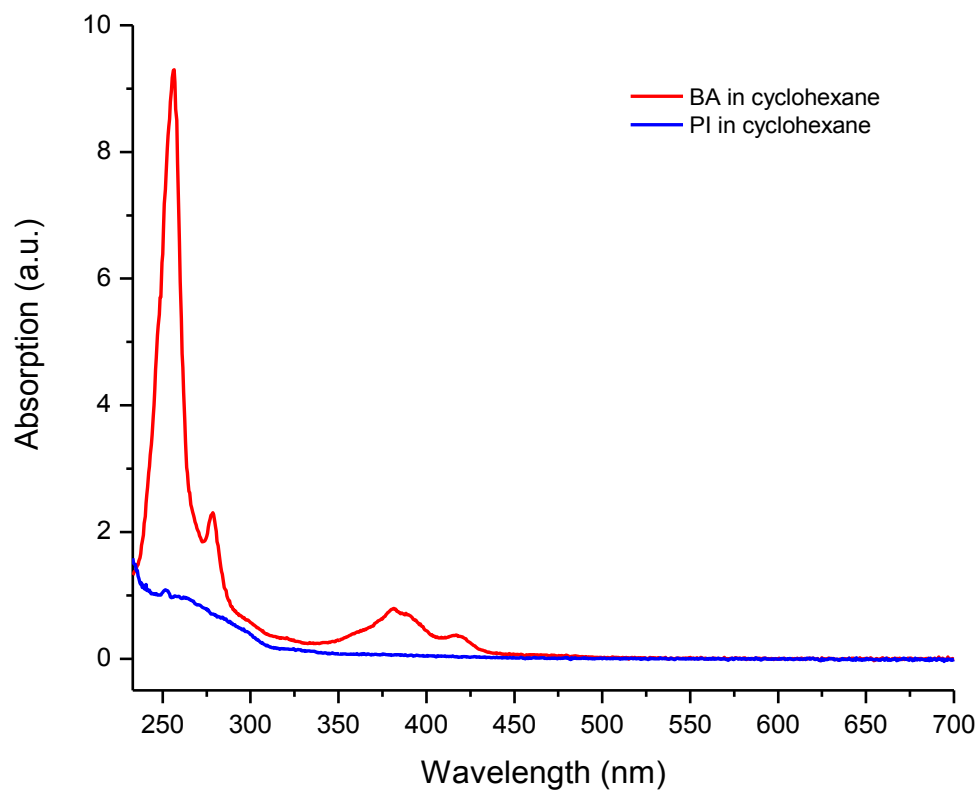
Figure 4.6: Corrected for reference absorption spectra (230 – 700 nm) of saturated solutions of BA (red) and PI (blue) in cyclohexane measured with Cary 50 absorption spectrometer. Cyclohexane is transmitting down to deep-UV wavelengths
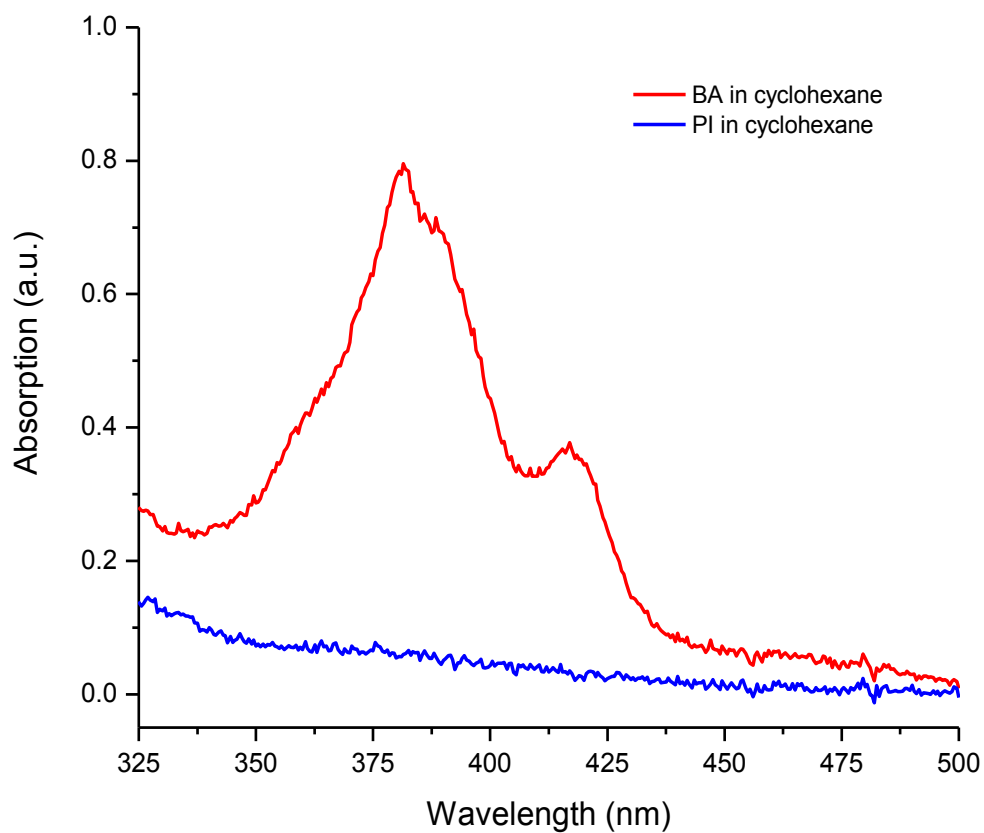
Figure 4.7: Corrected for reference absorption spectra (325 – 500 nm) of saturated solutions of BA (red) and PI (blue) in cyclohexane measured with Cary 50 absorption spectrometer. PI does not absorb in this spectral region
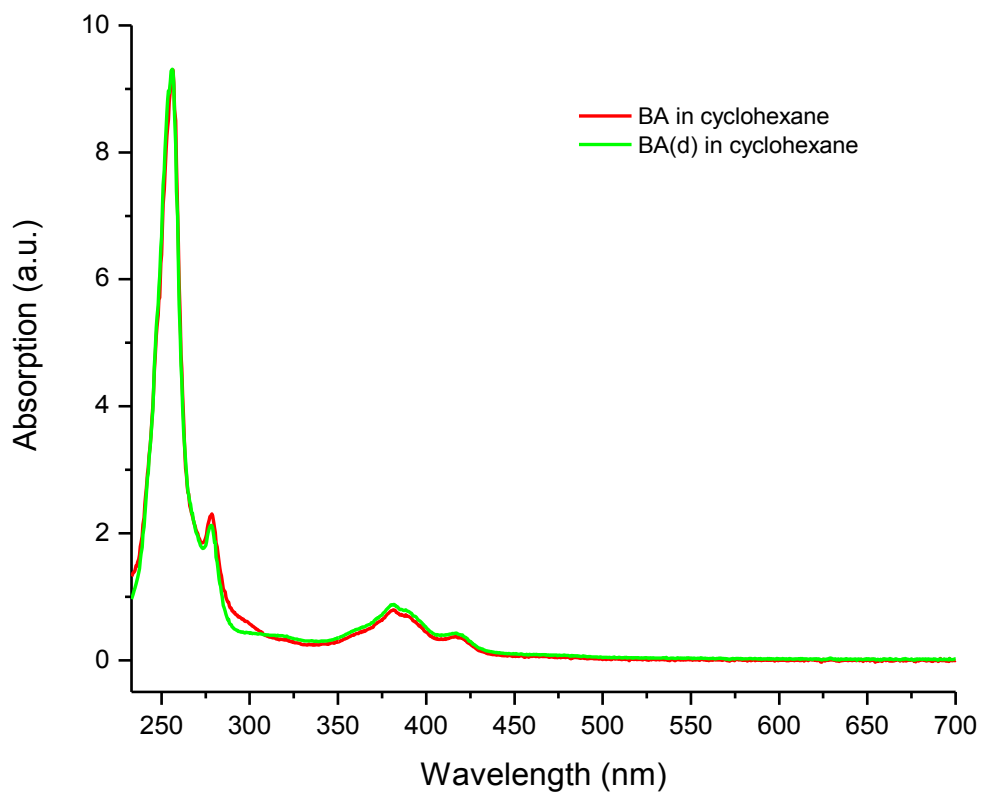
Figure 4.8: Corrected for reference absorption spectra (230 – 700 nm) of saturated solutions of BA (red) and selectively deuterated BA(d) (green) in cyclohexane measured with Cary 50 absorption spectrometer. Their absorption spectra are identical

Absorption at high-pressure with a Diamond Anvil Cell

Natural diamond, the essential elements of each Diamond Anvil Cell, are typically doped with various types of impurities. Some of them can manifest themselves as a change in a color of the diamond gem. Nitrogen is the main impurity in colorless Type I diamond and thus limiting its uses in optical and infra-red spectroscopy due to bands obscuring important vibrational regions in these spectra. Type II diamonds differ in that they have no measurable impurities introduced by nitrogen and appear to be colorless as well. Figure 4.9 represents absorption spectra of Type I (black spectrum) and Type II (red spectrum) diamond from 200 to 700 nm region. Both were recorded in an identical fashion: on VARIAN Cary 500 spectrometer equipped with a pair of UV lenses located within the sample compartment. Between the two quartz lenses, in the focal point, the DAC was positioned on an x,y,z-holder.

As can be seen from the Figure 4.9, the Type II diamond seems superior to the Type I diamond in at least three important aspects in absorption measurements involving samples absorbing at shorter wavelengths.

The Type I diamond's optical density (OD) at every wavelength shown above is higher by at least 0.5 when compared to Type II. It is important to maintain as low OD introduced by the DAC and the set of lenses as possible. Certain samples such as BA feature multiple absorption regions of various intensity depending on the wavelength. The higher OD introduced by the chosen

set of diamonds adds to the OD of the sample film and limits the maximum concentration of a sample dispersed within a polymer film under investigation.

Depending on the type of a sample in study, the fine structure in the absorption spectrum of Type I diamond between 420 – 350 nm may overlap with important absorption bands (in BA with low-intensity bands between 450 – 350 nm). This fine structure cannot always be easily corrected for in the final steps of spectral evaluation by means of numerical division of the signal by the baseline.

The OD of the Type I diamond increases sharply past around 350 nm towards the shorter wavelength (high energy) end of the absorption spectrum. This is an important disadvantage of Type I diamond when compared to Type II. The deep-UV absorption band of BA and 9TBA (as shown in Chapter V) are all obscured by the absorption of the nitrogen impurities present within the Type I diamond in the UV region below 350 nm.

The Type II diamond is transparent to light down to around 235 nm and thus the absorption bands of BA present at around 257 nm are resolved provided the concentration of the sample within the polymer does not exceed the OD limits imposed by the spectrometer. In infra-red spectroscopy, both types of diamonds have multiple absorption bands up to ~ 4000 cm^{-1}, Figure 4.10. However, only the Type I diamond has an absorption band with very low transmittance around 1250 cm^{-1}, while the Type II diamond has no bands around this wavelength thus allowing possible molecular vibrations to be resolved.
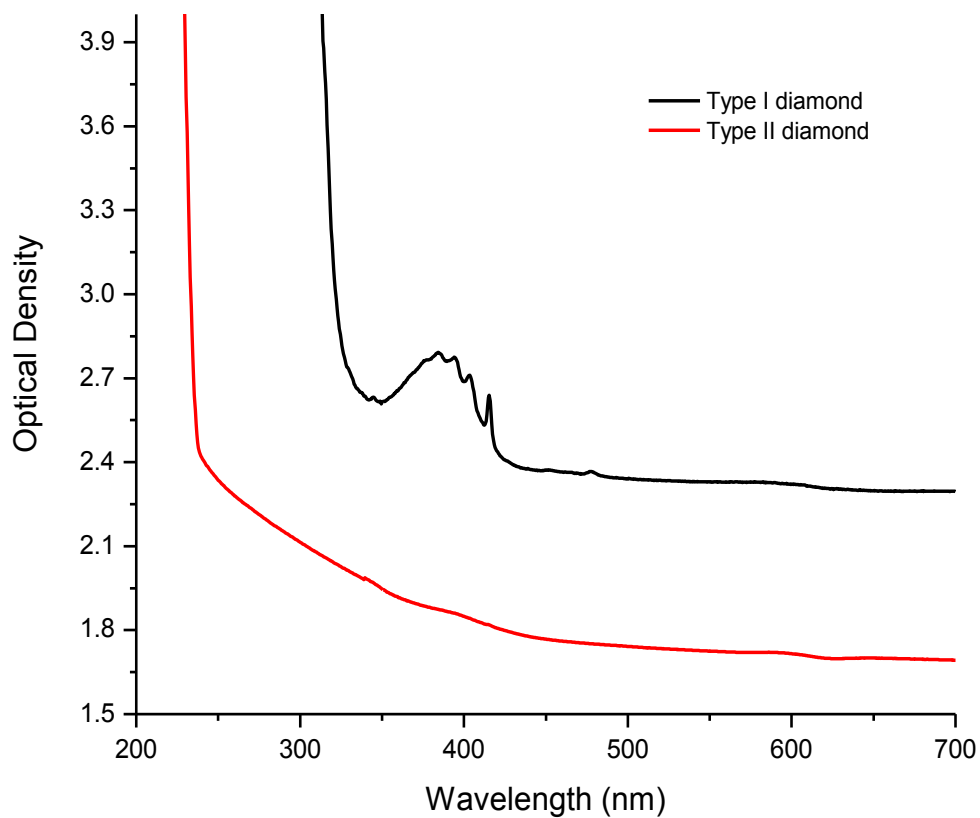
Figure 4.9: Absorption spectra of a natural, transparent diamond culets used in high-pressure spectroscopy: Type I (black) and Type II (red)
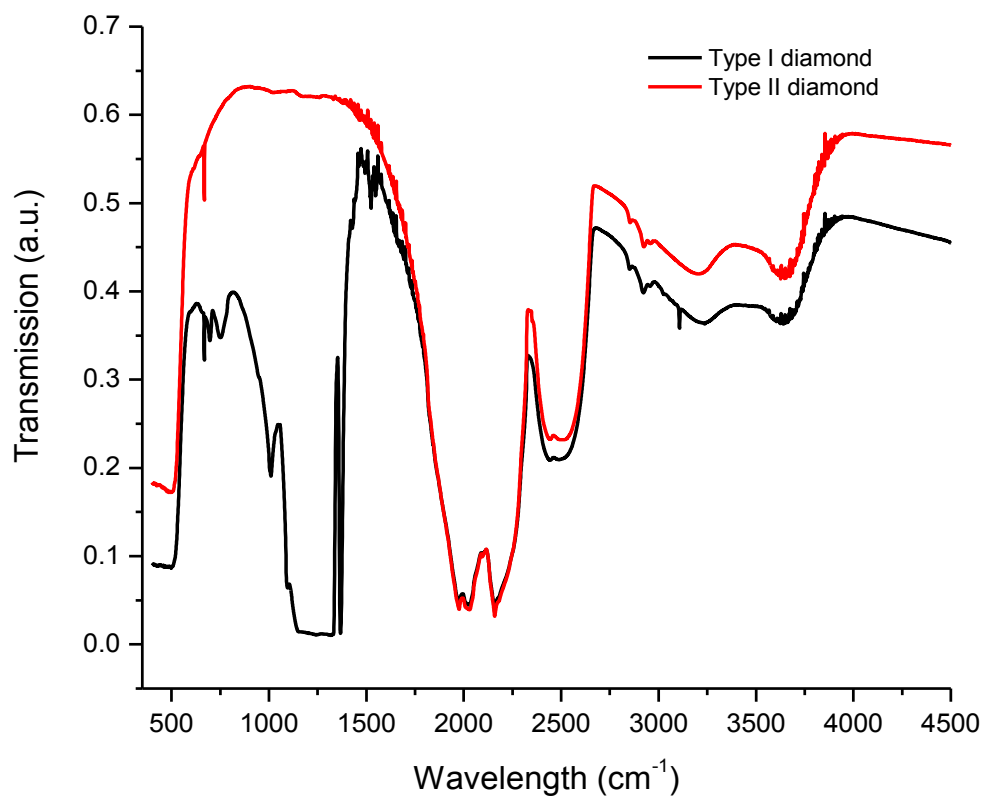
Figure 4.10: IR transmission spectra of natural, transparent diamond culets used in high-pressure spectroscopy: Type I (black) and Type II (red). The transmission/absorption values depend greatly on the thickness of the diamond

4.2.2 Temperature- and Pressure-Dependent Absorption Measurements

Pressure-dependent absorption measurements

With the use of DAC, mechanical force was applied to a freshly prepared PI (through the means of illumination of BA) dispersed in Zeonex in the range from around 6 kbar to 30 kbar, each time replacing the sample film. At each pressure point, a small amount of ruby dust was added into the sample compartment for pressure calibration (± 0.5 kbar). The spectral evolution was followed as a change in the area under the maximum of absorption of BA, near the ~ 257 nm peak (value at ambient pressure). Eventually, the evaluated kinetic traces were plotted as a function of time clearly showing signs of accelerated recovery of BA (from PI) as pressure was applied.

To raise the pressure within DAC to desired value, it is essential to lower the time it takes to turn the three identical Super Invar bolts which press one half of the DAC against the other. In our measurements the pressure was raised within ~ 10 seconds.

In temperature-dependent absorption measurements, the BA/PI/Zeonex film was carefully placed within a DAC with its gasket removed and assembled with the three Super Invar bolts loose. At ambient pressure, the gasket is redundant and contributes to additional attenuation of the absorption signal. The resistively-heated DAC was used in an unconventional manner in that it provided

a holder for the small chip of the sample film at ambient pressure. Most importantly, the temperature across the sample film was uniform thanks to the fact that a pair of diamonds were in direct contact with the Zeonex polymer. Diamond is a material that is well known to be an excellent heat conductor. In addition, the relatively bulky DAC metal casing prevented the temperature from fluctuating beyond a few centigrades from the set temperature value.

The metal DAC was wrapped in a few layers of an electrically resistive tape which was connected to a Variac (variable transformer). The temperature was thus controlled simply by changing the voltage that was applied to the resistive tape. The temperature was monitored using a thermocouple (type K, Omega HH22) in direct contact with the DAC's metal casing. The temperature-dependent measurements varied from room temperature to a maximum of around 63 °C.

Each scan spanned from 700 to 200 nm with the use of Varian CARY 500 spectrometer, 0.5 nm/step with 0.2 s integration time. The time it took to complete each absorption spectrum was over 3 minutes. In all types of measurements with BA/PI films we used Type II diamond cullets, ~ 0.5 mm in diameter.

4.2.3 Emission Spectroscopy Measurements

The two fluorescent forms of bis-anthracene

When dissolved in cyclohexane, we were able to detect emission from a "matured" (6-months-old) solution of BA. Figure 4.11 presents the normalized absorption spectrum of BA overlaid with the excitation spectrum detected at 480 nm. As we will describe later in this section, the intensity of the emitted (and thus detected) signal increases with time as the solution ages.

Site-selective fluorescence can be applied to elucidate different conformations of emitting species, provided the investigated forms absorb and emit light at slightly different wavelengths. When dissolved in cyclohexane, the BA absorption spectrum reveals at least two bands (below 300 nm) of very different intensities: the smaller intensity band with a maximum of absorption at 274 nm, Figure 4.12 red arrow, and the larger with an absorption maximum at 257 nm, Figure 4.12 green arrow, with relative intensities 0.16 to 1, respectively.

Each absorption band is a superposition of numerous transitions in the energy level diagram: the principal 0-0 transition as well as higher order transitions (0-1, 0-2, 0-3 etc.). The higher the order of the transition, the higher the energy of the quantum of light which is absorbed in the process. An absorption band is not symmetric. It extends from its maximum to shorter wavelengths (higher energies). On the other hand, an emission band extends

from its maximum towards longer wavelengths (lower energies). In order to spectrally address only one conformation of BA molecules, one needs to approach a set of absorption maxima from the so called "red wing of absorption". I.e. exciting at 275 nm in Figure 4.12 with sufficiently narrow-band excitation light-source, the experimentator assures that only one conformation is excited by selecting only the 0-0 transition of BA molecules absorbing at 274 nm. The resulting emission spectrum (Figure 4.12, red) features emission exclusively from one population provided no energy transfer from the excited state takes place.

Exciting towards higher energies (Figure 4.12, 263 nm) addresses the 0-0 transition of species absorbing at ~ 257 nm as well as higher-order transitions of the ~ 274 nm population. The resulting emission spectrum (Figure 4.12, green) represents an emission from all species that absorb light at 263 nm, in this case a mixture of the two BA conformations.

Provided there was only one conformation of BA molecules present in the solution, the general shape of the emission spectra would not depend greatly on the wavelength of excitation.

A similar approach was used to uncover the different species in the 350 – 450 nm spectral region in the absorption of BA (Figure 4.13, black dashed spectrum). Exciting at 432 nm selectively addresses (mostly) one species of BA molecules (the resulting emission spectrum is shown in blue, Figure 4.13) while excitation at 375 nm selects all species absorbing at that wavelength (emission

spectrum in red, Figure 4.13). Here too the resulting emission spectra vary greatly in shape with the excitation wavelength.

The two fluorescent forms of BA identified by the means of site-selective fluorescence in cyclohexane could be attributed to the two conformers already described in the literature[7] and called BAt and BAr.
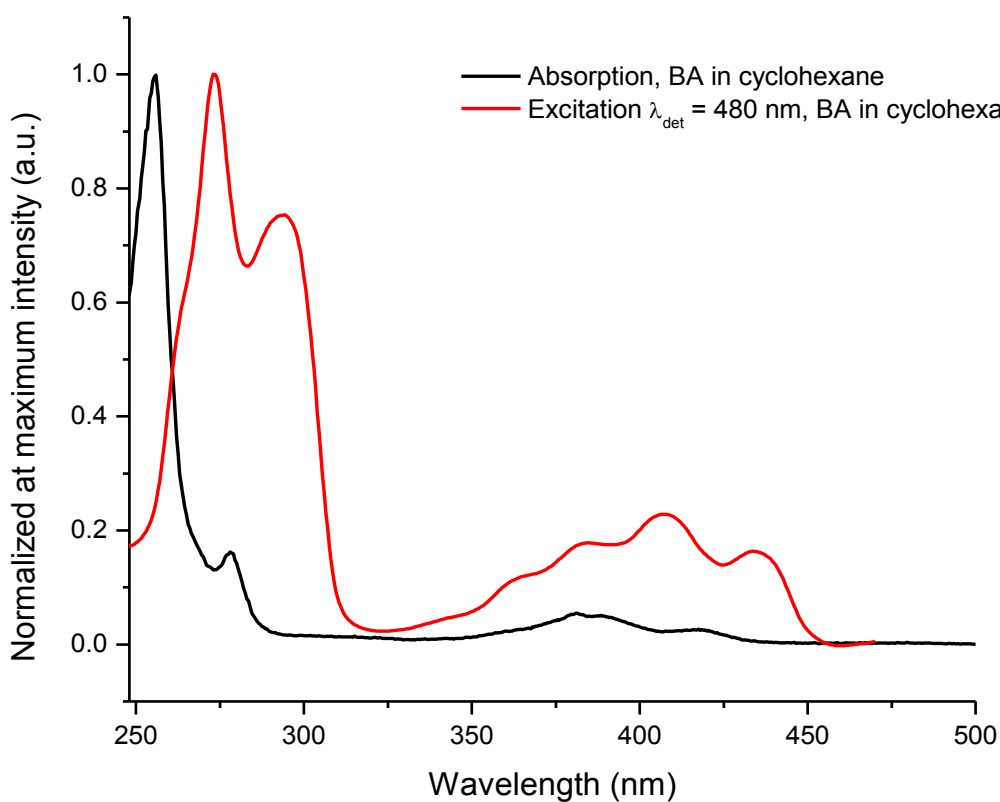
Figure 4.11: Spectra normalized at maximum of absorption and emission. Absorption, black, and excitation spectrum λ_{det}=480 nm, red, of ~ 6-months-old solution of BA in cyclohexane overlaid on one graph
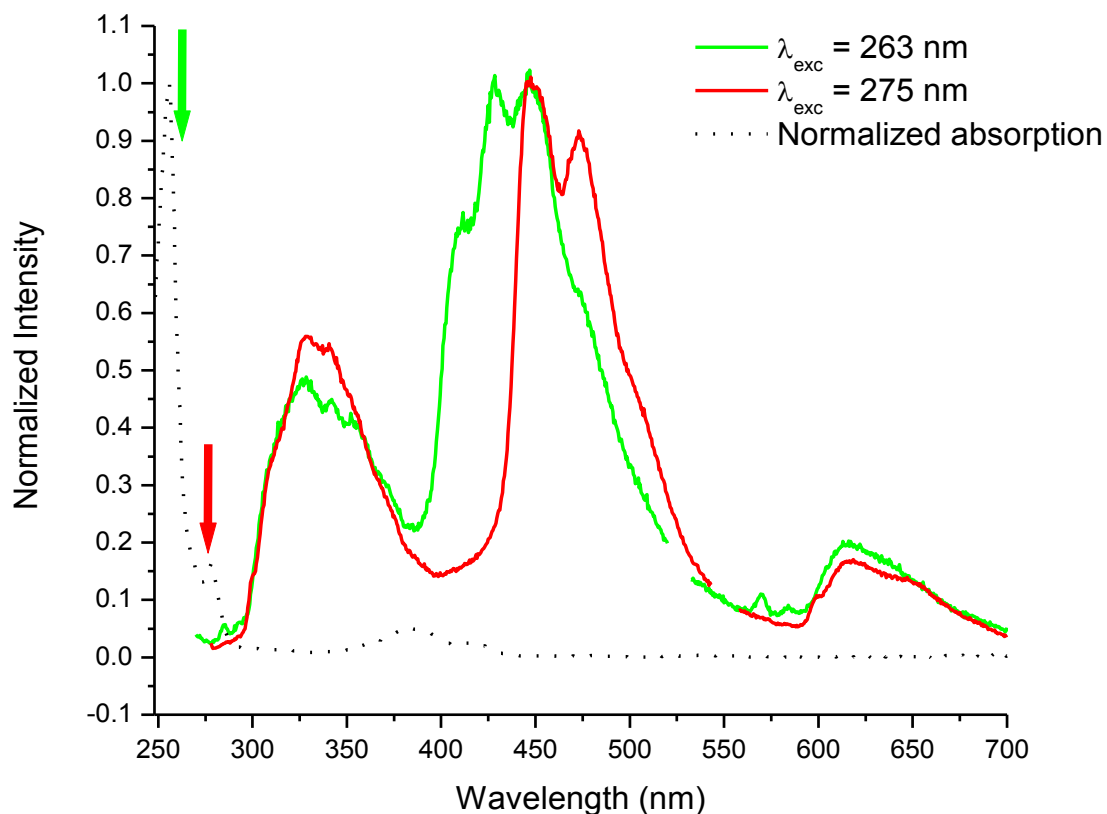
Figure 4.12: Absorption spectrum (black, dashed) of BA overlaid with normalized emission spectra (exc. at 263 and 275 nm). Exciting at 275 nm yields emission from only one fluorescent form (red spectrum). Exciting at 263 nm yields emission from two forms of BA (exciting in the vibronic region of the red-shifted form as well as in the 0-0 region of the blue-shifted form of BA)
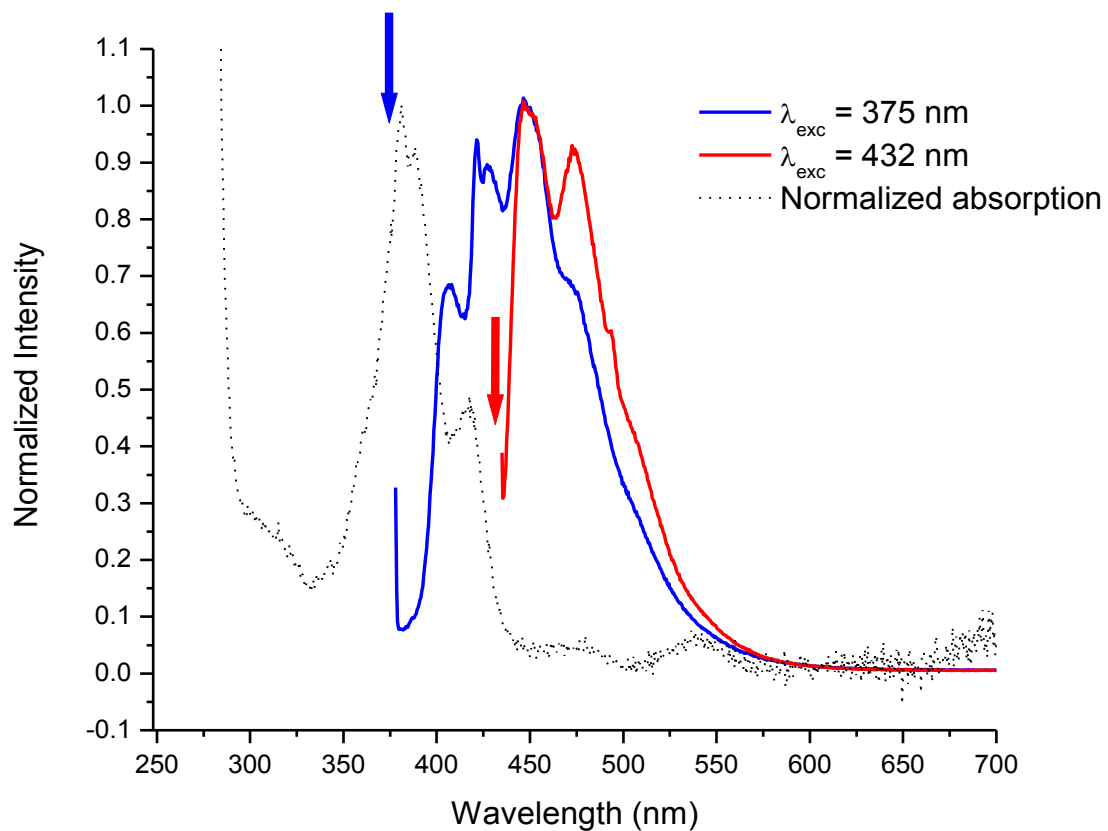
Figure 4.13: Absorption spectrum (black, dashed) of BA overlaid with normalized emission spectra (exc. at 375, blue and 432 nm, red). Shapes of the emission spectra vary with the excitation wavelength suggesting multiple (at least two) populations of emitting species present in the solution

Maturation of bis-anthracene in a solution

Unilluminated BA crystals were used to prepare three saturated solutions in cyclohexane. The difference between the three solutions was the amount of time each of them was let to spend in the dark: around 6 months, 16 days and freshly made (minutes after preparation). Excitation spectra were recorded for each of the solutions with detection wavelength fixed at 480 nm. The resulting normalized (at maximum of fluorescence) spectra are presented in Figure 4.14.

Three emission peaks can be clearly distinguished at ~ 262, ~ 273 and ~ 293 nm. The normalization procedure fixed the intensity of the principal peak of emission at ~ 273 nm to arbitrary 1 (the actual fluorescence intensities of all three peaks varied for each sample and the trend is shown in Figure 4.15 and Figure 4.16). With the ~ 273 nm peak fixed at 1 in Figure 4.14, the intensities of the other two peaks changed with the amount of time the BA sample spent in the dark in solution of cyclohexane in sealed vials.

As the BA ages in cyclohexane, the ~ 293 nm peak (with respect to the ~ 273 nm peak, Figure 4.14) is gaining in relative fluorescence intensity. The most blue peak (at ~ 262 nm) on the other hand did not behave consistently with that trend.

Based on the spectra shown in Figure 4.15 and 4.16, the intensity of emission at 480 nm (wavelength of detection) is larger the older the solution of BA. The mechanism of this aging observed here is not yet explained. It can be

speculated that this effect is related to the time-dependent polymerization of BA postulated by J. H. Golden in 1962[6]. It can be speculated further that BA is non-fluorescent while its polymerized form, grown with time from a cyclohexane solution decays radiatively from the excited state. This would explain the increase in fluorescence intensity seen with time.

Another explanation is that the two conformers[7] of BA, named It nad Ir have different fluorescence quantum yields. Once in solution, a transformation of less fluorescent conformer into a more fluorescent conformer takes place over time which contributes to the spectral evolution.
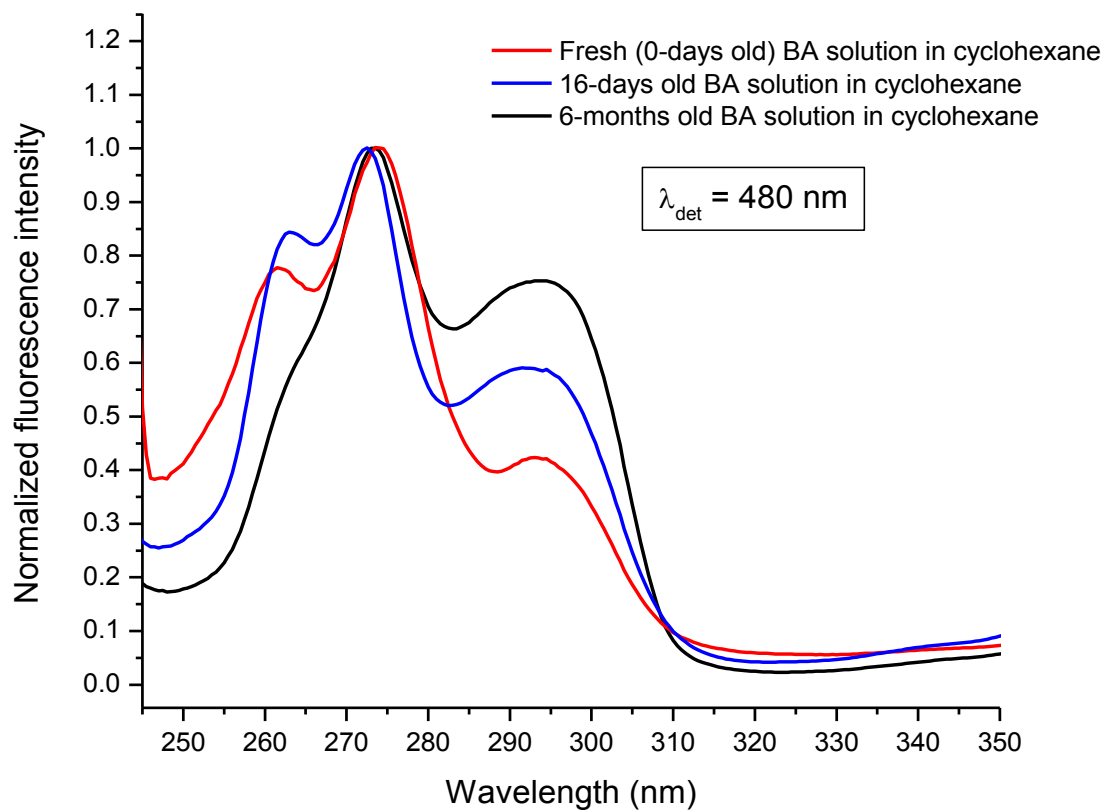
Figure 4.14: Normalized excitation spectra of three solutions of BA in cyclohexane in the deep-UV spectral region. The detection wavelength is fixed at 480 nm
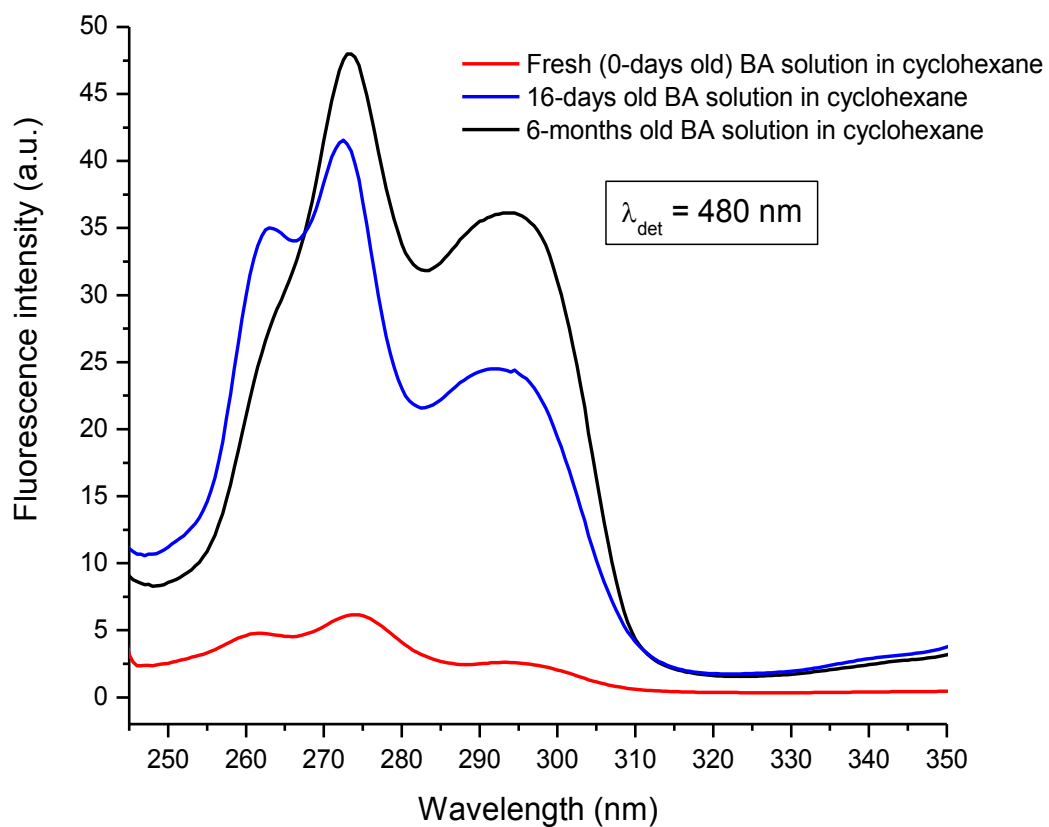
Figure 4.15: Excitation spectra of three solutions of BA in cyclohexane in the deep-UV spectral region. The emission intensity at 480 nm is higher the "more mature" the solution of BA is in a given sample
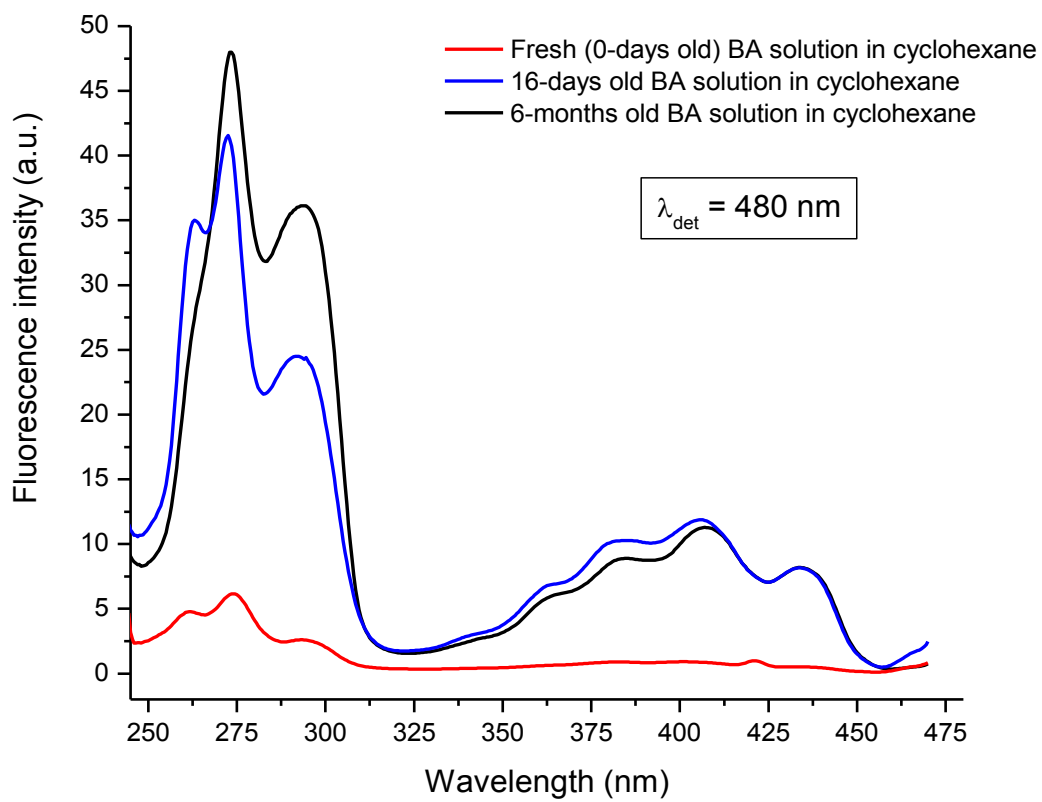
Figure 4.16: Excitation spectra showing full wavelength range from 245 to 470 nm
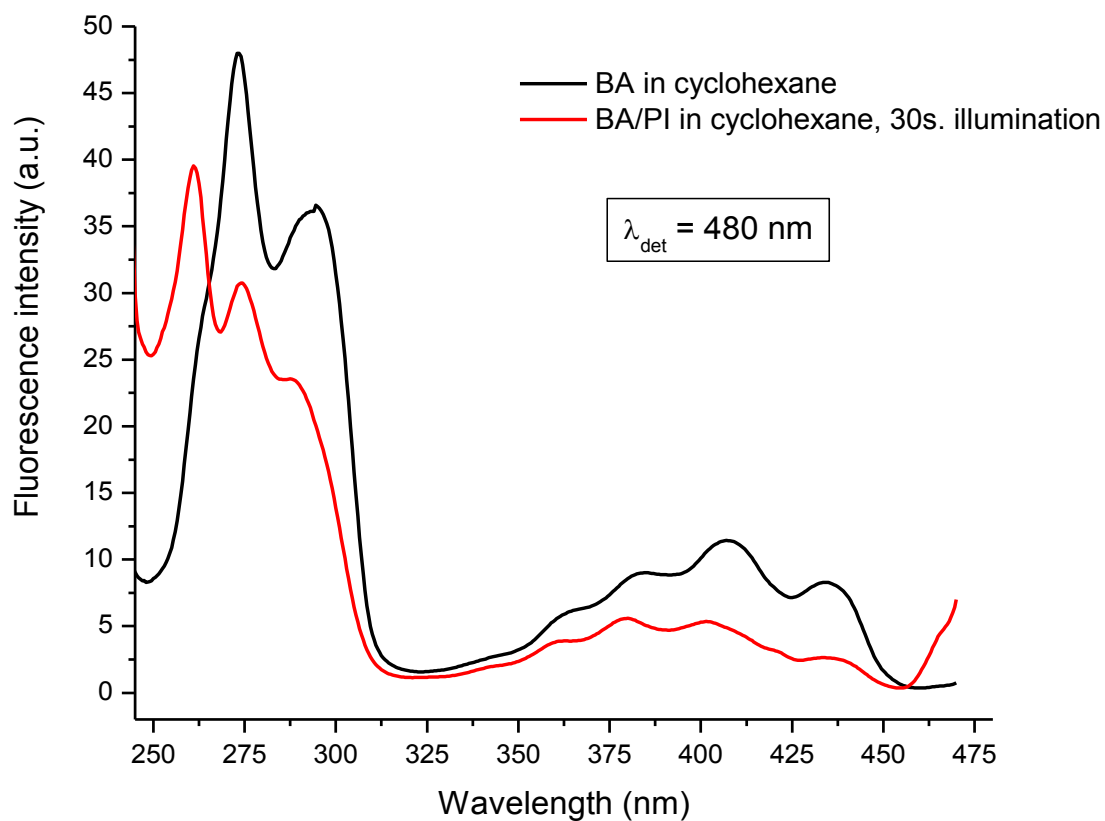
Figure 4.17: Excitation spectra of a 6-month-old solution before and after brief (30 s) illumination with a high-intensity halogen light source. The black spectrum shows the excitation of a BA solution while the red spectrum represents the excitation spectrum of partially converted (to PI) solution of BA. As expected, the excitation (and absorption, not shown here) spectrum lean towards the high-energy (UV) end of the spectrum

4.2.4 High-Resolution IR Spectra

Isotopic substitution is a widely used and accessible method in revealing the exact location and possible intermolecular interactions influencing molecular vibrations in studies involving IR spectroscopic technique. Replacing a hydrogen atom with its stable isotope, deuterium, doubles the mass of the atom, while preserving all chemical functionality of the molecule is study. Isotopic substitution can influence the rates of reactions (Kinetic Isotope Effect, KIE) but its primary application in experiments involving BA is to affect the vibrational frequency of the altered chemical bond. In general, heavier atoms display lower vibrational frequencies when engaged in chemical bonds with other atoms. In the simplest approach, a diatomic (A-B) molecule oscillates at a vibrational frequency described by a harmonic oscillator:

$$\nu = \frac{1}{2\pi} \sqrt{\frac{k}{\mu}}$$

$$\mu = \frac{m_A m_B}{m_A + m_B}$$

where μ is the reduced mass of the diatomic system and k is the spring constant associated with the chemical bond.

An exchange of a hydrogen atom to deuterium is not affecting the bond's spring constant k. When deuterium is combined with carbon (in a C-D bond) the value of the reduced mass, μ, approximately doubles as compared to a proton bound to carbon. According the equation for a harmonic oscillator, the frequency of the C-D bond is around 0.71 that of the unaffected, protonated carbon-to-hydrogen bond. On the other hand, replacing the involved carbon atom to one of its isotopes displays a much lower change in vibrational frequency as compared to the isotopic substitution of a hydrogen atom, resulting in modest changes in vibrational frequency in IR spectrum.

In order to determine the exact position of the vibrational stretches of the C-H bonds present exclusively within the dimethyl linkers of BA, we have replaced all aliphatic hydrogen atoms (eight atoms bound to four carbons for every BA/PI molecule), Figure 4.18, with its closest stable isotope, deuterium. This selective deuteration has the capability of allowing us to visualize (via IR measurements) other molecular vibrations coupled to the C-H/C-D vibrons in the crystals of BA/PI and reveal different local environments in which the linkers reside within a crystal. The synthesis of the selectively-deuterated BA, referred to as BA(d) is described in details in the Appendix. The formation of the desired product, BA(d), has been confirmed by the means of high-resolution MS spectra. The experimentally-determined C-D vibrational frequencies are compared to the calculated vibrational values for isolated molecules. Frequency calculations were

carried out with the use of one of the most advanced quantum analytical methods currently available within the Gaussian software packet (DFT-D, in 2012).

Two KBr pellets (Sigma-Aldrich, spectral grade, thickness < 1mm) were prepared from available crystalline material, BA and BA(d). After having recorded corresponding high-resolution IR spectra at low temperatures, each pellet was irradiated for a prolonged amount of time with a halogen lamp with the sole purpose of converting all material into photoisomers, PI and PI(d). Eventually, four types of high-resolution IR spectra were produced. In IR measurements, KBr-sample pellets were mounted on the tip of a closed cycle helium cryostat, inside the sample compartment of a high-resolution Bruker HR-120 FTIR instrument. Temperatures between 30 and 50 K were maintained for all four samples.

In the low-temperature IR spectra of protonated BA and PI, we have registered a congestion of indistinguishable peaks in the high-energy (2900 – 3200 cm^{-1}) end of the spectrum (spectra not shown). Unfortunately, this made it difficult for us to definitely assign any particular frequency to the symmetric or asymmetric aliphatic C-H stretches in the dimethyl linkers occurring within that region. The calculated C-H and C-D stretching frequencies are compared to experimental data for BA(d) and PI(d) and are summarized in Table 4.1.

As can be seen in Figure 4.19, the asymmetric vibrations (~ 2220 cm^{-1} in BA(d) and ~ 2240 cm^{-1} in PI(d)) show two peaks, closely located within ~12 cm^{-1}

from each other. We were unable to pinpoint the origin of these doublets. The possibilities however extend from the existence of different local environments surrounding the aliphatic hydrogens within the crystal lattice to the confirmed existence of two, similar in energy conformers of BA[7]. The latter case seems unlikely since such doublets cannot be possibly observed in PI, i.e. only one PI conformer was reported in the literature.

	Symmetric Stretches (cm^{-1})		Asymmetric Stretches (cm^{-1})	
	Calculated	FT-IR	Calculated	FT-IR
BA	2967	*	3076	*
BA(d)	2167	2150	2275	2223
PI	3007	*	3079	*
PI(d)	2192	2137	2283	2244

Table 4.1: Comparison between experimental and calculated energies of the C-H/C-D symmetric and asymmetric stretches in dimethyl linkers of BA/PI crystalline samples, in KBr. The energies of vibrations in protonated samples (empty fields, *) could not be assigned due to congestion in the range between 2900 to 3200 cm^{-1}

In another set of experiments, we monitored the spontaneous conversion of PI to BA at room temperature as a function of time by means of IR spectroscopy. As it turned out, we find the low-energy region between 640 and 820 cm^{-1} to be especially most convenient for recording the vibrational changes

occurring within 24 days between these two photoisomers, Figure 4.20. The low-energy modes are associated with wagging of hydrogen atoms bound to their aromatic subunits (substituted benzene in PI) in an out of the plane motion (~ 760 cm^{-1}). Lower in the energy scale, rocking motions of the carbon skeleton of the molecule causes changes in a dipole moment that manifest itself between ~ 600 – 700 cm^{-1} in Figure 4.20.

BA(d)   PI(d)
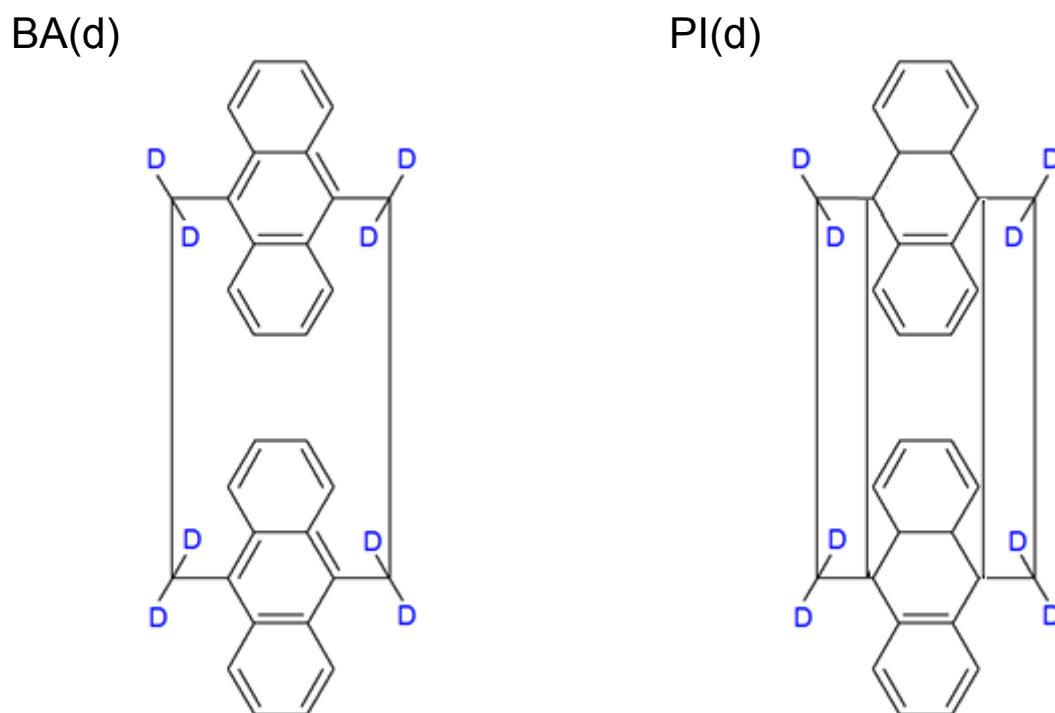
Figure 4.18: The selective deuteration in BA, left, targeted only the dimethyl linkers. Once synthesized, BA(d) can be easily converted to PI(d), right, by visible or/and UV light. The IR spectra reveal the stretching vibrations of the C-H and C-D chemical bonds positioned at very different energies
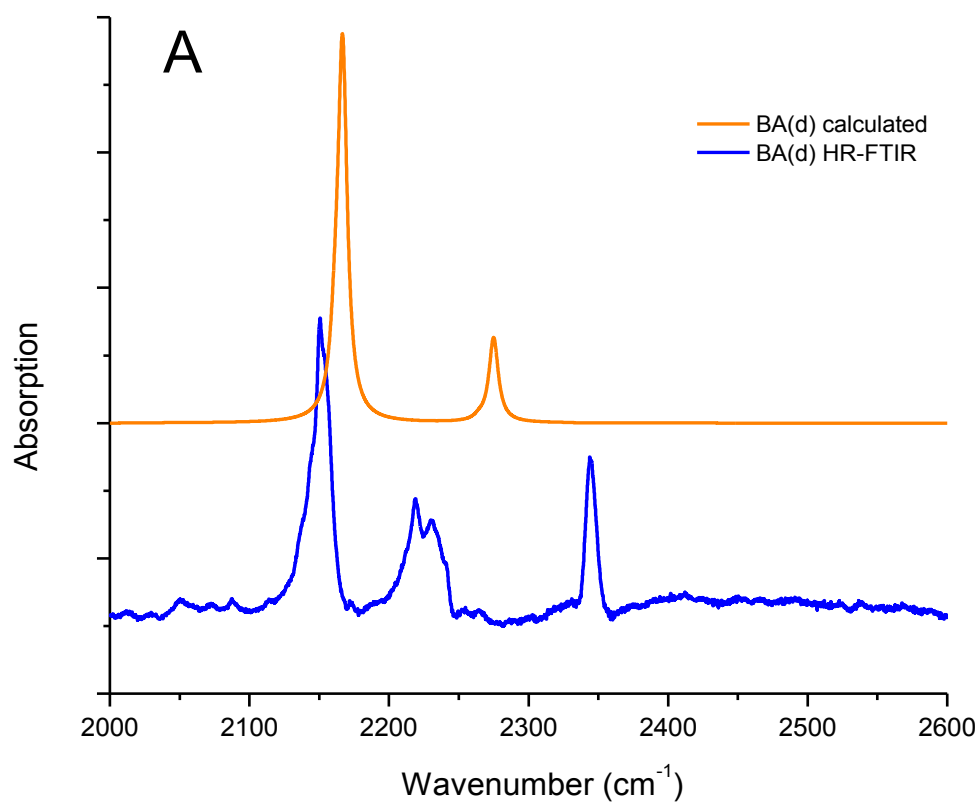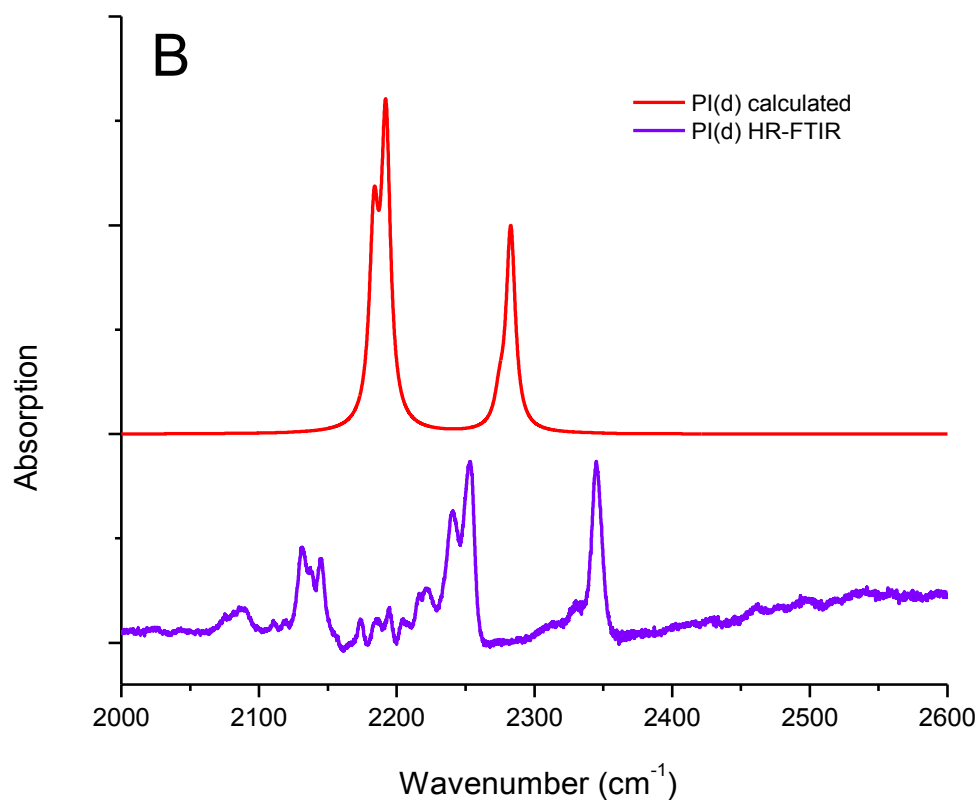
Figure 4.19: IR spectra representing the stretching vibrations C-D in aliphatic carbons of A: BA(d) and B: PI(d). The orange (or red) spectrum is the calculated vibrational spectrum of an isolated molecule, while the blue (or purple) spectrum represents the actual high-resolution experiment performed at < 50 K. The peak at ~ 2345 cm^{-1}, has been attributed to some residual CO_2 in the sample compartment and is present in all four samples at around the same energy
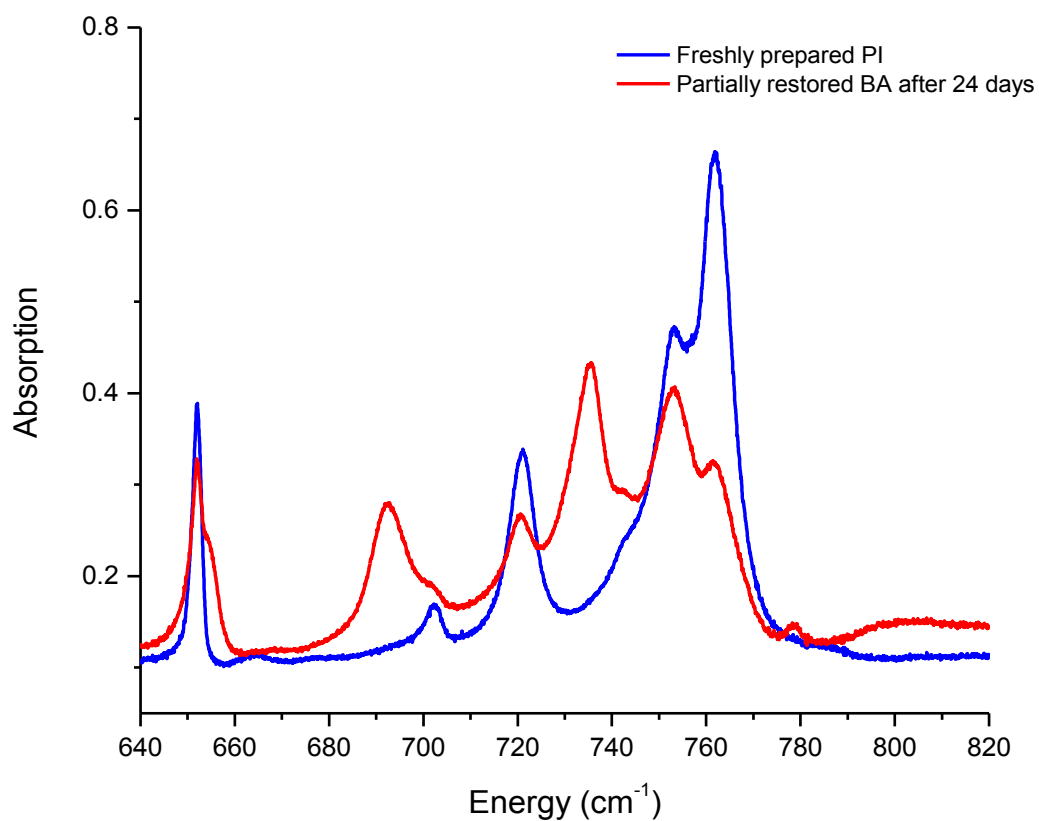
Figure 4.20: Room temperature, high-resolution IR spectra of PI (blue) and partially restored BA (red spectrum). The latter sample is a mixture of PI and BA with $t_{1/2} \sim$ 2 weeks. Differences is peaks' ratios along with new vibrations appearing in the IR spectrum are related to a spontaneous conversion of the highly-strained PI to BA

4.2.5 Inelastic Neutron Scattering

During an inelastic neutron scattering event there is an exchange of energy and momentum between the neutron and the atoms of the sample in study.

In a similar event involving a quantum of light, the transfer of energy from incident to outgoing photon is expressed by the formula[8]:

$$E = \hbar\omega = E_i - E_f$$

where E_i is the incident, E_f is the outgoing energy and ω is the frequency of light. As a result, if E is greater than 0, the scattered particle (photon) loses energy. In cases when E is less than 0, the scattered particle gains on energy.

The change in a frequency of a photon during an inelastic scattering event is given by[8]:

$$\omega = 2\pi c \left(\frac{1}{\lambda_i} - \frac{1}{\lambda_f} \right) = \omega_i - \omega_f$$

where λ_i and λ_f are the incident and outgoing wavelengths, correspondingly.

Taking into consideration the kinetic energy expression for a neutron, the frequency change for a neutron in an inelastic scattering event becomes[8]:

$$\omega = \frac{\pi h}{m_n}\left(\frac{1}{\lambda_i^2} - \frac{1}{\lambda_f^2}\right)$$

Inelastic scattering (cases when $\omega \neq 0$) with the application of low-energy (thermal, comparable to $k_b T$ at room temperature) neutrons allows for the study of molecular vibrations and even rotations competing therefore with IR, Raman and microwave spectroscopic methods. Due to selection rules, the latter methods are only sensitive to a limited types of molecular motions.

Neutron spectroscopy offers numerous advantages over the above mentioned experimental techniques. Neutrons are highly penetrating particles. Samples rich in hydrogen and opaque to photons may often respond to spectroscopic techniques involving neutrons. The intensity of the scattered signal from the sample in study can be predicted once a given molecular model is established. The other obvious advantage over traditional spectroscopy techniques is that thermal neutrons can exchange energy with a variaty of excitations and thus, unlike in IR and Raman spectroscopy, there are no selection rules for the transitions. In turns out however that thermal neutrons readily exchange energy with molecules rich in hydrogen atoms, the lightest element with mass very similar to neutrons. These excitations can be "turned-off" on demand in samples where proton is replaced by deuterium atom, isotope of

hydrogen with the two having very distinct cross-sections. Such "masking" is used in neutron scattering experiments to increase the contrast variation between two samples. The disadvantage of the inelastic neutron scattering method is the relatively low resolution when compared to other spectroscopic techniques.

We explored the contrast variation method in our studies on BA/PI molecular crystal with the goal of understanding the low-frequency vibrations in the dimethyl bridge, data that cannot be acquired with IR or Raman techniques at these frequencies, Figures 4.21 to 4.26. The Time of Flight experiment was perofrmed at Los Alamos National Laboratory, Lujan Center and the Filter Difference Spectrometer path was used. Scattered neutrons are selected by low-energy band pass filters made of Be and BeO which are placed between the sample and the detector. Selective deuteration was performed on BA exclusively within the dimethyl bridge yielding BA(d). This procedure is described in the Appendix section.
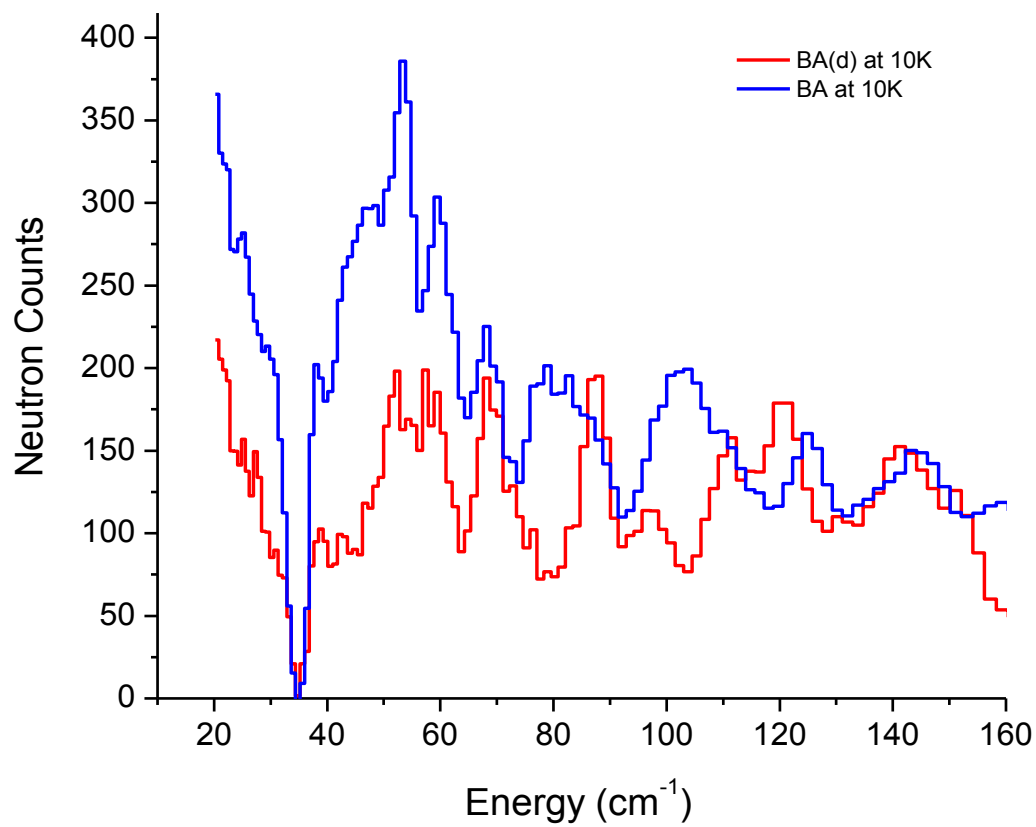
Figure 4.21: Low-temperature BA(d), red, and BA, blue, inelastic neutron scattering spectrum, 20 – 160 cm^{-1}
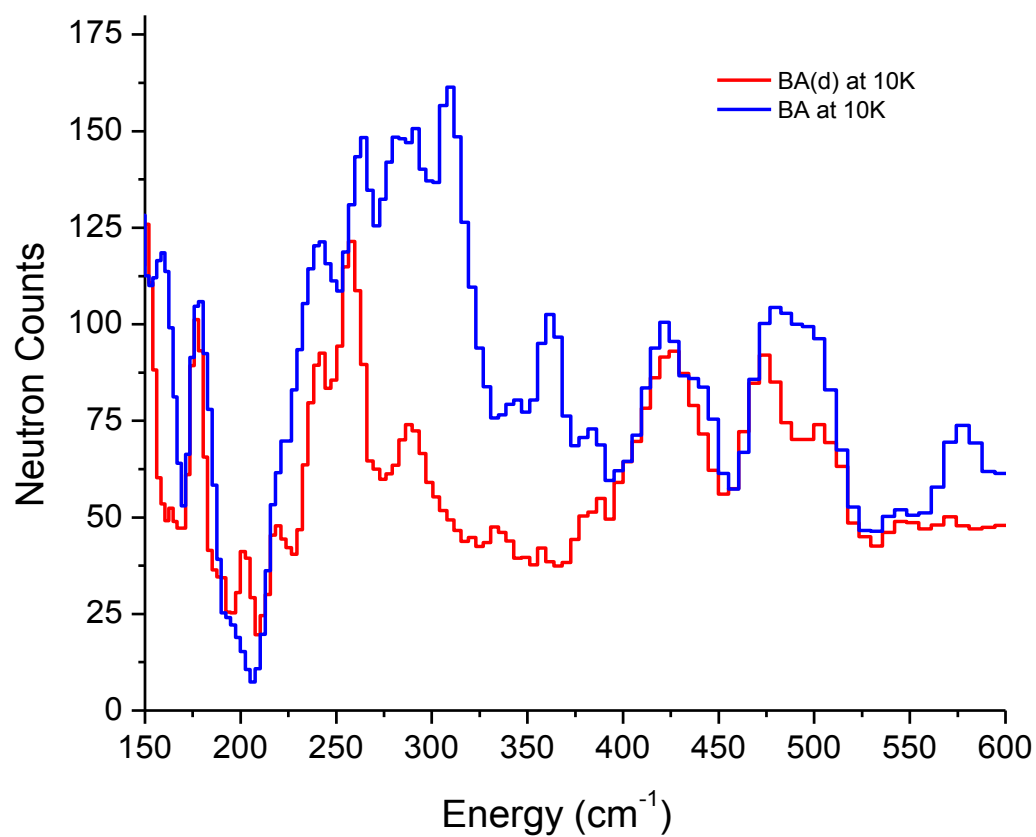
Figure 4.22: Low-temperature BA(d), red, and BA, blue, inelastic neutron scattering spectrum, 150 – 600 cm^{-1}
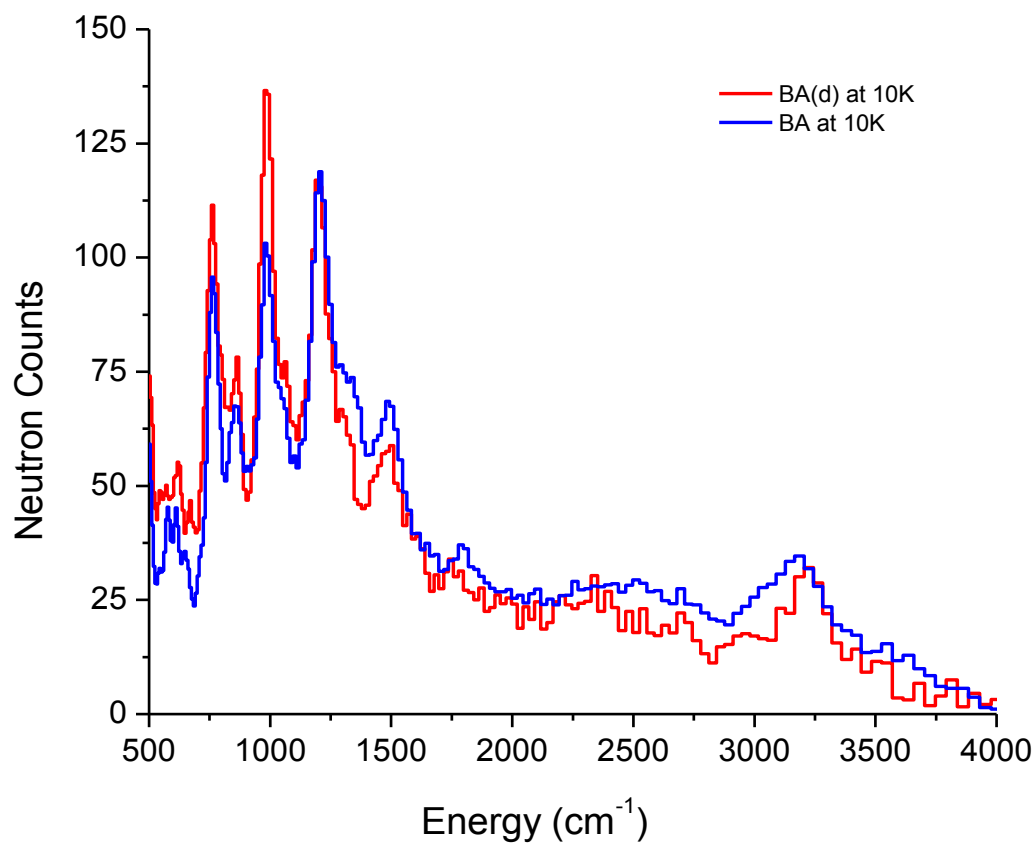
Figure 4.23: Low-temperature BA(d), red, and BA, blue, inelastic neutron scattering spectrum, 500 – 4000 cm^{-1}
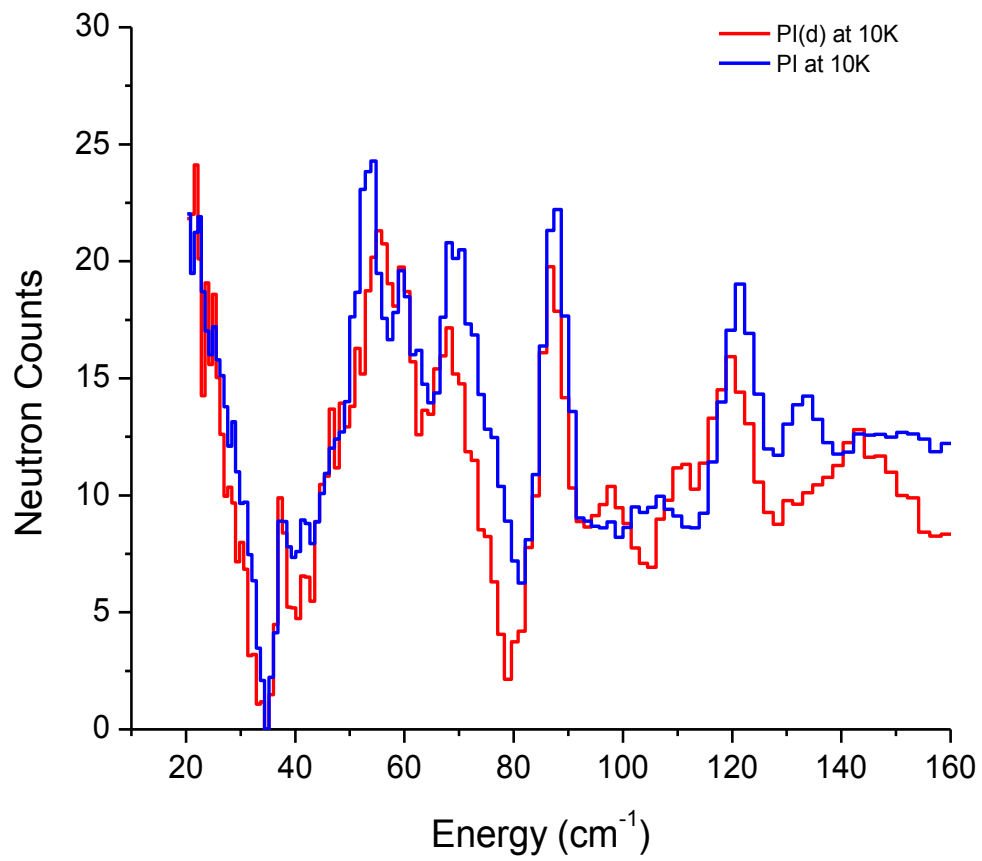
Figure 4.24: Low-temperature PI(d), red, and PI, blue, inelastic neutron scattering spectrum, 20 – 160 cm^{-1}
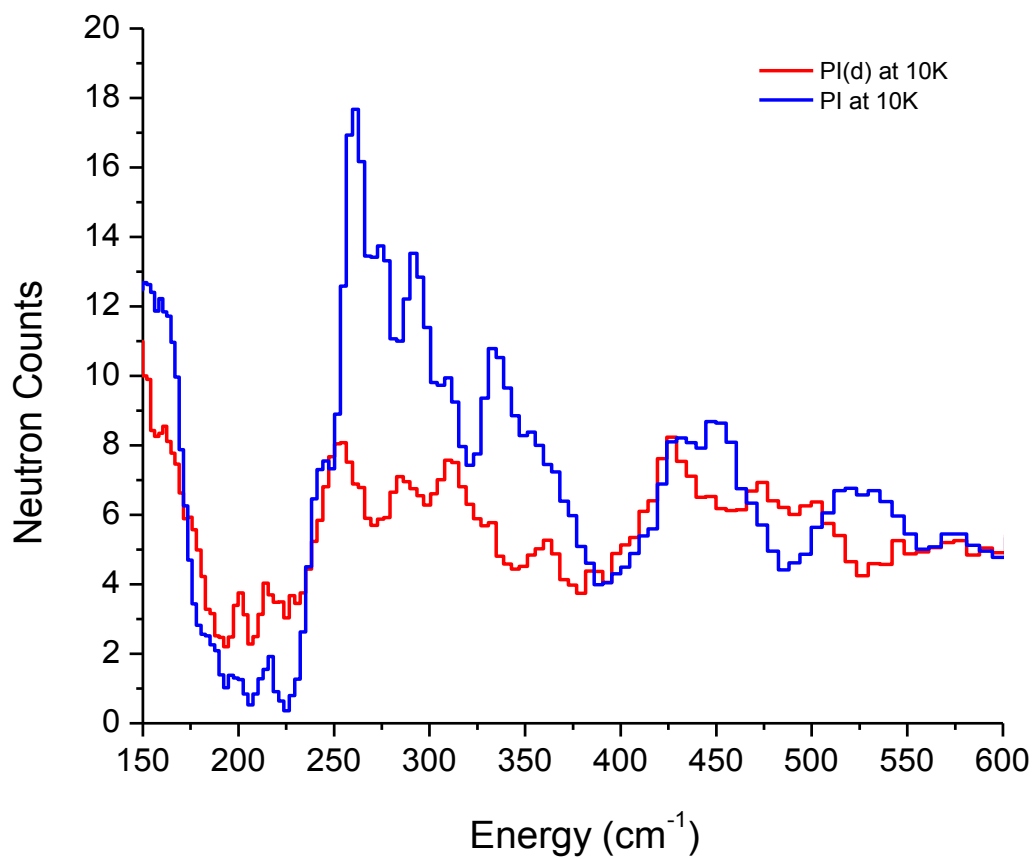
Figure 4.25: Low-temperature PI(d), red, and PI, blue, inelastic neutron scattering spectrum, 150 – 600 cm^{-1}
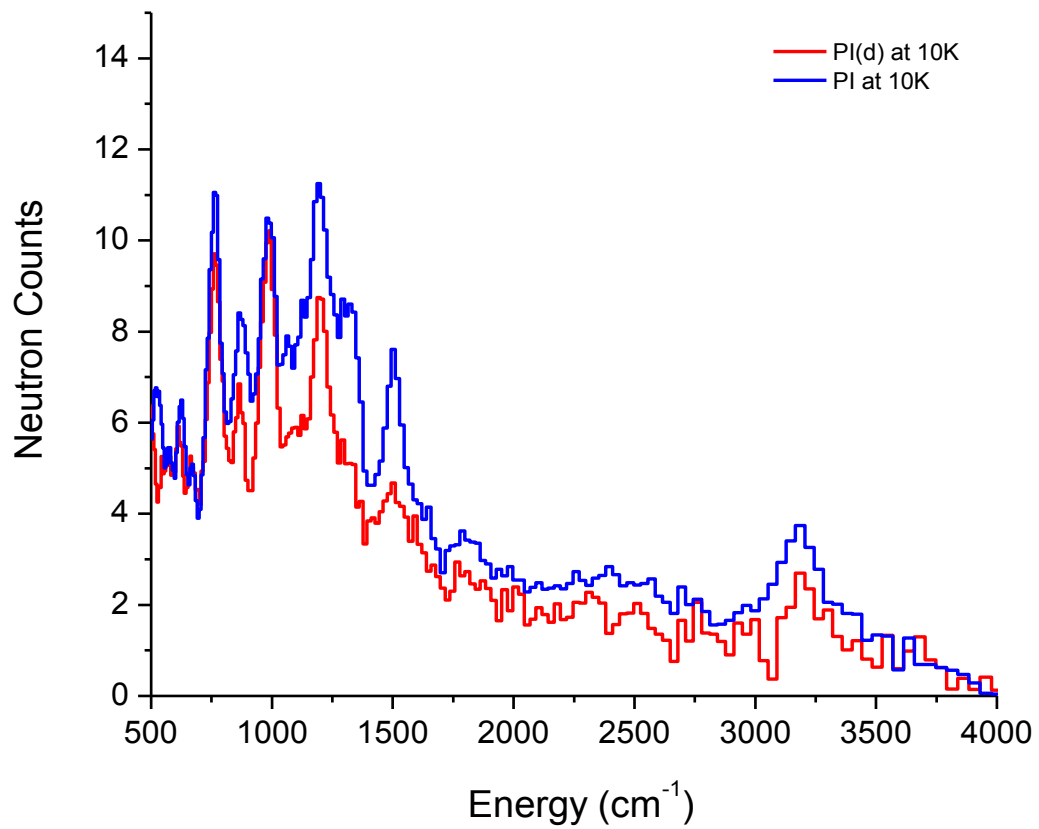
Figure 4.26: Low-temperature PI(d), red, and PI, blue, inelastic neutron scattering spectrum, 500 – 4000 cm^{-1}

4.2.6 DSC/TGA Measurements

Difference Scanning Calorimetry (DSC) analysis was performed on crystals of four different samples: BA, BA(d), PI, PI(d). DSC method is designed to register small differences in temperature between the sample and a reference (here empty Al_2O_3 crucible) while the sample is heated at a constant rate. The heating rate applied in this series of experiments is the often used 10 K per minute, up to 310 K. In order to avoid chemical reactions induced by high temperature between the sample and the oxygen in the air, the DSC analysis was performed in flowing argon, an inert gas. The measurements were performed on the Netzsch STA 449 C Jupiter Thermo-microbalance at Los Alamos National Laboratory, Lujan Center as a part of a demonstration in connection with our experiments with the use of inelastic neutron scattering technique on BA/PI.

Both crystalline and amorphous samples can be characterized with this sensitive thermal analysis equipment. In crystalline solids it is possible to determine the temperature and enthalpies of phase transitions, observe polymorphism and decomposition as they occur. In samples releasing small molecules into the gaseous phase (dehydration, thermal decomposition due to pyrolysis) the thermogravimetic (TG) analysis reveals the mass change (Δm) versus temperature and/or time with resolution better than 0.1 µg. DSC and TG

methods can be applied simultaneously in one run with the use of the STA 449 C

thermo-microbalance with identical measurement conditions on one sample.

Crystalline sample	Mass of sample in crucible	PI-to-BA conversion temperature	Pyrolysis temperature	Loss in mass due to decomposition
BA	12.34 mg	-	252.83 °C	5.81 %
BA(d)	1.10 mg	-	230.49 °C	7.84 %
PI	5.16 mg	114.21 °C	252.38 °C	9.40 %
PI(d)	2.37 mg	114.29 °C	245.57 °C	8.01 %

Table 4.2: Temperatures related to exothermic peaks in Figure 4.27 from DSC experiments of crystals of BA, BA(d), PI and PI(d). Loss in mass has been established in thermogravimetric (TG) measurements

Photoisomers of bis-anthracene (PI) were quantitatively prepared from BA

through illumination the same day. The illumination of BA crystals was carried-

out in vacuum in a sealed quartz ampule. High-intensity UV light source was

used to illuminate BA during which the ampule was shaken for ~ 1 hour. As the

photoisomerization progressed, the illuminated crystals changed their color from

bright orange (BA) to light yellow (PI).

The DSC data (Figure 4.27) show one exothermic peak for crystals of BA

and BA(d). This peak is associated with the thermal decomposition of the

molecular crystals. After having cooled down the decomposed sample, the

residue was extracted from a crucible and inspected under an optical

microscope. We were able to visualize partially decomposed orange crystals with relatively large amounts of amorphous carbon, the result of pyrolysis of BA.

The DSC traces for PI show a low-temperature exothermic peak at around 114 °C in both PI and PI(d). This exothermic peak marks the temperature-induced PI-to-BA transition. This reactions occurs in both types of PI crystals at the same temperature. The pyrolysis temperatures vary from sample to sample (Table 4.2). BA(d) decomposes irreversibly at ~ 230 °C. BA(d) derived from PI(d) shows an exothermic peak at ~ 246 °C. BA and BA obtained from PI decomposes at ~ 252-253 °C.

The thermogravimetric data are shown in Figure 4.28. At around 200 °C the masses of BA and BA(d) crystal samples, originally derived from their photoisomers, start to decrease, a sign that these two substances begin to sublime. A kink in the data at around 250 °C indicates however that the rate of releasing molecules into the gas phase has change abruptly. The change in mass associated with this thermal decomposition ~ 250 °C was found to be 6 to 9 %, Table 4.2. This corresponds well with the mass of acetylene molecule, $HC{\equiv}CH$ and $DC{\equiv}CD$, which most likely arises from one or both dimethyl linkers of decomposing BA and BA(d), accordingly.
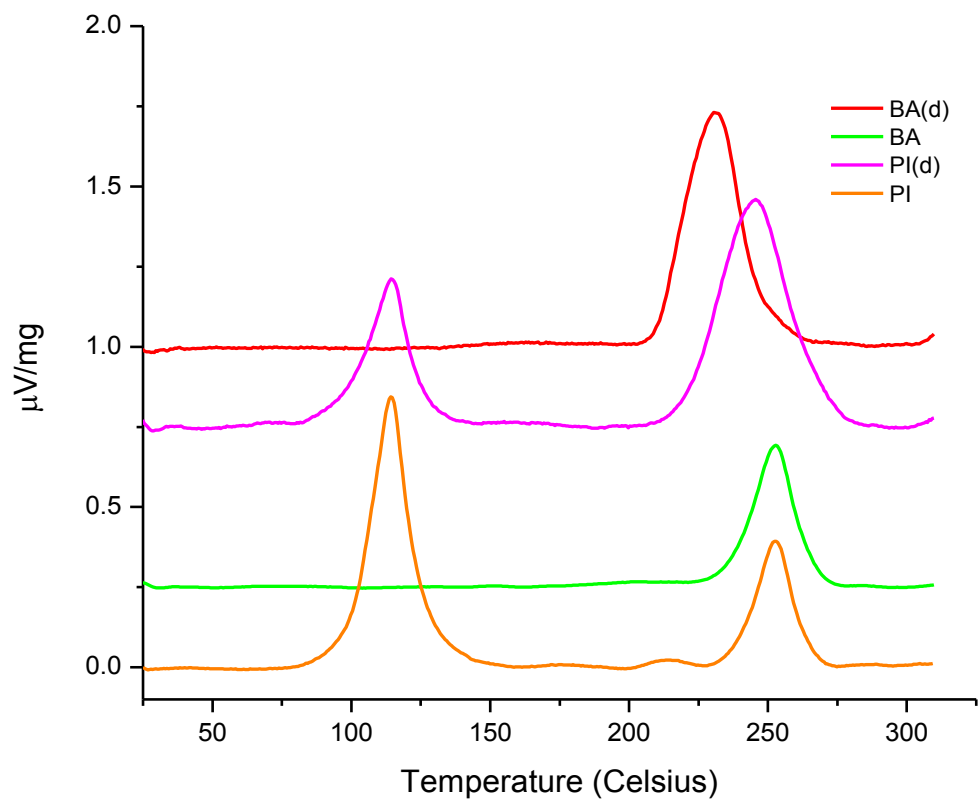
Figure 4.27: Difference Scanning Calorimtery (DSC) data of BA and its photoisomer, PI of both protonated and deuterated (d) forms. The sharp peaks in both PI samples around 114 K are related to the exothermic PI-to-BA transition induced by heat. The exothermic peaks above 230 K relate to the pyrolysis of the molecular crystals
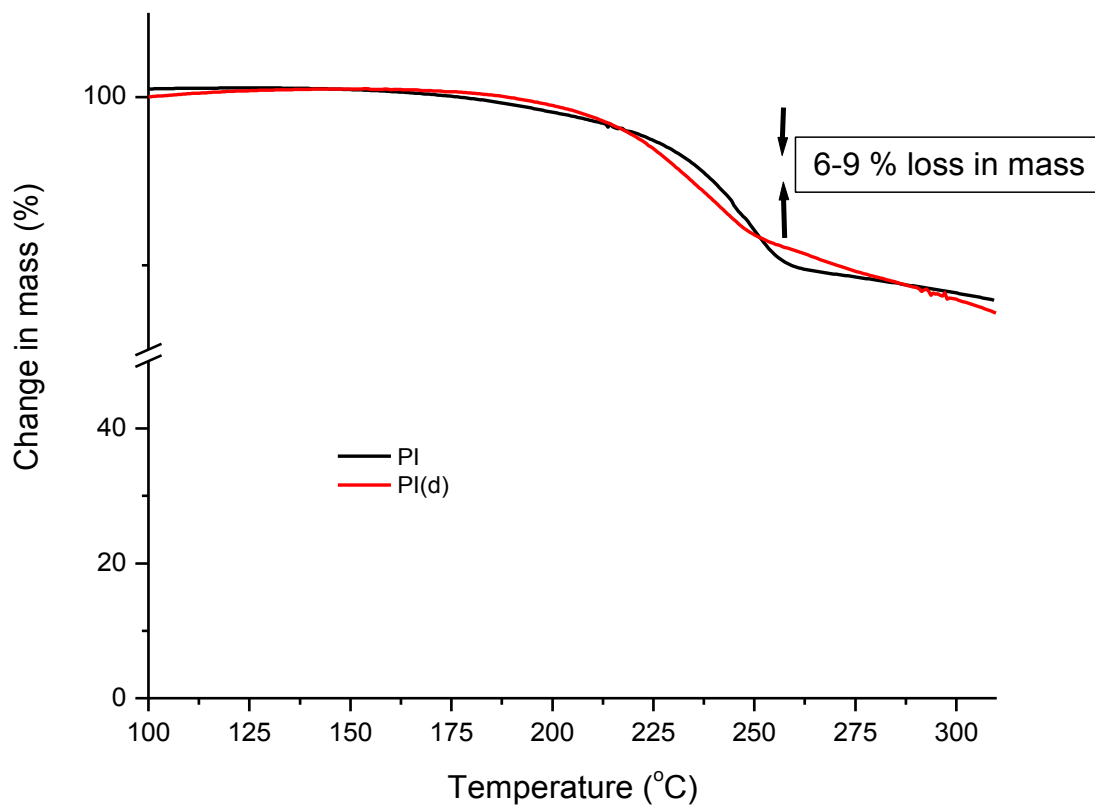
Figure 4.28: Thermogravimetric (TG) data for PI and PI(d). These two photoisomers convert reversibly to BA and BA(d) crystals at around 114 °C. Above this temperature the crystals begin to sublime at ~ 200 °C. At ~ 250 °C however the samples decompose irreversibly with the release of a small molecule, probably acetylene

4.3 Computational Modeling: Molecular Volumes, Thermodynamics and Structure Optimization

In general, in order to yield good level of accuracy, computations via higher-order *ab initio* wave functions with large basis sets, such as CCSD(T) could be performed on molecular systems of interest. Such approach however turns out to be most often cost inefficient even for relatively small molecular systems. The Kohn-Shan Density Functional Theory present in Gaussian with built-in semiempirical dispersion correction (DFT-D) bridges the gap between accuracy and costs, taking into consideration semiempirically-corrected non-covalent interactions in large aromatic carbon-based molecules (such as BA, PI and An_2) which intrinsically show dominant dispersion via Van der Waals interactions. These dispersion energies are significant for molecules with large surface areas of interaction and those with polarizable electron densities.

Uncorrected in any way, DFT appears to fail to treat such non-covalent interactions properly. In BA, it was found for instance that the enthalpy becomes overestimated[7] (~ 130 kJ/mol, DFT) as compared to DFT-D (86 kJ/mol[9]). From the numerous functionals tested[10] by Peverati *et al.*, the best performance in applications involving high degree of dispersive interactions has been found for the cost-effective B97D functional, used as the primary forcefield in all of our DFT-D based computations presented. These involve relative energies,

enthalpies of the photocycloaddition reactions as well as intermolecular distances and bond angles. The basis set chosen is the relatively large 6-31+G(d) to allow for the most accurate, and yet, achievable determination of such thermodynamic information in the ground state. We minimized the energies of all structures studied in vacuum at 0 kbar for isolated molecules. Once in their energy minima, both total energies and enthalpies of formation (through frequency calculations) were extracted from the output files.

The molecular volumes of BA/PI and An$_2$

Calculations regarding molecular volume are necessary for the interpretation of the pressure-induced PI-to-BA recovery that we are able to observe experimentally in the Zeonex polymer under stress in a Diamond Anvil Cell. For this purpose we have employed a procedure which is built in Gaussian, ver. 09W. It estimates the volume of neutral molecules to an accuracy of about 10% by defining a molecular volume as a volume inside of a 0.001 electrons/Bohr^3 density contour. Monte-Carlo integration is performed with the use of 10000 points. Each integration was repeated 100 times, and the resulting standard deviation for the calculated molecular volumes was less than 0.5%. The keyword "Volume" was specified along with an option "Tight" which further improves the integration accuracy by increasing the density of points. Known crystallographic structures of BA, PI and An$_2$ were selected from the literature

and directly used (no optimization) in the process of estimating molecular volumes.

4.4 References

(1)   Fritzsche, I. *J. prakt. Chem.* **1866**, *101*, 337.
(2)   Schmidt, G. M. J. *Pure and Applied Chemistry* **1971**, *27*, 647.
(3)   Al-Kaysi, R. O.; Bardeen, C. J. *Adv. Mater.* **2007**, *19*, 1276.
(4)   Durr, H.; Bouas-Laurent, H. *Photochromism Molecules and Systems*; Elsevier.
(5)   Trzop, E.; Turowska-Tyrk, I. *Acta Crystallogr B* **2008**, *64*, 375.
(6)   Golden, J. H. *Journal of the Chemical Society* **1961**, 3741.
(7)   Dunand, A.; Ferguson, J.; Puza, M.; Robertson, G. B. *Chemical Physics* **1980**, *53*, 225.
(8)   Sivia, D. S. *Elementary Scattering Theory*; Oxford University Press, 2011.
(9)   Jezowski, S. R.; Zhu, L. Y.; Wang, Y. B.; Rice, A. P.; Scott, G. W.; Bardeen, C. J.; Chronister, E. L. *J Am Chem Soc* **2012**, *134*, 7459.
(10)   Peverati, R.; Baldridge, K. K. *Journal of Chemical Theory and Computation* **2009**, *5*, 2772.

Chapter V

Mechanochemistry and Energetics of Selected Strained Photoisomers

5.1 Introduction

5.1.1 Methods of Applying Mechanical Stress

High-shear methods: mastication, grinding and milling

To induce chemical reactions brought about by free radicals in the bulk of material, grinding, milling and mastication are often applied[1], Figure 5.1D. These high-shear methods capable of inducing directional force are known to activate surfaces for a number of applications. Depending on the physical properties of the material to be machined, various designs of mills have been constructed: ball mill, vibratory mill, rolling mill, etc. Mechanical scission of covalent bond forms free radicals acting as active centers on the surface of the affected material. Sandblasting and milling may often generate excessive dust which when inhaled may display toxicity in living tissue. Upon grinding, one of the abundant minerals, calcite ($CaCO_3$) loses some of its carbon dioxide which was suggested

contributes to the elevated concentrations of this unpopular gas in the Earth's atmosphere.

Free radicals form as a result of shear-induced bond scission in the extrusion of wheat flour protein. Milling and grinding was shown to induce polymerization and crosslinking in polymers. This property is explored in the recycling of polymeric waste by shear pulverization. In the case of rubber, to reach desired rheological properties, such as the viscosity, mastication is being applied. In this homolytic bond cleavage, mechanoradicals are generated along with polymer chains being shortened.

Single-Molecule Force Spectroscopy

One of the few methods of applying directional force on the single-molecule scale is the Atomic Force Microscopy, AFM, Figure 5.1C. With this method it is possible to apply nanonewton forces with piconewton precision and measure the weak chemical-binding forces. With a single-bond resolution, the strength of covalent forces within molecules have been determined. Numerous important macromolecules such as proteins, polymers and even DNA have been stretched and their stretching curves analyzed. What is interesting, microruptures occurring before the main event are normally observed for various reasons as a result of the applied tensile force.

Collapsing cavitation bubbles

Polymer scission has been explored extensively with the use of the cavitation technique. Collapsing cavitation bubbles are created by ultrasounds in a solution (Figure 5.1B and 5.1C). Unfortunately, the mechanical activation by ultrasounds is accompanied by heating effects[2] caused by collapsing bubbles. It is important therefore to always perform additional temperature-dependent tests on the studied material. Extensive studies have been reported with the application of ultrasounds on mechanochemically reactive units, such as the spiropyran mechanophores, engineered into a polymer backbone[3]. Stretching the polymer reversibly transforms the colorless spiropyran form to a purple-red colored merocyanine structure[3].

Isotropic compressive force generated by Diamond Anvil Cell (DAC)

Mechanical force has the ability to change the potential energy surface of reacting molecules. DAC allows for the confining compression of material often to extreme pressures, Figure 5.1A. The sample within DAC can be conveniently cooled or heated while X-ray diffraction and optical spectroscopy can be performed on samples subjected to high pressures. Unlike the other high-pressure methods, DAC allows for a large variety of analytical methods to be applied to the sample and therefore is extensively used in geochemical research.

The BA/PI pair of mechanophores described in this Chapter has been studied with the use of DAC.
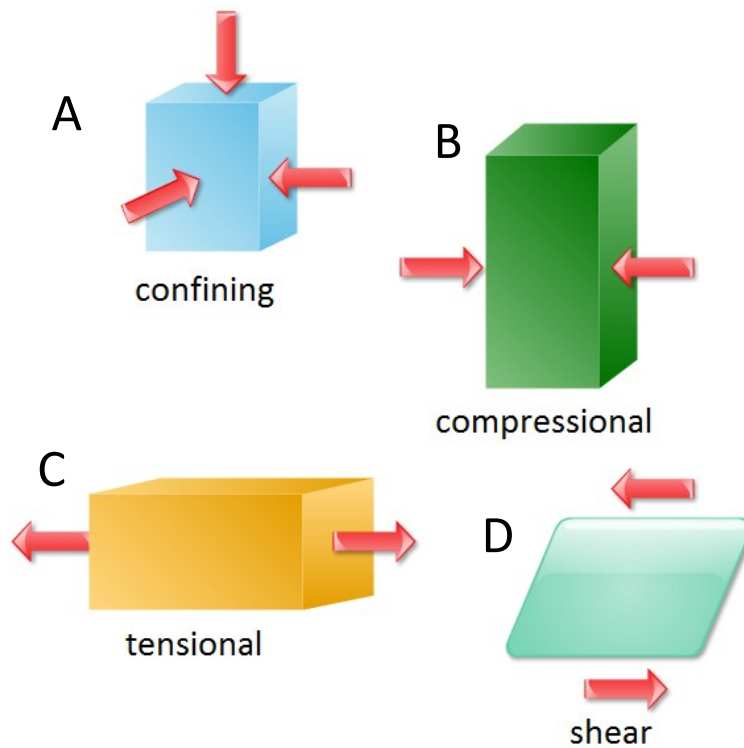
Figure 5.1: Schematic representation of the four types of stress on materials: confining stress, tensional stress, compressional stress and a shear stress

5.1.2 High Pressure as the Stabilizing Agent in the Formation of Photodimers

A limited number of high-pressure research has been conducted on photochromic systems undergoing [4+4] cycloaddition reaction. One example is the stabilization of the pentacene dimer, dipentacene, under high-pressure conditions[4]. Another, closely related example is the photodimerization of anthracene in a solution explored with the application of high pressure. Tanaka and Osugi were able to show that the well-studied light-induced dimerization, proceeding through an excited state, is slowed at higher pressure due to the decrease of the fluidity of a solvent, hexane[5]. Eventually, the mechanism of dianthracene cycloaddition has been explained in terms of an excimer formation between one molecule of anthracene in the excited state (M^*) and another anthracene molecule in the ground state (M, Table 5.1). An essential step in the mechanism of anthracene dimerization is the diffusion-controlled rate of excimer formation $(M:M)^*$. Since the molecular diffusion of anthracene is retarded in organic solvents at high pressures, the excimer cannot form efficiently within the life-time of an excited state of An^*, leading under ambient pressure conditions to the dianthracene dimer, M_2.

Another example with a radically different initial steps of the reaction's mechanism, Table 5.1, has been described by S. D. Hamann *et al.* in a

naphthalene derivative[6]. The highly polar groups in methyl 3-methoxy-2-napthoate facilitate the formation of a molecular pair of molecules in the "head-to-tail" arrangement in the ground state $(M:M)$[6]. This planar arrangement is the preferred form of orientation for the [4+4] cycloaddition to occur, with sufficient overlap between the adjacent p(z) orbitals.

The retarded fluidity of an organic solvent normally observed at high pressures does not interfere with the mechanism of the dimer formation in the case of napthoate. The researchers were able to demonstrate that a "head-to-tail" unreacted pair of molecules is present in the solution prior to the formation of an excimer required in all [4+4] cycloaddition reactions.

It was reported[6] that when pressure of 2 kbar is applied, the rate of the photodimerization reaction more than doubles (accelerates) due to the stabilizing conditions created by high pressure, brought about by the reduced volume of activation (negative) 10 cm^3/mol or 16.6 $Å^3$ for the transition state[6].

$$M+M^* \rightarrow (M:M)^* \qquad\qquad M+M \leftrightarrows (M:M)$$

$$(M:M)^* \rightarrow M_2 \qquad\qquad (M:M) \rightarrow (M:M)^*$$

$$(M:M)^* \rightarrow M+M \qquad\qquad (M:M)^* \rightarrow M_2$$

Table 5.1: Schematic depiction of the dimer formation mechanism in anthracene, left, and methyl 3-methoxy-2-napthoate, right. Unlike in napthoate, the initial step of the excimer formation in anthracene is diffusion-controlled

This picture, and thus the mechanism, can be applied to all molecular systems undergoing [4+4] cycloaddition reaction in which the reaction is not diffusion-controlled. This is true for numerous linked anthracenes, in which the intramolecular reaction induced by light operates on the principles of the mechanism outlined for the napthoate: the reacting moieties are in close proximity (2.76 Å in BA) and properly aligned prior to excitation. It is striking therefore to observe deviations from this picture in systems such as bis-anthracene. In the remaining parts of this Chapter we put much effort into trying to understand and explain the accelerated rate of dissociation of the linked bis-anthracene dimer (photoisomer, PI) with increased pressure.

5.2 Results and Discussion

5.2.1 The Unique Geometry of Linked Anthracenes

There is a fundamental difference between the way anthracene molecules react with each other and the intramolecular dimerization in bis-anthracene. While the linked anthracene moieties are already aligned with respect to each other in the case of BA, the intermolecular dimerization between two molecules of An can efficiently proceed only in a solution or in the gas phase due to

topological constraints in a solid phase. The photoinduced [4+4] cycloaddition in a crystal of BA was already explored by Golden[7]. Extensive X-ray studies[8] were later performed by E. Trzop *et al.* on crystalline BA (Figure 5.2) and PI (Figure 5.3).

In the presence of appropriate wavelength, the photocyclic reaction in bis-anthracene results in the formation of two bridging bonds between C(9)-C(9') and C(10)-C(10') coupled to a rehybridization (from sp^2 to sp^3) on these four carbon atoms and a loss of conjugation in the central anthracene ring. The newly formed covalent bonds in PI are much longer[8], ~165 pm, than typical C-C covalent bonds (153-156 pm) and longer than the already considered long bridging bonds in dianthracene[9] (~162 pm, X-ray data from Table 5.2).

Upon irradiation, the two anthracene planes of BA (or An) are transformed into four (substituted) benzene and two non-aromatic (central) rings. The molecule of the bis-anthracene photoisomer, PI, is structurally very similar to dianthracene, Figure 5.4. The difference is only in the additional two cyclobutane rings on either side present in PI formed upon irradiation. These highly-strained cyclobutane rings arise from the two dimethyl linkers adding only four aliphatic carbon atoms along with their protons to An_2.

Just like in dianthracene (An_2), the molecule of PI is stabilized by the dispersive (Van der Waals) attractive force of the four lateral benzene rings present only in the reacted forms. On the other hand, much of the separation

between the bonding carbons is due to the strong non-bonding interactions between the aromatic carbon atoms. Since this effect does not solely account for the ultra-long bonding carbon-to-carbon length in PI when compared to An_2, some of the strain in the cyclobutane rings (Figure 5.4) must contribute to the destabilizing increase in the bond's length when compared to An_2, lacking any aliphatic rings on either side. As a matter of fact, in unstrained An_2, the γ_{An2} angle, 106.1°, Figure 5.4, is close to 109.5° observed in sp^3 hybridized carbon atom in methane, whereas in PI, the same γ_{PI} angle, 86.2°, is greatly influenced (reduced) by the attached dimethyl linker.

	BA (pm) ANTMEU03	PI (pm) ANTMET05	An₂ (pm) DPANTH01
Crystallography[8,9]	276	165	162
Calculations[10] **(DFT-D)**	283	169	164

Table 5.2: C(9)-C(9') and C(10)-C(10') interatomic distances in BA, PI and An_2

In its unreacted form, BA shows also very short non-bonding carbon-to-carbon distance between C(9) and C(9') as well as C(10) and C(10'). This distance[8], 276 pm, is unusually short when compared to typical non-bonding C-to-C distance of 300 pm in unstrained compounds. As shown in Table 5.2, the trend between X-ray data and calculated (DFT-D) values for bonding and non-

bonding C-C distances is preserved and overall agree to within 2% with experimental values.

In a summary, we can describe PI as a strained photoisomer of bis-anthracene and BA as a confined (short, non-bonding distances), unreacted molecule.

The butterfly angle determination

The rehybridization and the loss of conjugation in PI and An_2 upon dimerization lead to some dramatic changes in of the planarity of the anthracene moieties measured by more commonly known parameters, the "butterfly" angle. The butterfly angle, Figures 5.5 and 5.6, is more specifically defined here as two times the angle between an imaginary line connecting C9 and C7, projected onto a plane (Figure 5.6, the AC line), and a plane perpendicular to an imaginary line connecting C14 and C11.

The butterfly angles from both calculations and X-ray analysis are summarized in Table 5.3. In perfectly planar anthracene molecule, the butterfly angle is 0°. As the edges of the ring move away from planarity upon dimerization or even due to the presence of dimethyl linkers, the butterfly angle increases. The parameters necessary for the butterfly angle determination have been extracted from both the calculated and X-ray structures of BA, PI and An_2 with

the help of the Gaussian package software. Identical set of geometrical calculations (Figure 5.6) have been conducted according to the pattern presented below.

From the projection of Gaussian lengths of a PI molecule on a plane, we can determine the following four parameters:

$|BC|$ = 1.36954 Å

$|AB|$ = 2.43429 Å

$2|OB|$ = 2.45774 Å

β = 179.00695°

From the law of cosines it follows that:

$$|AC|^2 = |BC|^2 + |AB|^2 - 2\,|BC|\,|AB|\cos(\beta),\ \text{thus:}$$

$$|AC| = \sqrt{|BC|^2 + |AB|^2 - 2\,|BC|\,|AB|\cos(\beta)}$$

$$|AC| = 3.8037\ \text{Å}$$

$$|AB|^2 = |BC|^2 + |AC|^2 - 2\,|BC|\,|AC|\cos(\delta),\ \text{thus:}$$

$$\cos(\delta) = -\frac{|AB|^2 - |BC|^2 - |AC|^2}{2|BC||AC|},\ \text{thus:}$$

$$\delta = 0.63154°$$

$$\sin(\mu) = \frac{|BO|}{|BC|}, \text{ thus:}$$

$$\mu = 63.80367°$$

$$\sigma + \delta + \mu = 90°$$

$$\sigma = 25.56479°$$

$$90° + \rho + \sigma = 180°$$

$$\rho = 64.43521°$$

$$\rho + \alpha + 90° = 180°$$

$$\alpha = 25.56479°$$

Therefore the butterfly angle is 2*α = 51.13° in PI

	BA		PI		An$_2$	
	calc.	X-ray[8]	calc.	X-ray[8]	calc.	X-ray[9]
C(9)-C(9') C(10)-C(10') (pm)	283	276	169	165	164	162
β angles	178.271	178.600	179.007	178.265	179.833	176.862
$|BC|$ (pm)	1.23502	1.21723	1.36954	1.34543	1.35558	1.34670
$|AB|$ (pm)	2.46240	2.41503	2.43429	2.40386	2.43509	2.41049
2*$|B0|$ (pm)	2.43388	2.40325	2.45774	2.43467	2.45961	2.45658
$|AC|$ (pm)	3.69704	3.63202	3.8037	3.74889	3.79070	3.75589
Butterfly angle	17.33°	16.51°	51.13°	32.49°	49.75°	44.38°

Table 5.3: The butterfly angles deduced from geometrical analogies and the law of cosines. Comparison between calculations and experiment

	BA ANTMEU03[8]	PI ANTMET05[8]	An$_2$ DPANTH01[9]
Space group	P21/c	P21/c	Pbca
a (Å)	10.27	9.85	12.08
b (Å)	12.77	13.00	18.85
c (Å)	8.45	8.53	8.14
α	90.00	90.00	90.00
β	112.86	118.89	90.00
γ	90.00	90.00	90.00
Molecular volume (Å^3), X-tal	510.253	506.50	463.594
Density (g/cm^3)	1.330	1.339	1.280
R-Factor (%)	4.09	5.52	4.0

Table 5.4: Unit cell parameters for BA, PI and An$_2$ derived from X-ray experiments
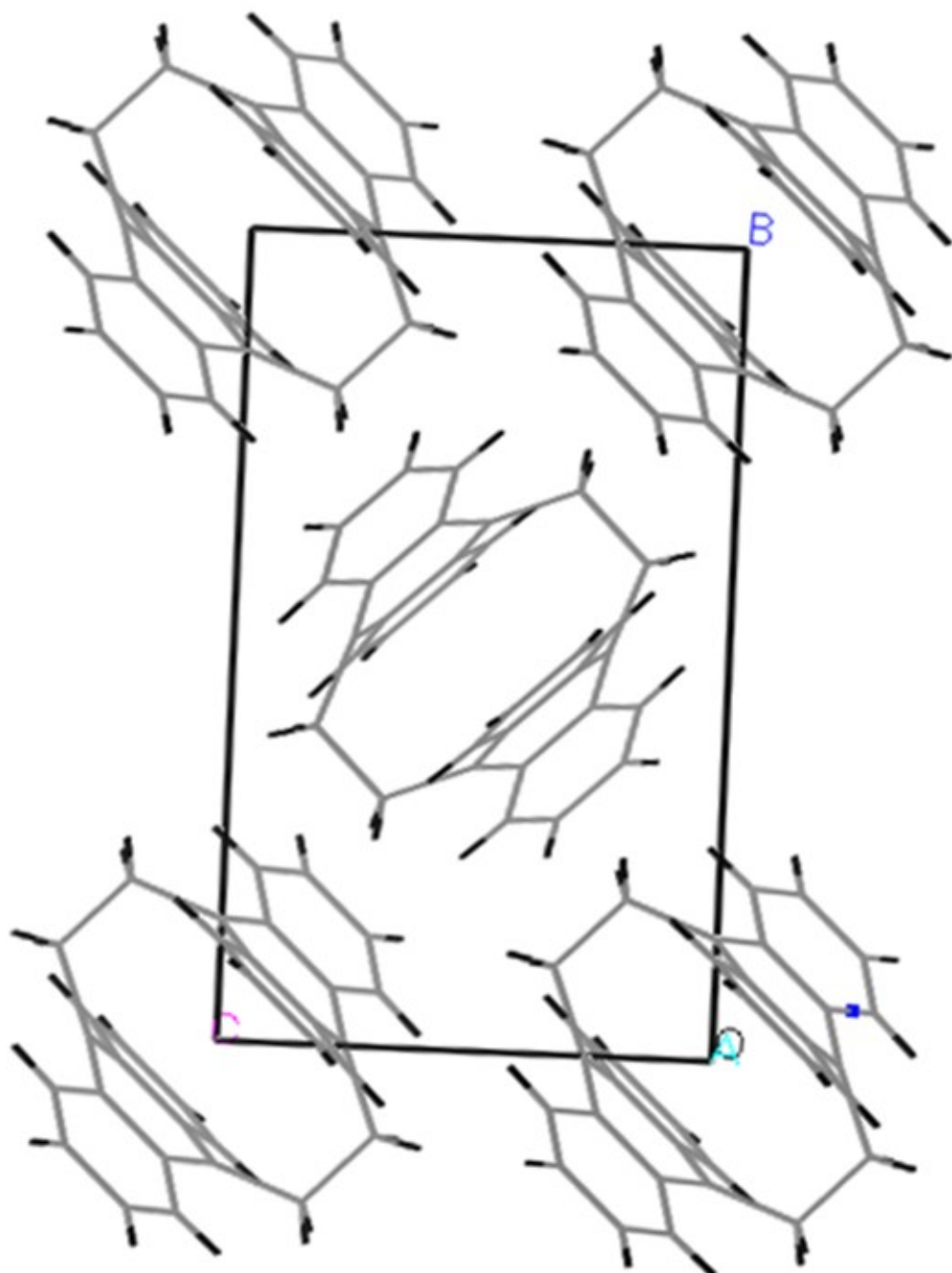
Figure 5.2: The unit cell of crystalline BA, designated ANTMEU03[8] in CSD. There are two BA molecules for every unit cell. The unit cell parameters are shown in Table 5.4
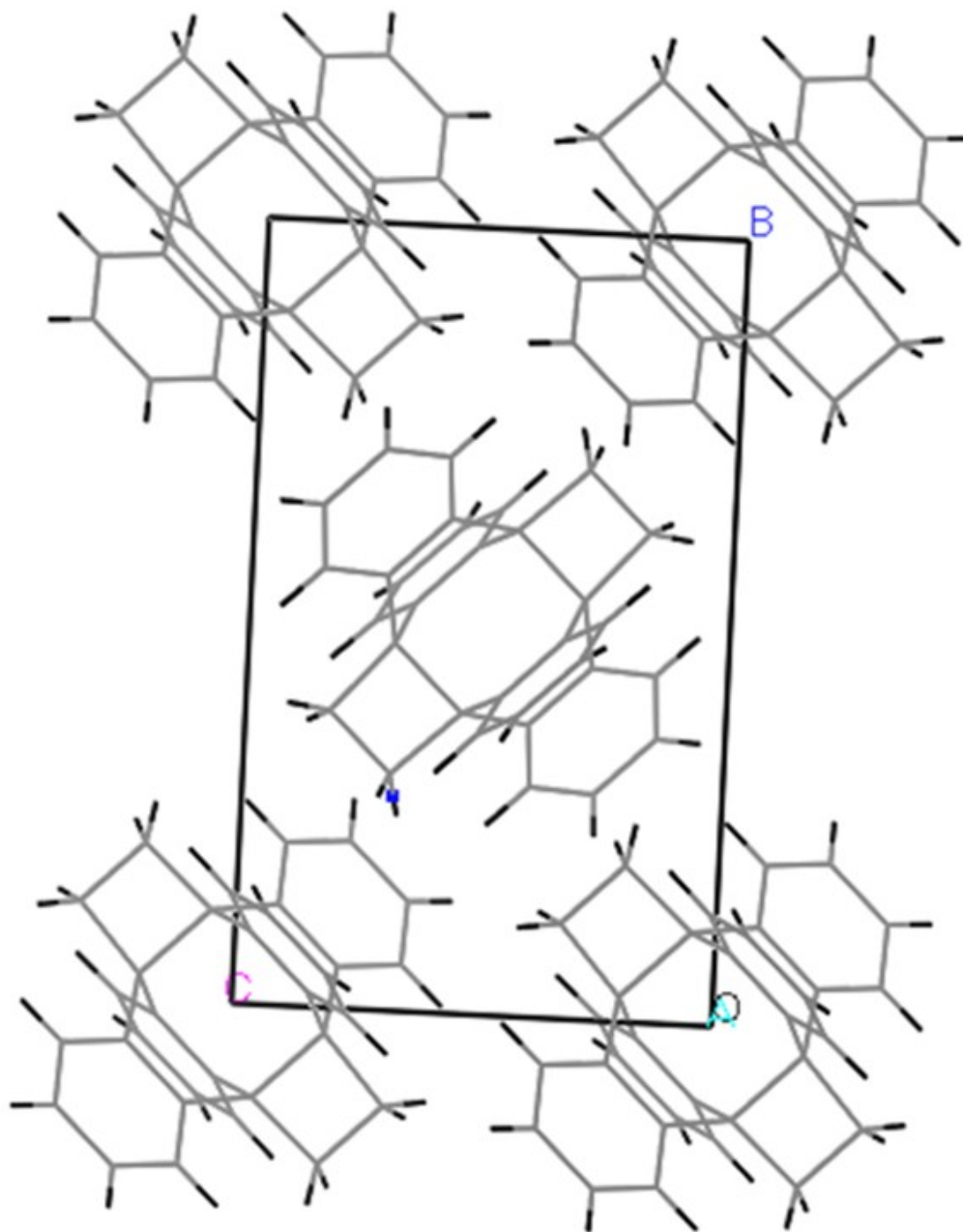
Figure 5.3: The unit cell of crystalline PI, designated ANTMET05[8] in CSD. There are two PI molecules for every unit cell. The unit cell parameters are shown in Table 5.4
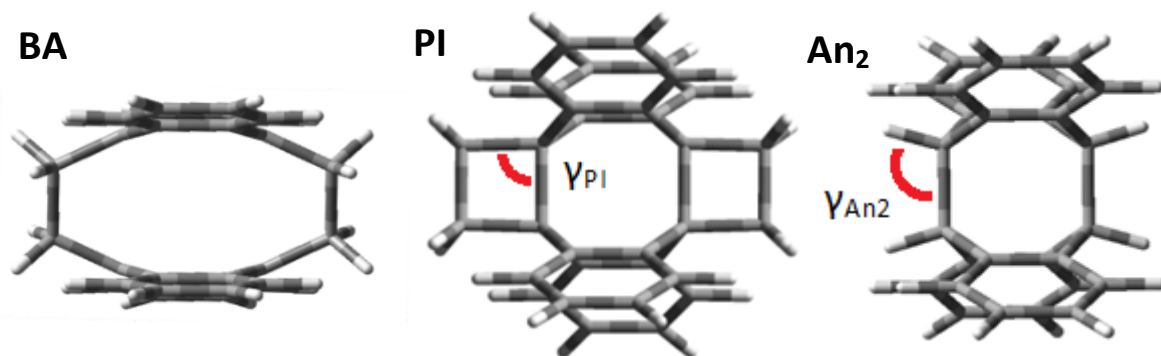
Figure 5.4: The structures of BA, PI and An$_2$ lined-up next to each other for comparison. PI and An$_2$ are structurally similar to each other; PI shows additional two cyclobutane rings on either side contributing to the destabilization of the C(9, 10) and C(9', 10') C-C bond. The γ angles around the sp^3 hybridized carbon atom is 106.1° in An$_2$ and only 86.2° in PI
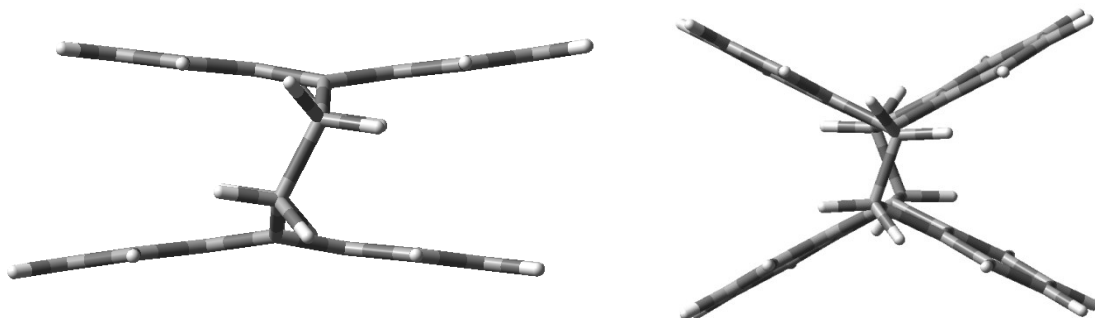
Figure 5.5: The lowest energy conformer of BA, left, and the strained photoisomer, PI, right, side-view. The anthracene moieties in BA are closer to planarity than the "roof" and the "floor" of PI composed of four orto-substituted benzene rings mutually bound to each other. This deviation from planarity is measured as the "butterfly" angle
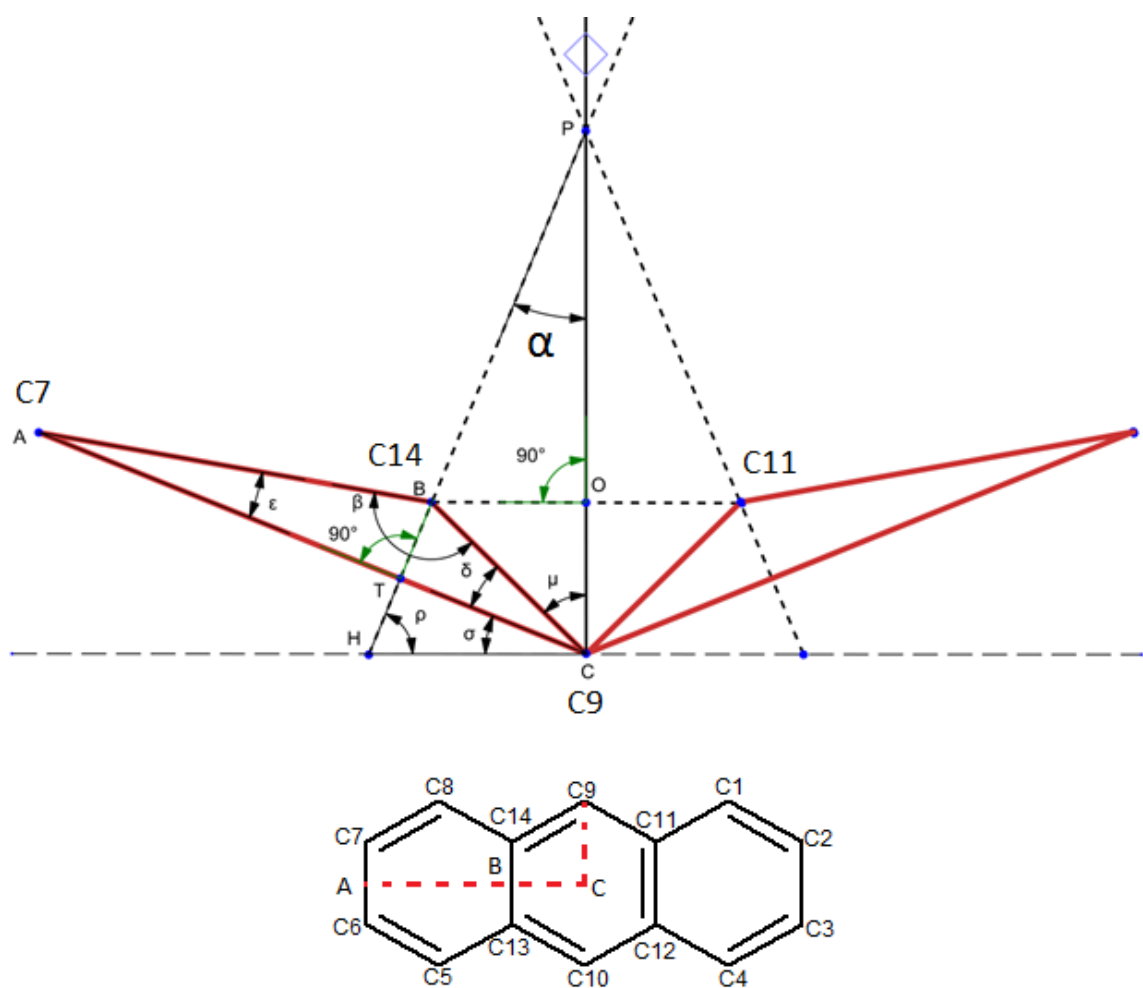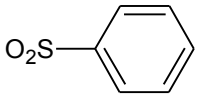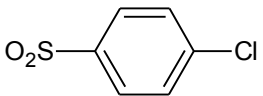
Figure 5.6: Projected on a plane interatomic distances and angles in this not-to-scale illustration aimed at presenting the butterfly angle, 2α. This diagram illustrates only the top portion (the roof) of the PI/BA/An$_2$ molecule

5.2.2 Tuning the Thermodynamic Properties of Linked Anthracenes

BA/PI pair of linked anthracenes (cyclophanes) undergoes the classic

[4+4] cycloaddition when illuminated with light. The reverse dissociation reaction

occurs spontaneously at room temperature and is accelerated with the

application of heat and other stimuli. Another class of linked anthracenes,

diazaanthracenophanes, have been studied by Usui *et al*. and it was shown that

their behavior at higher temperature is quite opposite[11] to that observed in the

BA/PI pair. The authors have observed that two from the series of compounds

(Figure 5.7, Table 5.5) quantitatively undergo intramolecular cycloaddition when

heated or illuminated. These orange-colored linked anthracenes have three-

member linkers, $-CH_2-NR-CH_2-$, with the R group originally replaced by a number

of substituents, Table 5.5. All of these seven compounds studied undergo

photodimerization when illuminated with light $\lambda > 340$ nm yielding colorless

photodimerization (cycloadduct) products.

The authors report that the forward reactions can always be activated with

light, however only compounds with A and C substituents (Table 5.5) cannot be

restored to their unreacted forms with heat. What is more, heat actually causes

the [4+4] cycloaddition reactions in these compounds, acting more like

electromagnetic (light) stimuli making them react.

	Substituent (R)	Activated with heat		Enthalpy of the back reaction
		Forward reaction	Back reaction	
G	CHO	no	yes	*not studied*
B	H	no	yes	*not studied*
D	O_2S—(benzene ring)	no	yes	positive
F	O_2S—(benzene ring)—Cl	partially	partially	positive
E	O_2S—(benzene ring)—CH_3	partially	partially	positive
A	$COCF_3$	yes	no	negative
C	$COC(CH_3)_3$	yes	no	*not studied*

Table 5.5: The influence of the substituent (R) on the enthalpies of reactions based on data[11] by M. Usui *et al*. The last two groups (A and C) show anomalous behavior when substituted as R into the linker
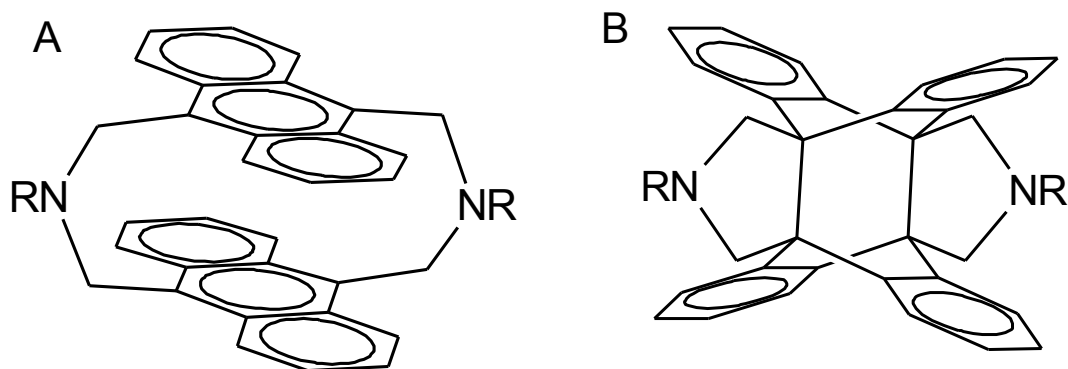
Figure 5.7: The general structure of diaza[3.3](9,10)anthracenophanes (A) and their cycloadduct (B) as described by Usui *et al.* Two anthracenes are linked in their 9-9' and 10-10' positions by three-member linkers with a general formula - CH_2-NR-CH_2-

Theoretical considerations

Inspired by the findings[11] of Usui *et al.*, we have performed simulations (DFT-D) on isolated molecules to establish dependencies between the linkers' length and the enthalpies of their back-reactions, Table 5.6, Figure 5.8.

While the flipped (positive) enthalpies of the back-reactions observed by Usui *et al.* do not result from various lengths of linkers (the length of linker was maintained constant), we found such dependency in our calculations and plotted them in Figure 5.8. According to the calculations, when a difference in the distance between of the 9-9' and 10-10' positions is more than ~ 0.9 pm, the back reaction features a negative enthalpy, i.e. heat is released as the reactant is restored. On the other hand, when the difference is less than ~ 0.9 pm, the enthalpy of the back-reaction flips its sign to positive. The largest, most positive

enthalpies for the back-reaction were observed for the shortest linkers, where the

smallest difference in the positions of the anthracene planes with respect to each

other can be seen between the reacted and unreacted species. Especially, the

cycloadduct featuring the –O– linkers (Table 5.6) requires over 224 kJ/mol to

revert back to its unreacted form. The lowest enthalpy of all studied systems and

thus the largest amount of heat given off can be seen in a molecule supported by

two dimethyl linkers - the BA/PI pair. In the case of reacted species, the presence

of linkers additionally reduces the spacing between the planes of the aromatic

rings. The attractive interaction between the neighboring π-systems causes the

enthalpy for the back-reaction to rise sharply below ~ 0.9 pm.

Linker	Energy (hartree)	Δ Energy kJ/mol	9-9' and 10-10' C-C, pm	Δ distance C-C, pm
None, unreacted (2x anthracene)	-1077.877972	-25.43	∞	-
None, reacted (dianthracene)	-1077.8682850		1.64	
-CH$_2$-CH$_2$- unreacted	-1232.517642	-87.80	2.83	1.14
-CH$_2$-CH$_2$- reacted	-1232.484201		1.69	
-CH$_2$-CH$_2$-CH$_2$- unreacted	-1311.5632106	-66.85	3.18	1.48
-CH$_2$-CH$_2$-CH$_2$- reacted	-1311.5377475		1.70	
-CH$_2$- unreacted	-1153.921901	+ 111.78	2.40	0.81
-CH$_2$- reacted	-1153.964477		1.59	
-CH$_2$-S-CH$_2$- unreacted	-2029.3516485	-76.05	3.29	1.60
-CH$_2$-S-CH$_2$- reacted	-2029.3226841		1.69	
-CH$_2$-NH-CH$_2$- unreacted	-1343.6037239	-58.26	3.18	1.49
-CH$_2$-NH-CH$_2$- reacted	-1343.5815324		1.69	
-CH=CH- unreacted	-1230.093246	-75.96	2.81	1.11
-CH=CH- reacted	-1230.064315		1.70	
-NH- unreacted	-1185.966165	+ 158.82	2.31	0.76
-NH- reacted	-1186.026658		1.55	
-O- unreacted	-1225.680559	+ 224.44	2.26	0.74
-O- reacted	-1225.766042		1.52	

Table 5.6: The influence of linker's length and type on the enthalpy of the back reaction. Energy calculations were performed with dispersion corrected Density Functional Theory (DFT-D), B97D, 6-31+g(d) on optimized structures of isolated molecules; the energy is a sum of electronic and zero-point energies
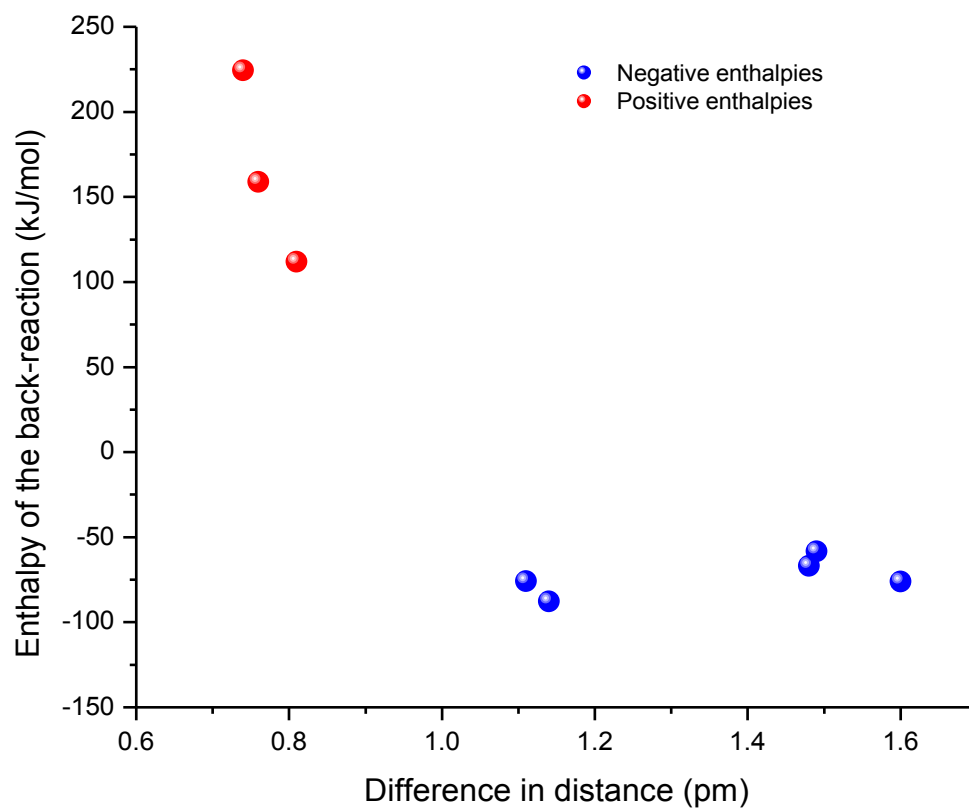
Figure 5.8: Plot of the energy of the back-reaction as a function of difference in distance between the anthracene 9-9' and 10-10' positions of reacted and unreacted forms; data extracted from Table 5.6

5.2.3 The Spontaneous Dissociation Reaction in the Photoisomer

5.2.3.1 Dissociation in Solution

In a set of absorption experiments we measured the spontaneous recovery of bis-anthracene photoisomer (PI) in cyclohexane over a course of 21 days. Two saturated solutions of BA and BA(d) in cyclohexane were illuminated with a halogen lamp to quantitatively photoconvert all material to PI. Once the conversion was completed, the solutions were let to spontaneously recover at room temperature.

The evaluation of spectral information in absorption was performed with the goal of determining the fraction of recovery expressed as a percentage of the original BA absorption spectrum before irradiation (set as 100%).

Numerical integration was performed (trapezoidal rule) for each spectrum in the region 234.5 nm (from the isosbestic point in absorption) to 573 nm with no residual absorption of BA. The resulting values are listed in Table 5.7.

Spectrum number	Type of absorption spectrum	Time after illumination (min)	Area under spectrum 234.5 – 573 nm (a.u.)	
			BA	BA(d)
1	Before illumination	–	14479	15913
2	Just after illumination	0	10084	10198
3	Follow-up	10240	11245	11795
4	Follow-up	12882	11961	12473
5	Follow-up	20332	12684	12838
6	Follow-up	21705	12382	13067
7	Follow-up	27408	13053	13736
8	Follow-up	30303	13218	14283

Table 5.7: Kinetic absorption data collected on spontaneous recovery of BA in a solution of cyclohexane

Since even after irradiation there are spectral bands left over between 700 and 200 nm (especially due to the benzene b-band at around 255 nm always present in PI), the area under the PI spectrum (after illumination) is a non-zero value. In order to correct for this non-zero area immediately after irradiation, the numerical area of each spectrum was adjusted. Eventually, such adjusted value "before illumination" served as the reference point for each spectrum. Each corrected recovery point in Figure 5.9 is a fraction of the PI-to-BA recovery with the "before illumination" spectrum set to maximum value.

We have been able to determine that the time after which half of the original concentration of PI spontaneously converted back to BA, the $t_{1/2}$ value, is around 14-15 days for both solutions, at room temperature and ambient pressure.
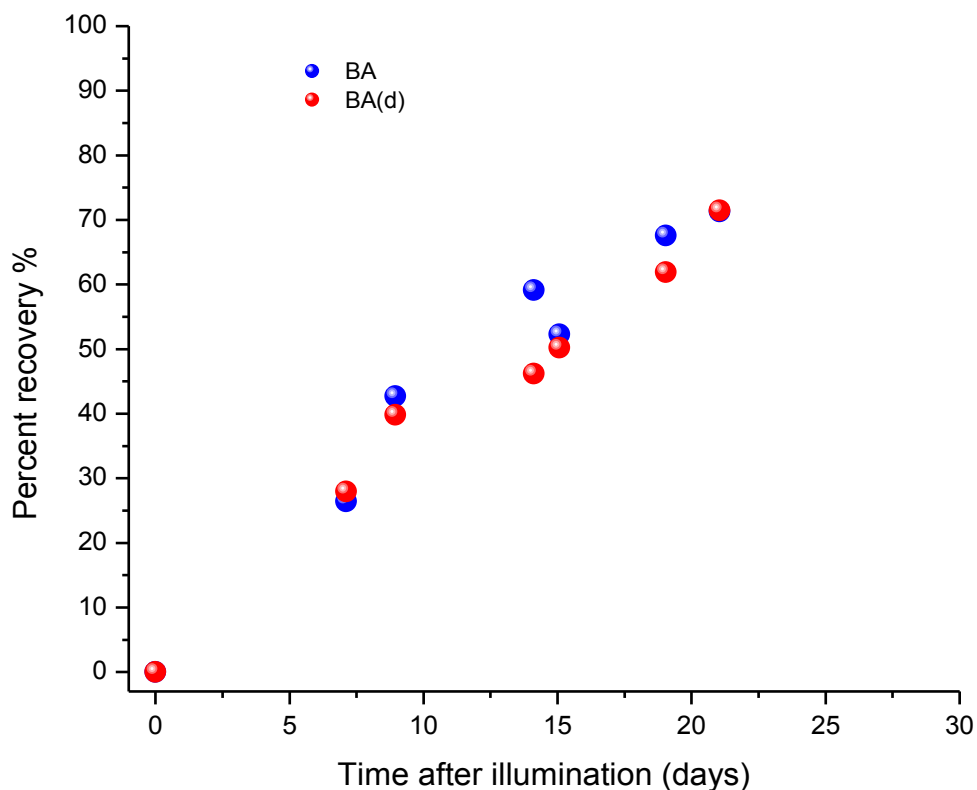
Figure 5.9: Plot representing the spontaneous recovery of BA and BA(d) from their photoisomers in cyclohexane, room temperature, referenced to a peak before illumination (100%). As can be seen, the $t_{1/2}$ value for the two solutions oscillates around 15 days (slightly over 2 weeks)

5.2.3.2 Dissociation in Crystalline Form

The spontaneous dissociation of PI to BA occurs in a solution as well as in a crystal phase. The back-reaction in crystalline PI yields only the β-form of BA crystals[12] and only that polymorph was studied by Mau *et al.* The thermally-induced back-reaction of PI to BA in a toluene solution yielded the activation energy barrier of 100.4 kJ/mol in a first-order kinetic process. Slightly higher energy barrier was measured in crystalline samples. The authors observed however that the back-reaction in crystals of PI did not follow the simple first-order kinetic process that was observed in toluene solution. Through a series of experiments they proposed that nucleation and spreading of the formation of BA accelerated the decay of PI. This could happen through the release of heat in an exothermic PI-to-BA reaction which in turn is transferred to the neighboring molecules of PI, reverting back to BA upon heating. This "chain reaction" is thus catalyzed by BA already formed. The two-step process occurring only in crystalline PI is outlined as follows[12]:

$$PI \xrightarrow{k_1} BA$$

$$PI + BA \xrightarrow{k_2} 2BA$$
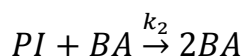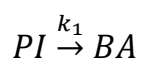
In another publication[13] the existence of two conformers of BA has been postulated. The distribution of these two conformers depends on their

environment: the BAt (translationally displaced) is mostly favored in solutions and BAr (rotationally displaced) in photoisomer hosts. They were described as showing different photophysical properties and spectral features. The authors found that the calculated enthalpy difference between BAt (higher enthalpy) and BAr is almost 9 kJ/mol[13].

5.2.4 Force-Activated Scission of Covalent Bond

Our initial studies on BA concentrated on the possibility of inducing intramolecular dimerization in BA in the dark, only with pressure. Such pressure-induced forward reaction (BA-to-PI) was considered to be feasible as the topological requirement for the anthracene arrangement is fulfilled along with short distance between the adjacent carbon reaction centers. With a number of experiments performed up to 73 kbar, we have not observed any spectral changes that would indicate a dimerization occurring in BA dispersed in a polymer film (Zeonex) in the dark. As a result of the increased pressure, the absorption spectrum of BA with a maximum of absorption at ~ 257 nm (0 kbar) shifts towards longer wavelengths (450 cm^{-1} for every 10 kbar) and slightly broadens due to the negligible inhomogeneity within the sample compartment in

DAC. The absorption spectra of BA exposed to high pressure are also time-independent. Similar spectral observations were made in films of Rhodamine 101 dispersed in PMMA, Figure 5.10. The maximum of absorption of Rhodamine 101 shifts towards the red part of the spectrum at higher pressures along with relatively large broadening. The integrated area under the main absorption peak is preserved – there is no increase or decrease in the population of the absorbing molecules with time indicating that no pressure-induced reactions take place in these films. After the pressure was released, the absorption spectra of BA as well as those of Rhodamine 101 both returned back to their original position and shape.

The situation looks dramatically different when a BA photoisomer, PI, is exposed even to very mild pressures of only few kbar. The spectral features changed within tens of seconds for what it looked like the recovery of bis-anthacene, BA, with its characteristic absorption spectrum, Figure 5.11. As the time progressed, the intensity of the main absorption peak kept increasing now at a slower rate than initially. In another experiment, BA was exposed to higher pressures and illuminated at the same time. We have observed that at these conditions the rate of formation of the photoisomer was retarded or even inhibited, as compared to ambient pressure depending on the magnitude of the pressure applied to the sample film within DAC.

We decided to observe the behavior of PI at various pressures as a function of time through absorption spectroscopy. The time-dependent kinetic traces for three different pressures are plotted in Figure 5.12. As the pressure increased, the recovery of the BA molecules accelerated in the PI-to-BA process.

This counterintuitive effect could have been explained in terms of the molecular volume change between the reactant and the product molecules (BA and PI). Significantly lower molecular volume of the product molecules, BA as compared to PI, would shift the high-pressure equilibrium of the recovery towards BA. The crystal cell volumes in each isomer have been determined by means of X-ray analysis[8].

We tested out hypothesis by simply defining molecular volume as a volume occupied by an individual molecule in a crystal unit cell. We equipartitioned all available space in a crystal lattice to all molecules occupying that volume. This approach is only justified in molecular crystals with no voids, or negligibly small voids when compared to the bulk of the molecule. As determined from crystallographic data, both species crystallize in space group P21/c and there are two molecules for every unit cell[8]. The literature-reported unit-cells' volumes are ~ 1013 Å^3 (ANTMET05, 299 K, R-Factor 5.52%) and ~ 1021 Å^3 (ANTMEU03, 299 K, R-Factor 4.09%) for PI and BA, respectively. Therefore we arrive at molecular volumes of 506.5 Å^3 and 510.2 Å^3 for every molecule of PI and BA, respectively.

The overall change in molecular volume associated with the photocycloaddition reaction (BA → PI) is a difference between these two values, which is only around 3.7 $Å^3$. Values derived from these crystallographic data basically indicate that the overall volume occupied by 1 molecule of BA decreased by nearly 4 $Å^3$ (0.92%) as the forward (BA-to-PI) reaction progressed to its final stages. For the back-reaction, i.e. the conversion of PI back to BA, the molecular volume increases by almost 4 $Å^3$. More detailed study on the progress of the molecular volume change as a function of time in crystals of BA and PI are discussed by E. Trzop[8] and co-workers.

Intrigued by the mechanism of the pressure-induced reaction in PI, we have performed calculations to determine the molecular volumes on crystal structures of the two isomers. After intense work we obtained virtually identical values: 504.3 $Å^3$ for BA and 504.5 $Å^3$ for PI with slightly (0.2 $Å^3$) higher molecular volume for PI. The discrepancy between crystallographic and calculated values, Table 5.8, may likely arise from the existence of voids in both crystals, possibly slightly larger between the more-strained PI molecules.

In the overall picture however, the mechanism for the pressure-induced reaction that we initially drew is lost. One could ask a question, what is the true reason for the accelerated recovery of BA (from PI) at higher pressures? The X-ray analysis along with calculations suggest that there is virtually no difference in molecular volumes between the two photoisomers, BA and PI. Therefore, the

back-reaction should not be favored at pressures of only few kbar. Pressures of at least 100 kbar are normally required to break covalent bonds such as the C-C bonds in PI. Similar high-pressure experiments on dianthracene dimer, An_2, did not yield anthracene up to ~ 30 kbar in DAC as a result of a covalent bond cleavage.

Puzzled by the observations, we conducted a series of experiments outlined in the following sections of this Chapter to understand and explain the mechanism behind the recovery of BA induced by mild and homogeneous static pressure.

	BA	PI
X-ray experiments[8]	510.2 $Å^3$	506.5 $Å^3$
Calculations[10]	504.3 $Å^3$	504.5 $Å^3$

Table 5.8: A comparison of molecular volumes found for BA and PI: experiment vs. calculations
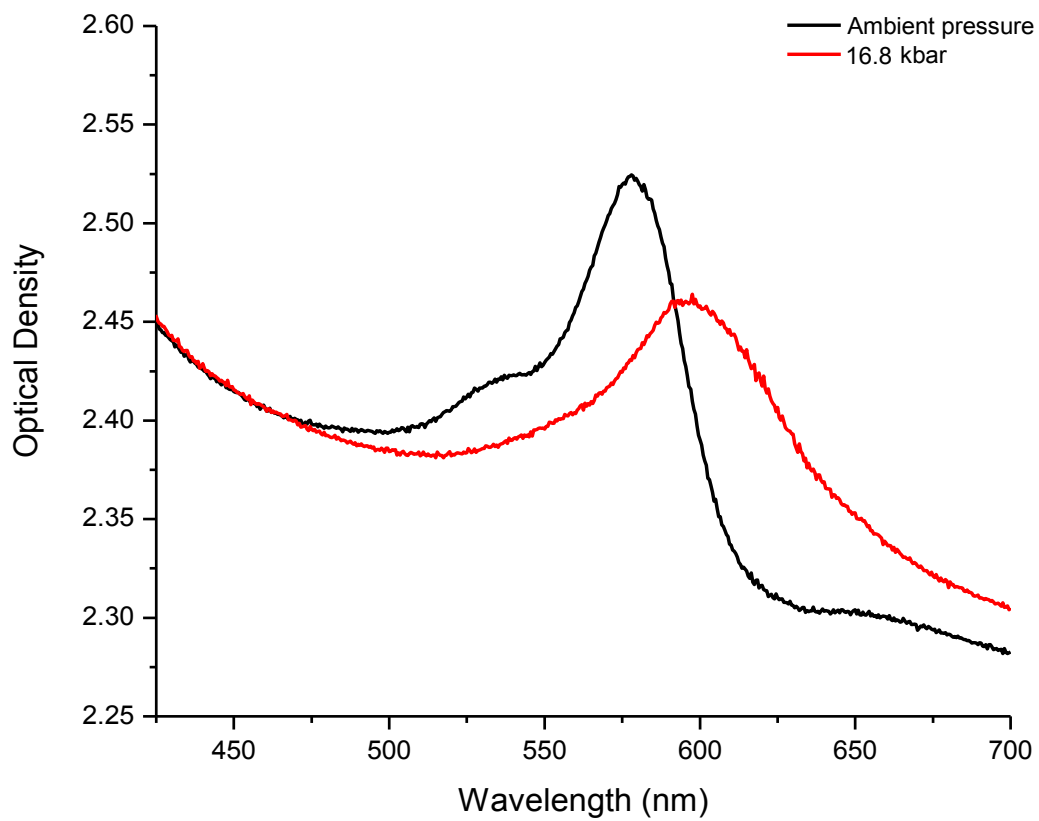
Figure 5.10: Absorption spectra of Rhodamine 101 in PMMA at ambient, black, and high pressure, red. The spectral areas of the absorption peaks are about the same
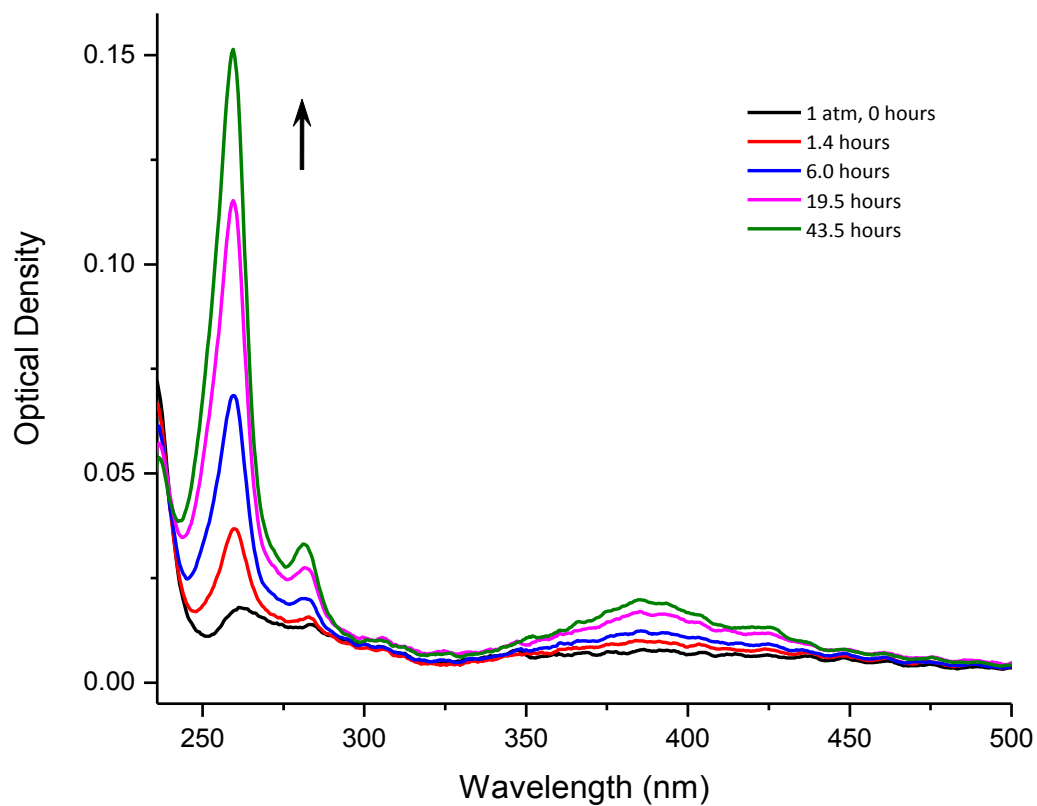
Figure 5.11: Absorption spectra illustrating the pressure-induced restoration of BA from PI at 6.2 kbar and room temperature. The black spectrum is the absorption of PI in Zeonex at ambient pressure
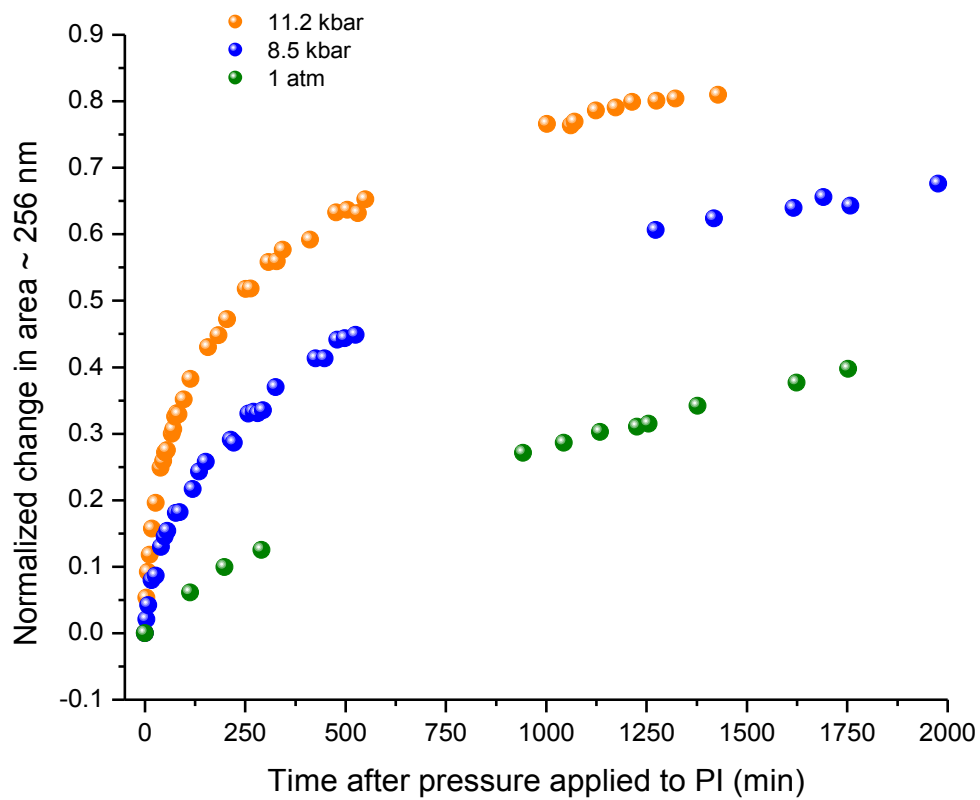
Figure 5.12: Kinetic traces for three selected pressures. The PI-to-BA conversion is accelerated at higher pressures

5.2.5 Theoretical Studies of the Thermodynamics; Structural Changes

Calculated at the DFT-D level total energies and enthalpies of formation of BA, PI, An$_2$, An and their differences defined as:

$$\Delta E = E_{PI} - E_{BA}, \ \ \Delta E = E_{An2} - 2E_{An}$$

$$\Delta H_f^\circ = H_{fPI}^\circ - H_{fBA}^\circ, \ \ \Delta H_f^\circ = H_{fAn2}^\circ - 2H_{fAn}^\circ$$

are presented in Table 5.9. These values have been derived after full geometry optimization of all four isomers.

The positive, absolute ΔE values indicate that the photocycloaddition reaction's products (PI, An$_2$) are higher in total energy than their corresponding reactants (BA and two anthracene molecules in various arrangements). Also as expected, their dissociation (back-) reactions are exothermic. There are three types of energy calculations performed on two anthracene molecules: two molecules at infinite distances, in parallel alignment separated by 162 pm and the third arrangement with An perpendicular to each other, Figure 5.13, with the distance of 379 pm between C(9) and C(9') or C(10'). Three energy differences (ΔE) are therefore reported in Table 5.9, with the parallel orientation showing the lowest difference in absolute energies.

	ΔE, forward reaction (kJ/mol)	ΔH°f, forward reaction (kJ/mol)
BA/PI	87.8	86.1 (literature[14]: 35.5)
2An/An₂	25.4 (infinity) 66.0 (perpendicular) 74.1 (parallel) for distances see text	22.8 (infinity) (literature[14]: 65.2)

Table 5.9: Comparison between calculated and reported in the literature energies and enthalpies

Based on the calculated values for the enthalpies of formation for each species and the heights of their activation energies found, we were able to reconstruct the most probable potential energy diagrams for the following back-reactions at 0 kbar pressure:

$$An_2 \rightarrow 2An, \text{ Figure 5.14}$$

$$PI \rightarrow BA, \text{ Figure 5.15}$$
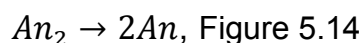
Calculations performed on anthracene molecules at infinite distances from each other represent the most ideal scenario in which no intermolecular interactions, such as the Van der Waals interaction can form between two anthracenes. This weak interaction however is accounted for in the case of the BA molecule since the two anthracene moieties are already aligned for a [4+4] reaction either in a solution or in a solid phase thanks to the presence of the pair of dimethyl linkers.

Anthracenes separated at the 162 pm distance are to represent the separation observed in dianthracene. The energy difference between An_2 and anthracenes at 162 pm distance is the largest that we found in Table 5.9.

And finally, in the perpendicular arrangement, the [4+4] cycloaddition cannot take place between two anthracene molecules due to the topochemical considerations. We only used this particular alignment for comparison.

The energies required for the forward [4+4] cycloaddition reaction are provided during illumination. The energy released in the back-reaction is expelled as heat and according to our calculations is higher for the BA/PI pair when compared to the $2An/An_2$ pair of isomers in either arrangement.

The enthalpy of the back-reaction found experimentally for the BA/PI photoisomers requires a small comment. The value found for the crystals of PI with the Difference Scanning Calorimetry (DSC), - 35.5 kJ/mol, have been reported as "unpredictably low"[14] in light of the enthalpy of the back-reaction found for anthracene/dianthracene crystals. Another calculated value[13], found with the DFT (no dispersion corrected) method in 1980, yielded an overestimated value of - 139 kJ/mol for the back-reaction.
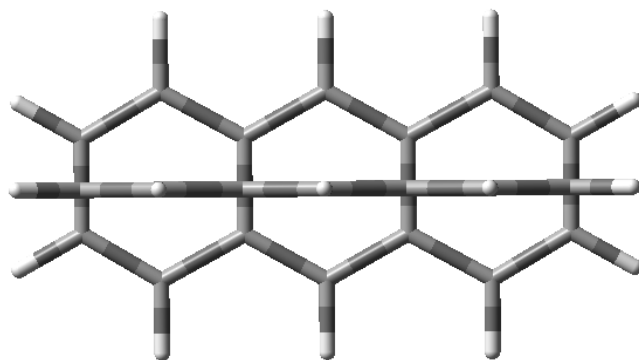
Figure 5.13: Two anthracene molecules in a perpendicular alignment. The distance between C(9) and C(9') or C(10') is 379 pm; top view. Arrangement submitted for molecular (DFT-D) calculations shown above
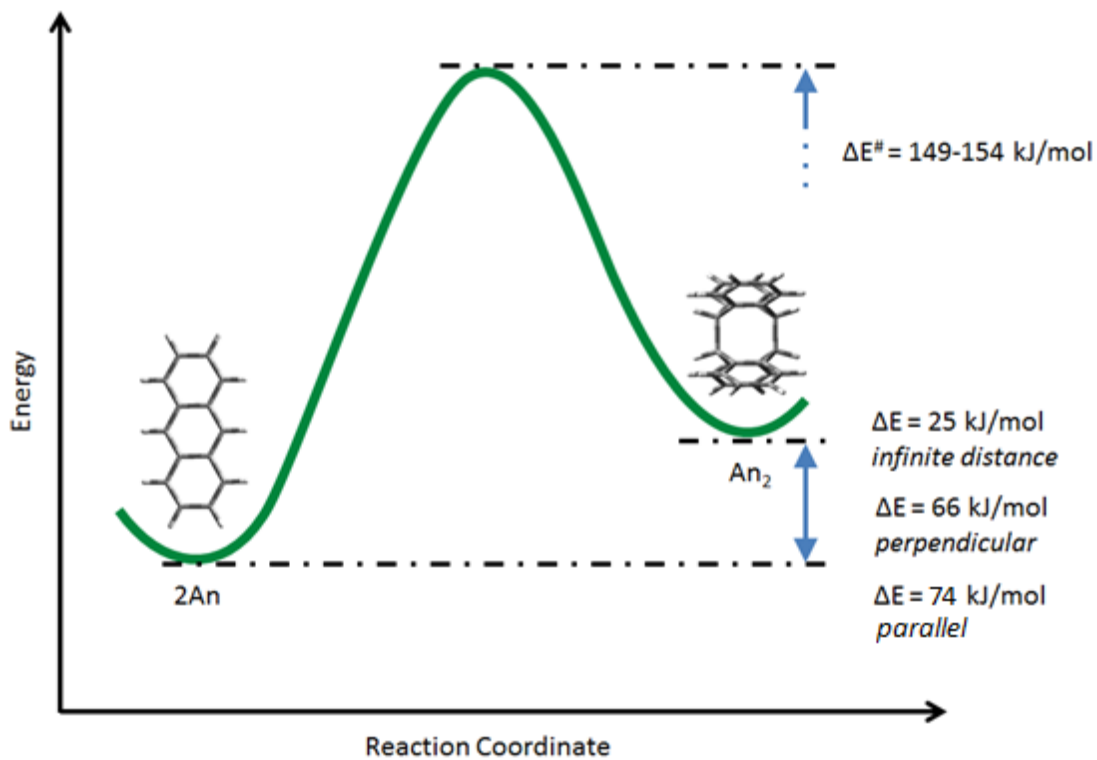
Figure 5.14: Potential energy diagram for An_2/An reconstructed from Table 5.9. The activation energy of 149 kJ/mol for the back-reaction was found in cyclohexane[15]; the 154 kJ/mol value was reported in benzene[16]
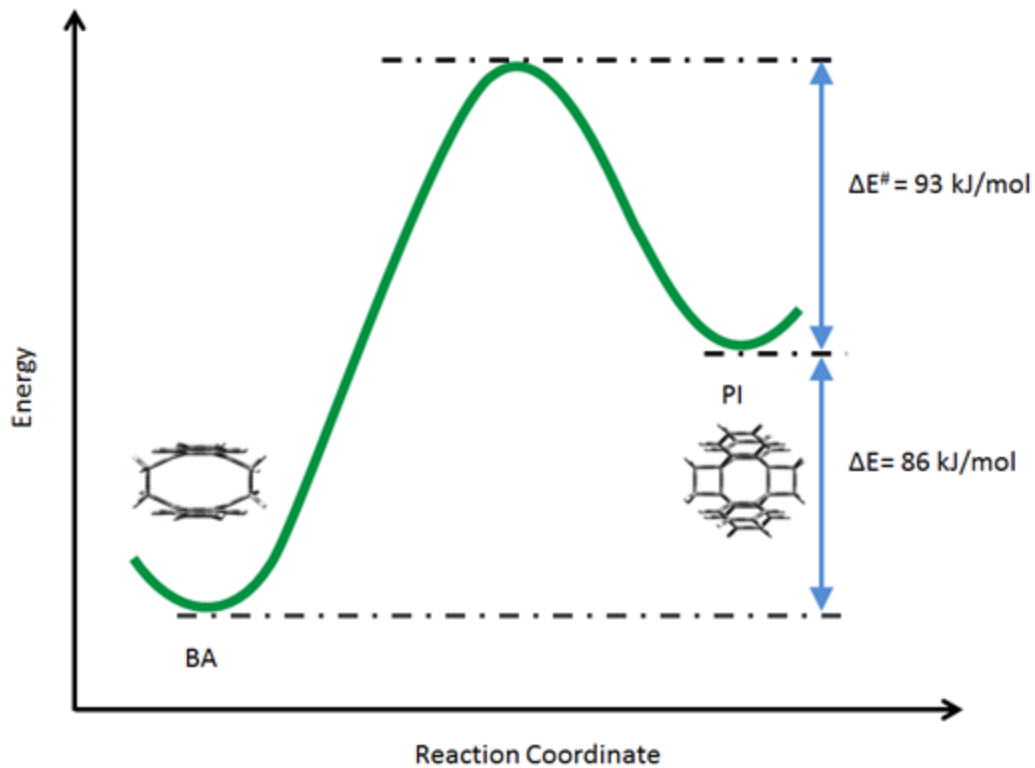
Figure 5.15: Potential energy diagram for PI/BA reconstructed from Table 5.9. The activation energy of 93 kJ/mol was found through experiments in a polymer film[10]

5.2.6 Kinetics of the Covalent Bond Scission

5.2.6.1 Shear Deformation

Mortar and pestle experiment

In this part of this Chapter, we have been able to demonstrate that the crystalline bis-anthracene photoisomer, PI, reacts back to BA when exposed to shear deformation during grinding with a combination of mortar and a pestle. The idea of applying shear-stress to induce physical and chemical changes was popular already among alchemists. The grinding of PI however turned out to be one of the most difficult experiments if quantitative information is to be retrieved via absorption spectroscopy in an organic solvent. The difficulties with this experiment involve the following:

- The photoreaction during which bulk amounts of BA (~ 1 gram) are to be transformed to PI prior to grinding;
- The very low solubility of either BA or PI popular in organic solvents;
- The slight difference in solubility between BA (more soluble) and PI (less soluble in organic solvents);
- The grinding produces small, powdery crystals rendering the solution opaque in absorption measurements;

- Inability to accurately quantify the grinding time and the force applied during the process;

The light-induced transformation from BA to PI is relatively easy to perform when very low concentration BA is dispersed within a polymer film. Gram amounts of powder of BA require illumination and constant shaking for the entire duration of the illumination. Even though BA absorbs in the blue part of the visible spectrum (between ~ 350 nm to 450 nm), more efficient transformation can be achieved when the powder is illuminated with deep-UV photons. This in turn requires a quartz container and the sample to be sealed with an inert gas or in vacuum. Photoreactions involving oxygen are known to contribute to the decomposition of an organic material (photobleaching) even when small amount of oxygen is provided for the duration of the illumination process.

To convert ~ 1 gram of BA to PI by light we have decided to mix the crystalline reactant with ~ 5 ml of cyclohexane and seal the suspension inside a glass container. The mixture was illuminated with a halogen lamp generating enough high-energy photons for the photoconversion to occur efficiently. At the same time the suspension was stirred with a magnetic bar coupled to a magnetic stirrer to ensure uniform illumination of all crystals. We have placed another glass container filled with water between the light source and the sample to filter-out as much infrared radiation as possible to avoid heating to the solvent, cyclohexane,

and the newly formed PI crystals known to decompose at elevated temperatures. The progress of the photoreaction was monitored every 5 minutes by sampling the solution for the presence of unreacted BA via absorption spectroscopy. It took approximately 20-30 minutes to quantitatively convert BA to PI in this fashion.

Once we were assured that only PI is present in the glass vial, all the cyclohexane was removed at room temperature by blowing compressed air over the suspended crystals yielding bright-yellow crystals of PI.

The differences in solubility between linked anthracenes and their photoproducts have been explored in organic synthesis to purify the reaction's product. Attention has to be paid that the solutions are not to become saturated with BA. As the grinding progresses, the changes in the absorption of the BA are investigated. If the solution becomes saturated with BA, no changes, increase or decrease in the absorption of BA will be recorded between 350 – 450 nm.

As the grinding continues, smaller and smaller, crystals of BA/PI are produced. Since the yet-unconverted PI is less soluble in cyclohexane, the microcrystals of PI tend to obscure the solution and thus the absorption spectrum by forming a suspension. We have used a centrifuge to successfully deal with this problem. Spinning for about 30 seconds of each sample produced optically-clear solutions. However, with the use of a centrifuge we were limited to the amount of solution that we could use for each sample. Only the 1 mm thick

quartz cuvettes accumulate small enough volume to allow us record absorption spectra shown in Figure 5.16.

As a result of continuous grinding, PI partially converted to BA on a much shorter time scale than during the spontaneous back-conversion at ambient pressure and temperature conditions ($t_{1/2}$ ~ 2 weeks).
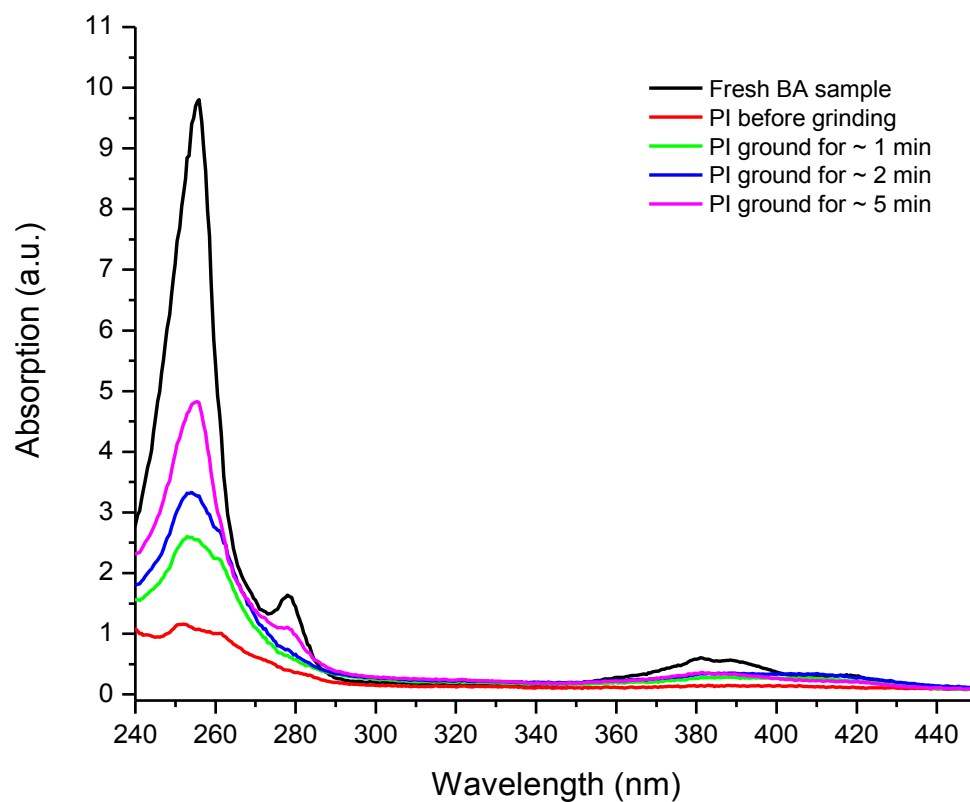
Figure 5.16: Changes in absorption of the BA/PI solution as a function of the grinding time with the use of mortar and pestle (glass). As the grinding continues, PI back-converts to its unreacted form, BA as a result of shear-deformation applied to the crystals of the photoisomer, PI

Sonication

Sound waves of high frequency (ultrasounds) were introduced into a cyclohexane suspension of PI by a cone-shaped tip coupled to a mechanical device and a generator. PI was prepared in a way that is described in the previous section: mortar and pestle experiment with the difference that the

solvent was not evaporated. High-frequency sound waves cause rapid changes in pressure of the solution coupled with the formation of microscopic size cavitation bubbles, also called liquid-free zones. Within the cavitation bubbles, the pressure is very low. The sound-wave cycles cause the cavitation bubbles to grow and shrink in size[17], until they become unstable and eventually collapse. This is the collapse event that suddenly induces a pull on molecules of solvent and solute and draws them into the void. The pull, inhomogeneous flow field, is responsible for the gradient in pressure and is often explored in elongation and the cleavage of the polymer chain in mechanochemically functionalized materials[17]. In contrast, the Diamond Anvil Cell (DAC) high-pressure tool is designed to produce homogenously-distributed pressure within the gasket compartment with no significant pull nor shear deformation associated.

Unfortunately, the collapse of a cavitation bubble produced by ultrasounds also causes unwanted effects: an increase in the temperature[2] of the local environment to thousands of Kelvins. The increase in the temperature of the solution during sonication is used to calibrate the tip and the generator by careful analysis of the changes in the temperature of the solution[17].

In experiments on BA/PI pair of mechanophores, sonication was performed with the use of a Branson Sonifier 450 VWR equipped with Branson ultrasonics converter set at maximum power. The tip of the probe was immersed in a large glass test tube to avoid accidental contact with the walls of the glass

container. The test tube with the sonicated solution was immersed in an ice bath with the solution (cyclohexane) temperature oscillating around 3 °C and at the same time protected from the ambient light to avoid reformation of the photoisomer, PI. Before each absorption spectrum was recorded with Cary 50, the sample solution was centrifuged for ~ 30 s to remove crystals of PI and thus improve the signal to noise ratio by limiting light scattering. Figure 5.17 shows the absorption spectra of BA and (almost entirely converted) PI as well as partially decomposed PI as a result of the sonication experiment. Some of the partially converted solutions, especially after 30 minutes of sonication most likely show signs indicating partial decomposition of BA (magenta, Figure 5.17). While no additional efforts were made to establish the products of the decomposition, we suspect that it might be due to the thermal decomposition of BA as a result of the substantial, local heating effects caused by the collapse of cavitation bubbles.
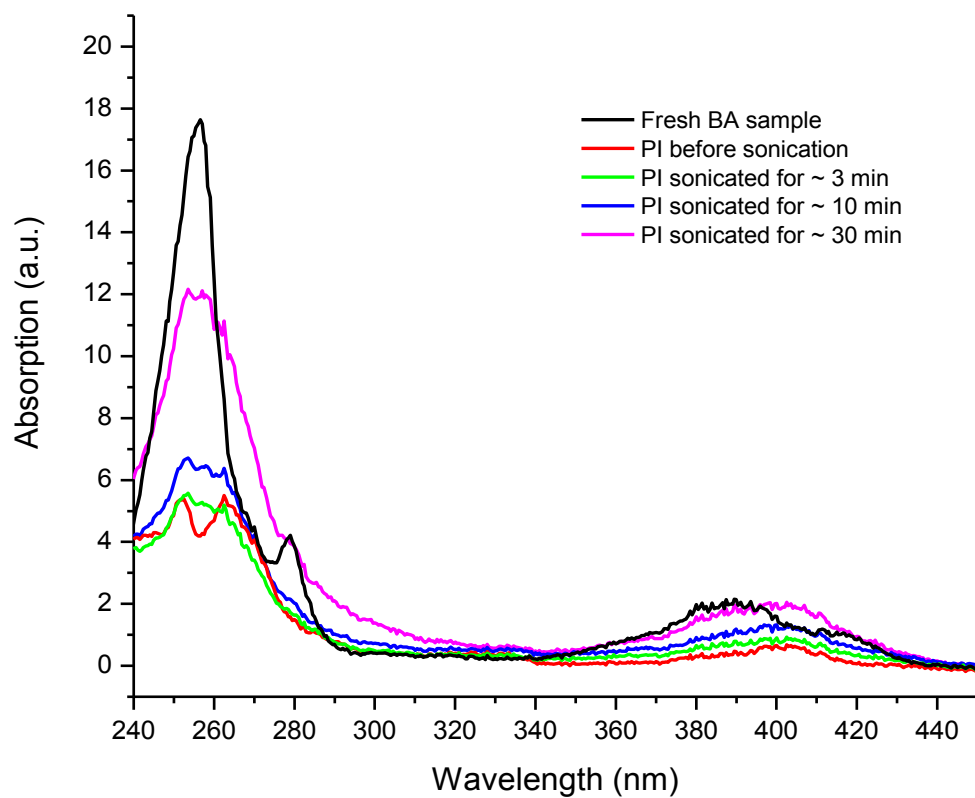
Figure 5.17: Absorption spectra of partially back-reacted photoisomer as a result of sonication in cyclohexane. The initial solution of PI contains small amount of unconverted BA, red spectrum

5.2.6.2 Mechanokinetics at Room Temperature

Rates of some common reactions greatly vary with pressure. This comes as a result of changes to concentration of reactants or products (for reactions in a gas phase) or by directly influencing the reaction's rate constant, k. The following equation represents the measure of a rate for a simple homogeneous reaction between *a* and *b*:

$$r = kc_a^n c_b^m$$

Reaction's rate changes with pressure can be interpreted with the help of the collision- and transition-state theories. The transition-state theory assumes that any given reaction achieves a state of maximum energy while on its way to product formation. Such high energy and thus thermodynamically unstable configuration is termed in the literature as the activated complex, Figure 5.18.

The activated complex may proceed down the potential energy hill with the formation of products. It may also become unstable and revert back with the reformation of reactants. The rate of success in the product formation cannot be easily predicted. For the photoreaction in which anthracene dimerizes in a solution, a diffusion-controlled process, only about 16% of the excimers end up as anthracene dimers with 84% of excimers reverting back to the ground state anthracene[18].

The transition-state theory leads to the relationship between the rate of a reaction, k_{rxn}, and the activation volume of that reaction, $\Delta V^{\#}$ expressed as:

$$\left(\frac{\delta \ln k_{rxn}}{\delta P}\right)_T = \frac{-\Delta V^{\#}}{RT}$$

The activation volume is defined as the difference in molecular volumes between the activated complex, $X^{\#}$, and the reactants. The activation volumes are positive for reactions involving dissociation or breaking of covalent bonds. Negative activation volumes are associated with the formation of new covalent bonds as is the case in the napthoate [4+4] dimerization reaction (-10 cm^3/mol) described earlier in this Chapter.

In a series of kinetic high-pressure experiments we evaluated the activation volume in the PI-to-BA process. This unimolecular reaction between a pair of tethered anthracenes in a concentration-independent process and is schematically depicted as:

$$PI \rightarrow BA + heat$$

and the reaction rate can be expressed as:

$$r = kc_{PI}^n$$

At the beginning of each series of kinetic absorption measurements, a fresh sample of BA in Zeonex was loaded into DAC. The sample film was illuminated with a halogen lamp to quantitatively convert all BA molecules into its

photoisomer, PI. Within 10-20 seconds the pressure was applied and the DAC was carefully mounted within a Varian CARY 500 sample compartment between two plano-convex lenses. After a prolonged period of time, some of the BA was restored and the sample film replaced. The absorption spectra were numerically evaluated as outlined in the Appendix section.

After having evaluated all spectra at pressures ranging from 0.0 to 25.6 kbar, we have studied numerous fitting strategies to the kinetic traces of the BA/PI system in Zeonex. The fitting approach initially involved monoexponential fits, stretched exponential functions and bi-exponential fits. For all the three main types of fits to the data in the pressure-dependent series at room temperature and the temperature dependent series at ambient and high pressure, we chose the bi-exponential function to describe the type of growth observed for reasons explained later in this section of this Chapter.

The entire bi-exponential function is a sum of two basic exponential growth functions with equal contributions to the total change observed, multiplied by a normalization factor:

$$BA(t) = X_0\big(0.5(1 - e^{-k_1 t}) + 0.5(1 - e^{-k_2 t})\big)$$

When overlaid with the experimental data points, Figure 5.19 (only a representative kinetic trace shown), the functions fit reasonably well, yielding parameters with a physical meaning that could be interpreted in the BA/PI system.

Once the growth model was established, the pressure-dependent rate constants and their respective contributions were extracted for each series with the help of the least square method. The fitting function performed well when one of the rate constants, described here as k_2, was fixed at constant value (pressure-independent), 0.0012 min^{-1}, and its contribution into the total recovery of absorption of BA/PI in Zeonex was 50%. The k_2 rate constant represents temperature- and pressure-independent contribution into the BA recovery process. The other rate constant, k_1, is assumed to be dependent both on temperature and pressure. With these assumptions in mind (i.e. k_2 = 0.0012 min^{-1} at 50% in all of our fits) we later evaluated the temperature time-dependent series described in the following section. The parameters extracted from the fits for each pressure at room temperature are grouped in Table 5.10.

The partitioning of the recovery kinetics into two rate constants, k_1 and k_2, is a simple model which is meant to represent two different conformers of BA, each with very different susceptibilities to temperature and pressure conditions. The two conformers of BA have been postulated[13] but their individual dependencies on temperature or pressure have not been established in the literature.

The rate constants in Table 5.10 determined with the bi-exponential growth function at different pressures were plotted on a logarithmic scale against pressure, Figure 5.20. The slope of the straight line fit yields the activation

volume, $\Delta V^{\#}$. The activation volume is constant up to ~ 15 kbar, Figure 5.20.

Above that pressure, the activation volume becomes negligible. We interpret that

effect as the competing stabilization of the photoisomer up to the ~ 25.6 kbar

pressure maximum.

Pressure	Rate constant k_1:	Rate constant k_2:	Contributions of k_1/k_2:
0.0 kbar	0.0003 min^{-1}	0.0012 min^{-1}	0.5/0.5
6.2 kbar	0.0012 min^{-1}	0.0012 min^{-1}	0.5/0.5
7.1 kbar	0.0089 min^{-1}	0.0012 min^{-1}	0.5/0.5
8.5 kbar	0.0053 min^{-1}	0.0012 min^{-1}	0.5/0.5
9.3 kbar	0.0343 min^{-1}	0.0012 min^{-1}	0.5/0.5
11.2 kbar	0.0142 min^{-1}	0.0012 min^{-1}	0.5/0.5
14.0 kbar	0.0604 min^{-1}	0.0012 min^{-1}	0.5/0.5
19.5 kbar	0.0788 min^{-1}	0.0012 min^{-1}	0.5/0.5
25.6 kbar	0.1035 min^{-1}	0.0012 min^{-1}	0.5/0.5

Table 5.10: The experimental parameters of pressure-dependent PI-to-BA recovery at room temperature. The k_1 rate constant is pressure and temperature dependent while k_2 does not depend on either of the two thermodynamic variables

As is the case for the PI-to-BA reaction, the rates of recovery steadily

increase with pressure, yielding negative activation volume of – 16 $Å^3$. We are

perplexed by the outcome of our pressure-dependent measurements. The

volume of the activated complex is smaller than the volume of the photoisomer,

Figure 5.21, PI in spite of the reaction being a dissociation reaction. Two covalent

bonds are being cleaved by mechanical stress between C(9)-C(9') and C(10)-

C(10') positions and the rate of this back-reaction is increasing with pressure up

to ~ 15 kbar. In the napthoate dimerization reaction (outlined earlier in this

Chapter), with rates of the forward reaction enhanced by high pressure, the

observed activation volume is nearly identical to PI/BA, - 16.6 Å^3. The main

difference is that the high-pressure accelerats the formation, and not the

cleavage of covalent C-C bonds.
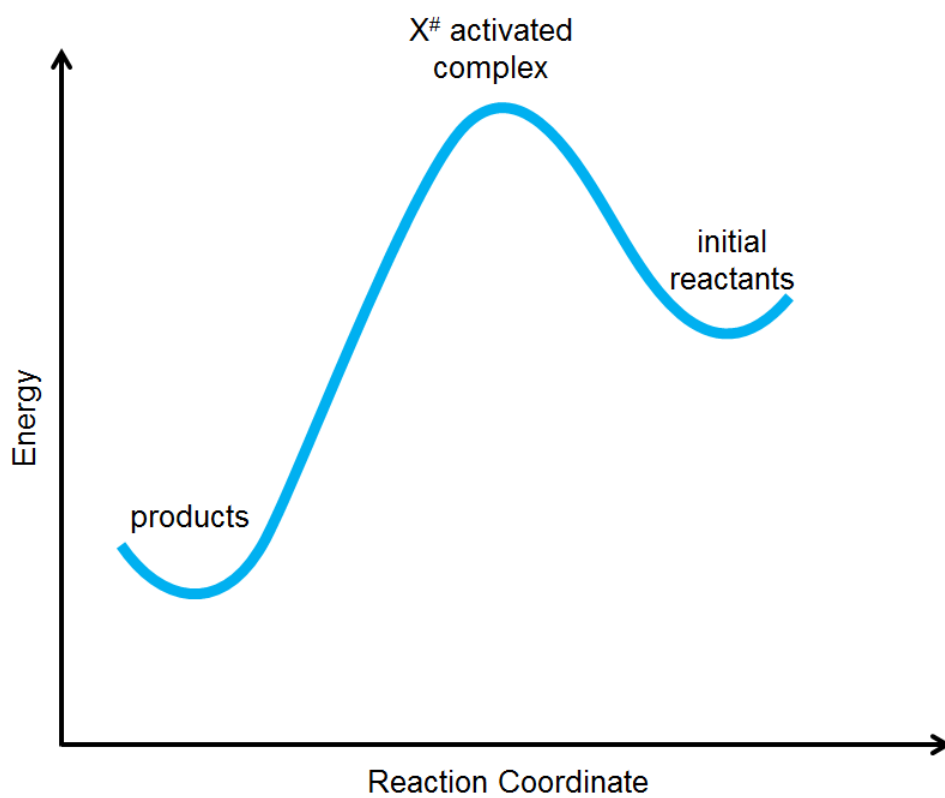
Figure 5.18: Typical reaction's profile outlined by the transition-state theory with the activated complex located in the saddle point
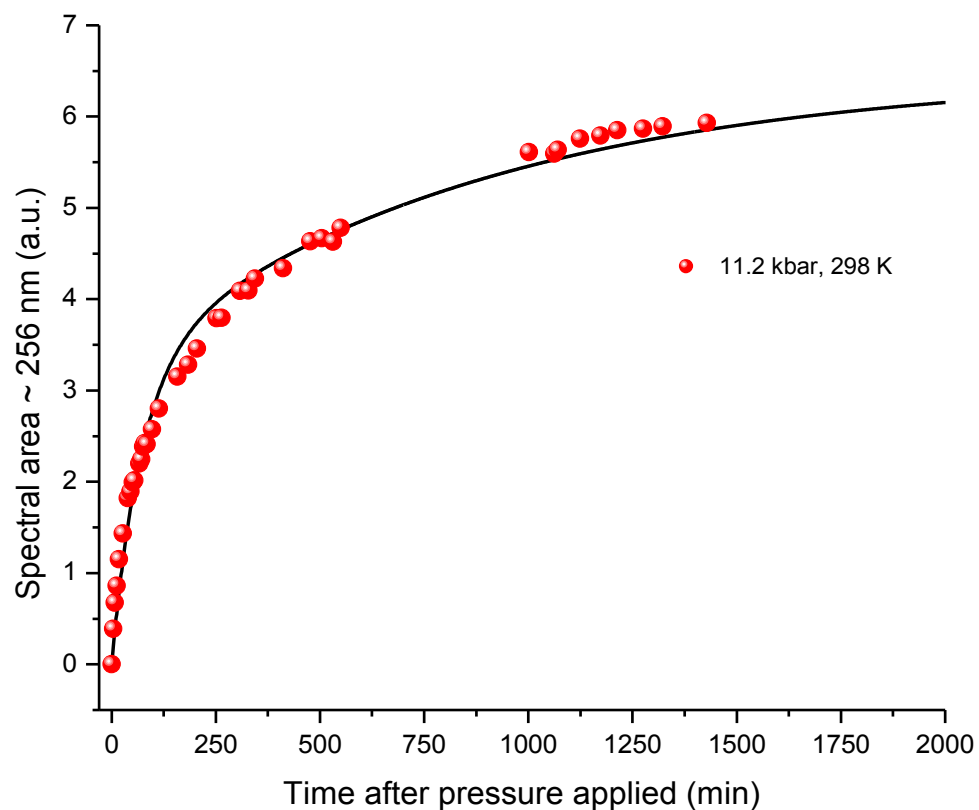
Figure 5.19: A representative figure showing a kinetic trace for the PI-to-BA recovery at 11.2 kbar at room temperature measured in DAC with absorption spectroscopy. The extracted fitting parameters from all pressures with the help of a bi-exponential growth model are shown in Table 5.10
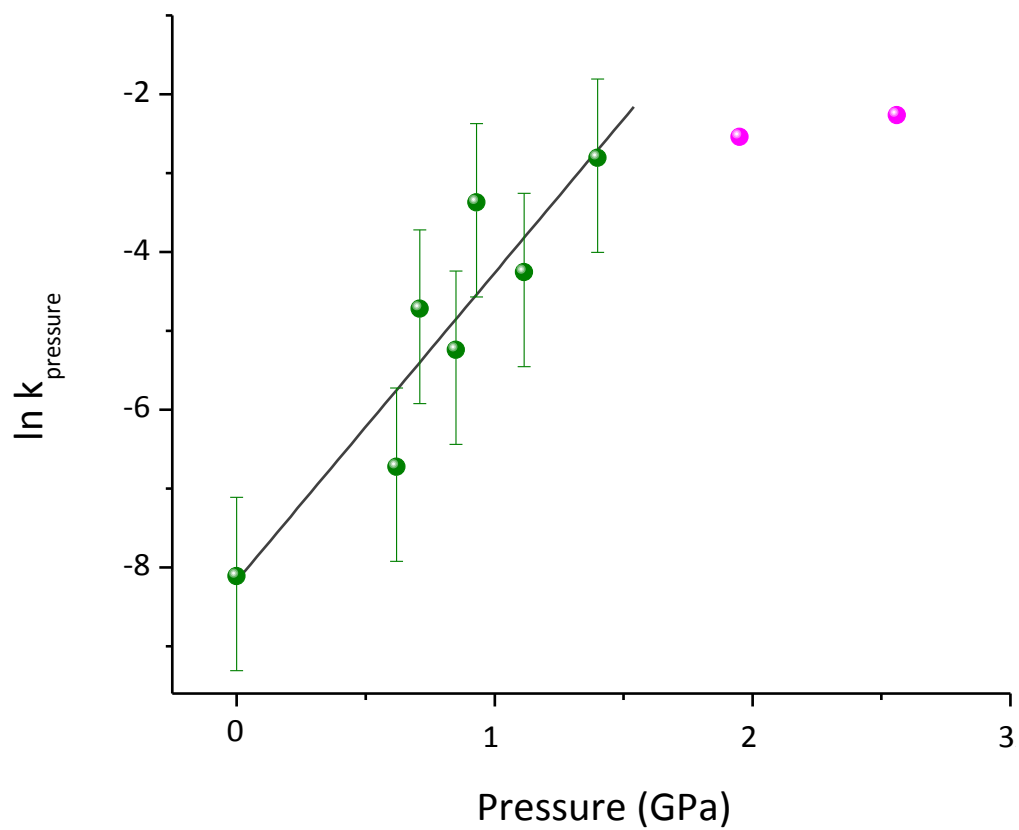
Figure 5.20: The activation volume in the mechanically-activated PI-to-BA reaction is negative (-) 16 $Å^3$ at room temperature. Plot based on data from Table 5.10
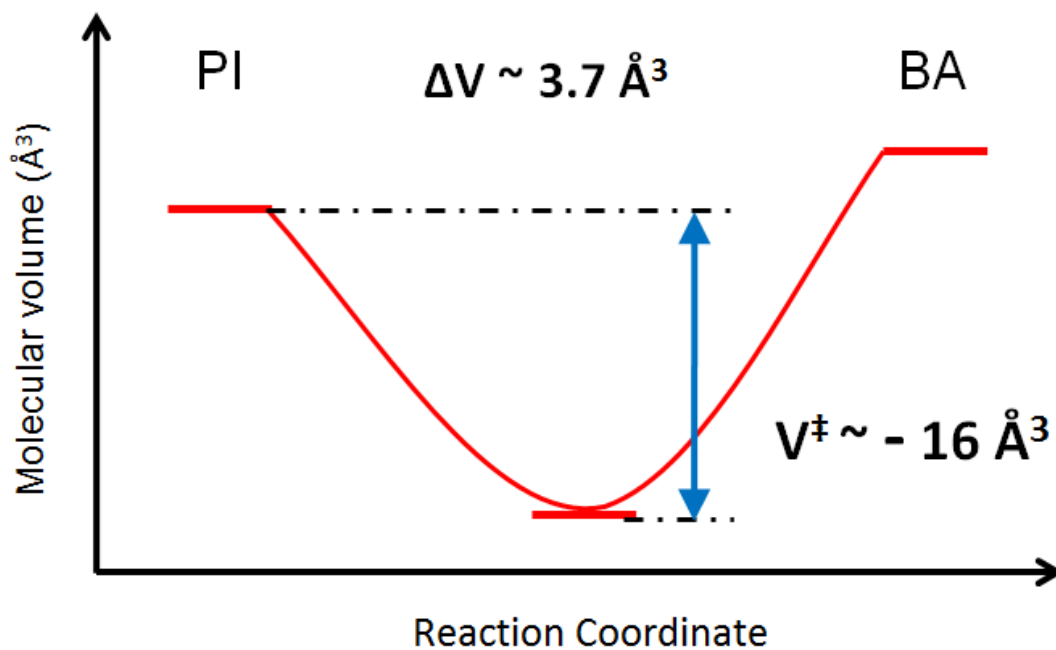
Figure 5.21: An illustration of the differences in molecular volumes between the reactant, PI, the product molecule, BA (3.7 Å^3) and the activated complex ($\Delta V^{\#}$ = -16 Å^3) in a PI-to-BA process

5.2.6.3 Bond Scission at Ambient vs. High Pressure; the Barriers of Activation

Temperature-dependent mechanokinetics at ambient pressure

The thermal free activation energy for the PI-to-BA isomerization at ambient pressure was determined with the help of a linear Arrhenius equation:

$$k = Ae^{-E_a/RT}$$

where k is the rate constant of reaction, A the pre-exponential factor, T the temperature, E_a the activation energy, and R is the universal gas constant.

Kinetic traces were followed at six different temperatures between room temperature and 63 °C. At the beginning of each series, a fresh sample of BA in Zeonex was loaded into DAC (no pressure applied) and irradiated with a halogen lamp in order to convert quantitatively all BA to PI. Soon after, the DAC and the sample were loaded into a Varian CARY 500 spectrometer and heated above room temperature with resistive tape as described in the Appendix section. After sufficient amount of BA was restored, the experiment was terminated and the sample film was replaced. A new kinetic set was recorded at another temperature with a fresh sample film.

The absorption spectra were evaluated as described in the Appendix section, with kinetic traces ranging from 270 minutes at highest temperature to 3200 minutes at lower temperatures. We applied our bi-exponential growth model outlined in the previous section of this Chapter which seems to work reasonably well on the BA/PI system. One of the rate constants, k_2, was fixed at 0.0012 min^{-1} value while the k_1 was allowed to vary with the 50% contribution from both conformers. The temperature-dependent rate constant values are shown in Table 5.11.

Temperature	Rate constant k_1:	Rate constant k_2:	Contributions of k_1/k_2:
298 K	0.0003 min^{-1}	0.0012 min^{-1}	0.5/0.5
308 K	0.0041 min^{-1}	0.0012 min^{-1}	0.5/0.5
310 K	0.0044 min^{-1}	0.0012 min^{-1}	0.5/0.5
318 K	0.0110 min^{-1}	0.0012 min^{-1}	0.5/0.5
324 K	0.0100 min^{-1}	0.0012 min^{-1}	0.5/0.5
336 K	0.0327 min^{-1}	0.0012 min^{-1}	0.5/0.5

Table 5.11: The experimental parameters of the temperature-dependent PI-to-BA recovery at ambient pressure. The k_1 rate constant is pressure and temperature dependent while k_2 does not depend on either of the two thermodynamic variables

Eventually, the activation free energy for the PI-to-BA back-reaction at ambient pressure was extracted from the linear Arrhenius equation and plotted in Figure 5.22. Surprisingly, the value that we obtained in our experiments is identical to the one reported in the literature[14]: 93 kJ/mol. Jones *et al.* found the activation energy through scanning calorimetry measurements in solids[14]. It is perhaps important to stress here that we have made no efforts in our model to match the value of the activation energy in any way to the one found by Jones *et al.* A similar value was reported[12] by Mau *et al.*: an activation energy barrier of 100.4 kJ/mol was found in a toluene solution.
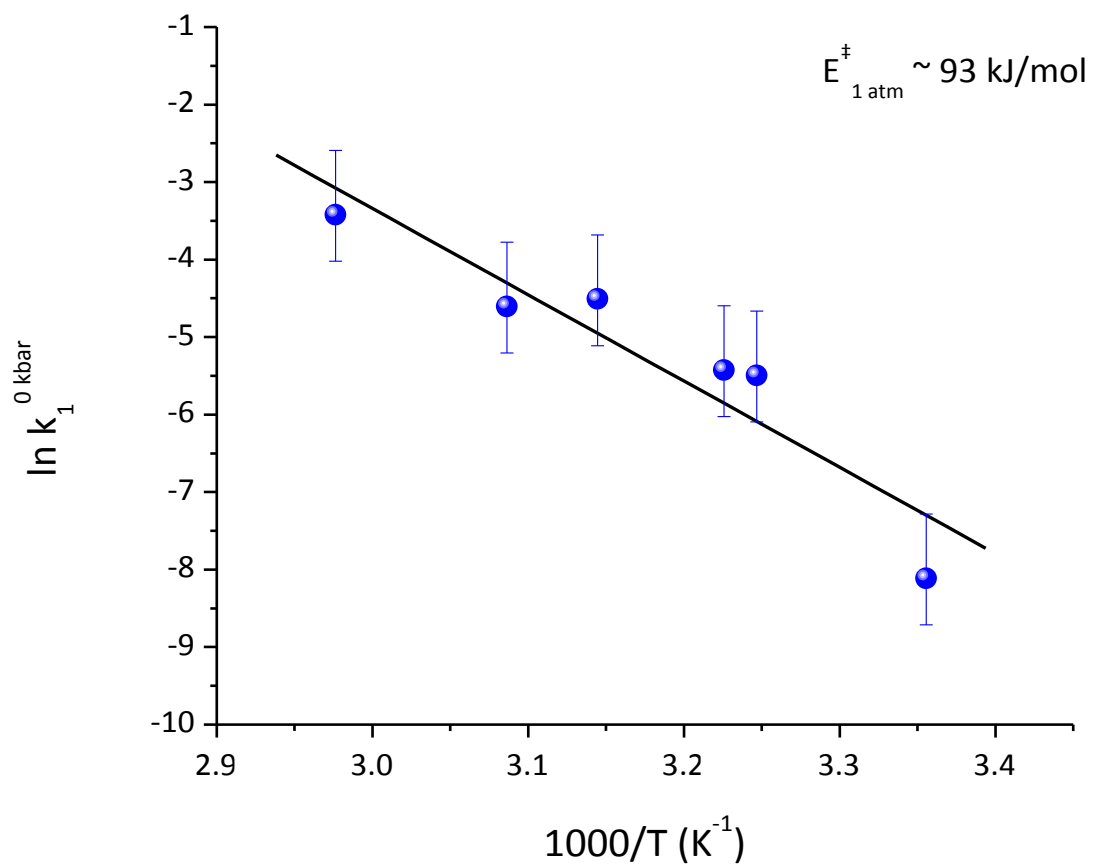
Figure 5.22: Linear Arrhenius model was fit to temperature-dependent rate constants; the extracted height of the activation energy barrier at ambient pressure (0 kbar) is ~ 93 kJ/mol in this thermally-induced PI-to-BA recovery process

Temperature-dependent mechanokinetics at 9 kbar

In a similar way, a series of kinetic-traces were recorded as a function of temperature in the range from 296 K to 314 K at 9.3 kbar of static pressure applied to the sample film (BA/PI/Zeonex) in DAC. To maintain identical static pressure at different temperatures throughout the course of the experiment, the sample film has not been unloaded or replaced. Therefore after having restored nearly all BA (from PI), process accelerated by pressure and temperature, our sample had to be irradiated while in DAC, subjected to 9.3 kbar of static pressure at the same time. Consequently, at the start of each series of pressure-induced recovery, to restart the system, i.e. remove virtually all BA from the sample film and convert it quantitatively into PI, the illumination time with the halogen light source was further increased by ~10 seconds as compared to the original value outlined in the experimental section. As we discussed earlier in this Chapter, the BA-to-PI conversion process is retarded with pressure.

Overall, while exposed to 9.3 kbar of pressure, the BA/PI sample film was recycled in one series 5 times, each time at a slightly different temperature (see Table 5.12).

During the course of the experiment we looked for spectral evidence of any pressure- or light-induced degradation to the material in study throughout multiple irradiation and restoration events in the same sample film and we found no clues that could indicate fatigue of the sample material. It was advantageous

that the series took place within a hermetically sealed gasket compartment, without the possibility of oxygen to photobleach either BA or PI during illumination events.

At each temperature point, the spectral evolution was followed with time in absorption spectroscopy after which spectra were evaluated as already outlined in the experimental section. Each kinetic trace is at least 1500 min long with the longest lasting around 3000 minutes.

Temperature:	Rate constant k_1:	Rate constant k_2:	Contribution of k_1/k_2:
296 K	0.0343 min^{-1}	0.0012 min^{-1}	0.5/0.5
306 K	0.0437 min^{-1}	0.0012 min^{-1}	0.5/0.5
307 K	0.0478 min^{-1}	0.0012 min^{-1}	0.5/0.5
311 K	0.0270 min^{-1}	0.0012 min^{-1}	0.5/0.5
314 K	0.0494 min^{-1}	0.0012 min^{-1}	0.5/0.5

Table 5.12: The experimental parameters of the temperature-dependent PI-to-BA recovery at 9.3 kbar

The bi-exponential growth model presented earlier in this Chapter was applied with the same basic assumptions that were made for a recovery at high pressure (justified by the existence of two conformers of BA recovering at different rates). The kinetic traces and their bi-exponential fits are shown in

Figure 5.23. Once again, the crucial parameters were extracted from these fits and grouped in Table 5.12. Eventually, we applied the linear Arrhenius equation once more in which only the temperature- and pressure-dependent k_1 reaction rates constants were used to determine the free activation energy barrier.

Based on the experimental parameters from Table 5.12, the Arrhenius model predicts that the height of the energy barrier for the PI-to-BA conversion is around 7 kJ/mol at 9.3 kbar static pressure, as plotted in Figure 5.24. This change cannot be considered without comparison to the ambient pressure activation barrier height, 93 kJ/mol. The difference, more than 1 order of magnitude, is overall a dramatic reduction in the thermal energy required for the back reaction to take place. It also reassures us that PI/BA is truly a mechanophoric pair.

With the activation barrier reduced considerably at higher pressures, we can now replot our potential energy diagram for BA/PI system, Figure 5.25. We also could not rule-out an increase in the difference between the ground-state energies of BA with respect to PI at increased pressures which is reflected in the diagram.
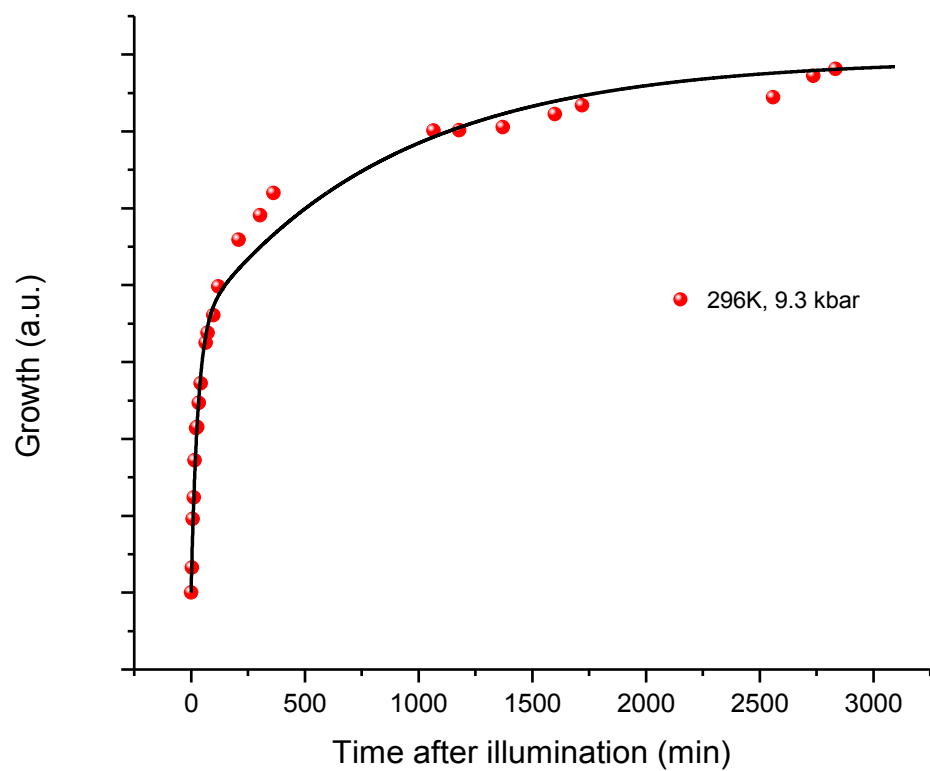
Figure 5.23: A representative temperature-dependent kinetic trace of PI-to-BA recovery at 9.3 kbar and its bi-exponential fit
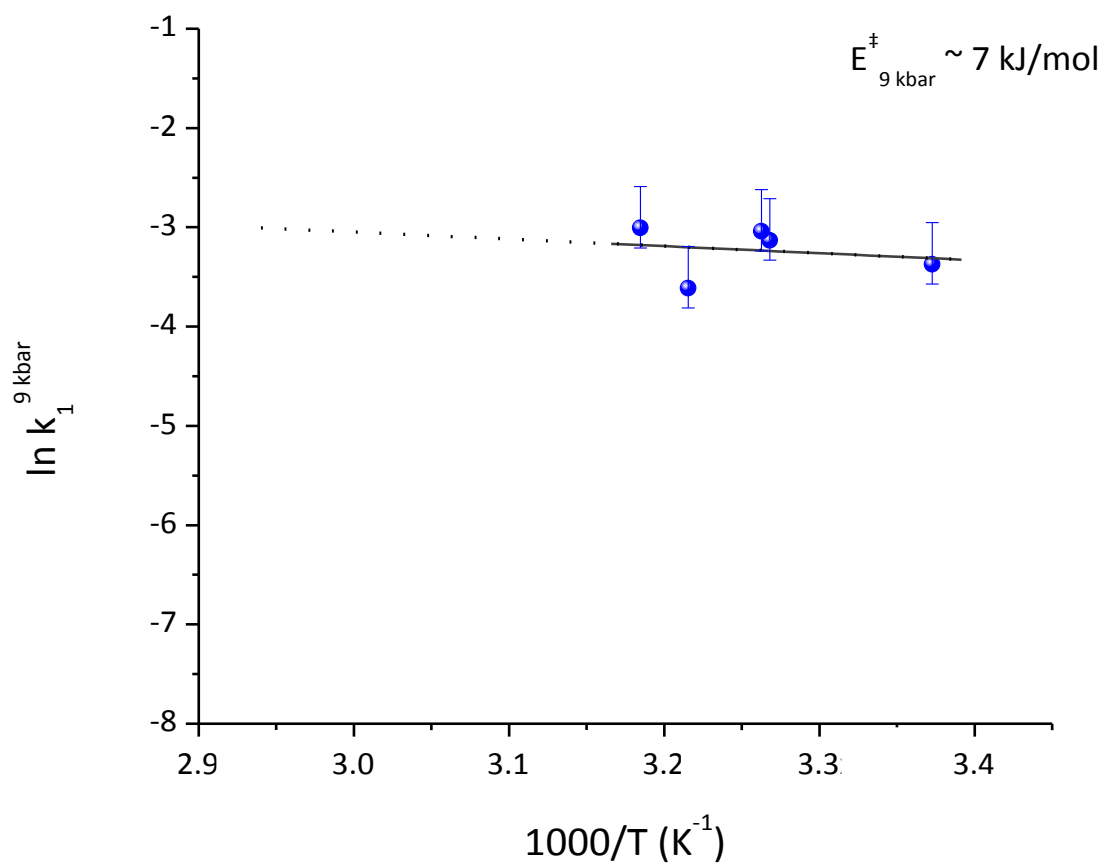
Figure 5.24: Linear Arrhenius model was fit to temperature-dependent rate constants; the extracted height of the activation energy barrier at 9.3 kbar is ~ 7 kJ/mol in the PI-to-BA process as opposed to 93 kJ/mol at ambient pressure
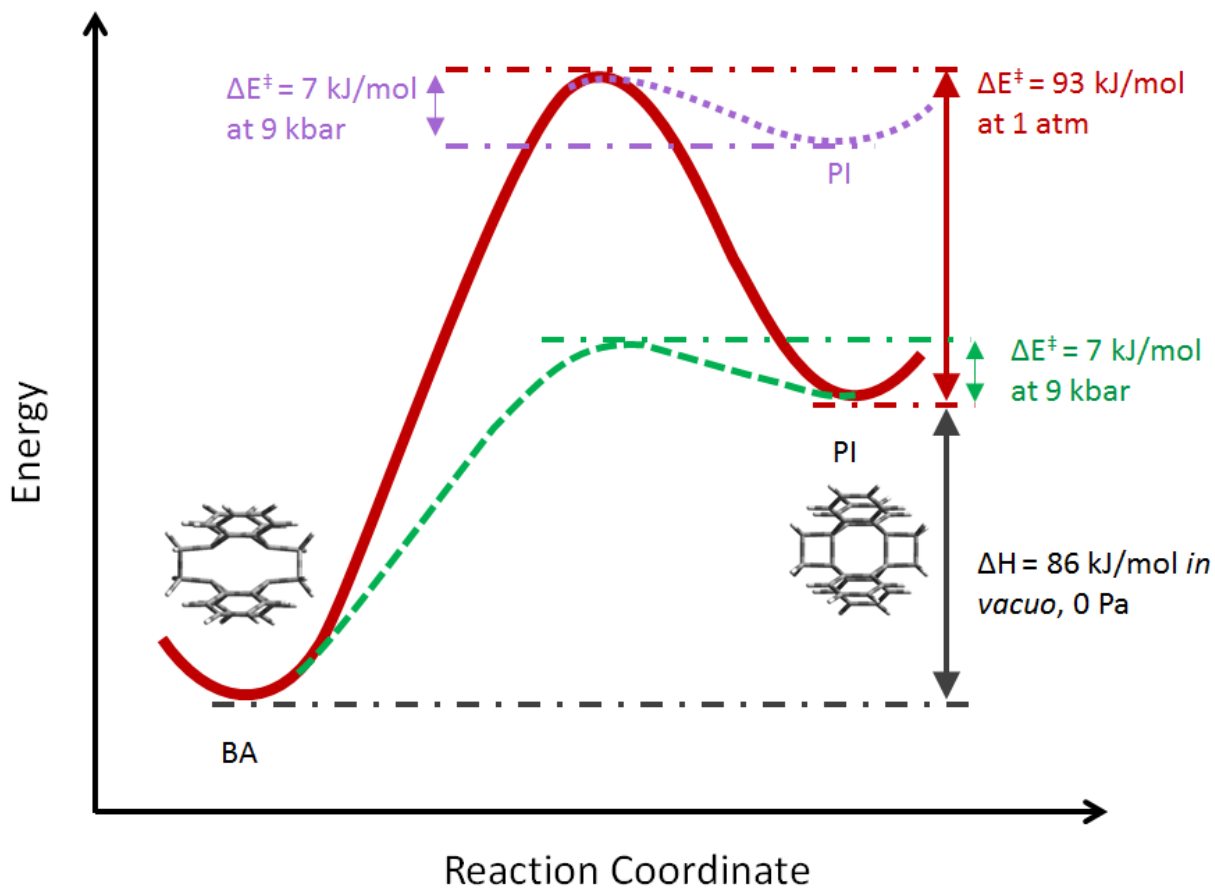
Figure 5.25: The updated version of the potential energy diagram for BA/PI system. The activation energy barrier is reduced at high pressure from 93 kJ/mol to ~ 7 kJ/mol at 9 kbar or the relative ground state energies of PI and BA have changed

5.2.7 Comparison to Selected, Geometrically-Strained Photoisomers

5.2.7.1 Dianthracene

Dianthracene (An_2) is the least geometrically-strained and linkerless photoisomer, which can be converted back to anthracene (An) by illumination with high-energy UV photons or by heating, insert in Figure 5.26, near its melting point ~ 200 °C. It shows relatively high barrier for the back-reaction (149-154 kJ/mol)[15,16] and atypically long carbon-to-carbon bonds between its reaction centers (162 Å). In the first experiment on the An/An_2 system we looked into conversion of An_2 by moderate heat in just the same way we were able to thermally revert PI back to BA.

Dianthracene dispersed in PMMA, 0.5% by weight, was heated up to 80 °C and changes in absorption were followed. Anthracene has very characteristic absorption spectrum, shown in Figure 5.26. Easy to spot spectral features between 300 to 390 nm would indicate that the back reaction (An_2-to-An) took place at elevated temperatures. The technical details of the set-up used in the temperature-dependent spectroscopic studies are described in the Appendix section.

The black spectrum in Figure 5.27 shows the absorption spectrum of a dianthracene/PMMA film at ambient conditions (temperature and pressure)

loaded into a DAC for an improved thermal contact. After 25 hours of heating (80 °C) to the dianthracene film, the red absorption spectrum in Figure 5.27 was recorded. We have not seen any changes indicative of dianthracene decomposition and the formation of anthracene at these conditions.

With our experimental set-up it was not possible to heat the sample film to temperatures that are known to thermally accelerate the back reaction in dianthracene (~ 200 °C). For a comparison, temperatures around 50 °C already cause the decomposition of PI back to BA within minutes at ambient pressure.

In this set of experiments, dianthracene film in PMMA was illuminated for ~ 5 minutes with monochromatic light, 250 nm, from a spectrometer (via grating, Xe lamp). The absorption spectrum after illumination, Figure 5.28, is dramatically different from the one before illumination in that new peaks indicative of anthracene being formed as a result of the illumination to An_2 film are shown.

The same film with partially restored An did not revert back to An_2 upon illumination with longer ~ 366 nm light for ~ 1 hour, Figure 5.29.
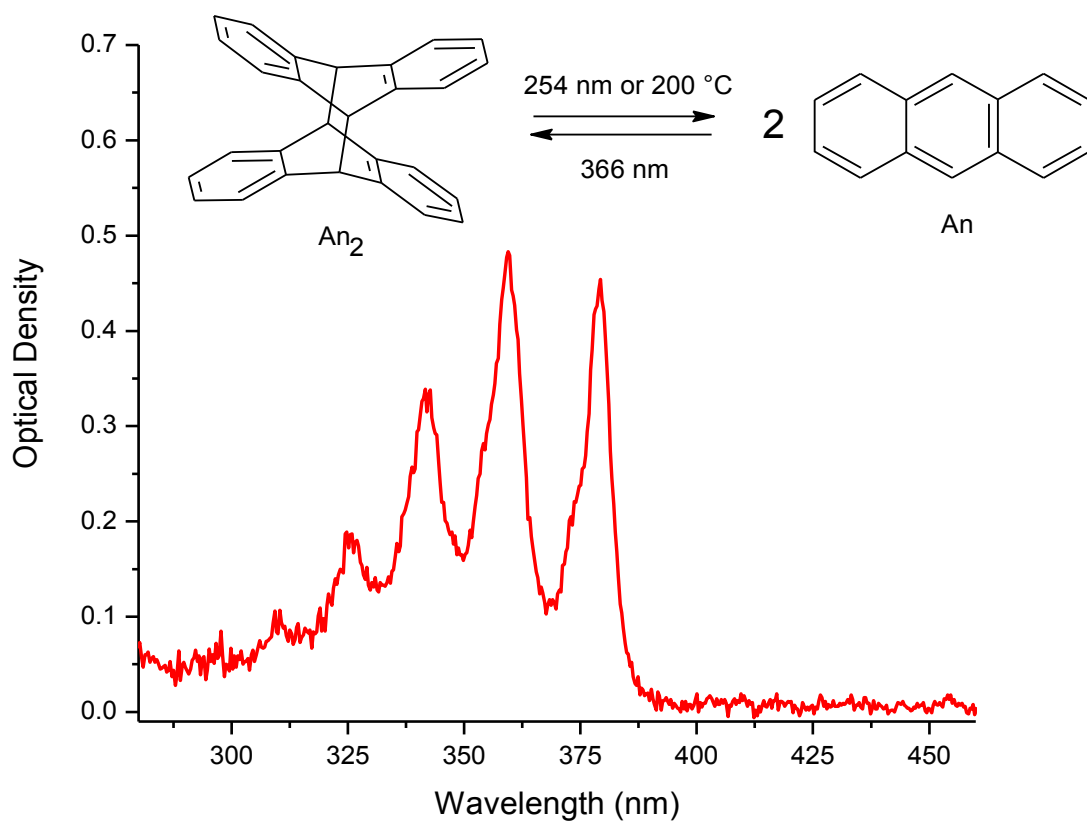
Figure 5.26: Absorption spectrum of anthracene. Insert: anthracene (An) dimerizes upon deep-UV illumination in solution with the formation of dianthracene (An_2). The reverse reaction takes place with even shorter wavelength illumination or with intense heating
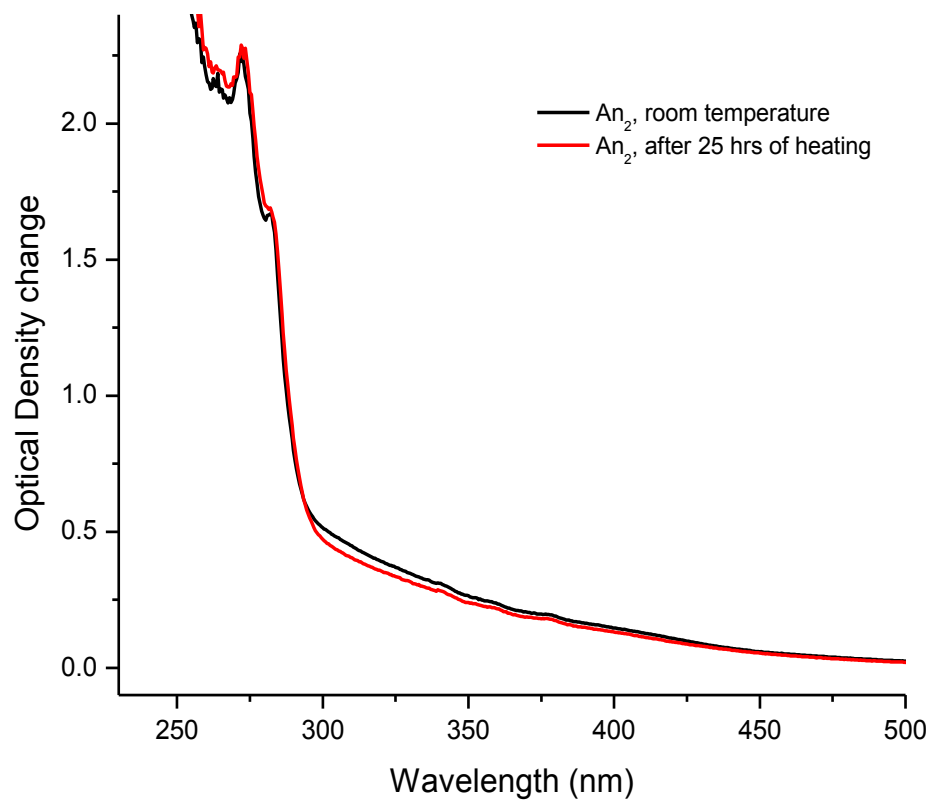
Figure 5.27: Absorption spectra of dianthracene in PMMA (uncorrected for DAC absorption) before (black) and after (red) heating for 25 hours at 80 °C. The absence of anthracene absorption between 300 – 390 nm indicates that no anthracene formed within the timeframe studied, as opposed to the thermally-induced PI-to-BA reaction (not shown)
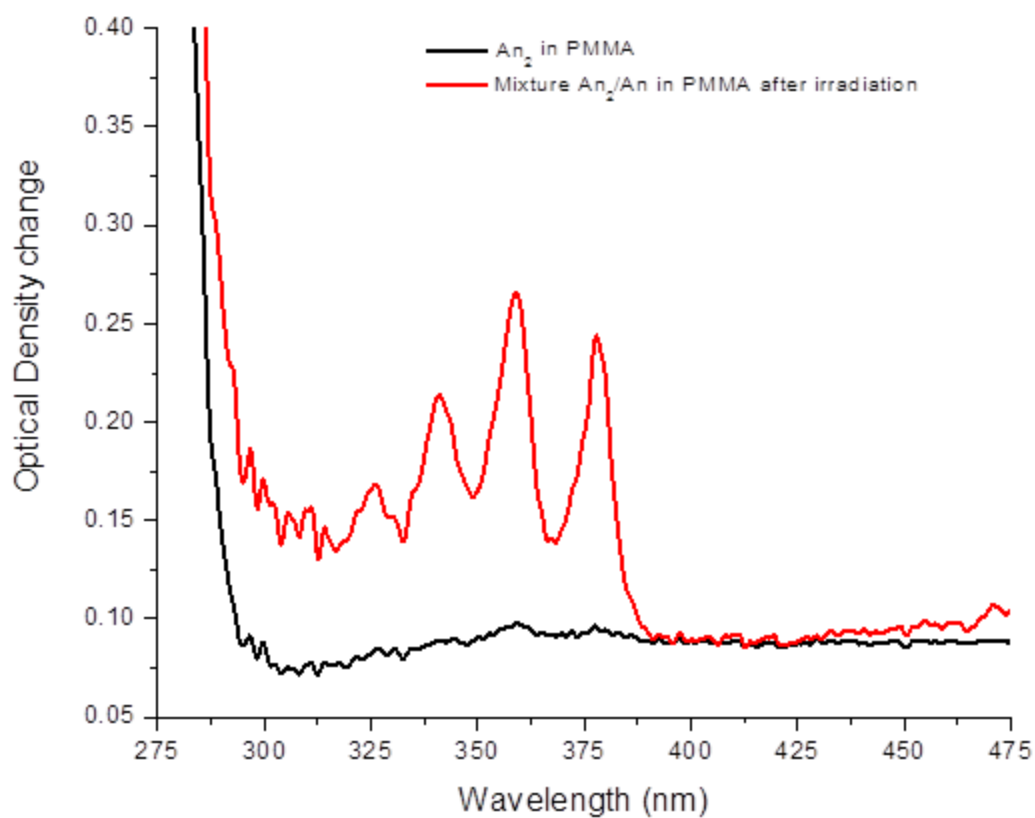
Figure 5.28: Absorption spectra of dianthracene/PMMA before, black, and after, red, brief illumination with a 250 nm light
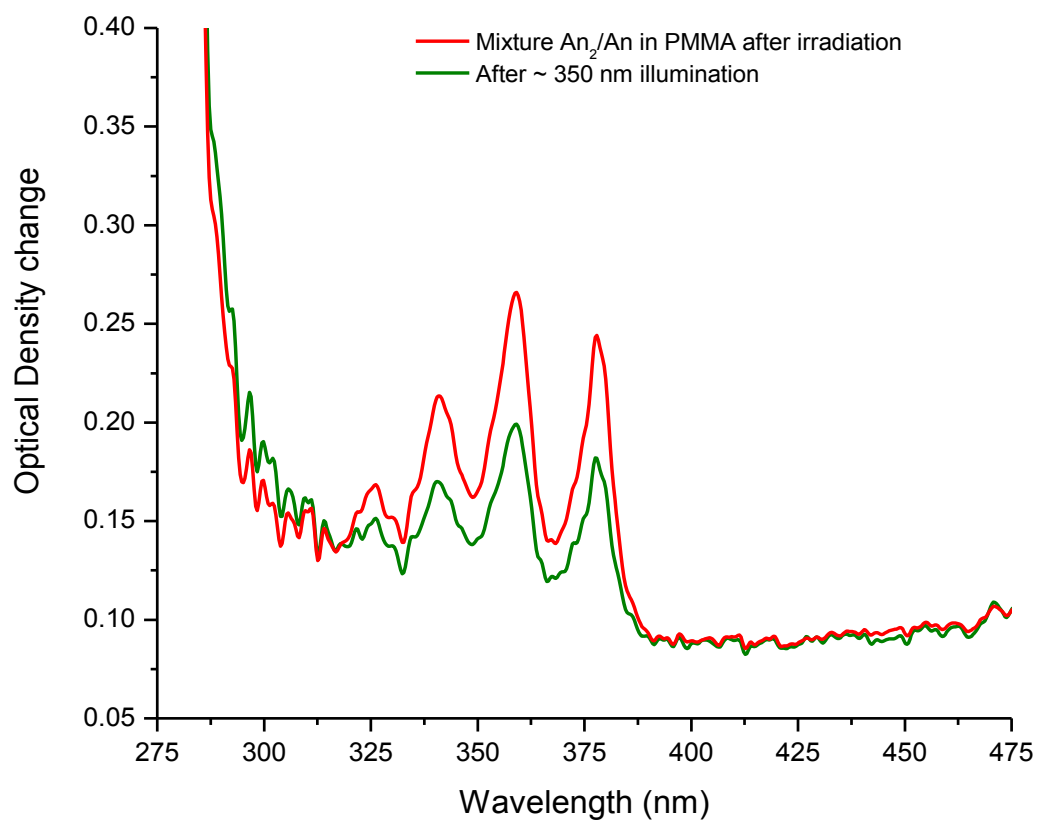
Figure 5.29: Absorption spectra of dianthracene/anthracene mixture in PMMA film as in previous Figure before (red) and after (green) illumination with 250 nm high-energy UV photons. Both spectra feature anthracene absorption peaks. The illumination lasted for ~ 1 hour

Anthracene/dianthracene at ~ 30 kbar

High pressure (~30 kbar) was applied to An_2 film in PMMA in a DAC for the duration of ~ 20 hours. After that time an absorption spectrum was recorded. There were no signs of anthracene being formed in the process at room temperature. An analogous experiment with films of An at high pressure (up to 30 kbar) did not yield An_2, spectra not shown.

To conclude our experiments on the An_2/An pair of photoisomers, we need to stress that in spite of the many similarities (mainly structural) to the BA/PI pair, there are very pronounced differences in the physical and chemical behavior between these related systems. An_2 is a more stable molecule ($t_{1/2}$ ~ $3*10^5$ years) than PI ($t_{1/2}$ ~ 2 weeks) and unresponsive to moderate, static pressures up to ~ 30 kbar.

5.2.7.2 Photoisomer of 9-Anthroic Anhydride

We also investigated some of the spectral properties of a related cyclophane, 9-anthroic anhydride, and its [4+4] photoisomer, Figure 5.30, generously received from Dr. C. Bardeen. This cyclophane is composed of two anthracene moieties bound by a single anhydride linker, R-(C=O)-O-(C=O)-R.

Preliminary absorption data suggest that very mild spontaneous recovery at ambient conditions (temperature and pressure) might occur within ~ 4 weeks in a cyclohexane solution between 200-250 nm, Figure 5.31. We also dispersed some of the photoisomer in Zeonex polymer and produced polymer films. 18.7 kbar static pressure was applied to the film in DAC for a duration of 19 hours. Unfortunately, we have not observed any changes that may suggest that a pressure-assisted recovery occurred in this photoisomer (data not shown).
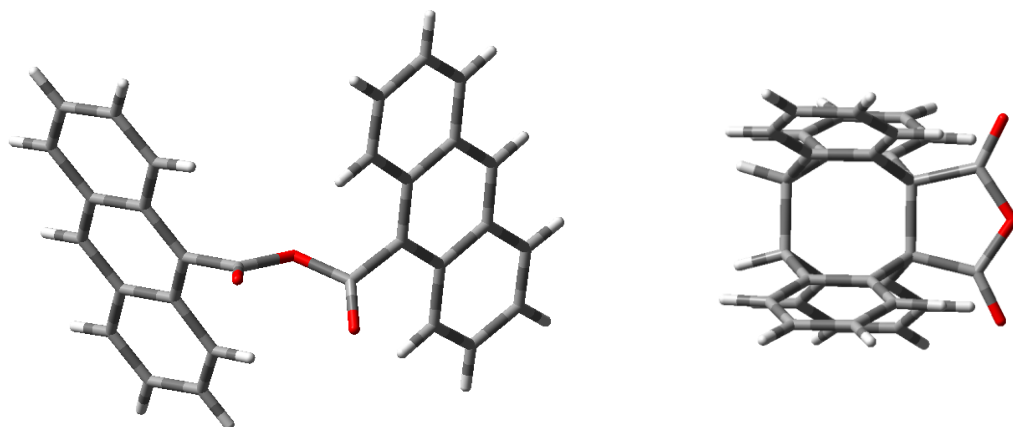
Figure 5.30: The structures of 9-anthroic anhydride[19], IFIGEJ, left, and its [4+4] intramolecular photoisomer, right. Oxygen atoms are marked in red
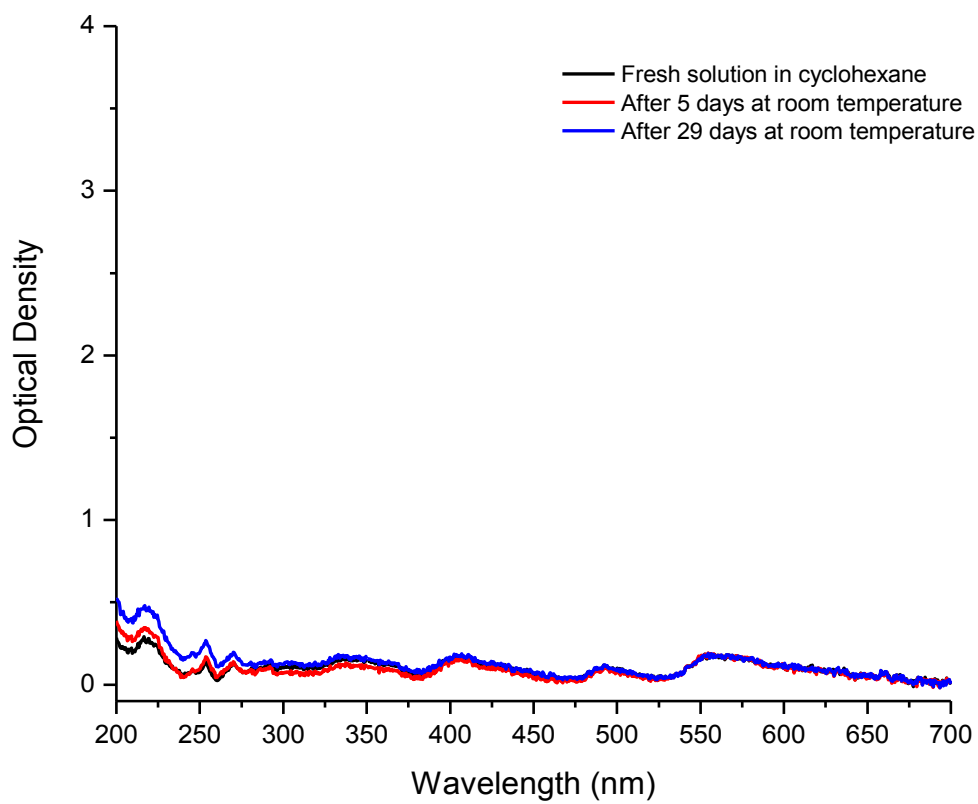
Figure 5.31: The mild spectral evolution observed in the solution of the 9-anthroic anhydride photoisomer in cyclohexane within 29 days and at ambient conditions evaluated in absorption

5.2.7.3 Dewar Photoisomer

9-tert-butylanthracene undergoes reversible photoisomerization upon illumination with UV light into Dewar's product[20], Figure 5.32. The back-reaction occurs spontaneously at room temperature within hours. The structure of 9TBA involves only one anthracene moiety bound to a tert-butyl group in the 9-position and as a result of the the intramolecular photoisomerization, significant, structural rearrangements occur in this photoisomer, Figure 5.33, coupled with a rehybridization on two carbon atoms. Upon illumination, the central ring loses its aromaticity with the formation of an unusually long (162 pm[21], same length as in An_2) covalent C-C bond and two distorted cyclobutane units around two highly strained sp^3 carbon atoms, Table 5.13. Also, the nearly flat anthracene moiety in 9TBA becomes heavily bent upon isomerization. With our experience with the BA/PI pair of photoisomers we tested the 9TBA/Dewar response to pressure in a polymer (polystyrene) film. The 9TBA samples already dispersed in a polystyrene were received from Dr. Chris Bardeen, University of California, Riverside.

In much the same way as for the BA/PI pair, we calculated the molecular volumes for each isomer and compared them to the crystallographic values[21] in Table 5.14.

The calculated and experimental molecular volumes are similar to each other for the 9TBA (difference ~ 2.1 Å^3) and slightly different for the Dewar photoisomer (difference ~ 11.3 Å^3). The crystallographic data[21] indicate that the molecular volume of the photoisomer (Dewar) is slightly higher than that of the 9TBA by ~ 2.8%.

The film of 9TBA dispersed in polystyrene was illuminated at ~ 360 nm until no further drop in intensity of the absorption band between ~ 300 – 500 nm was observed, Figure 5.34. The absorption of the Dewar photoisomer is located beyond the possibility of the absorption spectrometer, below 230 nm.

Once only the Dewar photoisomer was present within the polymer film, we followed the recovery kinetic traces at three distinct pressures with absorption spectroscopy, Figure 5.35. The evaluation of the absorption spectra was performed with the use of a numerical integration method, the trapezoidal rule, between 300-500 nm. The optical arrangement was identical to the one described for the BA/PI. All absorption experiments of 9TBA/Dewar films described in this section were performed in DAC, at room temperature and with the use of Varian Cary 500 spectrometer.

A fitting procedure on the kinetic traces was performed. With the least-square method we attempted fitting monoexponential functions as well as, in a separate trial, bi-exponential growth functions for each pressure, as described in the earlier sections in this Chapter. The resulting fitting parameters are grouped in Table 5.15.

	An$_2$	PI	Dewar	9-anthroic anhydride photoisomer
C-C distance (X-ray)	162 pm[9]	165 pm[8]	162 pm[21]	161 pm[19]
γ angle	106.1°	86.2°	85.6°	103.0°

Table 5.13: The longest C-C bonding distances and γ angles in the four photoisomers. The γ angle is the smallest angle around the strained sp^3-hybridized carbon atom and describes the strain upon illumination: the lower the value, the more strained the angle

	9TBA	Dewar
Crystallography[21]	325.32 Å^3	334.55 Å^3
Calculations (DFT-D)	323.21 Å^3	323.25 Å^3

Table 5.14: Experimental and calculated molecular volumes for 9TBA and the Dewar photoisomer. The standard deviations are 1.20 and 1.32 Å^3, respectively. The R-Factors are 4.0% and 3.8%, respectively

	Monoexponential k	Bi-exponential	
		k_1	k_2
0.0 kbar	0.0010 min^{-1}	2.8e-5 min^{-1}	0.004 min^{-1}
4.2 kbar	0.0026 min^{-1}	9.0e-4 min^{-1}	0.014 min^{-1}
13.2 kbar	0.0048 min^{-1}	2.6e-3 min^{-1}	0.039 min^{-1}

Table 5.15: The fitting parameters extracted from the kinetic pressure-dependent traces on the 9TBA/Dewar pair of isomers in polystyrene

While we cannot present any molecular model to justify the bi-exponential growth observed in the film of the Dewar isomer, in Figure 5.36 we plotted the derivative of the bi-exponential growth function with respect to the time on a logarithmic scale.

It has been observed in the group of Dr. C. Bardeen that the illumination times aimed at photoisomerization (from 9TBA to Dewar) are significantly increased at higher pressures. This observation correlates well with a similar pressure effect in the light-induced intramolecular isomerization of the linked anthracenes in the BA-to-PI reaction.

One significant difference however between the linked anthracenes studied in this Chapter and the 9TBA/Dewar pair is the retardation of the recovery process with pressure in the latter system. The preliminary results indicate that the higher the pressure the slower (times > ~1000 min) the kinetics of the recovery to 9TBA in polystyrene, at room temperature.
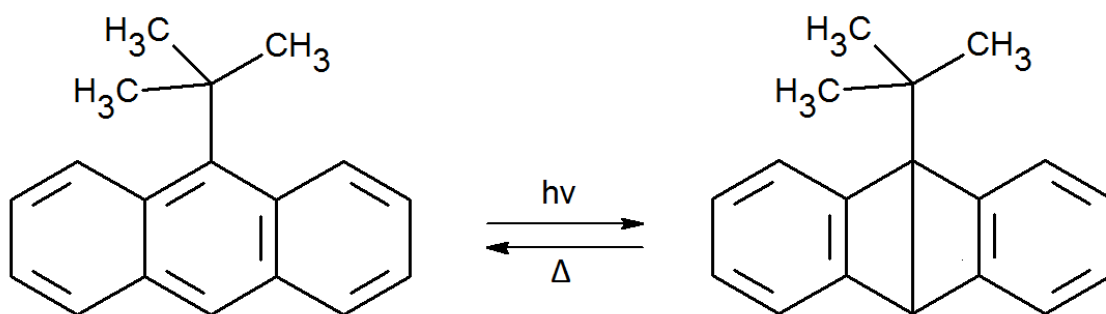
Figure 5.32: The reversible photoisomerization of 9TBA, $C_{18}H_{18}$, into Dewar's photoproduct. The reaction is reversible at room temperature within hours
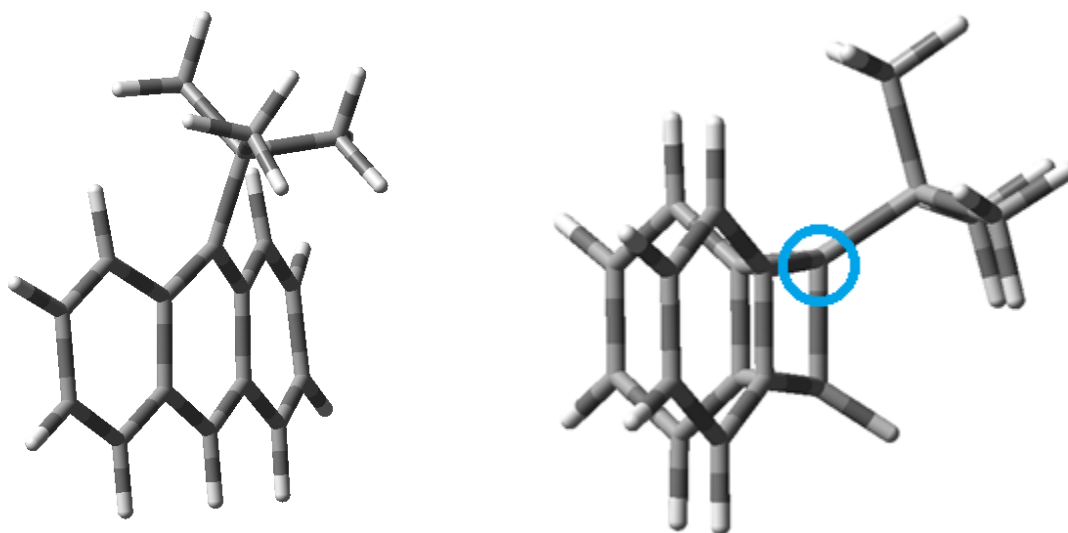
Figure 5.33: The geometries of 9TBA, left, and the Dewar photoisomer. Their CSD designators are CIVMOJ10 and CIVMUP10, respectively[21]. The blue ring marks the position of one of the strained sp^3-hybridized carbon atoms
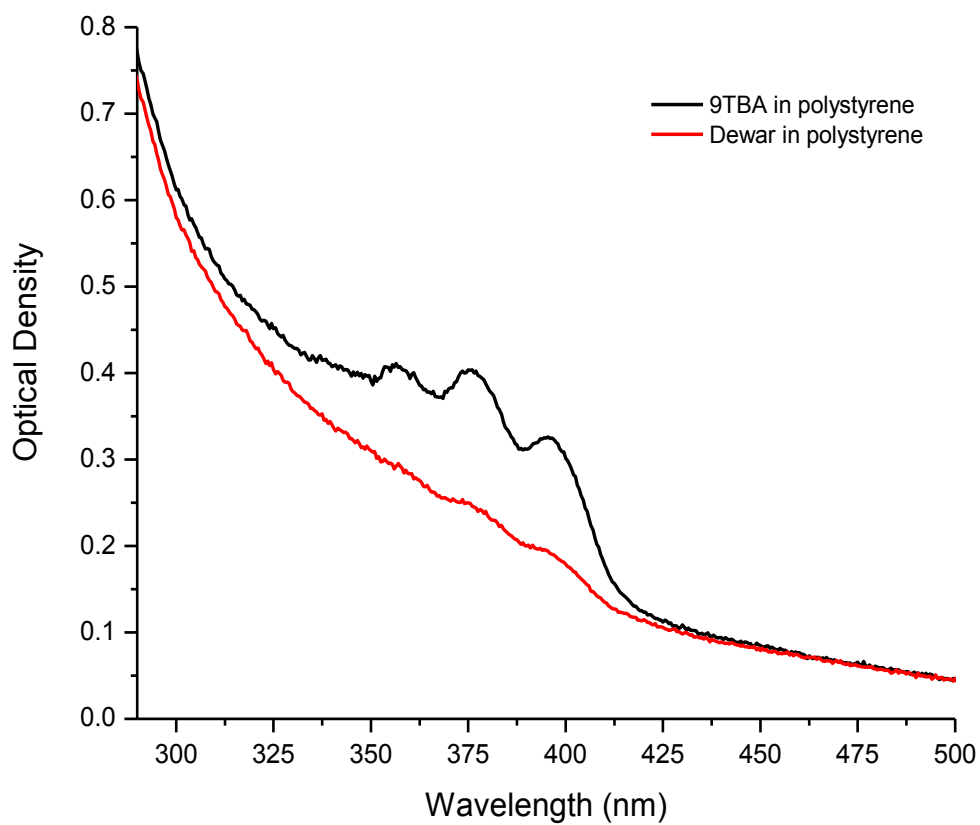
Figure 5.34: Uncorrected for the diamond absorption spectra of 9TBA in polystyrene, in DAC, black, before and after UV light illumination with the formation of the Dewar photoisomer, red spectrum
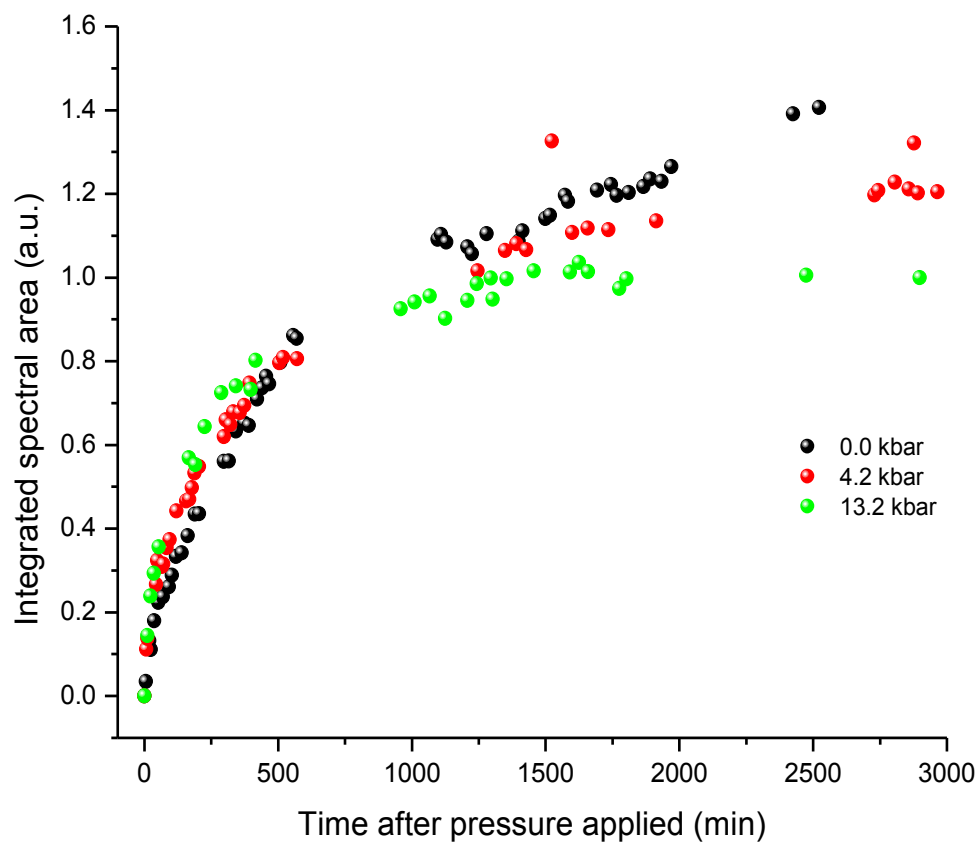
Figure 5.35: Normalized pressure-dependent kinetic traces for the recovery of the Dewar photoisomer back to 9TBA measured in a polystyrene film in DAC at room temperature
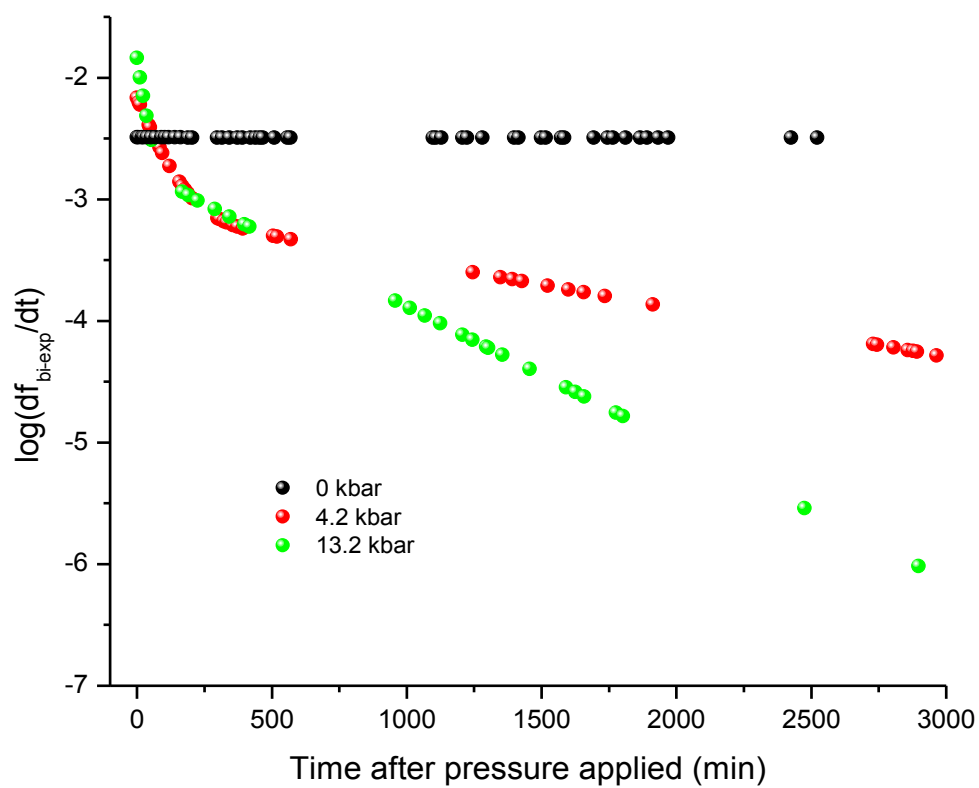
Figure 5.36: Plot representing the differences in the kinetics of the recovery of 9TBA as a function of time. The recovery of 9TBA is retarded at higher pressures. Plot is based on the bi-exponential growth function fitting parameters from Table 5.15

5.2.8 The Two-Step Model for the Back-Reaction in Bis-Anthracene Induced by Mechanical Strain

A model has been drawn to explain the pressure-induced back-reaction observed in PI induced by homogeneous pressure on the molecular level. As shown earlier in this Chapter, the lowering of the activation barrier at higher pressures by more than an order of magnitude along with the negative activation volume by - 3 % both suggest that this is the transition state that is most sensitive to pressure. Molecular volume calculations that we have performed did not show any significant differences in molecular volumes that would account for the changes that have been observed.

For the transition state to have smaller volume than the reactant molecules, PI, the aromatic moieties have to flatten prior to rehybridization and dissociation. The decrease in the butterfly angle precedes the cleavage of the carbon-to-carbon covalent bond within the cyclobutane rings attached at either side, Figure 5.37. Once the molecular volume decreased, the reaction continues rapidly, ending with the fully restored, flattened anthracene moieties in BA and two covalent bonds cleaved in this reversible process.
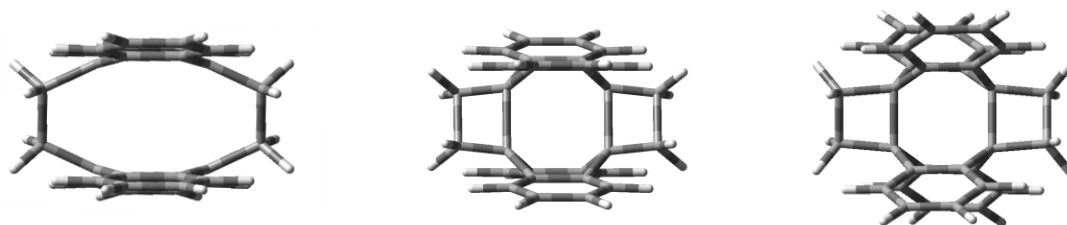
Figure 5.37: An illustration of the structures of bis-anthracene, left, the transition state, middle, and the strained photoisomer, right. The postulated transition state consists of nearly flat aromatic planes coupled to two cyclobutane rings at either side

5.2.9 Engineering the Desired Thermodynamic Parameters in Linked-Anthracenes

We performed molecular simulations showing that the enthalpy and thus the magnitude of the heat released in the back-reaction can be tuned with the length of the tethering linkers. Usui *et al.* were also able to demonstrate[11] that the heat evolved, or supplied, depends of the type of groups attached to the linker.

Without appropriate experimental work, we can only speculate on the thermodynamic properties of linked anthracenes upon modification. We strongly believe however that with carefully designed molecular engineering techniques it is possible to further improve many properties of these systems, for instance the enthalpy of the back reaction. We think that this can be achieved by manipulating

the length of the aliphatic linkers. In addition, substituting other heteroatoms into the linker will have pronounced effects not only on the thermodynamics of the back-reaction. The thermal stability at ambient conditions will be affected as well, Figure 5.38, as we learned from experiments on the photoisomer of 9-anthroic anhydride presented in this Chapter in which the lack of an additional "straining" linker on one side greatly prolongs the $t_{1/2}$ time of the photoisomer when compared to PI.

By decorating the linkers with bulkier groups, Figure 5.39, for instance within the tert-butyl group, we could possibly achieve increased sensitivity to pressure and when combined with a longer linker, achieve increased thermodynamic stability at ambient conditions at the same time.

We also postulate that it is possible to increase the spectral overlap between the absorption and the solar emission spectrum for energy harvesting purposes. By replacing anthracene molecules with tetracene or pentacene aromatic moieties, Figure 5.40, the absorption properties of these modified linked systems will be extended towards the lower energy end of the spectrum. We envision that the ability for these systems to undergo [4+4] photoisomerization will be preserved.

It is also possible to utilize BA and its photoisomer in stress-sensing and self-healing materials. This project would involve advanced work aimed at the incorporation of these mechanosensitive units into a polymer backbone. Once

the damage has incurred, such functionalized polymer can be restored back to its

sensing state through illumination with light.
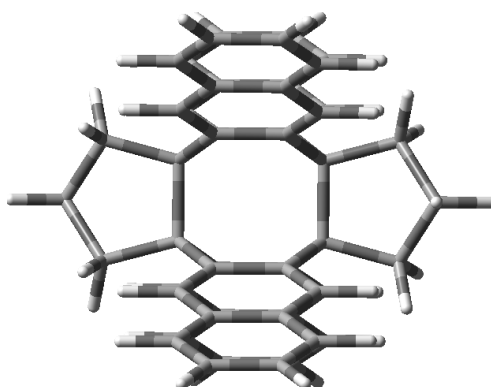
Figure 5.38: The thermal stability of the photoisomer at ambient condition can be tuned by affecting the length of the linker
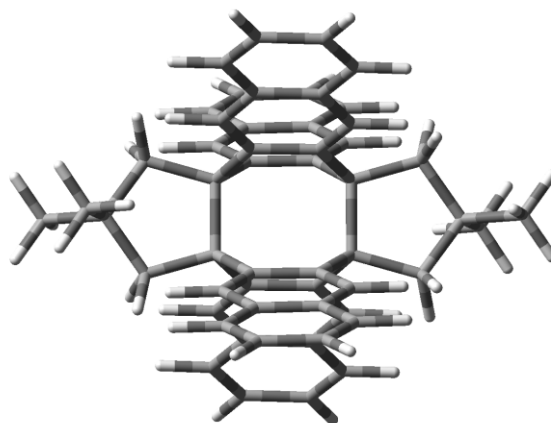
Figure 5.39: The increased sensitivity to pressure can be engineered by decorating the linkers with bulky groups, such as the tert-butyl group
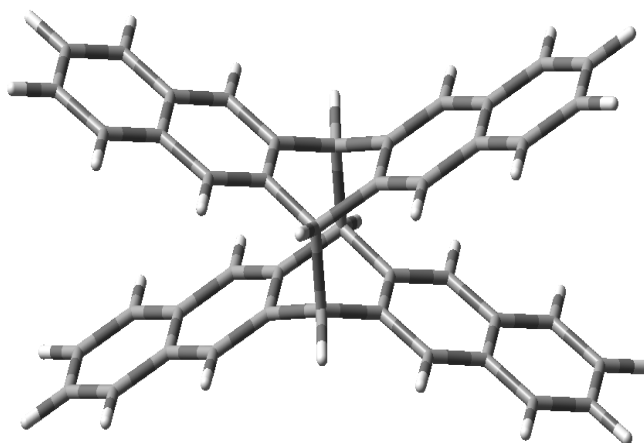
Figure 5.40: Increased conjugation in the aromatic moieties (here pentacene) will enhance the spectral overlap with the solar emission spectrum

5.2.10 Possible Applications

5.2.10.1 Solar Energy Conversion Recycled by Pressure

Linked anthracenes along with other photoisomers with relatively large enthalpies for their back-reactions used to be of interest as solar harvesting and clean energy conversion materials[14]. The principle of operation is a fairly simple one: the solar energy is converted into its chemical form by means of high-energy covalent bond formation induced by photons. The chemical energy can be stored and eventually released in the form of heat at elevated temperatures in

the most convenient moments of time. No pollutants are produced at any stage and no CO_2 is released from the plant as these chemical fuels are fully regenerated in a closed cycle. A few requirements need to be fulfilled for a system to qualify for such use as "chemical fuel". First of all, the reversibility of these reactions is the most important criterion. The forward reaction must be induced by light and the back-reaction with heat in a closed-cycle. The addition of a catalyst for the back-reaction is allowed but is not favored as an efficient purification procedure needs to be deployed. Other criteria are the magnitude of the enthalpy of the back-reaction, the quantum efficiency, the spectral overlap with the emission spectrum of the Sun and the ease of operation. It comes without saying that the costs associated with the use and storage of the chemical fuel play an important role as well.

A schematic transducer that converts the solar energy into heat has been outlined by G. Jones[14] *et al*. In literature devoted to the solar energy conversion by chemical methods, a new term has been coined: the energy density per molecule. Bis-anthracene and its photoisomer, along with other systems have been considered as possible chemical fuels, capable of recycling solar energy, with conveniently high energy densities.

In this Chapter we have been able to demonstrate that high pressure acts like a switch in a bis-anthracene photoisomer, PI, releasing the stored energy as heat at room temperature, without the need for a catalyst. This trigger has its

advantages as well as drawbacks as compared to the heat-induced recycling. The induced-by-pressure reaction is reversible as well and the fuel can operate in a closed cycle. There is no need to purify neither the reactants nor products. As speculated in an earlier section of this Chapter, it is possible to engineer greater sensitivity to pressure and modify the enthalpy for the back-reaction in linked anthracenes. We also envision some problems that may inhibit the development of this field such as the limited solubility of linked anthracenes in most organic solvents. It is necessary therefore to maintain close collaboration between engineers and organic chemists to overcome similar issues.

5.2.10.2 Strain and Damage Sensing

The process of coupling the mechanical energy to structural response has been facilitated by the incorporation of mechanophoric units into a polymer backbone[17] to give rise to materials that send warning signals before a structural damage occurs. A change in color is probably the easiest to detect. The other possibilities span from the differences in emission to differences in the Raman spectrum. Such functionalized polymers may be incorporated into parachute cords, airplane wings, climbing ropes, paintings and smart coatings in the years

to come. The most well-known example of a mechanophoric, ring-shaped unit, is the ring-opening reaction in spiropyrans[3]. As a result of the reversible, force-induced reaction, the functionalized polymers turn purple-red from initially colorless just before they snap. Now we know that the shape of a ring is not a prerequisite for molecules to act as mechanophoric units. The BA/PI pair of mechanophores undergoes reversible covalent-bond scission at low stress conditions with the change in absorption (from orange to yellow in their free state) and in emission spectrum.

5.2.10.3 Mechanically-Activated Nanoheater

We propose to couple other chemical reactions to PI while converting back to BA upon the application of mild pressure. The (solar) energy accumulated within a molecule of PI, Figure 5.41, can be represented as a potential energy stored within a compressed helical spring (red). The application of pressure is the trigger for opening the latches and relaxing the strained spring (blue). Mild pressure releases the stored chemical energy in the form of heat and provides a modest amount of thermal energy which can be coupled to reactions that are induced by heat and not by light. These "nanoheaters" based on the

reversible process that occurs in linked anthracenes such as BA/PI, are triggered by mild pressure and can operate in a closed cycle.
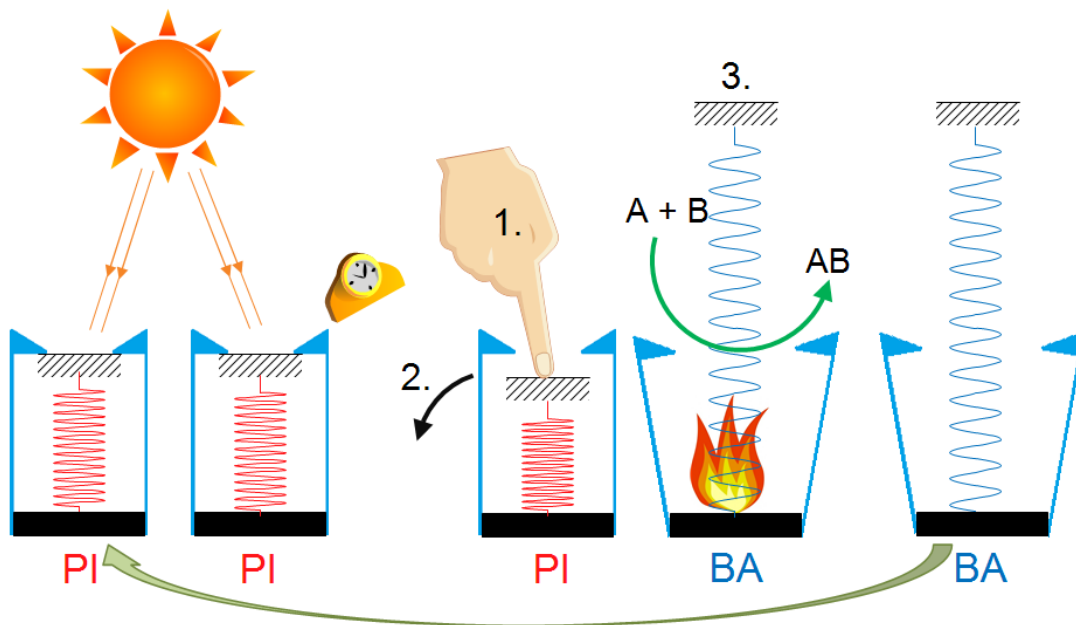
Figure 5.41: PI molecule is represented in this illustration as a compressed helical spring. Pressure (1.) releases the latch (2., breaks covalent bonds) and the spring relaxes (3.), expelling enough heat to induce chemical reactions between the A and B reactants with the formation of a product, AB. The enthalpy of the back-reaction can be tuned with molecular engineering techniques accordingly

5.3 Summary and Conclusions

In this Chapter we reported on the mechanically-activated shifting of the equilibrium between two isomers of BA coupled with a covalent carbon-to-carbon bond scission and simultaneous rehybridization on four equivalent carbon atoms. We also compared our results to several other photoisomers.

Many organic molecular systems do not display mechanical action via selective bond breaking up to at least 100 kbar. The observed covalent bond scission in PI not only occurs at mild pressures but is also selective and reversible with light.

The BA/PI system already found its applications in the industry as early as in 1979. A patent was filed for the "Optical display system based on the photoisomerization of anthracene cyclophanes". It makes use of the heat-induced back-reaction occurring within an optical display. Writing on such device is accomplished with an intense light source, converting the orange BA into the bright-yellow PI. The restoration is accomplished by heat.

Adding mild pressure to the list of the thermodynamic parameters that induce the back-reaction, greatly enhances the applicability of this mechanophoric pair of organic molecules. Earlier in the Chapter we were able to demonstrate through absorption spectroscopy that the BA/PI pair can be

recycled multiple times in a Zeonex polymer without affecting its efficiency through degradation. We irradiated BA at 9 kbar static pressure and let it recover at various temperatures. This experiment allowed us to determine that the barrier of activation is significantly lowered in the back-reaction at higher pressures.

Through a set of experiments we found a negative activation volume in the PI-to-BA process induced by pressure. On the contrary to our observations, negative activation volumes are normally observed in reactions in which new covalent bonds are formed. The example of a photoreaction in which the rate of dimerization is increased with pressure is the [4+4] dimerization of methyl 3-methoxy-2-napthoate. The forward dimerization reaction in napthoate shows negative activation volume as a result of new C-C covalent bonds being formed.

Through sonication experiments we found out that the heat generated by the collapse of the cavitation bubbles may actually contribute not only to the restoration of BA from its photoisomer but also to the irreversible disintegration of bis-anthracene. We also independently observed that shear deformation accelerates the back-reaction in a straightforward experiment that involves mortar and a pestle.

When heated, PI first decomposes reversibly to BA with the release of heat and at even higher temperatures, BA pyrolyzes possibly with the release of acetylene. Out of the four types of photoisomers studied in this Chapter, two showed unusually strained angles around some of the sp^3 hybridized carbon

atoms - PI and the Dewar compound, both ~ 86°. These two showed the kinetics of photoinduced isomerization of their unreacted forms to be pressure-dependent. The intramolecular photoisomerisation reactions are retarded in both BA and 9TBA. Once in their reacted forms, it is only PI however that shows dramatic acceleration of the recovery in the early stages when subjected to high, homogeneous pressure in DAC. On the contrary, the recovery of 9TBA from the Dewar photoisomer is retarded mostly in the final stages (above 1000 min) of the pressure-induced back-reaction.

PI shows close structural resemblance to An_2 but manifests very different behavior when exposed to thermodynamic stimuli. While PI can be converted back to its unreacted form by very mild heating and pressure, Figure 5.42, An_2 can only revert back with deep-UV illumination or temperatures as high as ~ 200 °C, showing no pressure dependent recovery at least up to 30 kbar.

The emission spectra of BA in cyclohexane can be explained in terms of at least two unreacted photoisomers present in the solution. We also can see a maturation process occurring in the BA solution with time. This observation needs more detailed investigation. We can only speculate that perhaps a polymerization observed by Golden[7]. may take place between the molecules of BA in a solution of cyclohexane.

Unlike most other mechanophores reported in the literature to date, BA is a non-spiropyran based, solely hydrocarbon, with no heteroatoms present in its

structure. Bis-anthracene displays topologically-favorable arrangement of the two anthracene moieties for the [4+4] intramolecular photoisomerization. The aromatic units are tethered in a face-to-face alignment with respect to each other, at short distances.

Overall, we are positively surprised to have observed mechanochemical action within DAC, with homogeneously redistributed pressures up to 73 kbar. Up till now there were no reports of covalent bond breaking at moderate, homogeneous pressures induced within DAC. Along the experimental work on the BA/PI pair, we found the Zeonex polymer to be relatively stable at that pressure range and most importantly, unlike most other polymers, it allowed us to probe spectral properties of BA down to ~ 230 nm.

We think that certain properties of mechanophoric systems such as the sensitivity to pressure, stability at ambient conditions and the absorption profile can be further enhanced with molecular engineering. One day we may even be able to build a solar power-plant which utilizes BA-based solution to store and recycle the energy provided by the Sun in the form of heat. By the time this futuristic vision becomes a reality, we will most likely use mechanophores ourselves in applications that require damage sensing and as an integral part of intelligent materials, undergoing the process of self-healing.
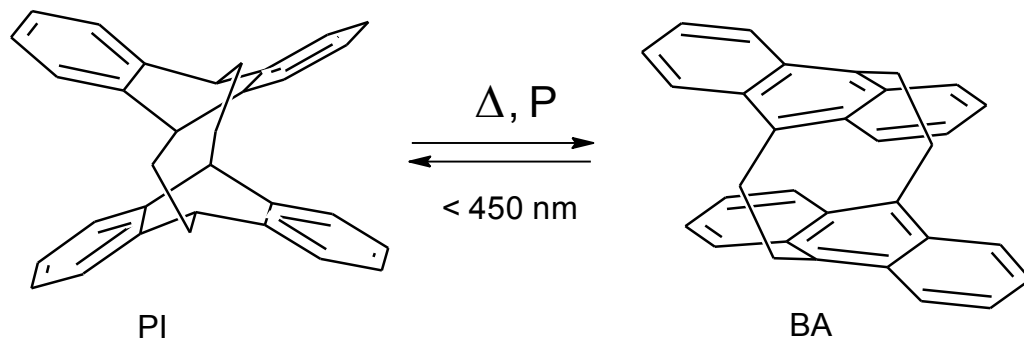
Figure 5.42: The PI-to-BA back reaction can be initiated with heat and mild pressure

5.4 References

(1)   Beyer, M. K.; Clausen-Schaumann, H. *Chemical Reviews* **2005**, *105*, 2921.
(2)   Karthikeyan, S.; Sijbesma, R. P. *Nat Chem* **2010**, *2*, 436.
(3)   Davis, D. A.; Hamilton, A.; Yang, J.; Cremar, L. D.; Gough, D. V.; Potisek, S. L.; Ong, M. T.; Braun, P. V.; Martinez, T. J.; White, S. R.; Moore, J. S.; Sottos, N. R. *Nature* **2009**, *459*, 68.
(4)   Berg, O.; Chronister, E. L.; Yamashita, T.; Scott, G. W.; Sweet, R. M.; Calabrese, J. *J Phys Chem A* **1999**, *103*, 2451.
(5)   Tanaka, F.; Sasaki, M.; Osugi, J. *Rev Phys Chem Jpn* **1972**, *41*, 18.
(6)   Hamann, S. D.; Linton, M.; Sasse, W. H. F. *Aust. J. Chem.* **1980**, *33*, 1419.
(7)   Golden, J. H. *Journal of the Chemical Society* **1961**, 3741.
(8)   Trzop, E.; Turowska-Tyrk, I. *Acta Crystallogr B* **2008**, *64*, 375.
(9)   Choi, C. S.; Marinkas, P. L. *Acta Crystallogr B* **1980**, *36*, 2491.
(10)   Jezowski, S. R.; Zhu, L. Y.; Wang, Y. B.; Rice, A. P.; Scott, G. W.; Bardeen, C. J.; Chronister, E. L. *J Am Chem Soc* **2012**, *134*, 7459.
(11)   Usui, M.; Shindo, Y.; Nishiwaki, T.; Anda, K.; Hida, M. *Chem Lett* **1990**, 419.
(12)   Mau, A. W. H. *Journal of the Chemical Society-Faraday Transactions I* **1978**, *74*, 603.
(13)   Dunand, A.; Ferguson, J.; Puza, M.; Robertson, G. B. *Chemical Physics* **1980**, *53*, 225.
(14)   Jones, G.; Reinhardt, T. E.; Bergmark, W. R. *Sol Energy* **1978**, *20*, 241.
(15)   Bendig, J.; Buchwitz, W.; Fischer, J.; Kreysig, D. *J Prakt Chem* **1981**, *323*, 485.
(16)   Greene, F. D. *Bulletin De La Societe Chimique De France* **1960**, 1356.
(17)   Potisek, S. *Mechanophore-linked polymers for studying mechanochemical response*; ProQuest LLC, 2008.
(18)   Yang, N. C.; Shold, D. M.; Kim, B. *J Am Chem Soc* **1976**, *98*, 6587.
(19)   Cicogna, F.; Ingrosso, G.; Marchetti, F. *Acta Crystallogr C* **2002**, *58*, O359.
(20)   Minaylov, V. V.; Gurman, V. S.; Vorobiev, A. K. *J Photoch Photobio A* **1995**, *87*, 67.
(21)   Angermund, K.; Claus, K. H.; Goddard, R.; Kruger, C. *Angew Chem Int Edit* **1985**, *24*, 237.

APPENDIX

A.1 The Fast MOSFET Piezoelectric (PE) Actuator Driver

The main features of the custom-made MOSFET PE driver include:

- Fast operation: within only 80 µs the output signal changes from 0V to 130V on each 7 µF PE, provided a TTL-shaped input signal; in combination with the 2nd generation dDAC, compression rates up to 1400 GPa/s can be reached;

- Wide range of operation: 0V to 200V;

- Each PE is driven by an identical, separate MOSFET stage;

- Separate output for voltage control;

- Embedded circuitry to promptly discharge the PE capacitance during the OFF state;

- Embedded high-voltage AC to DC converter;

- Galvanically isolated mains voltage from the TTL-input signal and from the TRIGGER OUT signal;

- Galvanically isolated TRIGGER IN and TRIGGER OUT signal;

- BNC connectors for ease of operation; two fuses built-in;

- Various modes of operation (see description);

The MOSFET PE driver described in Chapter 3 can be driven by TTL-like (fast rise time, square wave only) input signals from 5 up to 9V. The high-voltage output signal is designed to charge up large capacitance (several µF) in a relatively short period of time (80 µs for 7 µF from 0 to 130 V). The output signal is a square wave only. The input signal is split: it drives the high voltage end-stage 3 transistors (MOSFET) and provides a trigger signal for the oscilloscope, Figure A1. Each input/output is galvanically isolated from each other with the application of a battery of optoisolators. The color of the LED diodes informs the user of the mode of operation (ON or STAND-BY).

In the ON mode, the high voltage is supplied by a variable transformer, Figure A2. The high voltage setting can be tested upon pressing the button "Test High Voltage (HV)" mounted on the box chassis with a volt meter connected. In the test mode, no high voltage is delivered to the PE.

In the STAND-BY mode, high voltage is cut off from the PE actuators but it can be tested. The MOSFET box operates on two 9V batteries, one 12V line from an outside transformer and the required high-voltage. The MOSFET box integrates the AC to DC high voltage converter and a circuitry to assist prompt discharge of the PE capacitance through a low-value resistor. The MOSFET box features a fan to cool-off the three discharging resistors. The necessary power to the fan is delivered from the 12V line.
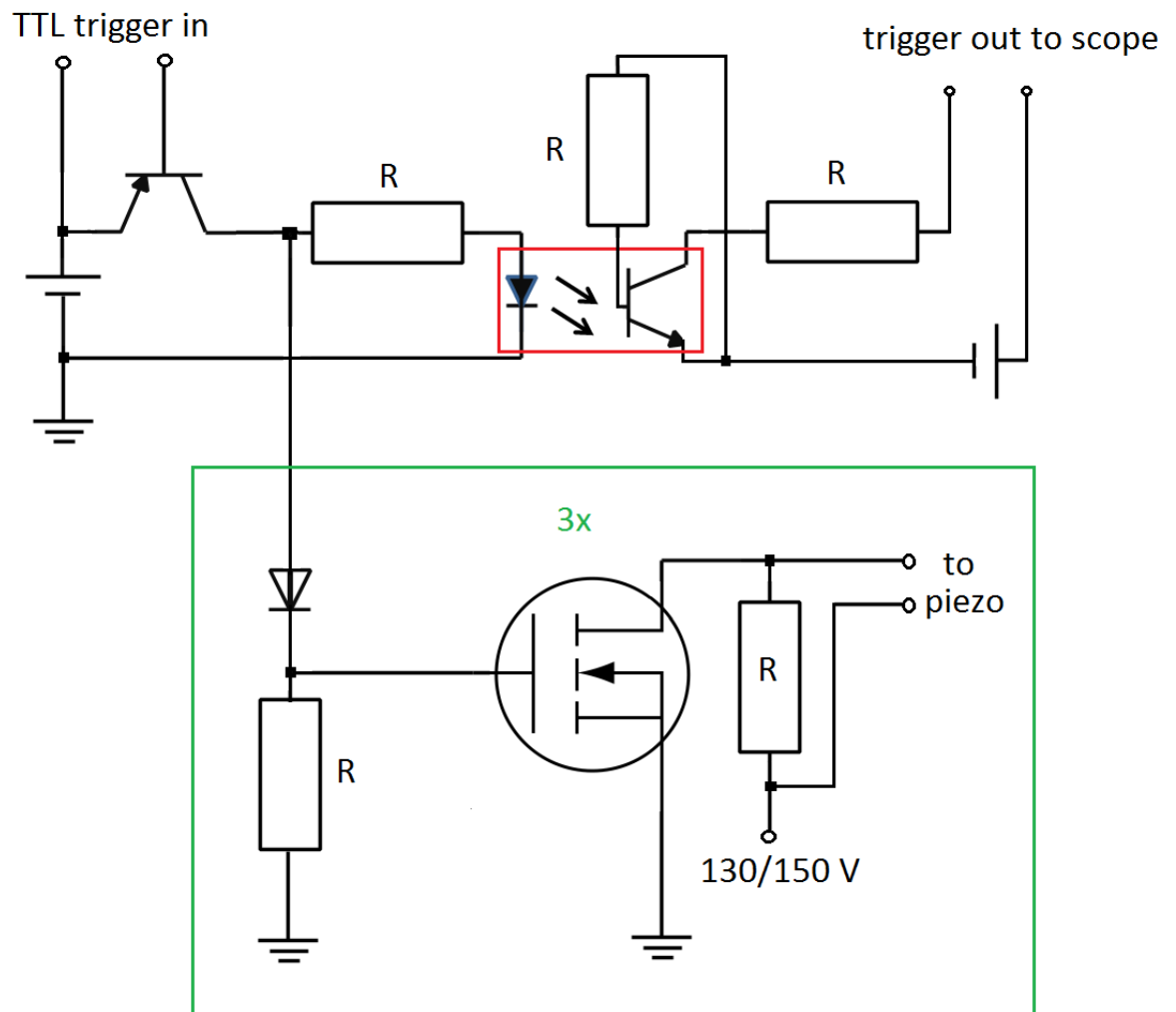
Figure A1: Simplified schematics for the MOSFET piezoelectric driver
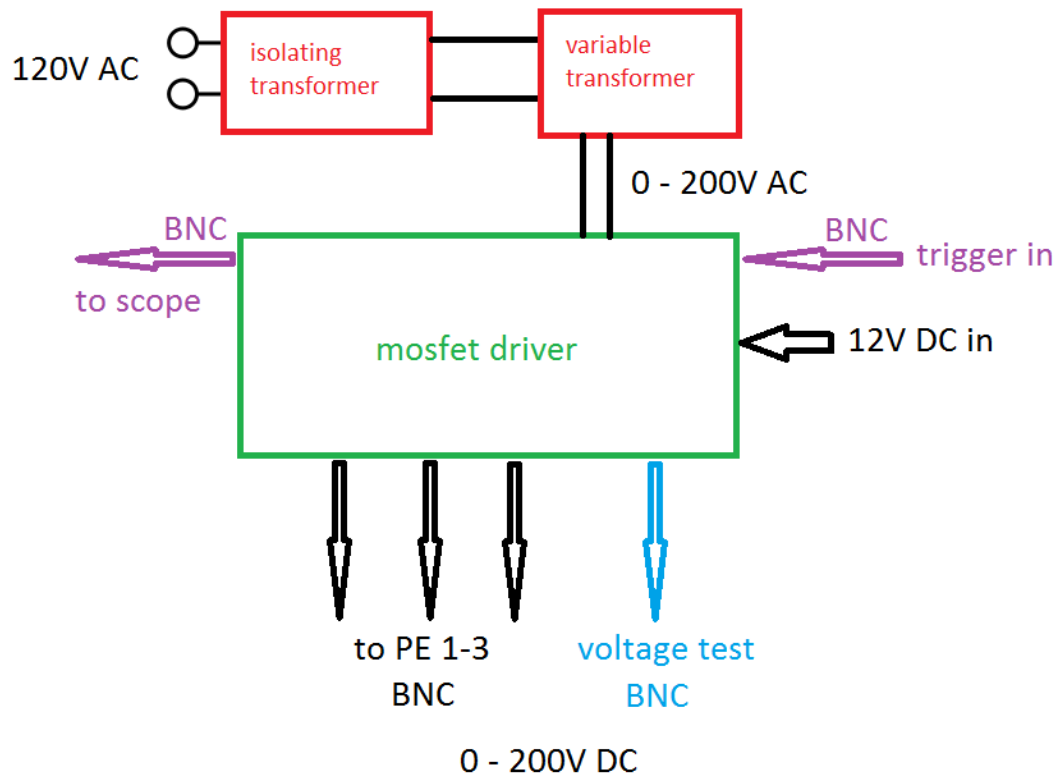
Figure A2: Block diagram; the MOSFET driver requires an isolating transformer and a variable transformer (Variac) to work
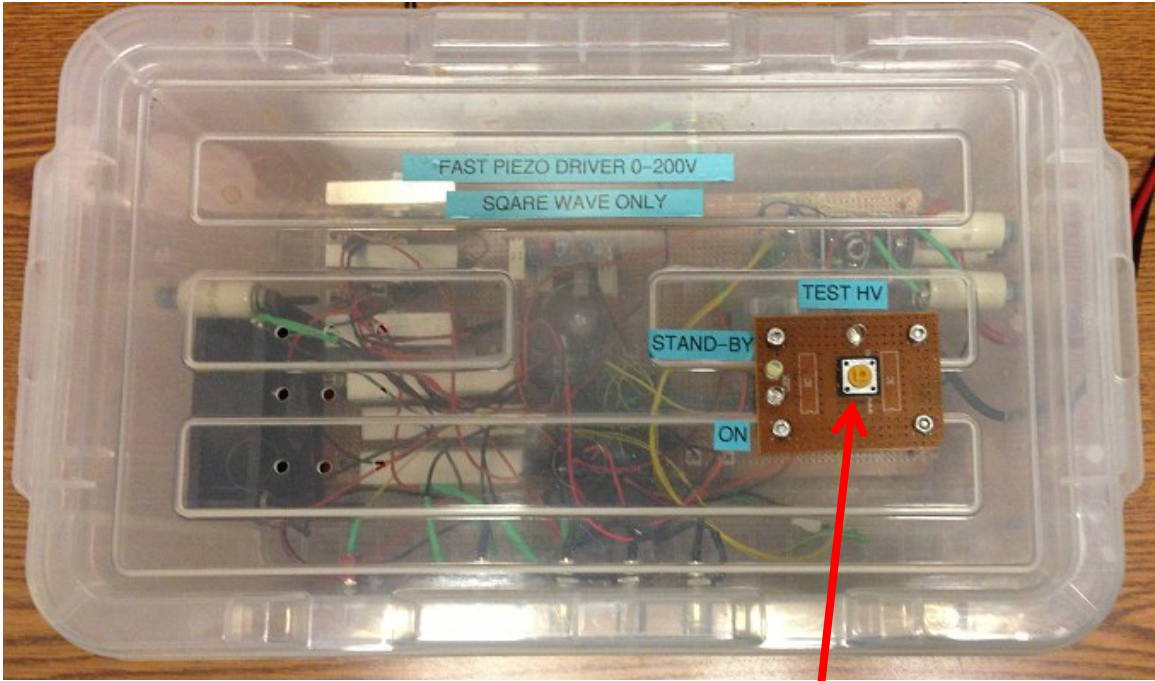
Push-button to test the value of the high-voltage delivered to the piezoelectric actuators

Figure A3: The MOSFET driver; top panel
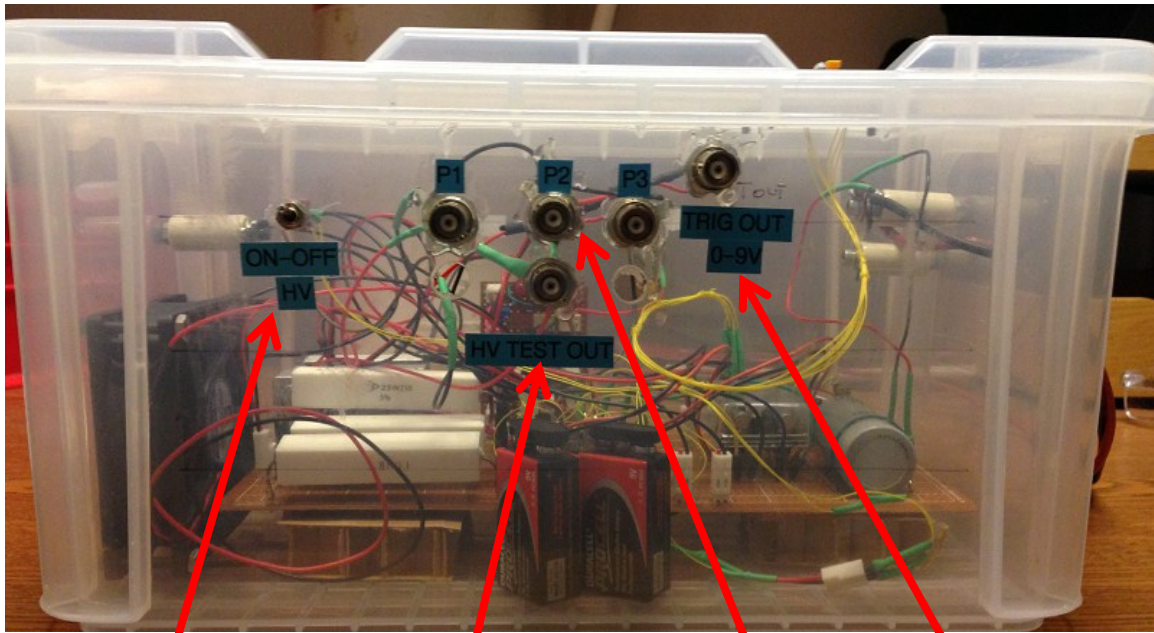
Figure A4: The MOSFET driver; front panel; the AC high-voltage connector cables can be barely seen on the right hand side (red/black)
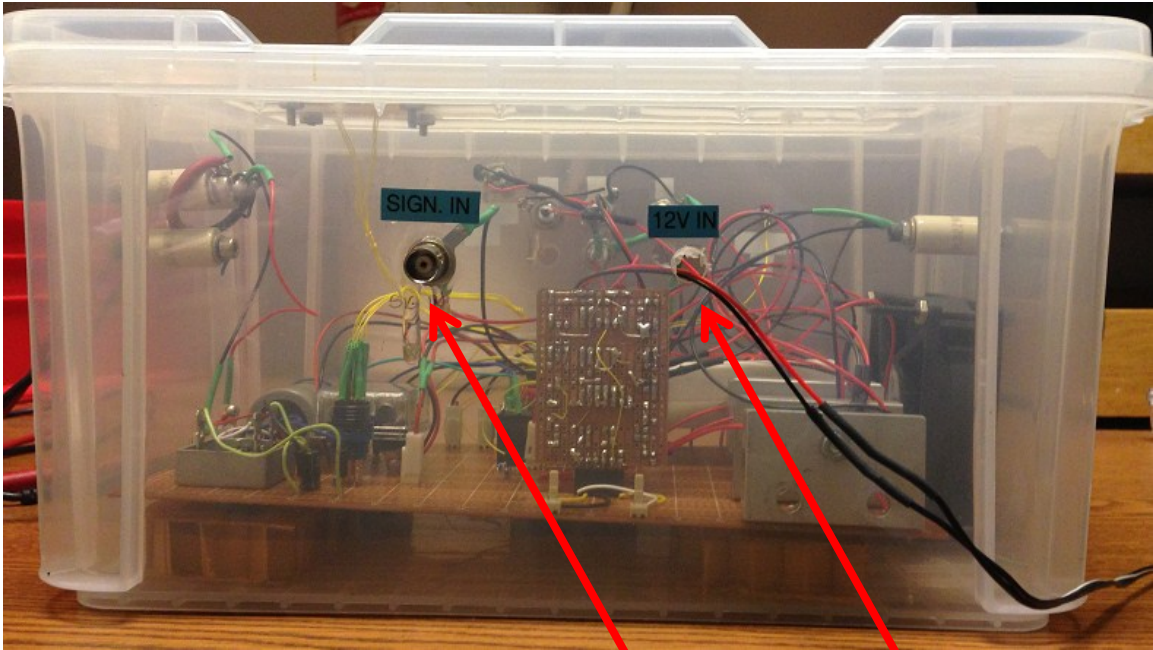
TTL signal (trigger) in   To 12V power supply

Figure A5: The MOSFET driver; view from the back

A.2 The Monochromator Driver and Data Collection System

Main features of the custom-made driver and data collection unit include:

- Platform upgraded from DOS to Windows;

- Automatic data collection with LabVIEW visual programming language by NI; user interface is provided;

- Automated operation: setting up the wavelength, scanning rate and data collection;

- 14-bit analog input resolution from the detector (PMT);

- Visual indicators for data collection and error message through software;

- Data are saved as ASCII file and can be moved with any USB pendrive in Windows XP environment;

- Emergency OFF switch - stops the monochromator instantaneously and resets all settings;

The monochromator (SPEX) driver and data collection system revived the obsolete optical equipment through improvements in user interface and method of data transfer, Figure A6. The desired starting and ending wavelength can be set in Windows, the desired step in wavelength and signal averaging duration can be chosen through the user interface. The analog signal can be monitored in

real time during the data collection process. The data collection can be interrupted at any time with a mechanical switch. The circuitry can detect out-of-range points, below and above the physical possibilities of the SPEX monochromator. These errors are signaled to the user through the interface, Figure A6.

This system communicates with the SPEX via TTL level signals, coupled through an ATmega328 microcontroller to the PC. The microcontroller runs on the Arduino platform and is programmed in C++ language. Commands are exchanged between LabVIEW interface, the microcontroller and the digital-to-analog 14 bit acquisition system (DAQ). The interconnecting block diagram is shown in Figure A7. The system is composed of three independent units, Figure A7, called A, B, and C. The unit C is only composed of connectors to the SPEX monochromator, with a parallel (LPT connector) arrangement. All signals from the unit C are labeled "LPT" below. The system makes use of the hardware interrupts available in the ATmega microcontroller.

Unit A	Unit B
D GND digital ground	GND ground
P0.0	Digital 2
P0.1	Digital 3
P0.2	Digital 5
P0.3	Digital 6
P0.4	Digital 7
P0.5	Digital 10
P0.6	Digital 12

Table A1: Electrical connections between module A and B as in Figure A7

Unit B	Unit C
Digital 4	3 LPT
Digital 8	13 LPT
Digital 9	12 LPT
Digital 11	15 LPT
Digital 13	2 LPT
Ground GND	25 LPT

Table A2: Electrical connections between module B and C as in Figure A7

Unit C	Description
8 LPT	Requires 5V from the B module
25 LPT	GND for all signals
13 LPT	Signal from SPEX: hardware limit exceeded when HIGH (limit 1)
15 LPT	Signal from SPEX: hardware limit exceeded when HIGH (limit 2)
2 LPT	HIGH/LOW TTL level pulses for the stepping motor
3 LPT	Scanning direction: if HIGH, SPEX scans up; LOW- down
12 LPT	Emergency triggered by a switch: if triggered, the SPEX will stop ASAP

Table A3: Explanation of the signals required to drive the SPEX; these are sent from module C
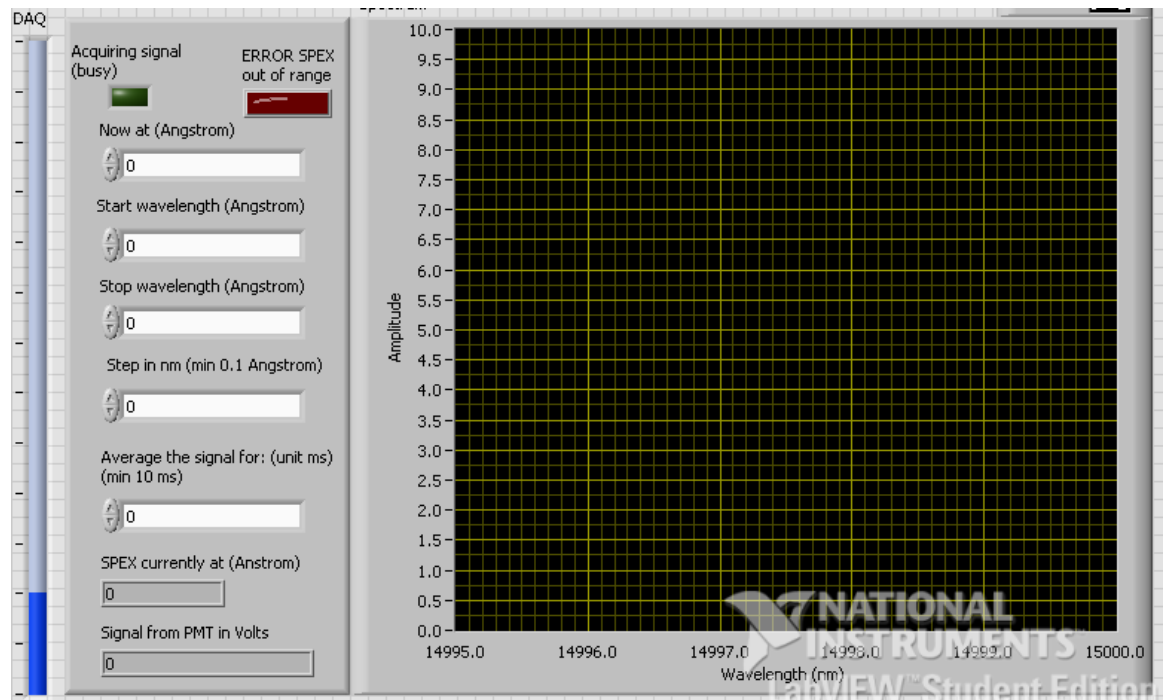
Figure A6: The SPEX monochromator LabVIEW user interface
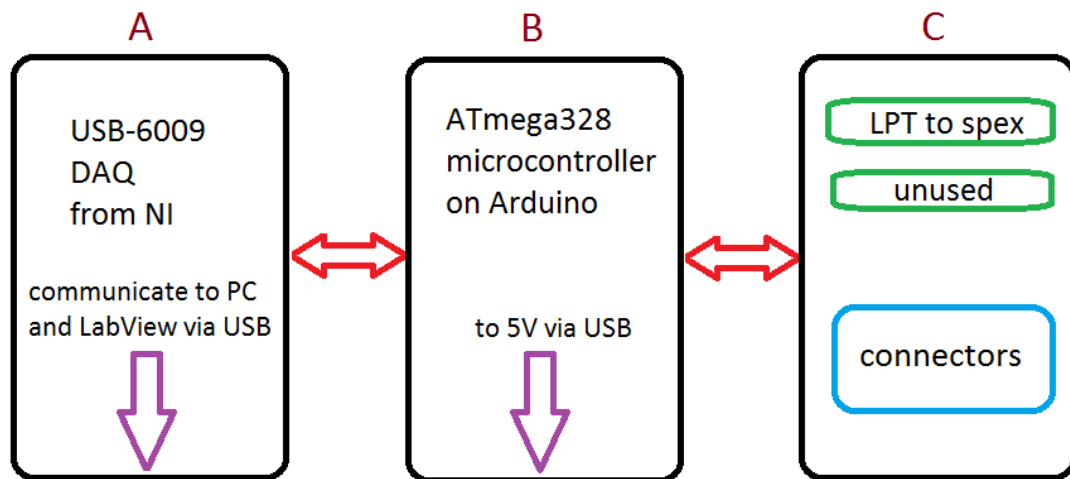
Figure A7: Block diagram for the driver and data collection system; the PMT analog out is connected to the unit A, DAQ
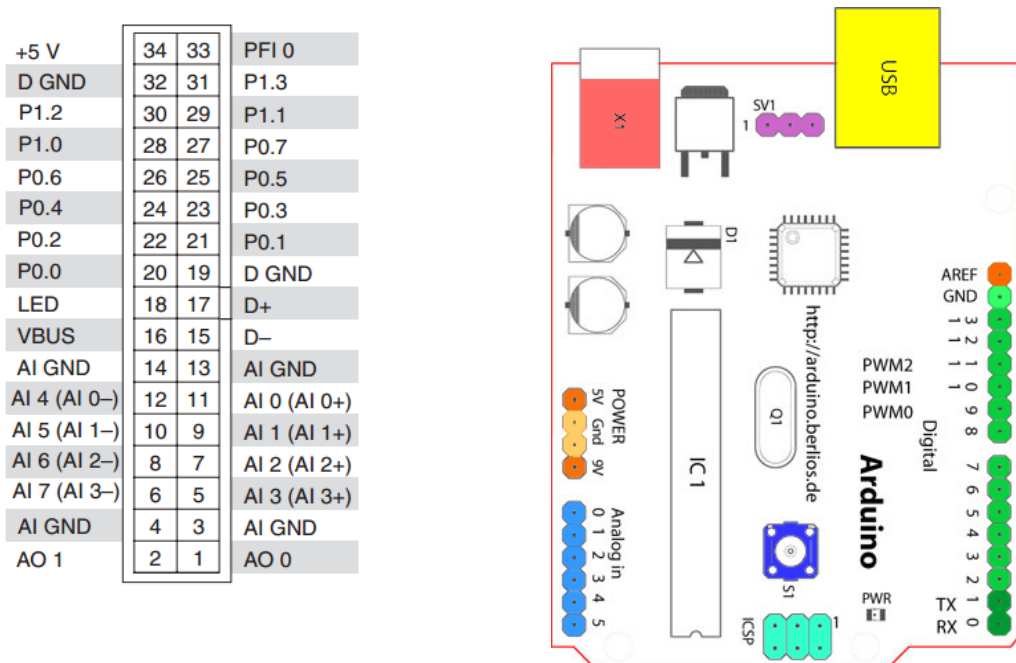
Figure A8: The electrical connectors on DAQ (A), left and the Arduino microcontroller (B), right

Listing of the custom-made C++ program uploaded into the Arduino microcontroller, unit B:

```cpp
volatile long triggerup=0;

volatile int by60=0;

volatile long triggerdown=0;

int i = 0;



void setup(){

  attachInterrupt(0, interrupttriggerup, FALLING);  //Interrupt 0 is Digital Pin 2

  attachInterrupt(1, interrupttriggerdown, FALLING); //Interrupt 1 is Digital Pin 3


  pinMode(13, OUTPUT); //pulses to stepping motor (1nm is 399.83 pulses)

  pinMode(4, OUTPUT); //direction of scan (HIGH is up, LOW is down)

  pinMode(9, INPUT); //ability to stop the SPEX with a switch at any time

  pinMode(6, OUTPUT); //busy moving spex to DAQ digital input (HIGH: spex is still moving, wait
for LOW)

  pinMode(8, INPUT); //SPEX out of range: from SPEX 1st limit; active when HIGH

  pinMode(11, INPUT); //SPEX out of range: from SPEX 2nd limit


  pinMode(10, OUTPUT); //SPEX out of range; signal error to DAQ digital input so LabView
shows the Red LED on

}


void loop(){

  if (triggerup < 0) {triggerup=0;}

  if (triggerdown < 0) {triggerdown=0;}
```

```
  if (digitalRead(9) == HIGH) { //Manual request to stop the SPEX

   delay(1000); triggerup=0; triggerdown=0;

  }

  if ((triggerup > 0) or (triggerdown>0)) { //check if still busy moving the spex before collecting
signal from analog input on DAQ

   digitalWrite(6, HIGH); //yes, still moving the spex: do not collect the signal

 } else {

   digitalWrite(6, LOW); //no, OK to collect the signal from the PMT now

  }


  if ((digitalRead(8) == HIGH) or (digitalRead(11)) == HIGH) {     //check if SPEX is out of range
before next move

   digitalWrite(10, HIGH); //here if out of range

   if ((triggerup > 0) and (triggerdown>0)) { //very unlikely to be in this "if case"

     delay(2000); triggerup=0; triggerdown=0; digitalWrite(10, LOW);

   }

   if (triggerup > 0) { //error from SPEX triggered while moving up; move down then to get out by 5
nm

     delay(1000);

     for (int help = 0; help < 2000; help++)  {

       i = movedown();

     }

    triggerup=0; triggerdown=0;

   }


   if (triggerdown > 0) { //error from SPEX triggered while moving down; move up then to get out
by 5nm

     delay(1000);

     for (int help = 0; help < 2000; help++)  {
```

```
      i = moveup();

    }

  }

  triggerup=0; triggerdown=0;

}

else {

  digitalWrite(10, LOW); //SPEX is within the allowed range

}


if (triggerup > 0) { //perform the basic function of scanning UP

 i = moveup();

 triggerup = triggerup -1;

}


if (triggerdown > 0) {//perform the basic function of scanning DOWN

 i = movedown();

 triggerdown = triggerdown -1;

}

}


int moveup() {

 digitalWrite(4, HIGH); //set the direction of scan to UP

 by60 = by60 +1;

 if (by60<190) {

 for (int qq = 0; qq < 40; qq++)  {

  digitalWrite(13, LOW);

  delayMicroseconds(150);

  digitalWrite(13, HIGH);
```

```
    delayMicroseconds(150);

   }

  }

  if (by60==190) {

  by60=0;

  for (int qq = 0; qq < 41; qq++)  {

    digitalWrite(13, LOW);

    delayMicroseconds(150);

    digitalWrite(13, HIGH);

    delayMicroseconds(150);

   }

  }

 digitalWrite(13, LOW);

 digitalWrite(4, LOW); //RESET direction of scan

}


int movedown() {

 digitalWrite(4, LOW); //set the direction of scan to DOWN

 by60 = by60 +1;

 if (by60<190) {


 for (int qq = 0; qq < 40; qq++)  {

   digitalWrite(13, LOW);

   delayMicroseconds(150);

   digitalWrite(13, HIGH);

   delayMicroseconds(150);

   }

  }
```

```
  if (by60==190) {
  by60=0;
  for (int qq = 0; qq < 41; qq++)  {
    digitalWrite(13, LOW);
    delayMicroseconds(150);
    digitalWrite(13, HIGH);
    delayMicroseconds(150);
    }
 }
 digitalWrite(13, LOW);
 digitalWrite(4, LOW); //RESET direction
}



void interrupttriggerup(){
  if (triggerup < 1) {by60 = 0;}
triggerup = triggerup +1;
}


void interrupttriggerdown(){
   if (triggerdown < 1) {by60 = 0;}
triggerdown = triggerdown +1;
}
```

A.3 Experimental Details for the Synthesis of Bis-Anthracene, Preparation of Zeonex Polymer Samples, and Spectroscopic Methods

A.3.1 Synthesis of the Protonated and Selectively Deuterated Bis-Anthracene

Bis-anthracene can be prepared in the condensation reaction of 9,10-bis(chloromethyl)anthracene, Figure A9, in acetone described by Golden[1]. In this synthesis, we used this commercially available chemical supplied by TCI America. It was used without further purification. Step 1 only concerns the synthesis of a selectively deuterated 9,10-bis(chloromethyl)anthracene.

In Step 1 of this synthesis we prepared the selectively-deuterated ,10-bis(chloromethyl)anthracene, a reactant necessary to obtain BA(d), with the goal of getting more insight into the IR stretching frequencies of aliphatic C-H and C-D bonds in BA (in dimethyl linkers). With the inelastic neutron experiments described in Chapter 5, we were mainly interested in the low energy molecular dynamics that could reveal the C-H/π hydrogen interaction in crystalline BA/PI system. As a result of this two-step synthesis, deuteration was carried out selectively on the dimethyl linkers.

Step 1: *Preparation of d-9,10-bis(chloromethyl)anthracene*

Selectively deuterated 9,10-bis(chloromethyl)anthracene, Figure A10 was prepared. A synthetic route described by Cloninger *et al.* was modified[2]. Equal moles of deuterated (instead of protonated) paraformaldehyde were applied, Figure A11.

48 mmol (4.59 g of d-paraformaldehyde, 99% atom D, Aldrich) were mixed with 63 mL of protonated glacial acetic acid (CH_3COOH, Fisher Scientific). The white slurry was bubbled with gaseous DCl, formed separately in a reaction between anhydrous d-sulfuric acid (D_2SO_4 99.5% atom D, 96-98 wt. % in D_2O, Sigma-Aldrich) and crystals of NaCl (Fisher Scientific) until the white suspension of d-paraformaldehyde cleared in the solution in the reaction with DCl. In a separate flask, 55 mmol (9.9 g) of (protonated) anthracene (min. 97%, TCI America) were mixed with another 65 mL of glacial acetic acid. The two solutions were mixed in a three-neck flask equipped with a condenser and stirred under flowing nitrogen atmosphere at around 60 °C for 20 hours. The reaction ceased once the mixture was poured over ice. The yellow solid was filtered and dried over P_2O_5 in an exicator *in vacuo* for around 24 hours. The yield of this reaction was found to be around 80%, whereas the reported literature value in which the protonated paraformaldehyde and gaseous HCl were originally used was 92%. The deuterated 9,10-bis(chloromethyl)anthracene was found to be readily soluble is acetone and benzene. The difference in solubilities between the reactant and

the reaction's product was later used to purify BA and BA(d) from the much

better soluble in organic solvents unreacted reagent. d-9,10-

bis(chloromethyl)anthracene was eventually recrystallized from benzene and

used in the last step of the synthesis, which directly lead to the formation of

BA(d) with both dimethyl linkers deuterated.
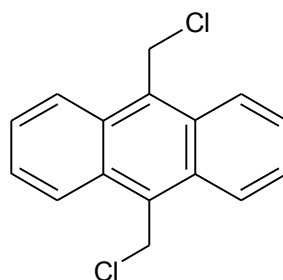
Figure A9: Protonated 9,10-bis(chloromethyl)anthracene, molecular mass M = 275.16 g/mol
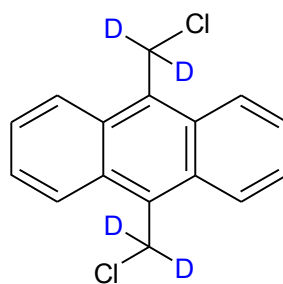
Figure A10: Selectively deuterated 9,10-bis(chloromethyl)anthracene, molecular mass M = 279.18 g/mol
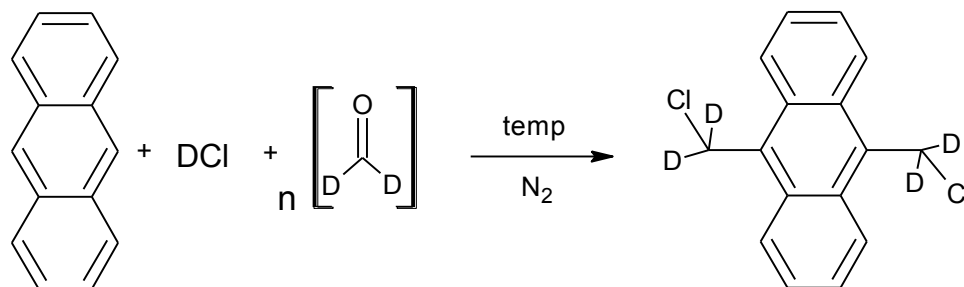
Figure A11: Schematic representation of the synthesis performed in Step 1

Step 2: Condensation and the formation of BA(d)

In the second and last step of the synthesis, the selectively deuterated 9,10-bis(chloromethyl)anthracene was condensed in the presence of NaI yielding the desired product- BA(d) and I_2 as a byproduct in a redox reaction. Around 5 g of d-9,10-bis(chloromethyl)anthracene was mixed in a flask equipped with a condenser with 15 g of sodium iodide (Fisher Scientific) in 250 mL of acetone (Fisher Scientific). The mixture was stirred at its boiling temperature for around 12 hours. As the reaction progressed, the solution turned red-brown and was filtered hot. The residue was washed with acetone in order to remove free iodine and any unreacted d-9,10-bis(chloromethyl)anthracene and later with water to dissolve remaining crystals of NaI. Eventually the dry yellowish precipitate was boiled with benzene three times and filtered hot. Even though BA is sparingly soluble in benzene, the procedure was carried out to ensure that the BA has no residual d-9,10-bis(chloromethyl)anthracene present.

When dry, the powder of BA(d), Figure A12, is clearly much brighter (bright orange-yellow color) in appearance when compared to its protonated isotopologue, BA, Figure A13, which is orange in appearance, Figure A14. While neither BA nor BA(d) are soluble in acetone in amounts necessary for the process of purification, and only slightly better in benzene, they were found to be readily soluble in 1-chloronapthalene even at room temperature.

High-resolution mass spectrometry was performed in order to verify the products of the two synthetic routes (1 and 2). All four samples were submitted for analysis in 1-chloronapthalene as the ultimate solvent. Due to the intrinsic character of this analytical method, the mass spectrometry shows protonated ions of BA and BA(d) as their respective masses (BAH^+ and BAH_d^+, Table A4, Figure A15 and A16). The accurate masses found in the MS experiment are in good agreement with their predicted formulas. Moreover, in the case of BA(d), no pollution by BA (smaller mass-to-charge ratio) was found in the MS spectrum.

The mass spectra of protonated and selectively deuterated 9,10-bis(chloromethyl)anthracene (products of synthesis 1) both show their accurate masses (summarized in Table A4) in good agreement with the predicted formulas with one Cl atom per each molecule lost during the ionization process.

Molecule Analyzed	Experimental Mass-to-Charge ratio	Calculated mass (g/mol)	Deviation in ppm
BAH$^+$, C$_{32}$H$_{25}^+$ (added proton)	409.1966	409.1951	3.7
BAH$_d^+$, C$_{32}$H$_{17}$D$_8^+$ (added proton)	417.2461	417.2453	1.9
9,10-bis(chloromethyl)anthracene C$_{16}$H$_{12}$Cl$^+$	239.0623	239.0622	0.4
d-9,10-bis(chloromethyl)anthracene C$_{16}$H$_8$D$_4$Cl$^+$	243.0876	243.0873	1.2

Table A4: Experimentally found mass-to-charge rations in a MS experiment involving purified products of BA synthesis
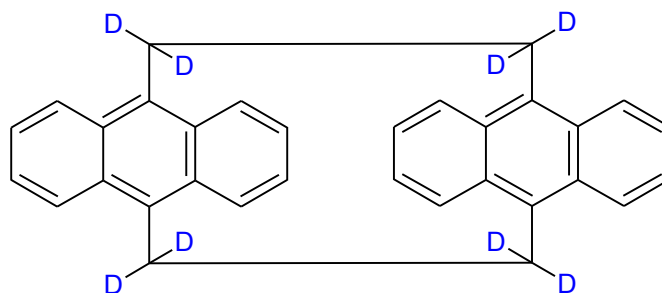
Figure A12: Selectively deuterated dimethyl linkers in modified BA(d), molecular mass M = 416.56 g/mol
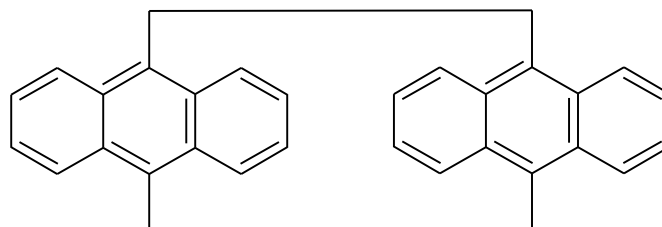
Figure A13: Protonated BA, molecular mass M = 408.51 g/mol

Figure A14: A photograph of the orange crystals of BA, right, and orange-yellow crystals of selectively deuterated BA(d), left
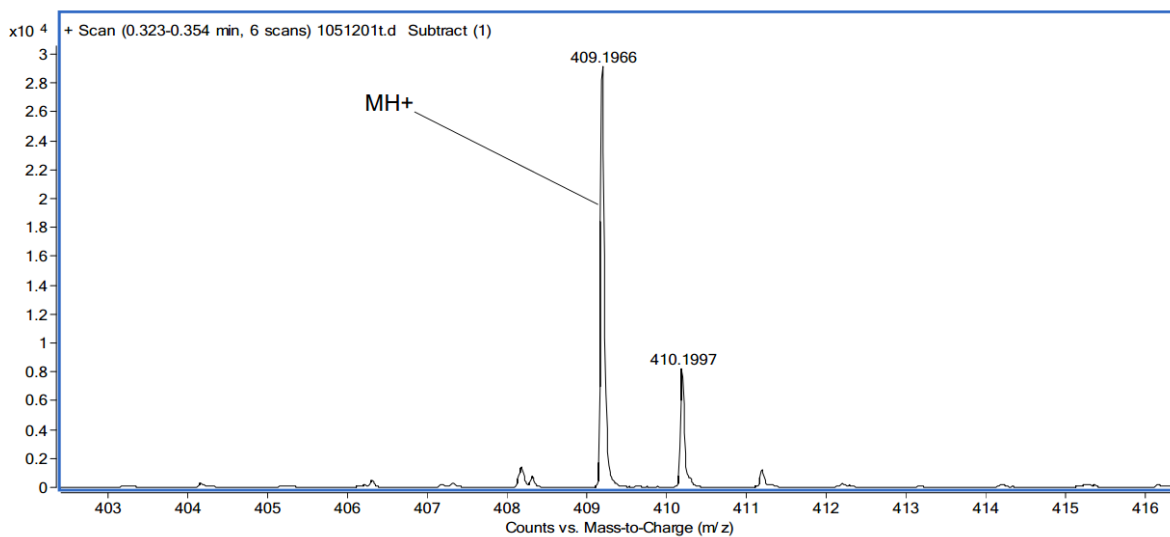
Figure A15: Mass spectrum of protonated BAH$^+$ ion with a maximum at 409.1966
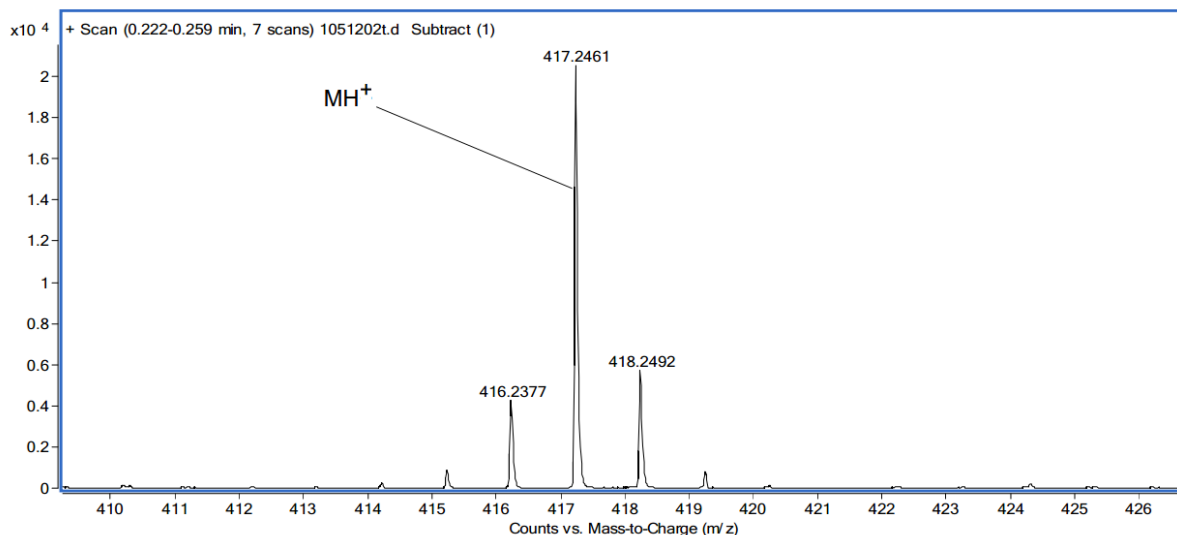
Figure A16: Mass spectrum of selectively deuterated BAH_d^+ ion with a maximum at 417.2461

A.3.2 Polymer Sample Preparation and Control Measurements

A.3.2.1 Criteria for Choosing the Most Suitable Solvent

Several common solvents were tested for the solubility of BA. Acetone shows the highest solubility for BA than any other common solvent (besides 1-chloronapthalene). However, cyclohexane was eventually chosen as the solvent for BA absorption experiments for the four important reasons:

- Cyclohexane is spectrally transparent in the UV as well as in the visible spectral region 200-700 nm as shown in Figure A17, red spectrum. Acetone intrinsically absorbs from ~210 to 325 nm, obscuring the main absorption peak of BA around 257 nm, Figure A17, blue spectrum;

- Cyclohexane is an inert medium in which no reaction between the non-polar solvent and the BA (or PI) molecules takes place during intense light illumination. Two samples of BA, one in cyclohexane, the other in acetone were illuminated for 3 minutes with halogen lamp. BA dissolved in acetone decomposed in an irreversible fashion (Figure A18) while BA dissolved in cyclohexane converted to PI (spectra shown in Figure A19);

- Only very miniscule amount of BA is necessary to prepare a saturated solution in cyclohexane. The peak at ~ 257 nm in the absorption spectrum features an OD of almost 4 in a 1 cm quartz cuvette on Cary 50 absorption spectrometer, which is very close to the limit of detection for this instrument;

- Cyclohexane is an excellent solvent for the Zeonex polymer which is a matrix of choice for the optical experiments on BA/PI;
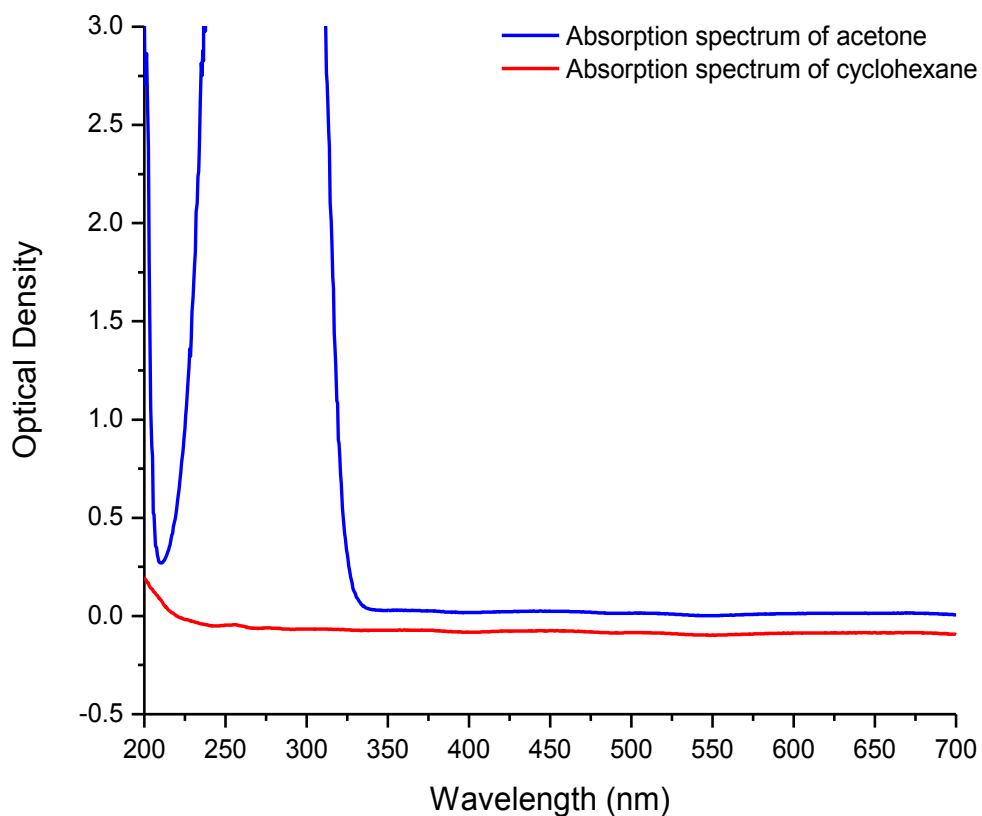
Figure A17: The absorption spectra of pure solvents in 1 cm cuvette, Cary 50 absorption spectrometer: acetone (blue) and cyclohexane (red). While cyclohexane transmits virtually all light in the wavelength region 700 – 200 nm, acetone presents strong absorption band in the relevant 325 – 210 nm spectral region
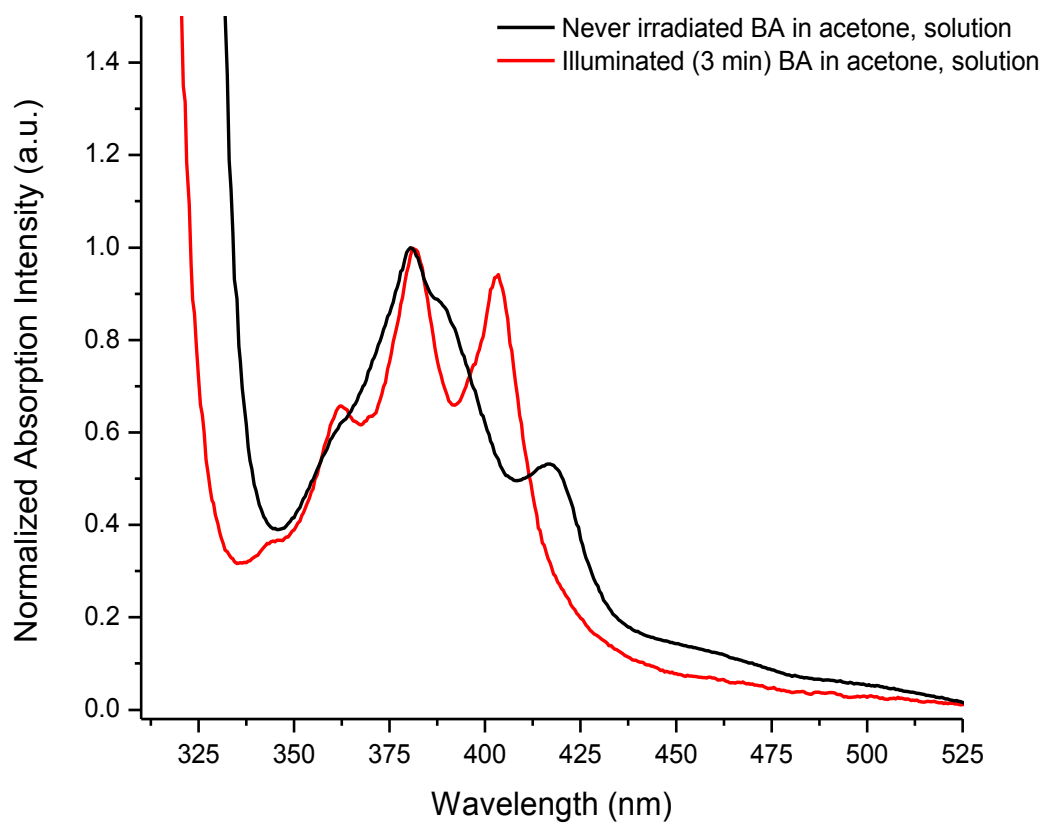
Figure A18: Normalized at maximum of absorption spectra of BA solution in acetone: before illumination (black) and after 3 min illumination (red) with a broadband white light source (halogen lamp). Illumination of BA in acetone induced a reaction in which PI was not the main product
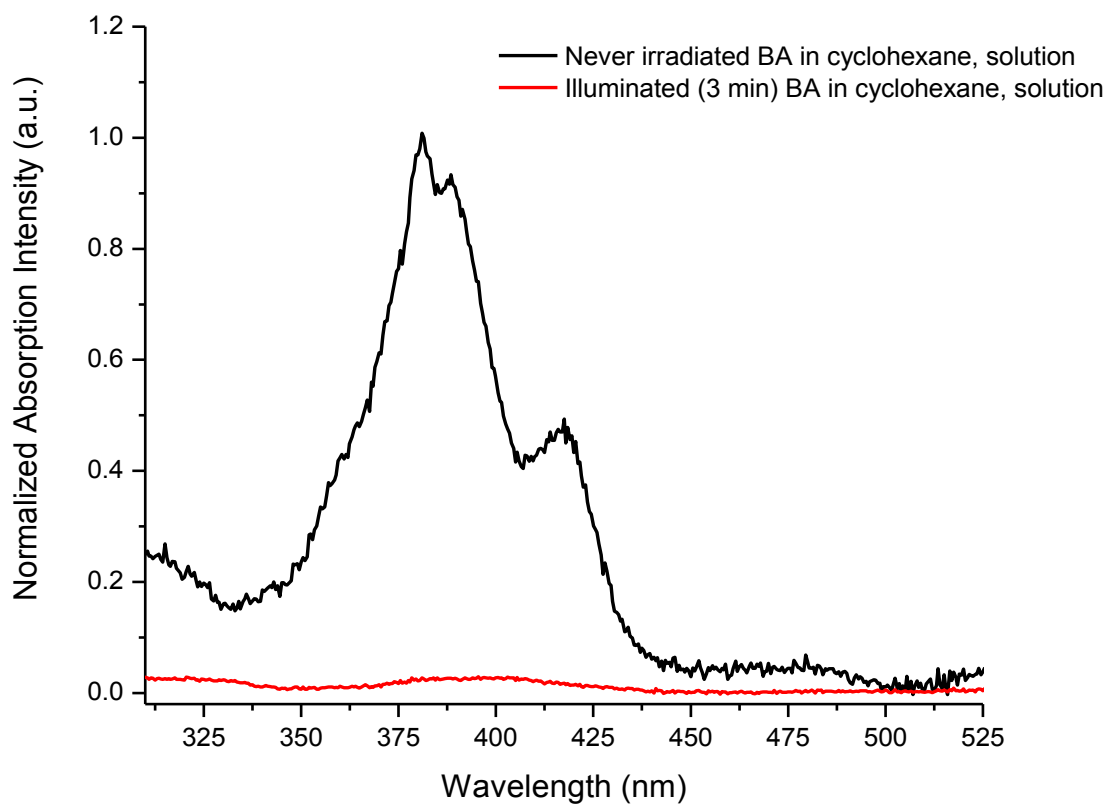
Figure A19: Absorption spectra of BA in cyclohexane: before illumination (black) and after 3 min illumination (red). The red absorption spectrum is characteristic of the PI photoproduct in the spectral range ~ 350 to 550 nm

A.3.2.2 Polymer Sample Preparation

All experiments described in Chapter 4 and 5, utilizing polymer films of BA or PI, were performed on crystals co-dissolved with a highly-UV-transparent (<230 nm) polycycloolefin resin (commercial name: Zeonex 480) showing excellent solubility in cyclohexane. BA/PI show only very mild solubility in this non-polar solvent. Orange crystals of BA and a few pellets of Zeonex (T_g=138-140 °C, Zeon Chemicals L.P.) were mixed with a few mL of cyclohexane (EMD ACS grade) sufficient to dissolve all polymer. The mixture was ultrasonicated in the dark for about two hours to accelerate the mixing process after which the solvent was evaporated by letting the solution dry in an open air for a few days at room temperature and in the dark. This way, yellowish and transparent films (thickness of around 0.24 mm) were obtained for our temperature- and pressure-dependent studies. When inspected under an optical microscope, individual, randomly oriented BA micro-crystals of various sizes were visible embedded in a polymer due to their poor solubility of BA in cyclohexane. A control experiment confirmed that the absorption signal registered is only due to the dispersed, individual molecules of this cyclophane. The microcrystals only contributed to the scattering of the signal, decreasing our signal-to-noise ratio. The dispersion of crystals in a polymer was necessary due to the ultra-high ε value for BA at maximum of absorption ~ 257 nm. The polymer matrix also serves as a

hydrostatic medium for uniform pressure redistribution throughout the relatively small sample compartment within DAC at elevated pressures.

In experiments with anthracene and dianthracene, we used samples produced by previous members of the group dispersed in a PMMA polymer matrix to a 0.5 % concentration by mass.

A.3.2.3 Optical Set-Up and Sample Illumination Procedure

The BA sample film was placed onto a 0.3 mm-thick Inconel (Ni-Cr) gasket and positioned between two Type II diamond culets (each around 0.5 mm in diameter) in a DAC for both pressure- and temperature-dependent measurements. Due to the excellent thermal conductivity of a diamond, uniform temperature redistribution throughout the film was guaranteed. Prior to each experiment involving high pressure, small amount of ruby dust was added into the gasket compartment for static pressure determination through fluorescence. The volume of the sample trapped within a gasket compartment at high pressures was estimated to be on average ~ 0.013 mm^3 assuming that the gasket's material dents by roughly 40% and the gasket hole diameter is on average 0.3 mm. For the purpose of illumination a halogen lamp was used as a

simple and efficient substitute for an ambient light source (Figure A20, emission spectrum) focused to an area of around 2.5 cm^2 by a single bi-convex glass lens. A 1 cm-thick water filter was employed to remove most of the infra-red part of the electromagnetic spectrum from the halogen light source which in turn reduced the amount of undesired heat transferred to the sample film during the irradiation process.

In cases when illumination was performed at ambient pressure and at room temperature, it was found that the illumination time necessary to quantitatively react all BA to PI was only ~ 10 s with the burning-power densities used. At times when relatively small static pressure was applied to BA in our temperature-dependent kinetic experiments, the time of illumination aimed at forming PI was further slightly increased to a total of 30 seconds.

Overall, there was a very mild overlap between the halogen light source emission spectrum and the absorption spectrum of BA in the 350 - 450 nm region. We did not observe and did not expect any significant overlap between the emission spectrum of our source, halogen lamp, and the deep-UV absorption peak of BA at around 257 nm.

Burning-power densities (P/A) of ~ 120 mW/cm^2 (measured over the entire visible spectrum) were used, of which only about 10 mW (~8 %) was absorbed in the 350 – 450 nm region, Figure A21. The burning times (t_b) oscillated between ~ 15 to 20 s (30 s and more at 9.3 kbar) for each unreacted to reacted (BA-to-PI)

photoconversion reaction. Thus, burning densities (Pt$_b$/A) applied to crystals dispersed in a Zeonex film were typically around 2.4 J/cm^2 (3.6 J/cm^2 at 9.3 kbar). All illumination events were carried out outside of the Cary 500 absorption spectrophotometer due to the lack of space in the sample compartment. Broad-band absorption spectra (data interval of 0.5 nm; averaging time of 0.2 s) were recorded with the use of only one channel (every spectrum referenced against air). A home-made insert was mounted inside the sample compartment, consisting of two plano-convex, fused-silica lenses (SI-UV grade, focal length 38.1 mm, Esco Products, Figure A22) and the sample-loaded DAC placed in between, mounted on a x,y,z adjustable holder. The goal of the two lenses is to let as much light as possible through the relatively small opening drilled in the gasket material (~ 0.3 mm in diameter).

Absorption spectra were collected over a range of 700-200 nm within approximately 210 seconds necessary to record each scan, depending on the settings. We have determined the pressure applied to the sample inside the DAC from the relative shift in ruby fluorescence with the accuracy of around ± 0.5 kbar only after having completed the entire set of absorption spectra at every pressure point. We found that the even the attenuated green 532 nm laser light which is used to produce fluorescence in ruby, induces photochemical changes within the sample film and disturbs the equilibrium between BA and PI. Eventually, each absorption spectrum was corrected for the absorption of that same pair of

diamonds at ambient pressure and at room temperature with pure Zeonex film of similar thickness loaded into DAC.
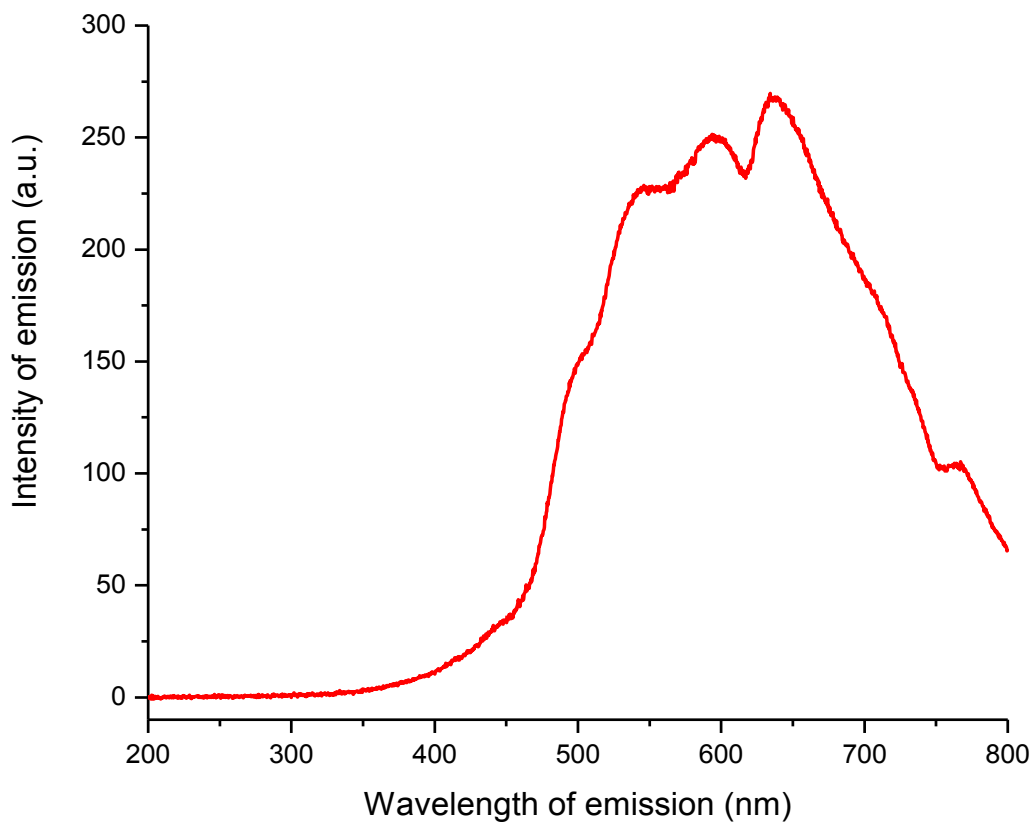
Figure A20: The emission spectrum of a halogen light source used in experiments involving the conversion of BA to PI
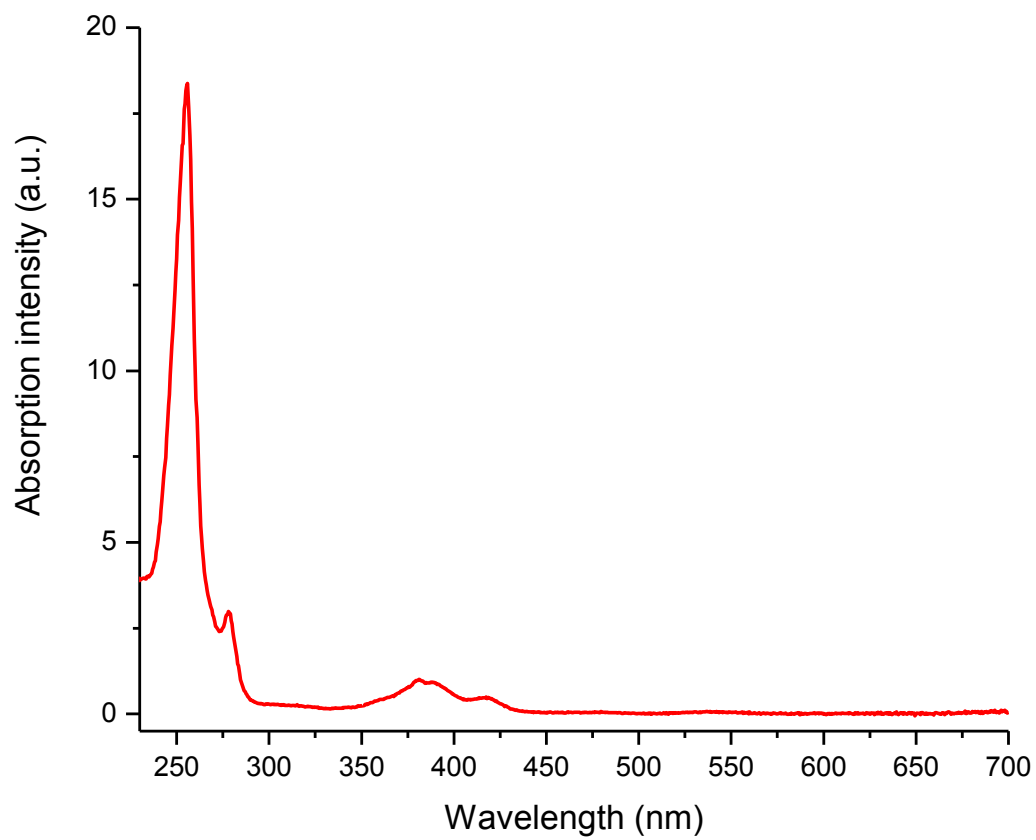
Figure A21: Absorption spectrum of BA in cyclohexane solution; range from ~ 230 nm to 700 nm
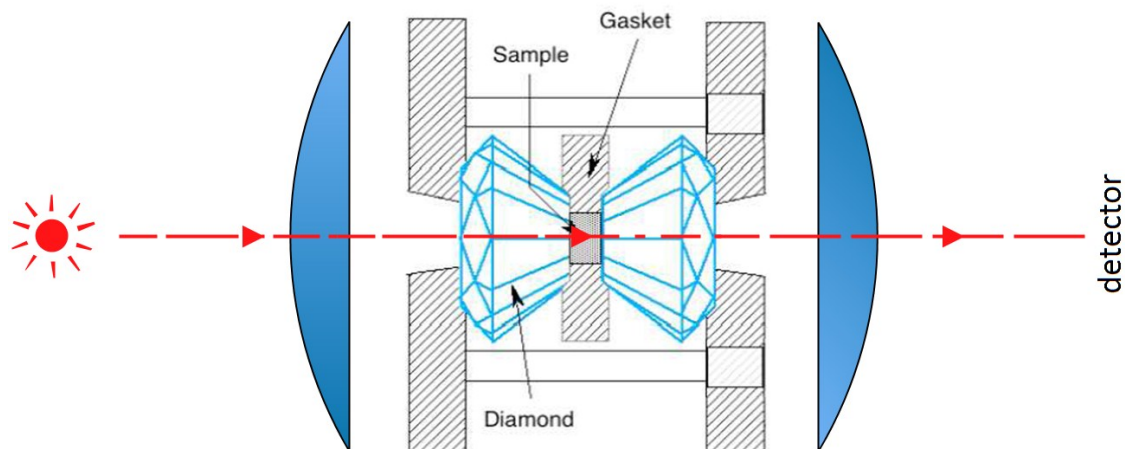
Figure A22: Set-up insert arrangement used in high-pressure experiments on BA/PI. The light source is the monochromatic light produced by a Cary 500 spectrometer

A.3.2.4 Methods of Spectral Evaluation

Spectroscopic changes can either be detected through absorption or fluorescence. In the latter, one can select a window of light detection either through a monochromator or a set of optical filters, where neither the polymer nor impurities influence the fluorescence signal to be detected, if at all possible. At other times, it is beneficial to monitor changes in absorption instead in emission which can usually be easier to interpret.

In absorption measurements spectra can suffer from a series of problems if the data is left untreated. The absorption measured is a complex function which depends on optical properties of all the materials that the light travels through during a scan such as lenses, diamonds within a DAC (Type I or Type II), polymer matrix and the sample itself. In addition to that, absorption spectra measured in a DAC over a prolonged period of time do change either because of essential changes occurring to the sample in study and/or changes that pollute the data with unwanted information. The latter may involve and is not limited to the polymer matrix undergoing a structural change that affects its absorption or simply the light source long-time (tens of hours) spectral instabilities (especially the appearance of new spectral peaks as the light source stays on). It has been observed that even in the case where the dispersed sample does not itself undergo pressure- or temperature dependent spectral changes (as is the case in rhodamine 101 in PMMA), high pressure within a DAC often causes absorption spectra to decrease in intensity at each wavelength by approximately the same offset value as compared to ambient pressure spectrum. This effect is greater the greater the pressure within the DAC. To correct for this anomaly, after the spectra collection, the absorbance at the low energy (~ 700 nm for BA-PI films) part of each spectrum were matched to one value (usually zero) within the noise level by careful examination the quality of which often depends on the skills of the spectroscopist. This part of the evaluation is very important as subtle

changes in the area under an absorption peak are being evaluated as a function of time.

In the next step of the evaluation, influence of the Type II diamond and the pair of quartz lenses on the absorption of the sample within the DAC were removed from each absorption spectrum. In order to achieve that, the raw absorption spectra were numerically divided by the absorption spectrum (recorded ahead of time) of a DAC equipped with a gasket and (only) Zeonex film placed between a diamond and a gasket within the sample compartment. This step is only necessary when there is no other identical lens-DAC-polymer film set-up that can fit within the sample compartment of a two-path spectrometer. In addition, the spectrometer used in the kinetic experiments (Cary 500) experiences a sudden jump in absorbance around 350 nm which is correlated with the automated change of a grating and a light source during each scan. The jump always occurs at the same wavelength but its magnitude depends on the absorption value at that wavelength. In most of the cases the division failed to correct for the sudden intensity jump and the offsetting had to be done numerically by raising or lowering the affected half of the absorption spectrum. This was achieved by adding or subtracting a constant value from each affected data point (offsetting) and putting these two halves of each affected file back together.

From this point on, each spectrum at all temperatures and pressures measured, are ready for numerical integration. In a simpler approach, the intensity of a particular peak could be used instead to extract important physical parameters. The numerical integration was performed using the trapezoidal rule. The region for the integration was chosen based on the spectroscopic differences between BA and PI in a polymer film. The largest differences between these two isomers occur within the ~ 294 and 239 nm and this region was chosen as boundaries for the numerical integration in the kinetic data evaluation in pressure- and temperature-dependent data sets. The Zeonex polymer is transparent to light within that spectroscopic UV region and thus does not interfere with the numerical evaluation.

In order to extract important parameters from either the pressure-dependent or temperature-dependent kinetic data, each set at each pressure or temperature was referred to the maximum absorption intensity of the BA peak absorption before illumination (transformation to PI by light). This was achieved by numerical integration of the essential region (between ~ 294 and 239 nm) in the very same sample film used in an experiment assuring first that any remaining PI is first converted to BA. To quantitatively convert any residual PI that might be present within a polymer sample to BA, the pressure within a DAC was raised momentarily and released after ~ 30 seconds (a pressure jump) ahead of the data-set collection. Once the pressure was released to an ambient

value, the transformation from BA to PI was carried out by the means of illumination with light.

In the final stage of the data evaluation, an integrated area of each peak within a data set was divided by the maximum value found before the BA-to-PI conversion by the "pressure jump" method. Only then the evaluated sets of pressure- or temperature-dependent kinetic experiments can be compared between each other (only for the BA-PI system, where no other reactions were observed to occur) and physical parameters such as the rate constants, k_1 and k_2, could be extracted.

A.3.2.5 Spectral Evolution of Zeonex Polymer Matrix at 16 kbar; Time Dependent Studies

Zeonex is a polymer of choice for the pressure and temperature-dependent study of BA and its photoisomer, PI. It is optically transparent with no spectral features, within the entire visible range (400 to 700 nm) as well as within the UV region, from 400 nm to around 235 nm where its absorption raises sharply. The maximum of absorption of BA at around 257 nm is well resolved within Zeonex matrix, however, the much blue-shifted maximum of absorption of

PI, four orthosubstituted benzene rings interconnected between each other, cannot be spectrally resolved within Zeonex, beyond the low intensity b-band with a maximum of absorption (coinciding with that of BA), at around 255 nm. To our knowledge Zeonex is the only polymer commercially available that has the widest spectral transparency within the UV and visible region.

Zeonex readily dissolves in cyclohexane at ambient conditions. This organic solvent has been used to produce films with BA or PI codissolved, a procedure which has been described earlier in this section. While cyclohexane is the ideal solvent for Zeonex, the solubility of either of the two cyclophane isomers (BA and PI) is sparse in cyclohexane. In spite of their very low solubility in general, the absorption at around 257 nm as well as between ~ 350 nm and ~ 450 nm can clearly be resolved in saturated solutions of cyclohexane with the use of a quartz cuvette and, with the right alignment and gasket size at least 0.3 mm diameter, can be resolved in Zeonex polymer film substrate loaded into a DAC at high pressure.

Zeonex is the trade name for the commercially available cyclic olefin copolymer (COC). Most COC polymers show great resistance towards acids and bases as well as many popular organic solvents which is not a feature that was exploited with our experiments. The structure of a typical COC is shown in Figure A23 below.

The influence of static pressure in a function of time on the spectral behavior of solely the Zeonex polymer matrix (no BA/PI added) were investigated as changes in absorption. A film of Zeonex polymer was loaded into a Type II Diamond Anvil Cell equipped with an elastic gasket and ruby dust for pressure calibration. A series of absorption spectra were recorded, the first one being an absorption spectrum at ambient pressure (in DAC) and the remaining a follow-up at 16 kbar. The changes in Zeonex absorption at 16 kbar were followed up to a maximum of ~ 81 hours. A reference absorption spectrum at ambient pressure was necessary for evaluation of the time-dependent changes occurring within the polymer. In evaluation, two absorption spectra were subtracted from each other: spectrum immediately after 16 kbar pressure was applied to the Zeonex polymer minus the reference absorption spectrum at ambient conditions. This resulted in a difference spectrum, shown in red in Figure A24 and in Figure A25. No dramatic change in absorption of the polymer film (expressed in optical density) has been observed roughly between 300 nm to 700 nm spectral region after high pressure was applied, within the time scale studied. A small set of two negative peaks in the high-energy UV region (245 to 285 nm, Figure A24 and Figure A25, red) was observed in the difference spectrum immediately after 16 kbar was applied which is a clear signal of a slight decrease in an OD (maximum difference of approx. 0.03) of the Zeonex polymer. This change has been followed with time with many difference spectra (not shown here). Eventually, within 4848 minutes, the trend reversed. The initially negative peaks between

245 to 285 nm evolved and partially regained their intensity resulting in changes in overall shape of the difference spectrum (Figure A24 and A25, blue). As a result of the time-dependent changes, a new maximum at around 265 nm was formed with a positive Δ OD at ~ 0.025 (Figure A25, blue). The red spectral end (~300 – 700 nm) of the difference absorption spectra remained essentially unaffected. The negligible pressure-induced spectral change in absorption of Zeonex illustrated in Figure A24 and A25 occurred within 81 hours.

The 234 to 315 nm spectral region is especially important in the evaluation of the changes in the PI/BA systems, i.e. in the kinetic traces of the pressure-induced BA recovery, the UV region between 234 to 315 nm is integrated. It contains all of the absorption peak of BA/PI with a maximum at ~ 257 nm (at ambient pressure).

Figure A26 presents the relative changes in the integrated spectral area between 234 to 315 nm. If no changes had occurred, the red data point would represent the entire situation at all times. In fact, the area in difference spectra drops to an arbitrary value (-1.0) after which it recovers rather quickly to one third of its initial value and continues to fluctuate between -0.5 to -0.3 for the next ~ 100 hours.

It is perhaps worth noticing that the change in OD of Zeonex has a reverse trend as compared to the PI/BA system, i.e. the pressure-induced change in Zeonex is negative and positive in co-dissolved PI in Zeonex.

In a summary it has been confirmed that the influence of moderate pressure on the Zeonex polymer's absorption is negligible. The stability of the co-dissolved BA-Zeonex film is reaffirmed in the following section of this Appendix.
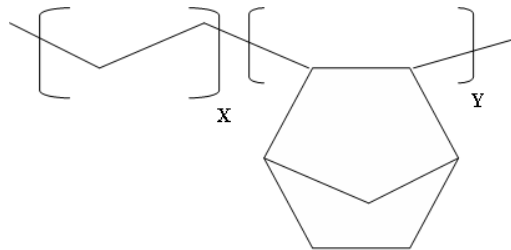

Figure A23: The general structure of a typical COC polymer, such as the commercially available Zeonex; reproduced with the permission from Wikipedia
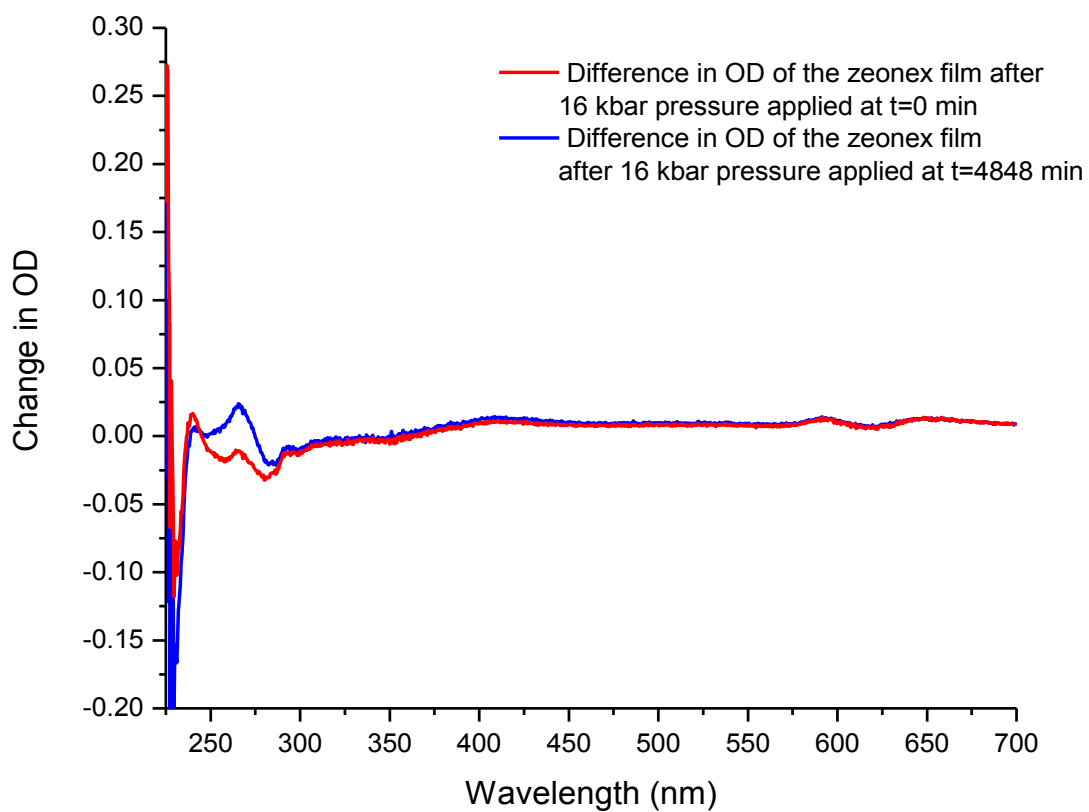
Figure A24: Difference absorption spectra which illustrate the changes in absorption of Zeonex polymer at high pressure (16 kbar) in a function of time. Evolving, negligible changes in absorption can be seen at wavelengths < 300 nm
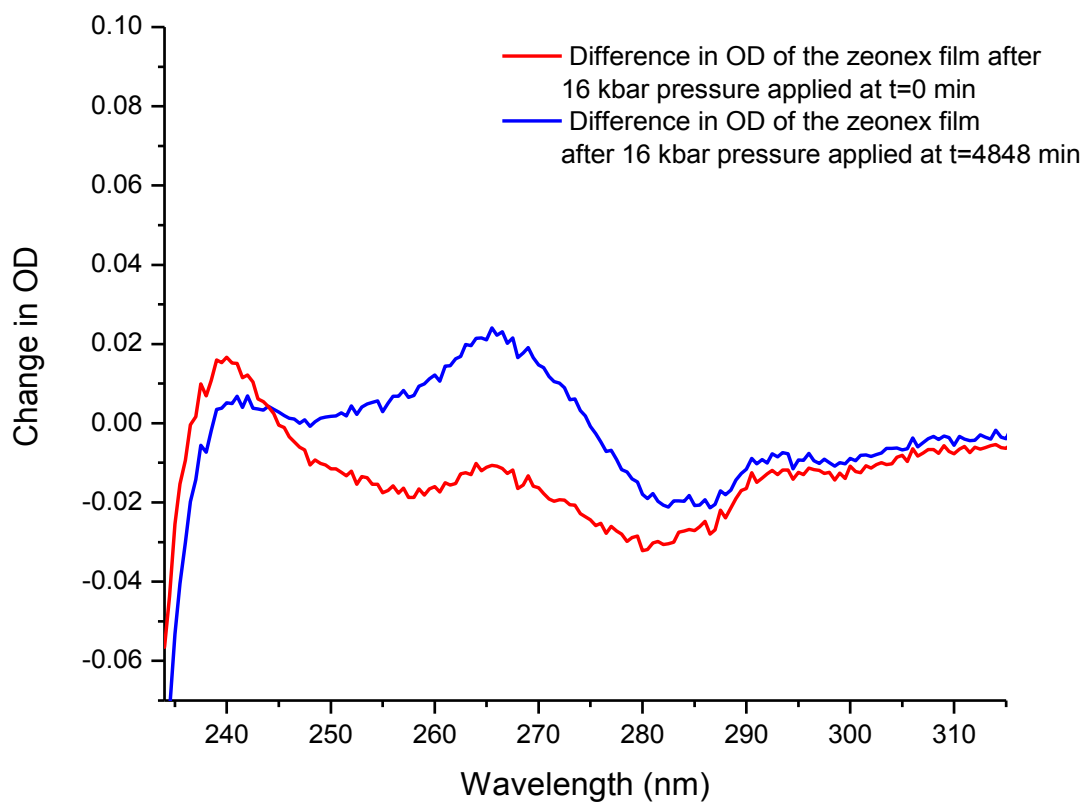
Figure A25: Selected 234-315 nm spectral region of the difference absorption spectra shown in Figure A24 above. The initially negative peaks (red difference spectrum) regain in intensity as a function of time
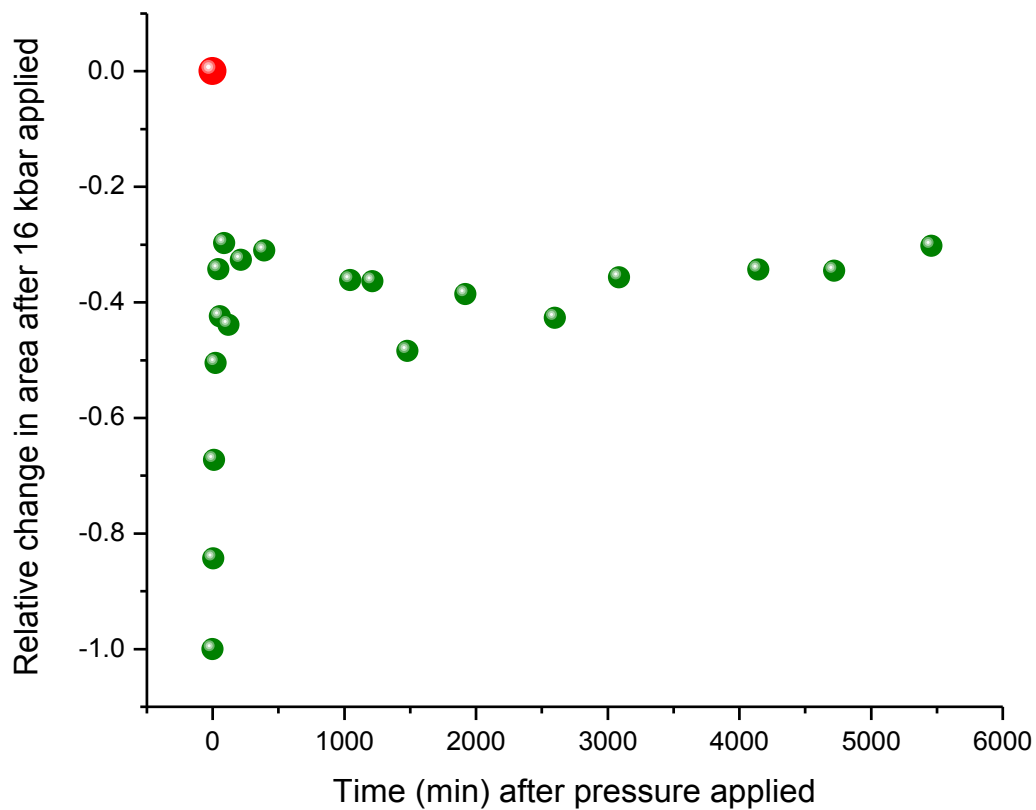
Figure A26: Difference spectra have been numerically integrated in the region between 315 and 234 nm (trapezoidal rule) and plotted as a relative change (green) with respect to a non-changing spectrum (red dot at 0). After 16 kbar was applied there was a sudden negative jump in the area (normalized at -1). With time, the spectral area quickly recovered, but only partially, to ~ 30% of its maximum change at ~ 300 minutes and overall stayed that way

A.3.2.6 Bis-Anthracene in Zeonex; High-Pressure, Time-Dependent Studies

An experiment was performed where the stability of BA dispersed in Zeonex was monitored with time at high pressure, ~ 26.7 kbar. It was necessary to determine whether BA itself is a stable molecule for the duration of the experiment at high pressures when embedded in a polymer. The spectral stability was probed with absorption spectroscopy technique with the use of Cary 500 spectrophotometer.

A film of BA in Zeonex (BA 0.5 % by mass) was prepared and treated with 60 °C for two hours in the dark and in a sealed vial. This thermal treatment converted any residual PI to BA within the film.

Figure A27 shows four control absorption spectra of the BA/Zeonex film at ~ 26.7 kbar, room temperature (no normalization) for up to 60 hours after high pressure was applied. At this pressure, the maximum of absorption of BA is red shifted (when compared to ambient pressure) to ~ 264 nm. No major changes in shape nor OD were seen in the film of BA between ~ 250 to 700 nm.

In yet another control experiment 73 kbar of static pressure was applied to BA dispersed in Zeonex, Figure A28. Excluding the red-shift of the maximum of

absorption, no other spectral changes occurred within ~ 3 minutes, the time it takes to record an absorption spectrum.

The lack of spectral changes as a function of time may suggest that BA is a stable molecule at high pressure within the time period studied and that no chemical reactions between BA and Zeonex take place. Therefore when changes are seen in absorption spectra of BA/PI, they are not related to the instability of BA in a Zeonex film at room temperature.
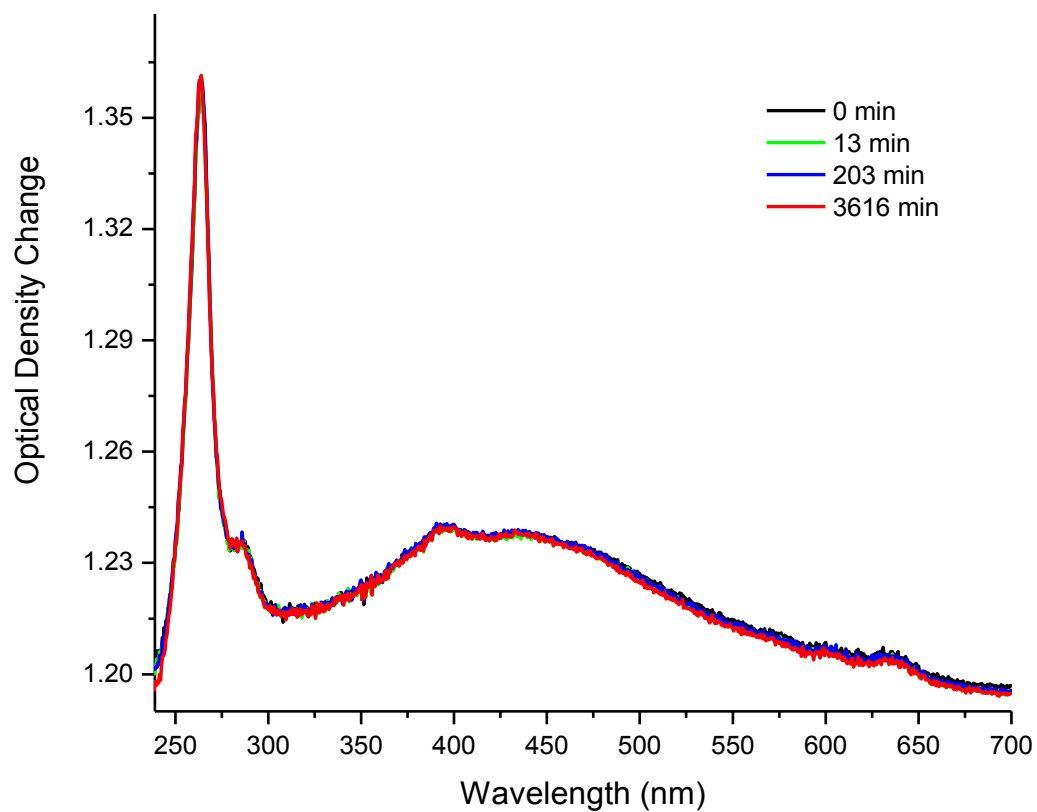
Figure A27: Selected absorption spectra of BA in Zeonex at 26.7 kbar monitored for up to 60 hours. No significant changes were seen suggesting that BA is a stable molecule at high pressure while in Zeonex at ~ 25 °C
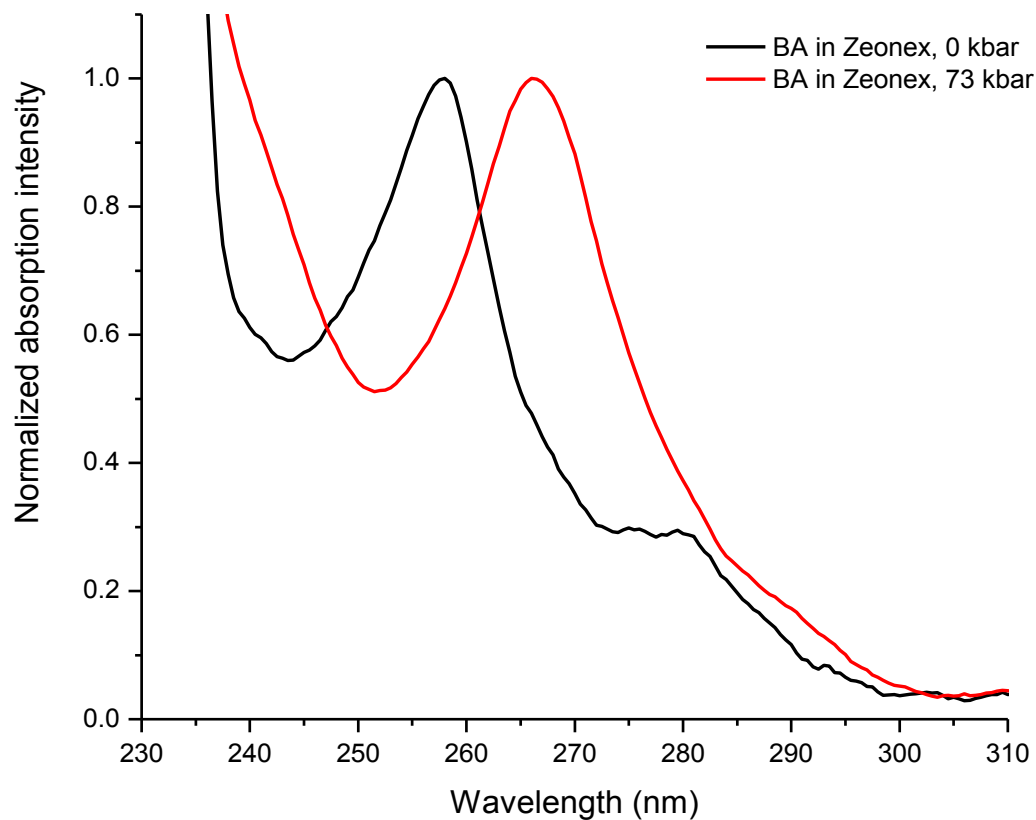
Figure A28: Uncorrected for the diamond absorption (in DAC) absorption spectra of BA in Zeonex before, black, and after, red, 73 kbar static pressure was applied to the sample film

### A.3.2.7 Spectral Reproducibility Control Measurements

A series of control experiments have been performed on films of BA dispersed in Zeonex polymer matrix. These were necessary to assure that no photochemical changes occur within the sample film exposed to light from the absorption spectrometer as well as whether the spectra collected are reproducible.

BA undergoes photoinduced intramolecular reaction when exposed to high-energy light. Monochromatic light is emitted from the absorption spectrometer that was used in data collection, Cary 500. Wavelengths used in our spectral experiments involve low- as well as high-energy photons (700 – 200 nm) of relatively low intensity. A film of BA dispersed in Zeonex was exposed to 20 absorption spectra lasting together over 60 minutes, in DAC at ambient pressure and room temperature conditions. The first absorption spectrum was compared to the very last in that series in Figure A29. The compared spectra are indistinguishable from each other which is a clear indication that the light emitted from Cary 500 did not induce photochemical changes within that time to the sample film.

We also removed the DAC with the polymer sample inside from its x,y,z-holder and put it back into the same position within seconds. The changes in the absorption spectra, Figure A30, reflect the slight difference in position of the DAC

within the focal point of the two plano-convex lenses. The variation in OD between the spectra at the maximum of absorption at ~ 257 nm is around 5.6 % and is most pronounced at shorter wavelengths.

In the last series we looked at changes occurring upon heating of the BA/Zeonex sample, Figure A31. A sample film was heated up in an air-tight glass capsule for about 2 hours at ~ 60 °C. After the sample film reached room temperature, the film was loaded into DAC and absorption spectrum was recorded. We have noticed slight differences between these two absorption spectra which are probably related to repositioning of the DAC within its holder (differences within 5%) rather than due to heating. Again, the changes are more pronounced at shorter wavelengths. We concluded that at temperatures up to 60 °C and times shorter than 2 hours no chemical reactions take place between BA and the polymer that we can register in absorption. Also, the molecules of BA did not seem to decompose nor react in any other way.
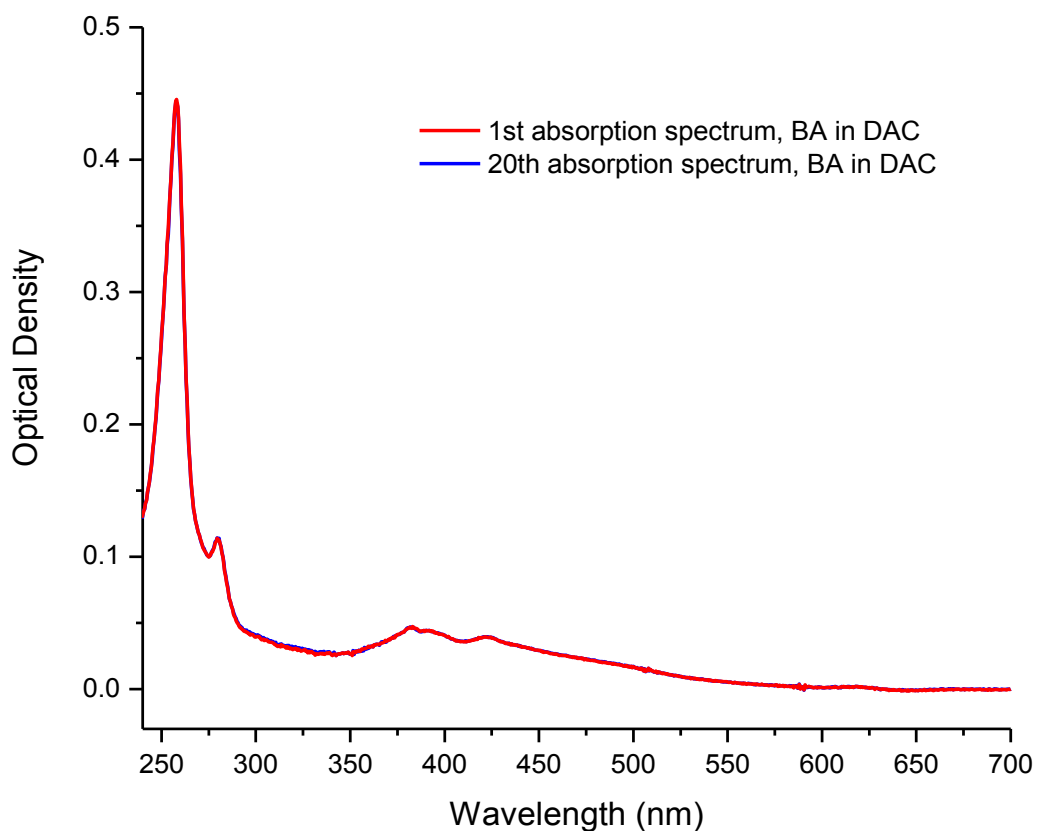
Figure A29: These two absorption spectra of BA/Zeonex film in DAC are indistinguishable from each other. This set represents a control experiment in which the sample film was kept within a DAC while numerous absorption spectra were collected. If the light emitted from the Cary 500 spectrometer caused photoreactions within the sample, the intensity of the BA absorption had decreased with each scan due to the formation of PI
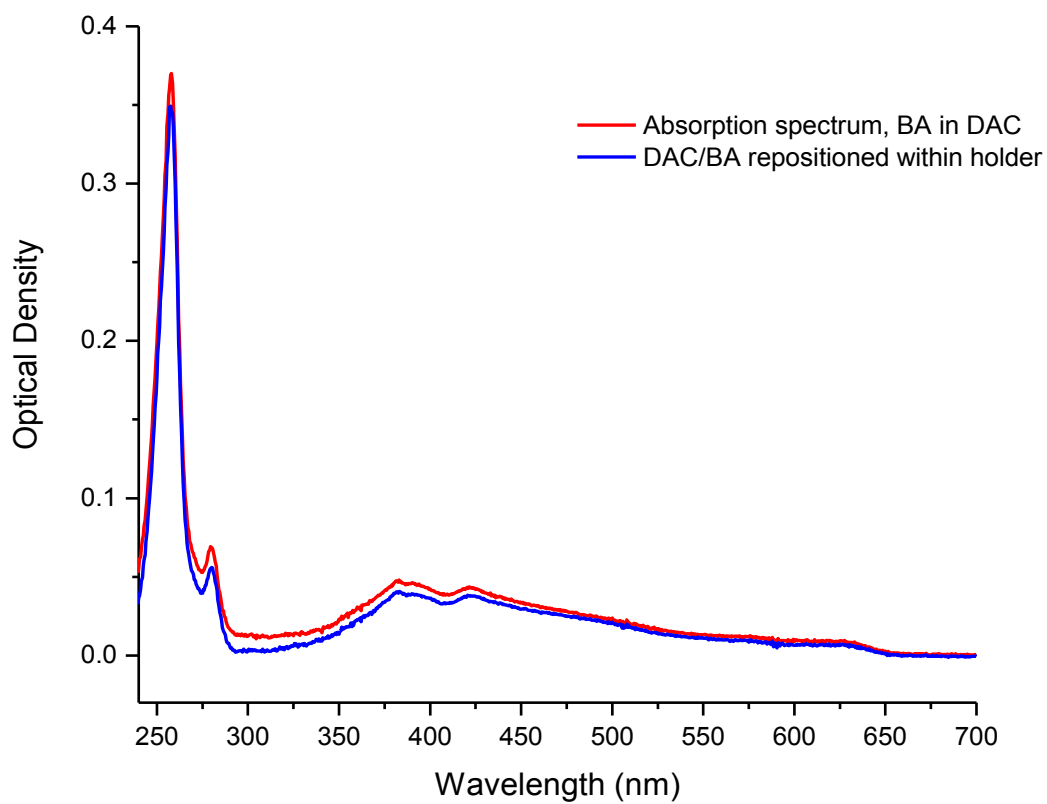
Figure A30: DAC with a BA/Zeonex film was removed from its holder within the Cary 500 spectrometer and put back in place. These absorption spectra represent the worst-case scenario. The reproducibility of the spectra at maximum of absorption ~ 257 nm is estimated at ~ 5.4%
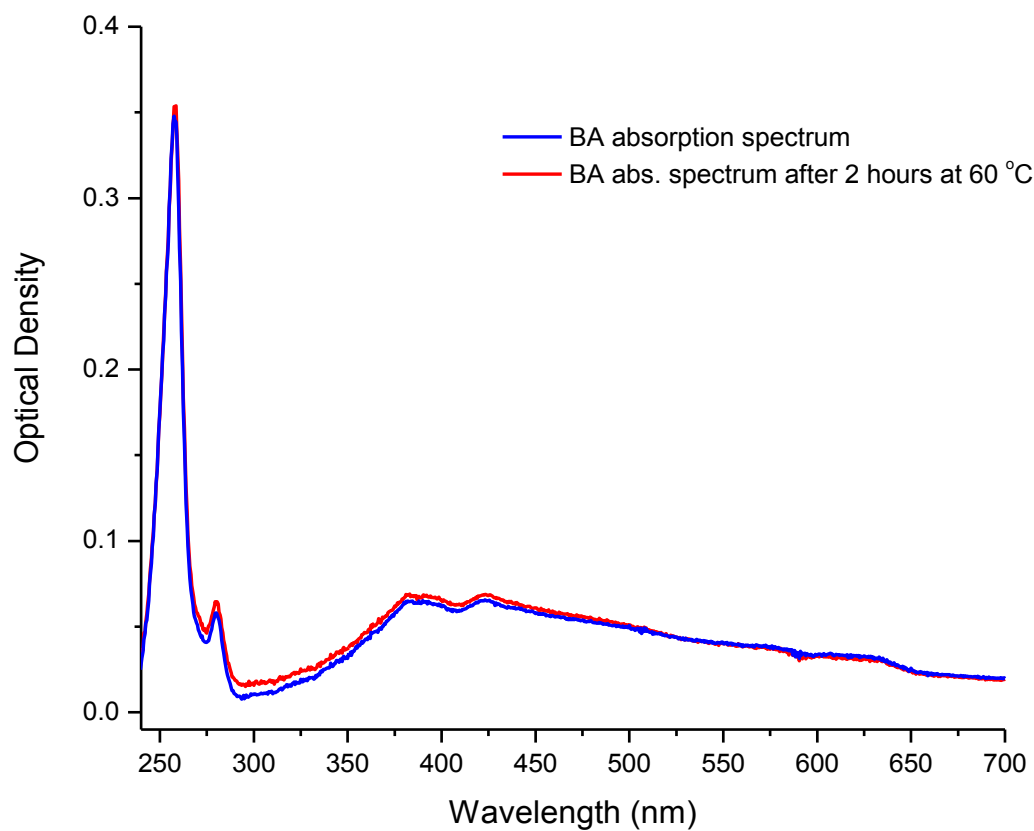
Figure A31: BA in Zeonex sample film was heated up to ~ 60 °C for about 2 hours and its absorption spectrum was compared to before heating. No significant changes have been observed between these two absorption spectra

A.3.3 References

(1)   Golden, J. H. *Journal of the Chemical Society* **1961**, 3741.
(2)   Cloninger, M. J.; Whitlock, H. W. *J Org Chem* **1998**, *63*, 6153.